MEASUREMENT OF THE $B_c^{\pm}$ MESON LIFETIME USING $B_c^{\pm} \to J/\psi\ \pi^{\pm}$ DECAYS

by

Hao Song

BE, Wuhan University, 2006

MS, Wuhan University, 2008

MS, University of Pittsburgh, 2010

Submitted to the Graduate Faculty of

the Department of Physics and Astronomy in partial fulfillment

of the requirements for the degree of

Doctor of Philosophy

University of Pittsburgh

2013

UNIVERSITY OF PITTSBURGH

DEPARTMENT OF PHYSICS AND ASTRONOMY

This dissertation was presented

by

Hao Song

It was defended on

October 25, 2012

and approved by

Professor Paul Shepard, Department of Physics and Astronomy

Professor Joseph Boudreau, Department of Physics and Astronomy

Professor Daniel Boyanovsky, Department of Physics and Astronomy

Professor Adam Lebovich, Department of Physics and Astronomy

Professor Manfred Paulini, Carnegie Mellon University Department of Physics

Dissertation Director: Professor Paul Shepard, Department of Physics and Astronomy

MEASUREMENT OF THE $B_c^{\pm}$ MESON LIFETIME USING $B_c^{\pm} \to J/\psi\ \pi^{\pm}$ DECAYS

Hao Song, PhD

University of Pittsburgh, 2013

This thesis describes a measurement of the lifetime of the $B_c^{\pm}$ meson in an exclusive decay channel $B_c^{\pm} \to J/\psi\ \pi^{\pm}$, where the J/ψ decays as $J/\psi \to \mu^+\ \mu^-$. The measurement uses a data sample with an integrated luminosity of 6.7 fb^{-1} collected at CDF. This is the first measurement of the $B_c^{\pm}$ meson lifetime in a hadronic channel and the measured lifetime, $\tau = 0.449\ ^{+0.054}_{-0.048}(stat.) \pm 0.019(syst.)$ ps, is in good agreement with previous results obtained from semileptonic decay channel and confirms previous measurements and theoretical predictions.

TABLE OF CONTENTS

LIST OF TABLES

LIST OF FIGURES

PREFACE

I would especially like to thank my advisor, Prof. Paul Shepard, for his encouragement and guidance throughout my graduate study. He has consistently supported me for the past three years and I would not be able to accomplish this without his help.

I greatly appreciate the effort of other committee members, Prof. Joseph Boudreau, Prof. Daniel Boyanovsky, Prof. Adam Lebovich, and Prof. Manfred Paulini, for the interesting questions and suggestions during my committee meetings.

I thank all the scientists, engineers and technicians from the CDF collaboration and the various divisions of Fermilab. I appreciate all the effort that they have made to make this result possible. I am grateful to have the opportunity to work with Dr. William Wester, Dr. Jeff Appel, Dr. Patrick Lukens, and Dr. Ronald Moore.

I would also like to thank my fellow students such as Guangtian Zhu, Xiaopeng Li, Feng Bi and Jen-Feng Hsu for their help during the past four years.

Finally, I thank my family for their encouragement and support throughout my life. I thank my parents, Fanyou Song and Jiangang Hu, for all of the love they have given me. They always allow me to pursue my interests and provide me unconditional support. My wife Yun Qin has played a significant role in my life since middle school. I feel so fortunate to have met her in my life. I thank her for all the help, support and understanding. I would also like to thank my grandparents, aunts, uncles and cousins for all the support they have provided. It really is a warm and big family.

1.0 INTRODUCTION

The B_c^- [2] meson is the ground state meson formed by a bottom quark b and a charm anti-quark $\bar{c}$, which was first discovered by the CDF collaboration at Fermilab in 1998 [3, 4]. Although its mass lies between that of the charmonium meson ($c\bar{c}$) and the bottomonium meson ($b\bar{b}$), the B_c^- meson is quite different because it is the only meson consisting of heavy quarks with different flavors. The charmonium and bottomonium mesons decay strongly and electromagnetically whereas the B_c^- meson decays weakly, which makes the B_c^- meson more stable and provides an unique window to study the weak decay. The B_c^- meson decay can be governed by the decay of the b or $\bar{c}$ quarks or can proceed through the annihilation of the b and $\bar{c}$ quarks. On one hand, the decay through the b quark to c quark provides a clean experimental signature since the decay products often contain a J/ψ meson, which further decays to $\mu^+ \mu^-$, that is very useful to reconstruct the decay event. On the other hand, the existence of the relatively heavy $\bar{c}$ anti-quark also has large contribution to the B_c^- meson decay width, resulting in the B_c^- meson lifetime being much shorter than other B mesons.

The lifetime of the B_c^- meson is the averaged proper decay time of B_c^- meson, where the proper decay time is defined as the time that a B_c^- meson can exist in its own rest frame $S^{'}$ before its decay. Since the measurement is carried out in a high energy collider where the B_c^- meson is produced with high momentum, any directly measured quantity is in the lab frame S, not the rest frame $S^{'}$. If we assume v is the velocity of the B_c^- meson in the lab frame and c is the speed of light, then the quantities β and γ, where $\beta = v/c$, and $\gamma = 1/\sqrt{1-\beta^2}$, can be used for a Lorentz transformation between the rest frame $S^{'}$ and the lab frame S. In the lab frame S, we can measure quantities such as the B_c^- meson mass m, its momentum p, and its decay length L which is the distance that a B_c^- meson can travel before its decay.

We then have following equations that relate these quantities

$$p = \beta\gamma mc \tag{1.1}$$

$$v = \beta c \tag{1.2}$$

$$L = vt \tag{1.3}$$

where t is the time that a B_c^- meson exists before its decay in the lab frame S. Based on these equations, t can be expressed as

$$\begin{aligned} t &= L/v \\ &= L/\beta c \\ &= \gamma mL/p \end{aligned} \tag{1.4}$$

The last step to calculate the proper decay time $t^{'}$ in the rest frame $S^{'}$ is simply a Lorentz transformation of time dilation, which gives

$$\begin{aligned} t^{'} &= \frac{t}{\gamma} \\ &= \frac{mL}{p} \end{aligned} \tag{1.5}$$

One can define another useful quantity, the proper decay length of the B_c^- meson, as the distance that light can travel during the lifetime of the B_c^- meson

$$ct^{'} = \frac{mcL}{p} \tag{1.6}$$

This quantity is useful because it is another way to represent the lifetime since these two quantities differ only by a constant quantity, the speed of light c. From Eq. 1.6 one can see that a lifetime measurement requires the determination of the B_c^- mass, its decay length and its momentum. The determination of decay length requires the measurement of two positions, the first being the position where the B_c^- meson is produced and the second being the position where it decays. Since the lifetime measurement in this thesis is carried out at the Collider Detector at Fermilab (CDF) which does not have a precise position measurement along the colliding beam direction (defined as the z direction) compared to the transverse plane, i.e., the $x - y$ plane that is perpendicular to the beam direction, the right hand side

of Eq. 1.6 is projected to the transverse plane by multiplying $\sin\theta$ to both the numerator and the denominator, where θ is the common polar angle for both $\vec{L}$ and $\vec{p}$ since these two vectors necessarily point to the same direction, and gives

$$\begin{aligned} ct' &= \frac{mcL\sin\theta}{p\sin\theta} \\ &= \frac{mcL_{xy}}{p_T} \end{aligned} \tag{1.7}$$

where L_{xy}, also known as L_T, is the transverse decay length that the B_c^- meson travels before its decay, and p_T is the transverse momentum. It should be noted that the transverse decay length L_{xy} is a very short distance. For example, using the current determination of the B_c^- meson mass [5] of 6.2756 GeV/c^2, a B_c^- meson with p_T = 8 GeV/c and proper decay time of 0.6 ps gives a result of $L_{xy} = 229$ μm, or 0.229 mm. Thus, a precise position measurement in this thesis is crucial to the determination of the B_c^- meson lifetime. The B_c^- meson lifetime measurement in this thesis uses the hadronic decay channel $B_c^- \to J/\psi\ \pi^-$ which is illustrated in Figure 1 where the decay is shown in the transverse plane. The B_c^- meson is produced at a primary vertex (PV) and decays at a secondary vertex (SV). The decay product J/ψ meson further decays as $J/\psi \to \mu^+\ \mu^-$. As a short-lived particle compared to the B_c^- meson, the J/ψ meson can be safely assumed to decay at the secondary vertex. Since the proper decay time in the rest frame (t') is used frequently while the decay time in the lab frame (t) is seldom, if ever, used, we will use t to represent the proper decay time and ct to represent the proper decay length from now on. Also, the term "lifetime" will be used interchangeably to represent either the averaged proper decay time or the averaged proper decay length, depending on the associated unit being ps or μm.

Many theoretical techniques, including the operator product expansion (OPE) and QCD sum rules, have been used to predict the lifetime of the B_c^- meson. These theories all agree that the B_c^- meson lifetime falls in the range of $0.4 \sim 0.7$ ps [6, 7, 8], which is about 1/3 of the B_u^- meson lifetime of 1.64 ps. However, their predictions for the B_c^- meson lifetime do not agree very well and the results depend on some input parameters such as the effective mass of the b and c quarks, and the weak decay constant f_{B_c}. Thus, a measurement of the B_c^- meson lifetime can test the most precise theoretical predictions. Previously, The B_c^- meson lifetime has been measured by CDF and D0 in the semileptonic channel

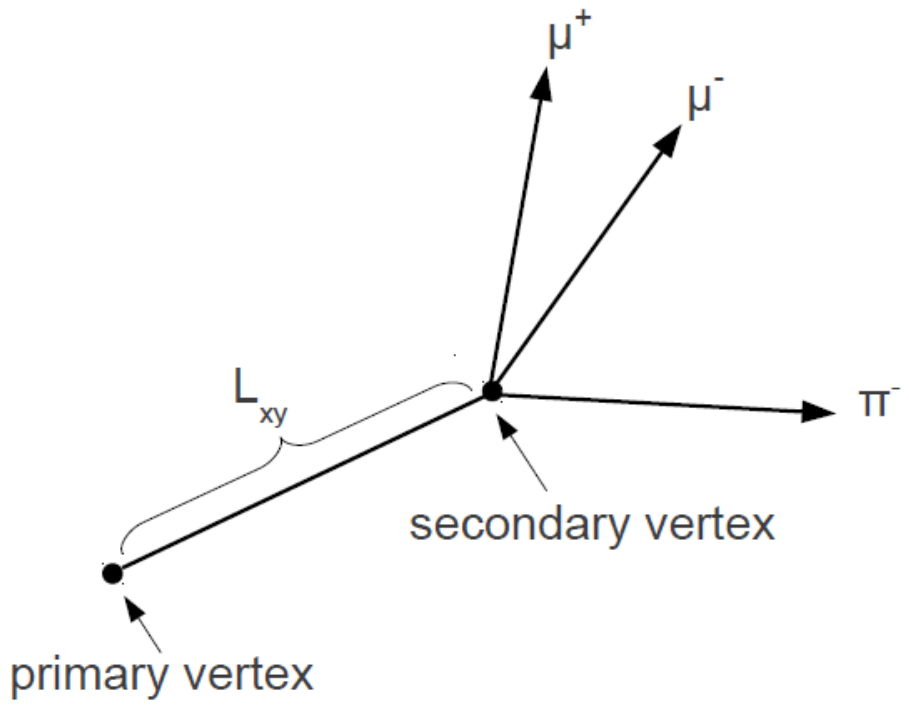

Figure 1: Illustration of $B_c^- \to J/\psi\ \pi^-$ decay in the transverse plane where J/ψ decays as $J/\psi \to \mu^+\ \mu^-$. The B_c^- meson is produced at primary vertex and decays at secondary vertex. L_{xy} is the distance between primary vertex and secondary vertex in the transverse plane. For a B_c^- meson with p_T equals 8 GeV/c and proper decay time of 0.6 ps, the L_{xy} is only 229 μm, or 0.229 mm.

$B_c^- \to J/\psi\ \ell^-\ X$ where the J/ψ decays to $\mu^+\ \mu^-$, ℓ^- is either an e^- or a μ^- and X is the corresponding neutrino. The observation of the B_c^- meson through the combined electron and muon channels at CDF measured its lifetime as $\tau = 0.46\ ^{+0.18}_{-0.16}(stat.) \pm\ 0.03(syst.)$ ps [3, 4]. A later CDF measurement carried out in the electron channel gives a B_c^- meson lifetime of $\tau = 0.463\ ^{+0.073}_{-0.065}(stat.) \pm\ 0.036(syst.)$ ps [9], and a D0 measurement carried out in the muon channel gives $\tau = 0.448\ ^{+0.038}_{-0.036}(stat.) \pm\ 0.032(syst.)$ ps [10]. A newer CDF result in the semileptonic decays which combines both electron and muon channels gives $\tau = 0.475\ ^{+0.053}_{-0.049}(stat.) \pm\ 0.018(syst.)$ ps [11]. These measurements are all consistent with the theoretical predictions. However, one disadvantage of the semileptonic channel measurement is having an undetected neutrino in the decay products, which makes it impossible to fully reconstruct the B_c^- meson decay events. The lifetime measurement in this thesis uses the hadronic decay channel $B_c^- \to J/\psi\ \pi^-$ that can be fully reconstructed. This thesis uses data collected from $p\bar{p}$ collisions at a center of mass energy of 1.96 TeV as recorded by the Collider Detector at Fermilab (CDF II). The result is based on a data sample with an integrated luminosity of 6.7 fb^{-1}, and is the first measurement of the B_c^- meson lifetime in a fully-reconstructed hadronic channel.

The thesis is organized as follows. Chapter 2 provides an overview of the standard model, and particularly the theory about the strong production and the weak decay of the B_c^- meson. Chapter 3 describes the Fermilab Tevatron and the CDF II Detector. Chapter 4 discusses the event reconstruction and selection used in this analysis. Chapter 5 describes the construction of the likelihood fitter which is used to extract the B_c^- meson lifetime, as well as the fitted lifetime result. Chapter 6 discusses the systematic uncertainties in the measurement. Chapter 7 discusses the comparison with previous measurements as well as the theoretical predictions, and gives the conclusion.

2.0 THEORETICAL OVERVIEW

2.1 THE STANDARD MODEL

The standard model is a theory that describes the interactions between elementary particles in particle physics. It is so far our best understanding of fundamental particles as well as their interactions. In the standard model, all fundamental particles are categorized into two groups based on their spin. Particles with half integer spin are called fermions while particles with integer spin are called bosons.

Table 1 shows twelve elementary fermions organized in three generations. Six of the fermions are called quarks while the remaining six are leptons. The six quarks can further be categorized as up-type quarks with electric charge of +2/3 and down-type quarks with electric charge of -1/3. The six leptons can be categorized as neutrinos with no electric charge and charged leptons with electric charge of -1. Particles in the first generation are the building blocks of ordinary matters. The proton, for example, consists of two up quarks and one down quark. Quarks and charged leptons in the second and third generations are heavier than those in the first generation and eventually decay to the corresponding particles in the first generation via electroweak interaction. The neutrinos were originally assumed to be massless, however, current experimental results have shown that they do have non-zero masses. Fortunately, their masses are far smaller than the other fermions in Table 1 and most of the time we can still safely assume they are massless.

The bosons listed in Table 2 are the force carriers in the standard model. The strong interaction is mediated by massless spin 1 gluons and is the strongest force. The electromagnetic interaction is mediated by massless spin 1 photon, its strength is less compared with strong interaction. The strength of weak interaction is even small, because of its massive

Table 1: Table of elementary fermions in the standard model

	Charge	1st Generation	2nd Generation	3rd Generation
Quarks	2/3	Up (u)	Charm (c)	Top (t)
	-1/3	Down (d)	Strange (s)	Bottom (b)
Leptons	-1	Electron (e)	Muon (μ)	Tau (τ)
	0	Electron neutrino (ν_e)	Muon neutrino (ν_μ)	Tau neutrino (ν_τ)

mediator $W^{\pm}, Z$ bosons. The strength of gravity is so small that we can normally ignore it.

Table 2: Table of elementary bosons in the standard model

Boson	Electric Charge	Carrying Force	Range (cm)	Relative Strength
gluon	0	Strong	10^{-13}	1
γ	0	Electromagnetic	∞	10^{-2}
$W^{\pm}, Z$	$\pm$,0	Weak	10^{-16}	10^{-6}
graviton	0	Gravity	∞	10^{-40}

It should be noted that for every particle in Table 1 and Table 2, there is a corresponding antiparticle with the same mass but opposite electric charge. The antiparticle is denoted by putting a bar over the corresponding particle, $u \to \bar{u}$, or simply changing the sign of the electric charge, $e^- \to e^+$. Particles that are their own antiparticles are electric neutral, such as γ and Z bosons. However, the reverse is not always true. For example, the antiparticle of electron neutrino ν_e is $\bar{\nu_e}$ instead of ν_e itself.

2.1.1 Electroweak interaction

In the 1960s, the electromagnetic interaction and weak interaction are unified in the electroweak theory by Weinberg, Salam and Glashow [12, 13, 14]. The theory describes an $SU(2)_L \times U(1)_Y$ gauge group that represents the local gauge symmetry in the Lagrangian.

To account for parity violation in the weak interaction, the $SU(2)_L$ symmetry only applies to the left-handed fermions and makes transformations within the quark doublets:

$$\begin{pmatrix} u \\ d \end{pmatrix}_L \begin{pmatrix} c \\ s \end{pmatrix}_L \begin{pmatrix} t \\ b \end{pmatrix}_L \tag{2.1}$$

and lepton doublets:

$$\begin{pmatrix} \nu_e \\ e \end{pmatrix}_L \begin{pmatrix} \nu_\mu \\ \mu \end{pmatrix}_L \begin{pmatrix} \nu_\tau \\ \tau \end{pmatrix}_L \tag{2.2}$$

The $U(1)$ symmetry has a corresponding gauge boson B, while the $SU(2)_L$ gauge bosons are described by the three component isospin triplet W^a. For the theory to be renormalizable B and W^a should be massless, but the experimental result shows that the mediating bosons of the weak force do have non-zero mass. This conflict is implemented through the so called Higgs Mechanism [15], which provides an additional scalar field and leads to massive boson through spontaneous symmetry breaking. Under this symmetry breaking, three out of four gauge bosons acquire a mass, while the remaining massless boson to be photon. The three massive bosons are the $W^\pm$ that mediate charged-current weak interaction and Z boson which mediates neutral-current weak interaction. The large masses of the gauge bosons are responsible for the short range of the weak force and the weakness of the weak interactions. The success of the electroweak theory was established by the observation of the neutral-current weak interaction in 1973 [16] and the discovery of the $W^\pm, Z$ bosons in 1983 [17]. The Higgs boson, the quantum of the Higgs field, has been the target of a long search in particle physics for many years. In 2012, the combined results from the CDF and D0 collaborations [18] have found evidence of a new particle consistent with the Higgs boson, and the ATLAS [19] and CMS [20] collaborations have observed a new particle in the same mass region as in Ref [18], which is also consistent with the long-expected Higgs boson.

In the electroweak theory, the basic interaction terms between gauge bosons and the fermions are shown in Figure 2 where the photon couples with two charged fermions of same flavor, $W^\pm$ bosons couple with one charged fermion and its corresponding neutrino, and Z boson couples with two charged fermions or two neutrinos of same flavor. In these diagrams time flows horizontally to the right and a line running backward in time (an arrow pointing to

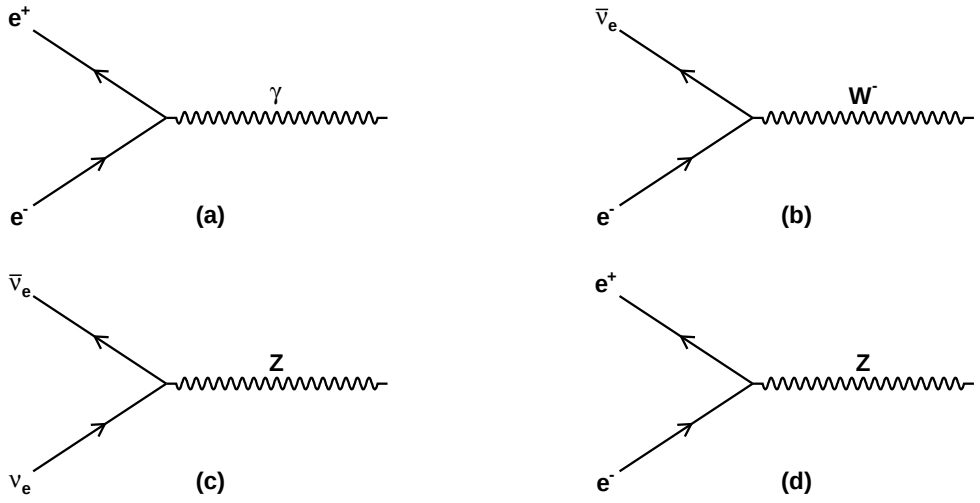

Figure 2: Basic interaction terms in the electroweak theory via the (a) photon, (b) W boson and (c), (d) Z boson. In these diagrams time flows horizontally to the right and a line running backward in time (an arrow pointing to the left) is interpreted as an antiparticle going forward in time.

the left) is interpreted as an antiparticle going forward in time. The strength of the coupling between the photon and the charged fermions is given by the fine structure constant:

$$\alpha = \frac{e^2}{\hbar c} \approx \frac{1}{137} \tag{2.3}$$

The coupling of the fermions with the massive gauge bosons is suppressed by the squared mass of the gauge boson relative to the photon coupling. The current determination of the $W^{\pm}$ and Z bosons mass are $m_W = 80.399 \pm 0.023$ GeV/c^2 and $m_Z = 91.1876 \pm 0.0021$ GeV/c^2 [21]. The basic interaction terms shown in Figure 2 can be used to construct the Feynman diagram, which is used to describe the electroweak interaction process. Figure 3 shows the leading order Feynman diagrams for e^+e^- scattering through the electroweak

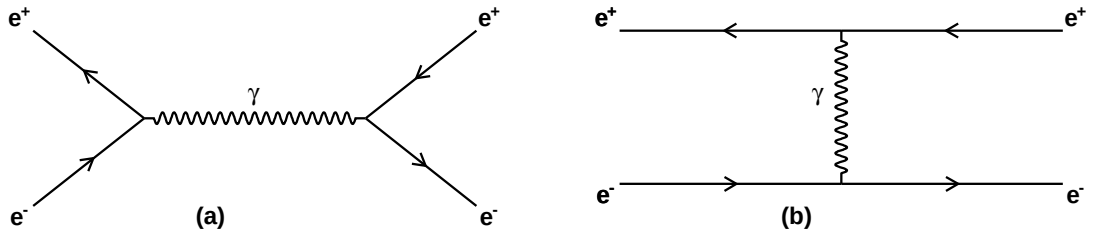

Figure 3: Leading order Feynman diagrams that represent e^+e^- scattering through the photon in the electroweak interaction. The two vertices in each diagram means that the amplitude is proportional to the square of the coupling parameter α.

interaction. The presence of two vertices indicates that the amplitude is proportional to the square of the coupling parameter α. The dominant contribution of the electroweak interaction comes from the leading order Feynman diagrams which have the least vertices since the coupling parameter α is very small.

It should be noted that the charged-current weak interaction via $W^{\pm}$ bosons is the only interaction that couples particles with different flavors. It is thus the only source for flavor changing in the Standard Model. The electromagnetic and strong interactions will only produce flavors in particle-antiparticle pairs, where the total flavor is unchanged between initial and final states.

2.1.2 Strong interaction

The strong force, also known as Quantum ChromoDynamics (QCD), describes the interaction between the quarks and the gluons. The strong interaction between the quarks makes them always found in composite particles named hadrons. The hadrons exist as either mesons with integer spins composited by $q_1\bar{q}_2$, or baryons with half integer spins composited by $q_1q_2q_3$ or $\bar{q}_1\bar{q}_2\bar{q}_3$. In the 1940s-60s when the concept of quark was not developed, a large number of particles were discovered, and the so-called Eightfold Way was introduced by Murray Gell-Mann in 1961 to arrange these particles into geometrical patterns according to their electric charge (Q) and a new quantum number called strangeness (S). Figure 4 shows the meson

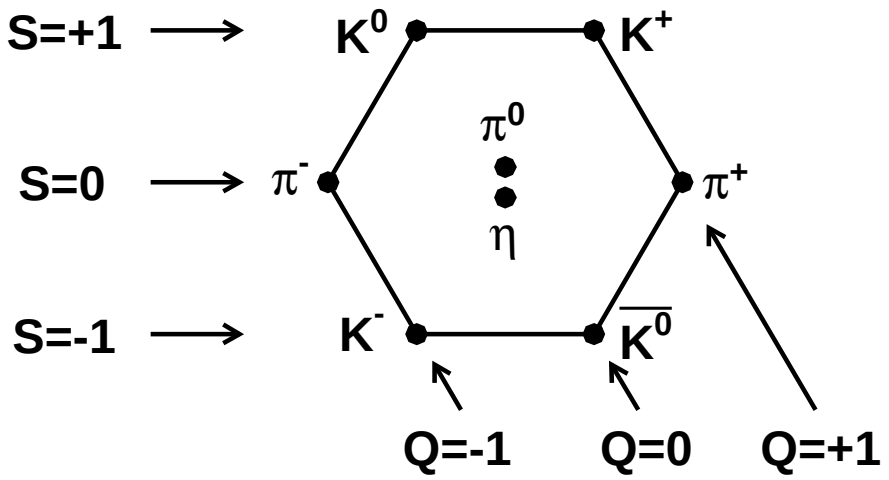

Figure 4: Mesons in the spin 0 octet.

octet for spin 0 mesons. The concept of quark was then proposed by Gell-Mann [22] in 1964 to explain this symmetric pattern of these particles, where the quarks come in three different flavors, known as u, d and s, forming mesons in quark-antiquark pairs or baryons in three quarks or antiquarks.

The color charge was later introduced [23] to explain the existence of the Δ^{++} particle, which consists of three u quarks with parallel spins. From Pauli exclusion principle we know that no two fermions can occupy the same state, so the existence of the Δ^{++} particle seems to be inconsistent with the Pauli principle since all three u quarks have the same spin. With

the new quantum number named color, each u quark carries a different color between red (r), green (g) and blue (b), thus the three u quarks that make up the Δ^{++} are not identical. The particles observed in nature are all "colorless", or more precisely they are in a color singlet state formed by the three colors. The gauge bosons of the strong interaction, gluons, are mixture of two colors in the color octet and thus carry colors themselves.

The interactions in the strong interaction between the gluons and the quarks are shown in Figure 5. Note that in the strong interaction the gauge bosons couples with themselves

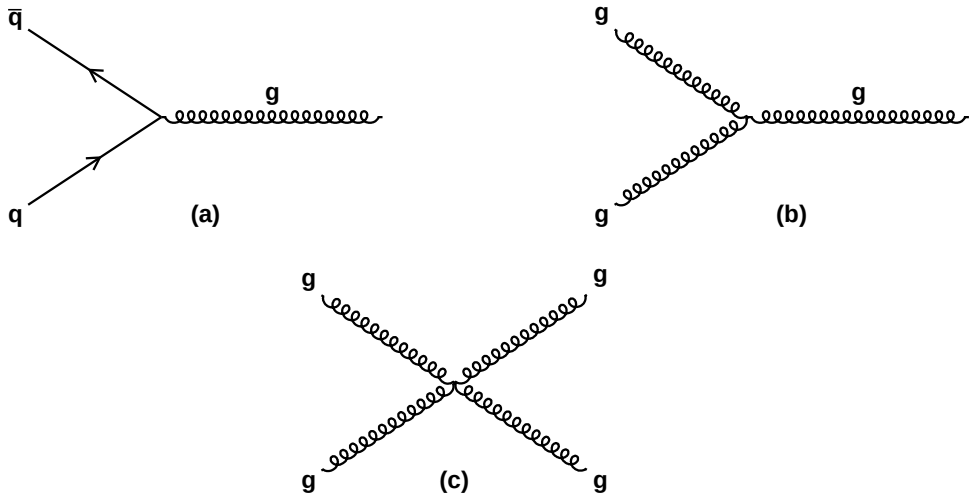

Figure 5: Basic interaction terms in the strong interaction.

as well since they also carry colors.

Another important feature of the strong interaction is the so called color confinement which states that color charged particles (such as quarks) can not be isolated and directly observed. As two quarks separate, the gluon fields form narrow strings of color charge which tends to bring the quarks together. This is quite different from the separation of electrically charged particle where the electric field between them diminish quickly. The energy in the gluon field increases as the separation distance between the quarks gets larger, and a new $q\bar{q}$ pair will be created from the vacuum when sufficient energy is available in the gluon field. The new $q\bar{q}$ pair and the original $q\bar{q}$ pair then preserve color confinement. Figure 6 illustrates the process of color confinement.

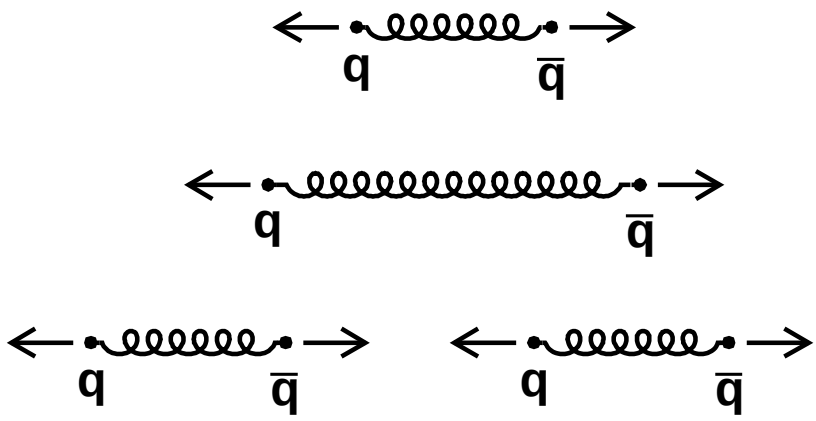

Figure 6: Illustration of color confinement.

The phenomenon known as asymptotic freedom [24, 25] states that the coupling constant of the strong interaction, α_s, is not a constant at all, but depends on the separation distance between the interacting particles. It is thus called running coupling constant which is quite small at very short distance (high energy scale), but gets bigger when the separation distance is relatively large (small energy) as shown in Figure 7 [26]. The result of the asymptotic freedom is that the coupling between quarks at high energy is relatively weak and can be treated with a perturbative expansion in powers of the coupling constant [27].

It should be noted here that the quarks not only couple with gluons through strong interaction, but also couple with γ, $W^{\pm}$, and Z bosons through electroweak interaction, as shown in Figure 8. The coupling through the γ and Z bosons are often suppressed by the strong gluon coupling. The coupling through the $W^{\pm}$ bosons, however, is important because it is the only source that changes the quark flavors, even between different generations.

Ordinarily, the coupling with the $W^{\pm}$ bosons should happen between quarks within the same generation since each generation is represented by a $SU(2)_L$ gauge group. For example, the c quark can decay to a s quark by coupling with a W^+ boson, but not to a d quark. If this were true, the meson which contains a s quark and a $\bar{u}$ anti-quark, K^-,

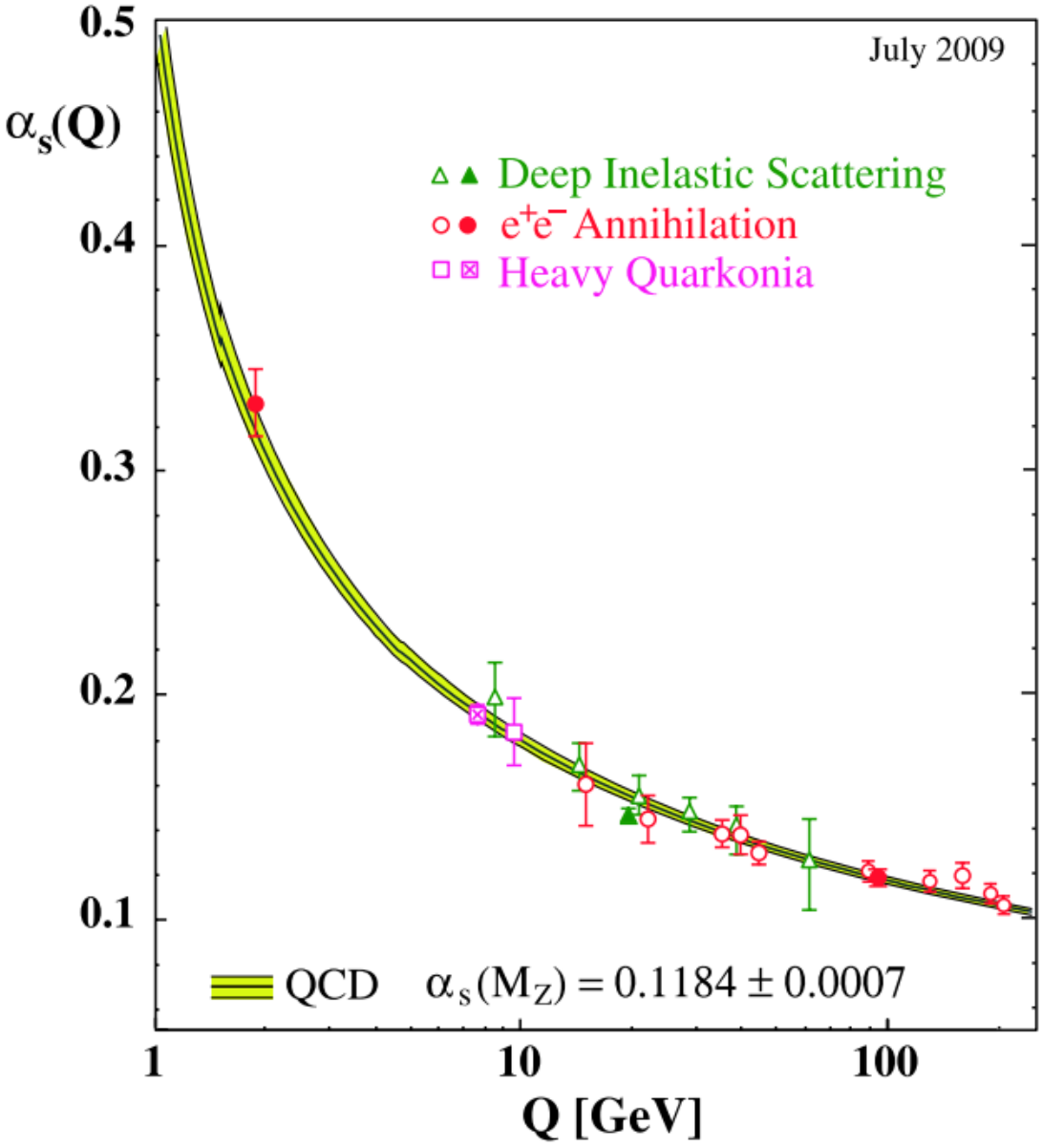

Figure 7: Summary of measurements of α_s as a function of the respective energy scale Q.

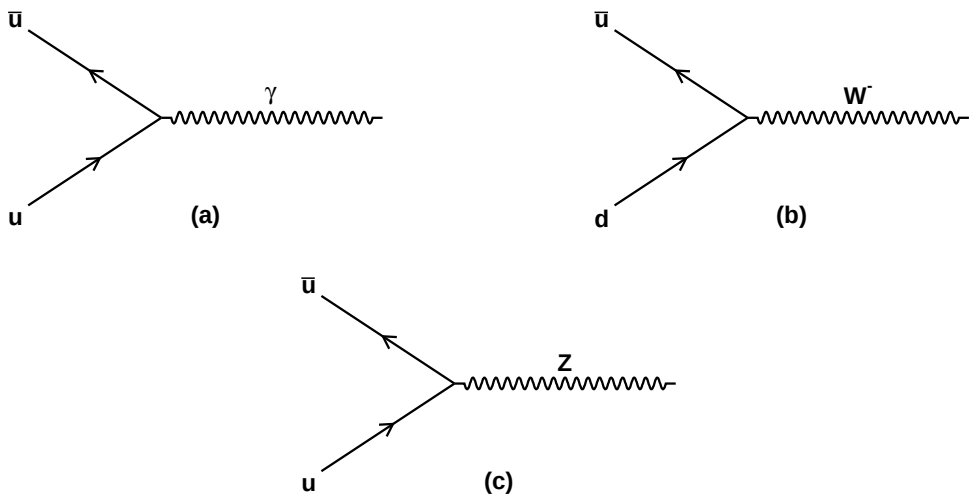

Figure 8: Coupling of quarks with electroweak gauge bosons.

should be a stable particle. However, the K^- meson is not stable, it can decay to $\mu^- + \nu_\mu$ 63% of the time, or to $\pi^- + \pi^0$ 21% of the time. This indicates that transition between quarks from different generations does exist. The solution for this problem is to use a set of weak eigenstates in the weak interaction that is different from their mass eigenstates. The Cabibbo-Kobayashi-Mashkawa (CKM) matrix is used to describe the mismatch between the two sets of eigenstates. This matrix was introduced by Kobayashi and Maskawa [28], adding one generation to the matrix previously introduced by Cabibbo [29] The CKM matrix relates the mass eigenstates of down-type quarks $|d\rangle$, $|s\rangle$, $|b\rangle$ to its corresponding weak eigenstates $|d'\rangle$, $|s'\rangle$, $|b'\rangle$ as

$$\begin{bmatrix} |d'\rangle \\ |s'\rangle \\ |b'\rangle \end{bmatrix} = \begin{bmatrix} V_{ud} & V_{us} & V_{ub} \\ V_{cd} & V_{cs} & V_{cb} \\ V_{td} & V_{ts} & V_{tb} \end{bmatrix} \begin{bmatrix} |d\rangle \\ |s\rangle \\ |b\rangle \end{bmatrix} \tag{2.4}$$

Currently, the best determination of the magnitudes of the CKM matrix elements [21]

$$\begin{bmatrix} V_{ud} & V_{us} & V_{ub} \\ V_{cd} & V_{cs} & V_{cb} \\ V_{td} & V_{ts} & V_{tb} \end{bmatrix} = \begin{bmatrix} 0.97428 \pm 0.00015 & 0.2253 \pm 0.0007 & 0.00347^{+0.00016}_{-0.00012} \\ 0.2252 \pm 0.0007 & 0.97345^{+0.00015}_{-0.00016} & 0.0410^{+0.0011}_{-0.0007} \\ 0.00862^{+0.00026}_{-0.00020} & 0.0403^{+0.0011}_{-0.0007} & 0.999152^{+0.000030}_{-0.000045} \end{bmatrix} \tag{2.5}$$

shows that the diagonal elements with magnitude ~ 1 and off-diagonal elements $<< 1$. Note that the CKM matrix is actually a complex matrix with the complex phase being responsible for the CP violation.

2.2 THE B_c^- MESON

The B_c^- meson, the ground state of $b\bar{c}$ bound states, provides a unique window for the study of weak decays. Although it is intermediate to the charmonium and bottomonium mesons, the B_c^- meson is quite different because it is the only meson consisting of heavy quarks with different flavors. The B_c^- meson cannot annihilate into gluons because it carries open flavor, which makes it more stable than the charmonium and bottomonium mesons with hidden flavor. The charmonium and bottomonium mesons decay strongly and electromagnetically whereas the B_c^- meson decays weakly. As a result, several theoretical approaches including potential models, operator product expansions, and QCD sum rules can be tested in the B_c^- system.

The following subsections contain a discussion of the theoretical approaches for calculating properties of the B_c^- meson including B_c^- production and B_c^- decay properties.

2.2.1 The B_c^- production

The production of B hadrons at Fermilab can be described by a two step process. The first step involves the production of $b\bar{b}$ pair from the $p\bar{p}$ collision, and the second step is the hadronization (or fragmentation) of the b quarks to form B hadrons.

At Fermilab, the proton and antiproton are colliding at a center-of-mass energy equal to 1.96 TeV. At such high energies, the interactions are between the quark and gluon components in the proton and antiproton instead of the colliding proton and antiproton as a whole. The interactions between quarks and gluons or between gluons themselves then produce $b\bar{b}$ pairs. The production process can be described by the Feynman diagrams, and some of them are shown in Figure 9. Note that these diagrams include not only the leading

order (α_s^2) but also the next leading order (α_s^3) contributions.

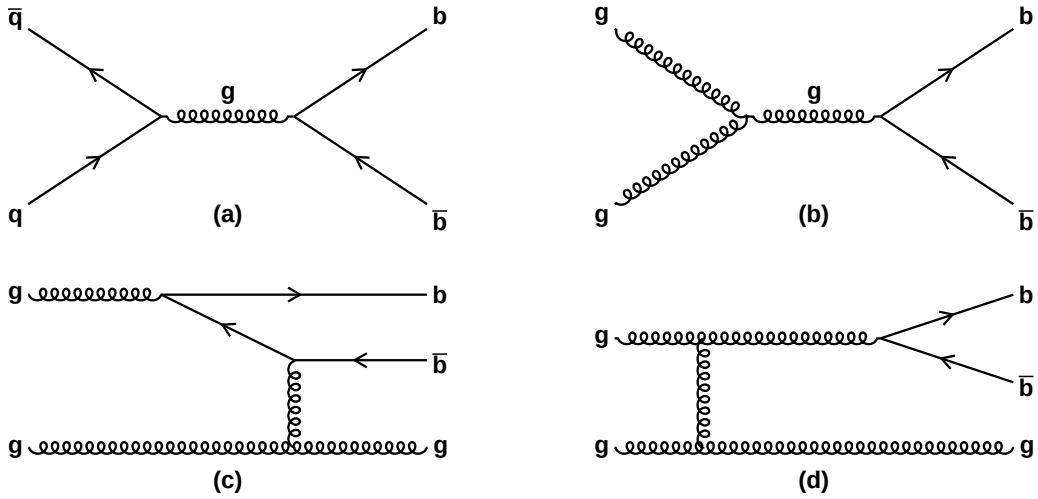

Figure 9: Representative Feynman diagrams for $b\bar{b}$ production in leading order α_s^2 ((a) and (b)) and next leading order α_s^3 ((c) and (d)).

The production of lighter B mesons, such as B_u^-, involves the production of a $b\bar{b}$ pair which subsequently fragment. The production of B_c^- meson is quite different in the sense that an additional heavy quark-antiquark pair ($c\bar{c}$) will also have to be created during the fragmentation of $b\bar{b}$ pair. In the Lund string model for fragmentation, the approximate ratios of $q\bar{q}$ pairs produced are $u : d : s : c \approx 1 : 1 : 0.3 : 10^{-11}$ [30]. This suggests that B_c production through fragmentation of $b\bar{b}$ will be quite rare compared to the production of the lighter B mesons. Table 3 shows the B hadron production fraction during the hadronization of the b quark.

Theoretical calculations based on perturbative QCD (pQCD) have shown that the dominant mode of the B_c^- production at Fermilab is through the gluon-gluon fusion process $g + g \to B_c^- + \bar{b} + c$ [1, 31]. Other processes also contribute to its production but less significantly. They include light quark-antiquark fusion, $q + \bar{q} \to B_c^- + \bar{b} + c$ where $q = u, d, s$, and heavy sea quark production $g + b \to B_c^- + c$ or $g + \bar{c} \to B_c^- + \bar{b}$. Figure 10 shows some Feynman diagrams that contribute to B_c production from these different processes. The general-mass variable-flavor-number (GM-VFN) scheme [32] is proposed to improve the

Table 3: Production fractions of B hadrons. Charge conjugate hadrons exist with the same production rates.

B Hadron	Production Fraction (%) [21]
B^0 or B_d	40.1 ± 0.8
B^+ or B_u	40.1 ± 0.8
B_s^0	10.5 ± 0.6
B Baryons	9.3 ± 1.6
B_c^+	$<< 1$

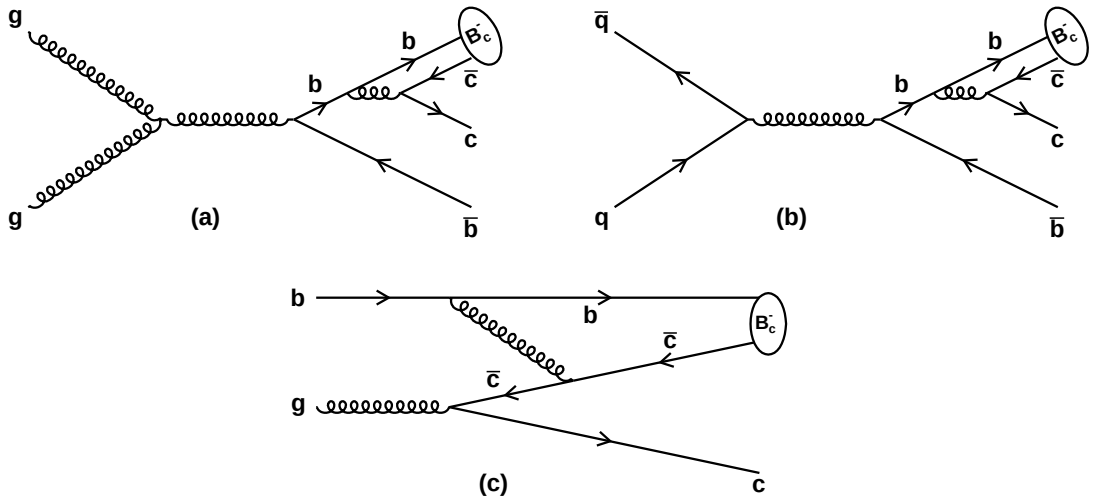

Figure 10: Representative Feynman diagrams that contribute to the production of B_c mesons in $p\bar{p}$ interactions. (a) represents dominant contribution from gluon-gluon fusion $g + g \rightarrow B_c^- + \bar{b} + c$. (b) represents small contribution from light quark-antiquark fusion $q + \bar{q} \rightarrow B_c^- + \bar{b} + c$ where $q = u, d, s$. (c) represents small contribution from heavy sea quark process $g + b \rightarrow B_c^- + c$.

fixed-flavor-number (FFN) [33] calculations for the B_c^- cross section. In the FFN calculation, the flavor content that participates in the B_c^- production is considered fixed and includes only the light flavors. The GM-VFN calculation, on the other hand, includes the production contribution from variable flavor numbers. An example of such contribution is that a gluon splits into an heavy quark-antiquark pair, and the quark or anti-quark then participates in a hard scattering with the gluon, producing a B_c^- meson. These heavy sea quark productions are essentially 2-body $\rightarrow$ 2-body processes in the order of α_s^3 (Figure 10 (c)), where the gluon-gluon fusion or light quark-antiquark fusion are 2-body $\rightarrow$ 3-body processes in the order of α_s^4 (Figure 10 (a) and (b)). In order to compute the contribution from these heavy quark productions, one needs to assume massless c (or $\bar{c}$) and b (or $\bar{b}$) parton distribution functions which is only valid to the physical process at high momentum transfer. The GM-VFN approach, as its name suggests, can correctly take into account the heavy quark mass dependence for physical process involving both high and low momentum transfer.

The GM-VFN approach is used in Ref. [1] to calculate the cross section of the B_c^- meson. In this reference, the cross section of the spin 1 excited state B_c^{*-} meson is also considered. The mass of the excited state B_c^{*-} meson, as calculated in Ref [34, 35], is less than 100 MeV/c^2 above the ground state, thus it can only decay to the ground state B_c^- meson with the emission of a photon. In fact, the predicted B_c^{*-} cross section (2.28 nb) is $\sim$ 3 times larger than that of the ground state B_c^- meson (0.709 nb) [1] in the $p_T > 4$ GeV/c and $|y| < 0.6$ region (y means rapidity whose definitions is given in Eqn. 3.2). In contrast, the cross section of the B_u^- meson is measured at Tevatron as 2.78 ± 0.24 μb [36] in the $p_T > 6$ GeV/c and $|y| < 1$ region. Although the p_T and $|y|$ regions are not the same, one can still find the significant difference between B_c^- and B_u^- mesons.

2.2.2 The B_c^- lifetime

The B_c^- meson decay processes can be divided into three classes, as shown in Figure 11:

- the b quark decays with a spectator $\bar{c}$ anti-quark.
- the $\bar{c}$ anti-quark decays with a spectator b quark.
- the annihilation channel $B_c^- \rightarrow W^- \rightarrow l\bar{\nu}_l$ (or $s\bar{c}$), where $l = e, u, \tau$.

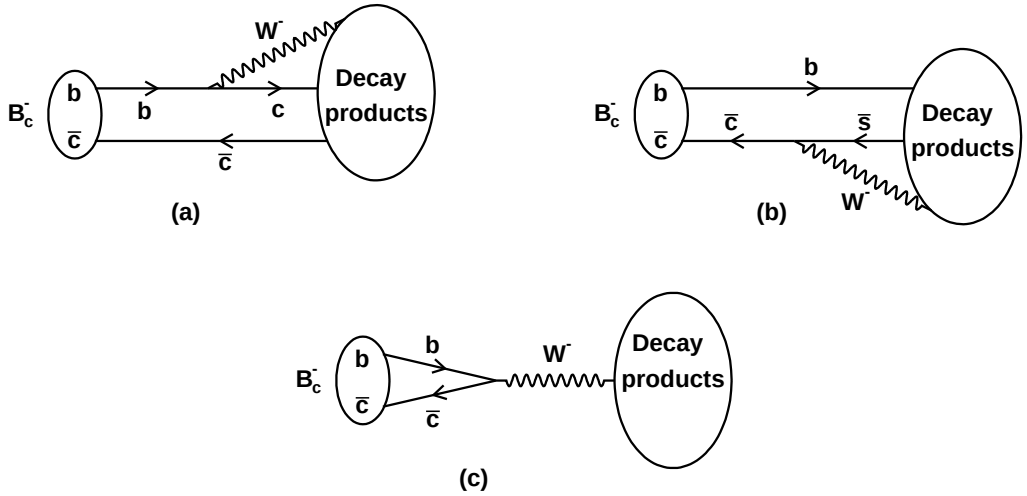

Figure 11: Inclusive decay modes that contribute to the B_c^- meson total decay width. Decays can happen through the b quark (a), the $\bar{c}$ anti-quark (b), or weak annihilation of the b quark and $\bar{c}$ anti-quark (c).

The total width is the sum of the partial widths

$$\Gamma(B_c^- \ \to X) = \Gamma(ann.) + \Gamma(b \to X) + \Gamma(\bar{c} \to X) \tag{2.6}$$

and the lifetime of the B_c^- meson is determined from its total width as

$$\tau(B_c^-) = \frac{1}{\Gamma(B_c^- \to X)} \tag{2.7}$$

The predicted contribution for each process can be evaluated using different theoretical models. The branching ratios of these processes, as predicted by the Operator Product Expansion (OPE) and sum rule methods, are given in Table 4 [37].

The partial width for the annihilation channel can be estimated by summing over the leptonic and quark decay modes given by the expression:

$$\Gamma_{ann.} = \sum_{i=l,q} \frac{G_F^2}{8\pi} |V_{bc}|^2 f_{B_c}^2 M_{B_c} m_i^2 (1 - m_i^2/M_{Bc}^2) C_i \tag{2.8}$$

Table 4: The branching ratios of different decay modes for the B_c^- meson.

Decay modes	OPE, %	Sum Rules, %
$B_c^- \to \bar{c}s$	7.2 ± 1.8	6.6 ± 0.7
$B_c^- \to \tau^- \nu_\tau$	2.9 ± 0.7	1.8 ± 0.2
$\sum b \to c$	25.0 ± 6.2	19.6 ± 1.9
$\sum \bar{c} \to \bar{s}$	64.3 ± 16.1	72.0 ± 7.2

where G_F is the Fermi coupling constant, V_{bc} is the CKM matrix element for b to c quark transition, f_{B_c} is the leptonic decay constant for the B_c^- meson, M_{B_c} is the B_c^- meson mass, m_i is the mass of the final state, and C_i is a factor that is different for the cases of leptons or quarks in the final states. For the case of leptons $C_i = 1$, for the case of final states with c and s quarks $C_i = 3|V_{cs}|^2 a_1^2$ where the factor of 3 accounts for the quark colors, $|V_{cs}|$ is the CKM matrix element, and $a_1 = 1.22 + 0.04$ [37] account for the hard gluon corrections. The decay constant of the B_c^- meson, f_{B_c}, is estimated to be 500 MeV [34] based on a potential model. The dominant transitions for the weak annihilation are to heavy τ and c generations due to helicity suppression of decays to the lighter quarks and leptons. In Ref. [6], the partial width of the weak annihilation of the B_c^- meson is estimated to be 0.194 ps^{-1}, which is $\sim 10\%$ of its total width.

The partial decay width of the spectator mode through the b quark or $\bar{c}$ anti-quark can be roughly estimated as the sum of the widths determined from the lifetime of the B^0 and D^0 mesons. This gives the total width of the B_c^- meson:

$$\Gamma(B_c^- \to X) = \Gamma(B^0) + 0.6 \cdot \Gamma(D^0) + \Gamma(ann.) \tag{2.9}$$

where an additional factor of 0.6 is included in the $\bar{c}$ anti-quark decay to account for the tightly constrained phase space in the B_c^- meson compared to the D meson [38]. The B_c^- meson lifetime obtained from this estimation is 0.4 ps [39].

One of the advanced calculations of the decay width of the B_c^- meson is the OPE method [6] which is based on the optical theorem. The optical theorem relates the decay width of a particle to the imaginary part of its forward scattering amplitude, which can be expressed as:

$$\Gamma_{B_c} = \frac{1}{2M_{B_c}} \mathrm{Im}\left(\langle B_c|\mathcal{T}|B_c\rangle\right) \tag{2.10}$$

where the transition operator $\mathcal{T}$ is defined by

$$\mathcal{T} = i \int d^4x T\{H_{eff}(x)H_{eff}(0)\} \tag{2.11}$$

where $H_{eff}(x)$ is the effective Hamiltonian describing the interaction between the b quark and $\bar{c}$ anti-quark at four-vector position x. The $T\{H_{eff}(x)H_{eff}(0)\}$ term denotes the time-ordered operator products of $H_{eff}(x)H_{eff}(0)$

$$T\{H_{eff}(x)H_{eff}(0)\} = \theta(x^0)H_{eff}(x)H_{eff}(0) + \theta(-x^0)H_{eff}(0)H_{eff}(x) \tag{2.12}$$

where $\theta(x^0)$ is the temporal step function. The OPE method states that this time-ordered product can be expanded into a set of local operator $\mathcal{O}_i(\mu)$ with the so called Wilson coefficient $C_i(\mu)$ [40] as

$$T\{H_{eff}(x)H_{eff}(0)\} = \sum_i C_i(\mu)\mathcal{O}_i(\mu) \tag{2.13}$$

where μ is the renormalization scale of the B_c^- meson and its typical value is several GeV. The important point about the OPE is that it effectively separates the calculation into two parts, the long-distance contribution which is contained in the local operator and the short-distance contribution which is in the coefficient. Since the physical observable can not depend on μ, the μ dependence of the coefficient has to cancel the μ dependence in the local operator. This cancellation of μ dependence involves several terms in the expansion in Eqn 2.13. Up to next-to-leading order, the expansion can be written as

$$T\{H_{eff}(x)H_{eff}(0)\} = \sum_{i=1}^{2}\{C_1(\mu)\bar{Q}^iQ^i + \frac{1}{m_{Q^i}^2}C_2(\mu)\bar{Q}^ig\sigma_{\mu v}G^{\mu v}Q^i + \frac{1}{m_{Q^i}^3}\mathcal{O}(1)\} \tag{2.14}$$

where $\mathcal{O}(1)$ is the identity operator and $Q(\bar{Q})$ marks the flavor of the heavy quark (b or $\bar{c}$). The $\bar{Q}^iQ^i$ term in Eqn 2.14 is the dominant contribution which corresponds to the

spectator decay of quark Q^i. The corrections to the spectator decays are given by the operator $\bar{Q}^i g\sigma_{\mu v}G^{\mu v}Q^i$.

The determination of the B_c^- lifetime in the OPE approach depends on some input parameters such as heavy quark masses, $|V_{cb}|$, and f_{B_c}. A result for the B_c^- lifetime of 0.52 ps is obtained when appropriate values of the parameters are chosen. The largest uncertainty comes from the mass of the c quark which is set to be 1.5 GeV/c^2. For this parameter ranging from 1.4 to 1.6 GeV/c^2, the calculated B_c^- lifetime falls in the range between 0.4 and 0.7 ps [6].

Another approach to calculate the B_c^- meson lifetime uses QCD sum rules [41] to estimate the semileptonic decay widths, and the factorization approach [42, 43] which evaluates the hadronic modes based on the semileptonic modes. The basic idea of sum rules is that one can calculate the correlation function of a certain number of quark currents in two ways. First, one can calculate this correlation function using quark and gluon fields in the asymptotically free region, which is called the theoretical part of the sum rules. Second, one can calculate the same correlation function in terms of hadrons with the same quantum numbers as the quark currents using the dispersion relations, which is called the phenomenological part of the sum rules. The result of the theoretical calculation is then matched to the result obtained from the phenomenological part, giving predictions of hadrons properties. Below, I will describe the general techniques used in the sum rule approach, detailed descriptions for sum rule can be found in Ref. [44, 45, 46].

The so called two-point sum rule calculates the correlation function of two quark currents

$$\Pi_{\mu\nu}(q^2) = \int e^{iqx}\langle 0|T\{j_\mu(x)j_\nu^\dagger(0)\}|0\rangle \; d^4x \tag{2.15}$$

where x is the difference of the four-vector position between the two quark currents, q is the momentum carried by the quark currents, and $j_\mu(x)$ is the quark current at x given by $j_\mu(x) = \bar{q}_1(x)\Gamma_\mu q_2(x)$. q_1 and q_2 are the quark spinors that corresponding to the relevant hadron, and Γ_μ depends on the hadron under consideration. For the pseudoscalar B_c^- meson studied in this thesis, $\Gamma_\mu = \gamma_5$ which corresponds to the pseudoscalar current $j_\mu(x) = \bar{c}(x)\gamma_5 b(x)$. To the lowest order the correlation function is simply the product of the relevant propagators, and the high order corrections can be calculated perturbatively at large spacelike momentum

transfer $q^2 < 0$. The diagrams corresponding to lowest order and $O(\alpha_s^2)$ corrections are shown in Figure 12.

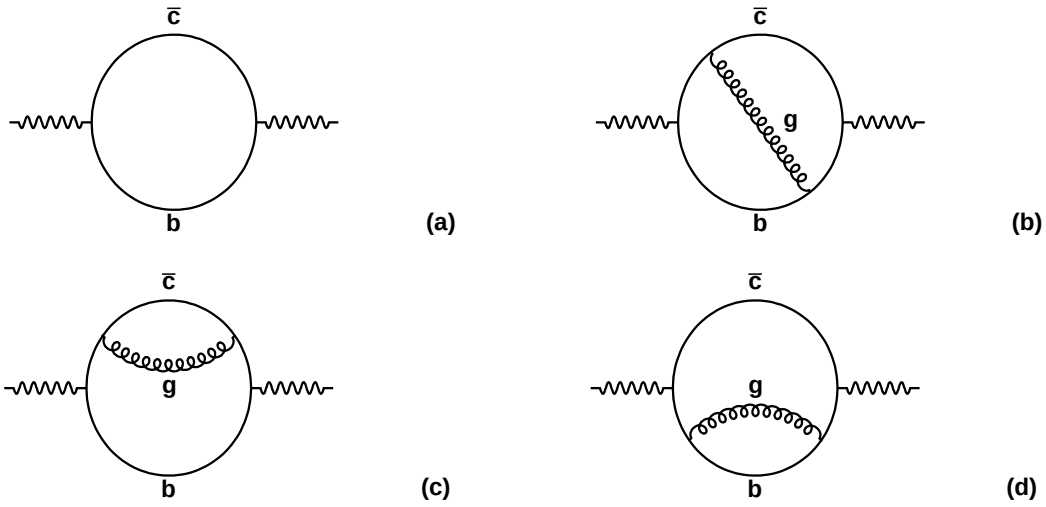

Figure 12: Diagrams of lowest order (a) and $O(\alpha_s^2)$ correction (b, c, d) to the correlation function of two quark currents.

As first pointed out in Ref [41], there are also non-perturbative effect to the correlation function due to the vacuum quark and gluon fields. One can include these contributions by the OPE method [40], which translates the non-perturbative effect into a set of vacuum expectations of the quark and gluon fields with Wilson coefficients. These contributions are called condensates, and typical examples are the quark condensates $\langle 0|m\bar{q}q|0\rangle$ and gluon condensates $\langle 0|G_{\mu\nu}G^{\mu\nu}|0\rangle$, where m is the quark mass, q and $G_{\mu\nu}$ are the quark and gluon fields. The diagrams corresponding to the contribution from quark and gluon condensates are shown in Figure 13. Note that the cross symbol indicates the vacuum quark and gluon fields. The final form of the correlation function in the theoretical part can be then written as

$$\Pi_{\mu\nu}(q^2) = C_I\mathcal{O}(1) + C_G\langle 0|G_{\mu\nu}G^{\mu\nu}|0\rangle + C_q\langle 0|m\bar{q}q|0\rangle \tag{2.16}$$

where C_I, C_G and C_q are the Wilson coefficients, $\mathcal{O}(1)$ is the identity operator which represents the contribution shown in Figure 12, $\langle 0|G_{\mu\nu}G^{\mu\nu}|0\rangle$ and $\langle 0|m\bar{q}q|0\rangle$ are the vacuum expectation of the gluon and quark fields which correspond to the contribution from Fig-

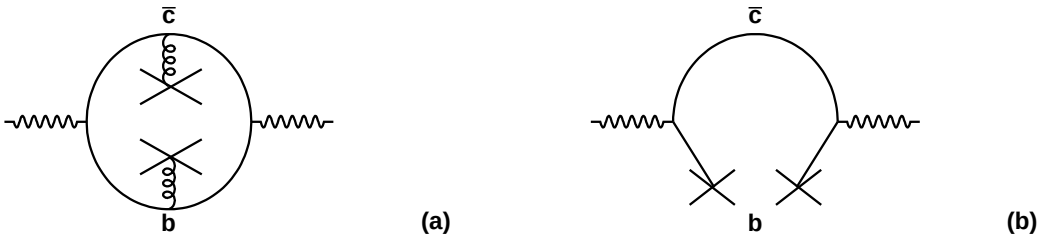

Figure 13: Contribution to the correlation function due to the gluon (a) and quark (b) condensates. The cross symbol indicates the vacuum gluon and quark fields

ure 13. Detailed calculation of the Wilson coefficient can be found in Ref [47]. It has also been shown [44] that the quark condensate has little contribution to the correlation function, and can be ignored or absorbed in the gluon condensate.

The phenomenological part can be related to Eqn 2.16 through the dispersion relation [48, 49], which gives the following formula

$$\Pi_{\mu\nu}(q^2) = \frac{1}{\pi}\int_0^\infty ds \frac{\rho(s)}{s+Q^2} + \text{subtractions} \tag{2.17}$$

where $Q^2 = -q^2 > 0$ and $\rho(s)$ is the spectral density function given by

$$\rho(s) = \sum_h \delta(s - m_h^2)\langle 0|j_\mu(x)|h\rangle\langle h|j_\nu^\dagger(0)|0\rangle \tag{2.18}$$

The subtraction terms are necessary if the integral diverges, and they contain only finite positive power of Q^2.

It should be noted that Eqn. 2.18 contains the sum over all intermediate hadrons created by the quark currents. However, we are only interested in the properties of the ground state B_c^- meson. A method called the continuum model [50] is then used to take into account the contribution of all the higher states in the spectral density function. The idea of the continuum model is that, starting from a threshold s_0, the excited hadronic states can be approximated by perturbative calculation in the same way as the theoretical part of the sum rule. Thus, the spectral density function can be written as

$$\rho(s) = \delta(s - m_{B_c}^2)\langle 0|j_\mu(x)|B_c^-\rangle\langle B_c^-|j_\nu^\dagger(0)|0\rangle + \theta(s-s_0)\cdot \text{ continuum} \tag{2.19}$$

Note that the matrix element $\langle 0|j_\mu|B_c^-\rangle$ is related to the decay constant of the B_c^- meson through the relation

$$\langle 0|j_\mu|B_c^-\rangle = \frac{f_{B_c} m_{B_c}^2}{m_b + m_c} \tag{2.20}$$

The Borel transformation [51] is then used to transform the dispersion integral into an exponential weighted function, its formula can be written as

$$\phi(\omega^2) = \lim_{\substack{Q^2, n \to \infty \\ Q^2/n = \omega^2}} \frac{1}{(n-1)!}(Q^2)^n \left[-\frac{d}{dQ^2}\right]^n \Pi(Q^2) \tag{2.21}$$

It can be shown that after the Borel transformation, the subtraction terms disappear and Eqn 2.17 becomes

$$\begin{aligned} \phi(\omega^2) \equiv B(Q^2 \to \omega^2)\Pi(Q^2) &= \frac{1}{\pi}\int_0^\infty \frac{\rho(s)}{\omega^2} e^{-s/\omega^2}\, ds \\ &= \frac{\pi}{\omega^2} e^{-m_{B_c}^2/\omega^2} \langle 0|j_\mu|B_c^-\rangle \langle B_c^-|j_\nu^\dagger|0\rangle + \text{continuum} \end{aligned} \tag{2.22}$$

The advantage of the Borel transformation is that the contribution of the excited hadronic states is exponentially suppressed in the integral, and the impact due to the continuum approximation is minimized. One can now match the expression obtained from Eqn. 2.16 to Eqn. 2.22, which can then be used to calculate the matrix element $\langle 0|j|B_c^-\rangle$. To subtract the continuum contribution from Eqn. 2.22, one can multiply by a factor of $(1 - e^{-s_0/\omega^2})$ in Eqn. 2.16, so that only the relevant part is kept in both equations.

Applying the two-point sum rule to the pseudoscalar quark current $j_\mu = \bar{c}\gamma_5 b$, one can calculate the decay constant of the B_c^- meson. This decay constant is later used as an input parameter to the three-point sum rule to extract the B_c^- lifetime. The difference between the three-point sum rule and the two-point sum rule is that one now considers a correlation function between three quark currents. In the phenomenological part, one considers an initial hadron h_i created from the vacuum that decays to a final hadron h_f and then annihilates to the vacuum.

In Ref. [7], the three-point sum rule is used to predict the lifetime of the B_c^- meson. It first estimates the semileptonic form factors of $B_c^- \to B_s(B_s^*)\ l^-\nu_l$ decay within the sum rule approach. Figure 14 shows the lowest order contribution to the three-point correlation function. The correlation function for the $B_c^- \to B_s(B_s^*)\ l^-\nu_l$ decay can be written as

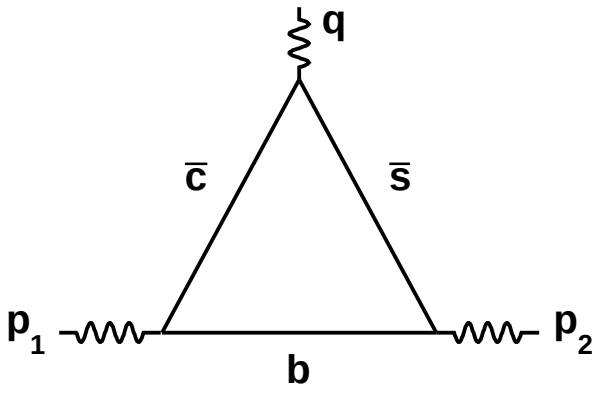

Figure 14: Lowest order diagram contribution to the three-point sum rule.

$$\Pi_\mu(p_1^2, p_2^2, q^2) = \int e^{i(p_2 x - p_1 y)} \langle 0|T\{\bar{s}(x)\gamma_5 b(x)\ V_\mu(0)\ \bar{b}(y)\gamma_5 c(y)\}|0\rangle\ d^4x d^4y \tag{2.23}$$

$$\Pi^{V,A}_{\mu\nu}(p_1^2, p_2^2, q^2) = \int e^{i(p_2 x - p_1 y)} \langle 0|T\{\bar{s}(x)\gamma_\mu b(x)\ J^{V,A}_\nu(0)\ \bar{b}(y)\gamma_5 c(y)\}|0\rangle\ d^4x d^4y \tag{2.24}$$

where $\bar{s}\gamma_5 b$ and $\bar{s}\gamma_\mu b$ are the quark currents corresponding to the pseudoscalar meson B_s and vector meson B_s^* respectively. p_1 and p_2 are the external momenta connecting to the B_c^- and $B_s(B_s^*)$ currents, q is the momentum transfer at the $c \to s$ transition point. $V_\mu(0)$ and $J^{V,A}_\nu(0)$ are the relevant quark currents for the $B_c^- \to B_s(B_s^*)$ transitions. In the following $B_s^{(*)} \equiv B_s(B_s^*)$ will be used to indicate both cases.

On the phenomenological part, the spectral representation can be obtained from a double dispersion relation, written as

$$\Pi_{\mu\nu}(p_1^2, p_2^2, q^2) = -\frac{1}{(2\pi)^2}\int_0^\infty ds_1\ ds_2\ \frac{\rho(s_1, s_2, Q^2)}{(s_1 - p_1^2)(s_2 - p_2^2)} + \text{subtractions} \tag{2.25}$$

where $Q^2 = -q^2 > 0$. The spectral density function $\rho(s_1, s_2, Q^2)$ can be written as

$$\begin{aligned}\rho(s_1, s_2, Q^2) &= \delta(s_1 - m_{B_c}^2)\delta(s_2 - m_{B_s^{(*)}}^2)\langle 0|\bar{s}\gamma_5(\gamma_\mu)b|B_s^{(*)}\rangle\langle B_s^{(*)}|F^{(*)}(Q^2)|B_c^-\rangle\langle B_c|\bar{b}\gamma_5 c|0\rangle \\ &\quad +\theta(s - s_0)\cdot\text{continuum}\end{aligned} \tag{2.26}$$

where $F^{(*)}(Q^2)$ are the form factors for the $B_c^- \to B_s^{(*)}\ \ell^-\nu_\ell$ decays, and the continuum approximation of the excited states contribution has been assumed. Note that in the spectral density function, the form factor expression is sandwiched by the decay constant of the B_c^- and $B_s^{(*)}$ mesons, thus one needs to compute the three decay constants f_{B_c} and $f_{B_s^{(*)}}$ in the two-point sum rule to calculate the form factor in the three-point sum rule. The form factors for the $B_c^- \to B_s^{(*)}\ \ell^-\nu_\ell$ decays are then obtained by matching the theoretical expression to the phenomenological expression in the three-point sum rule.

Having calculated the form factors for the $B_c^- \to B_s^{(*)}\ \ell^-\nu_\ell$ decays, Ref. [7] then calculated the hadronic decay widths of $B_c^- \to B_s^{(*)}\ \pi^-(\rho^-)$ using the factorization approach [42, 43], assuming the same form factors as in the $B_c^- \to B_s^{(*)}\ \ell^-\nu_\ell$ decays. To account for the correction due to the hard gluon in the hadronic decay, a factor $a(\mu)$ which depends on the scale μ of the effective Hamiltonian should be include [52]. The accuracy of the three-point sum rule calculation then depends on the choice of the scale parameter μ. By finding appropriate scale parameters to explain the observed experimental results for the D and B mesons, Ref [7] argued that the scale μ for a hadron should depend on two aspects. The first is the composite quarks of the hadron, and the second is the transition between the decaying quark and the resulting quark. Thus, a preferred scale parameter μ is obtained for the B_c^- meson in the decay of the $\bar{c}$ anti-quark. By evaluating total decay widths of $B_c^- \to B_s^{(*)}\ \pi^-(\rho^-)$, which are the dominant decay modes due to the $c \to s$ transition, and combining with the decay widths obtained from the $b \to c$ transition [53] as well as the annihilation amplitude [54], the lifetime of the B_c^- meson is predicted to be 0.48 ± 0.05 ps. It should be noted that, compared to the OPE approach, the dependence of the uncertainty in the heavy quark mass is much less in the sum rule method. The reason for this improvement is that the heavy quark masses are determined by studying the two-point sum rule for the charmonium and bottomonium mesons.

Table 5 gives a summary of lifetime estimates for the B_c^- meson in the references. These predictions all estimate that the B_c^- meson lifetime is considerably shorter than the other B mesons. The theoretical uncertainties in these predictions arise from either the uncertainty in the heavy quark masses or the scale of hard gluon corrections. A precise measurement of the B_c^- lifetime will test the most precise theoretical predictions which at the current

moment is the prediction using sum rules.

Table 5: Estimates of the B_c lifetime using various theoretical approaches.

Theoretical Approach	Calculated Value
Estimate from B, D meson Decays	0.4 ps [39]
Operator Product Expansion	$0.4 - 0.7$ ps [6]
Sum Rules	0.48 ± 0.05 psf [7]

3.0 THE TEVATRON AND THE CDF EXPERIMENT

3.1 THE TEVATRON COLLIDER

The Tevatron collider of Fermilab is a circular proton-antiproton synchrotron located in Batavia, IL. It collides bunches of protons and antiprotons at a center-of-mass energy of 1.96 TeV in two multipurpose particle detectors along the ring. CDF II detector is one of them and provides the measurements used in this thesis. In this chapter, the accelerator complex and different parts of the CDF II detector are discussed in detail. The CDF II detector was upgraded in many ways over the CDF detector in Run I during the 1992-1995 period.

3.1.1 Proton and antiproton production

Figure 15 shows a schematic of the Fermilab accelerator. To produce the protons used in the collision, the first step is to accelerate the H^- ion to 750 KeV using the Cockcroft-Walton accelerator. The ions are then injected into the Linac where the ions are accelerated to 400 MeV. After the Linac, the two electrons from the H^- ion are stripped and the protons are transfered to the booster where they are accelerated to 8 GeV. The protons are then transfered to the Main Injector which further raises their energies. These protons are then used to produce antiprotons or to prepare for collision in the Tevatron.

When the protons energies reach 120 GeV in the Main Injector, some of them are used to produce antiprotons by colliding with a thick nickel target. The beam is then passed through a dipole magnet which separates the negatively charged antiproton with an energy of 8 GeV and stores them in the Debuncher where the antiprotons are cooled to reduce their beam size. The antiprotons are then transfered to the Accumulator where they are stored

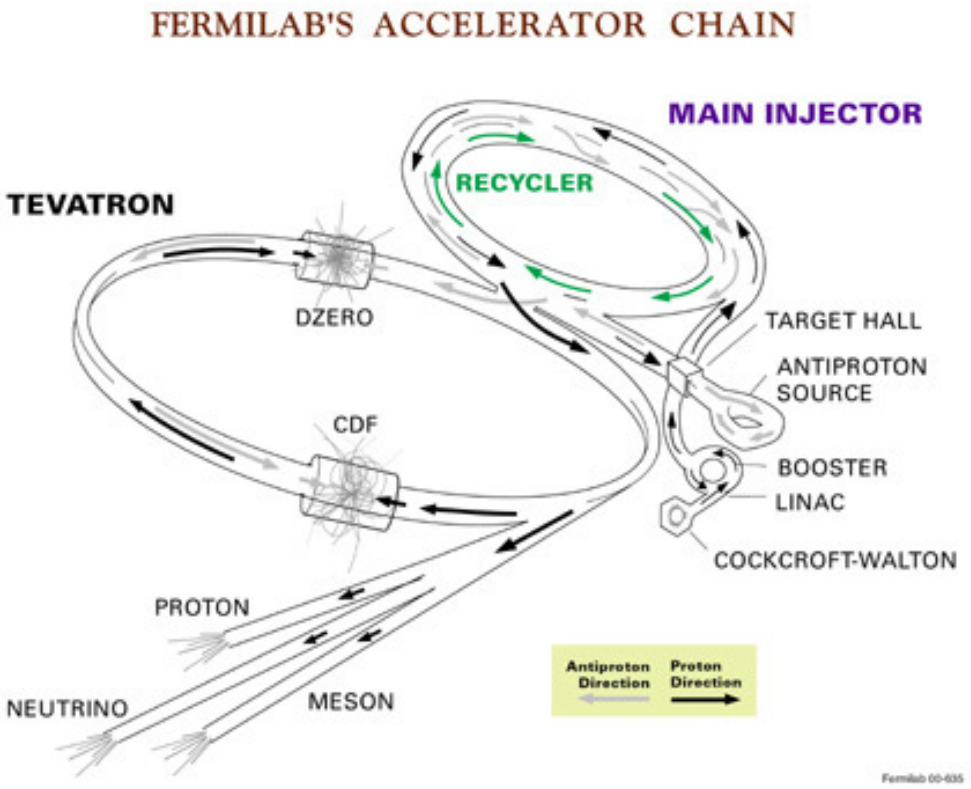

Figure 15: A schematic of the Fermilab accelerator

and cooled until transfered to the Recycler. The Recycler is a constant 8 GeV energy storage ring located in the same tunnel as the Main Injector, and provides additional storage for the antiprotons. From the Recycler, the antiprotons can be transfered to the Main Injector and accelerated to 150 GeV and finally injected into the Tevatron for colliding beam operation. The protons not used in the antiproton production have their energies raised to 150 GeV in the Main Injector until injected into the Tevatron.

3.1.2 Collision and luminosity

To create proton and antiproton collisions in the Tevatron, 36 bunches of protons are injected into the Tevatron first, followed by 36 bunches of antiprotons. Figure 16 illustrates the

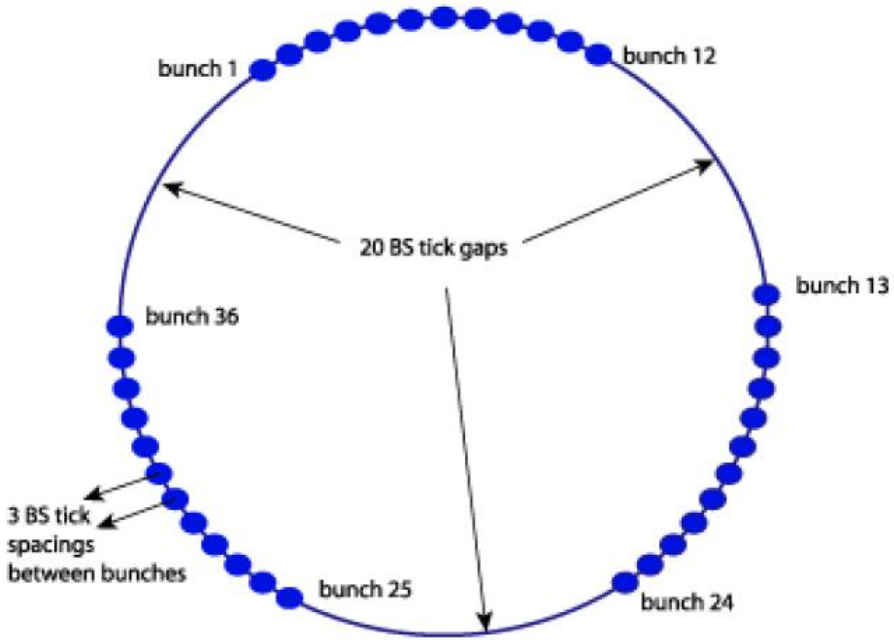

Figure 16: Illustration of the 36 proton bunch structure. The 36 bunches are separated by three trains of 12 bunches each. The trains are separated by 2.6 us, or 20 BS (beam sync) ticks. While bunches in each train are separated by 396 ns, or 3 BS ticks.

structure of the 36 proton bunches. The 36 bunches of protons are grouped into three trains

of bunches. Trains are separated by 2.6 us and each train has 12 proton bunches. Inside each train, the 12 bunches are separated by 396 ns. The antiproton bunches are injected into the Tevatron in a similar way, where 12 antiproton bunches form a train and three trains form the total 36 antiproton bunches. The antiproton trains are injected between the proton trains and circulated along the opposite direction from the proton trains.

The proton and antiproton beams inside the Tevatron are then accelerated to 980 GeV and are tuned to minimize the beam losses. A quadrupole magnet is then used to tightly focus the proton and antiproton beams at the interaction points inside the CDF II detector to initiate the collisions between the protons and antiprotons.

A single injection of beams into the Tevatron is called a store. A typical store will be ended after $\sim$ 20 hours because of the decrease of the instantaneous luminosity. The instantaneous luminosity is an important parameter to characterize the performance of an accelerator and can be expressed as:

$$L = f\frac{N_p N_{\bar{p}}}{A} \tag{3.1}$$

where f is the revolution frequency, N_p and $N_{\bar{p}}$ are the total number of protons and antiprotons, and A is the cross section of the interaction region. The luminosity has the unit of $\text{cm}^{-2}\text{sec}^{-1}$. The total number of production events N of a given process is related to the integrated luminosity by the cross section σ as $N = \sigma \times \int Ldt$. The typical averaged instantaneous luminosity for the Tevatron is $L \sim 1 \times 10^{32}$ $\text{cm}^{-2}\text{sec}^{-1}$. A typical store lasts for $\sim$ 20 hours, and has an integrated luminosity of $\int Ldt \sim 7 \times 10^{36}$ cm^{-2} which corresponds $\sim$ 7 pb^{-1} of data (1 b = 10^{-24} cm^2). The cross section for B_c^- production is $\sim$ 5 nb which means $\sim 3.5 \times 10^4$ B_c^- mesons are produced in a single store. The measurement discussed in this thesis uses the data sample corresponding to an integrated luminosity of 6.7 fb^{-1} between February 2002 and February 2010.

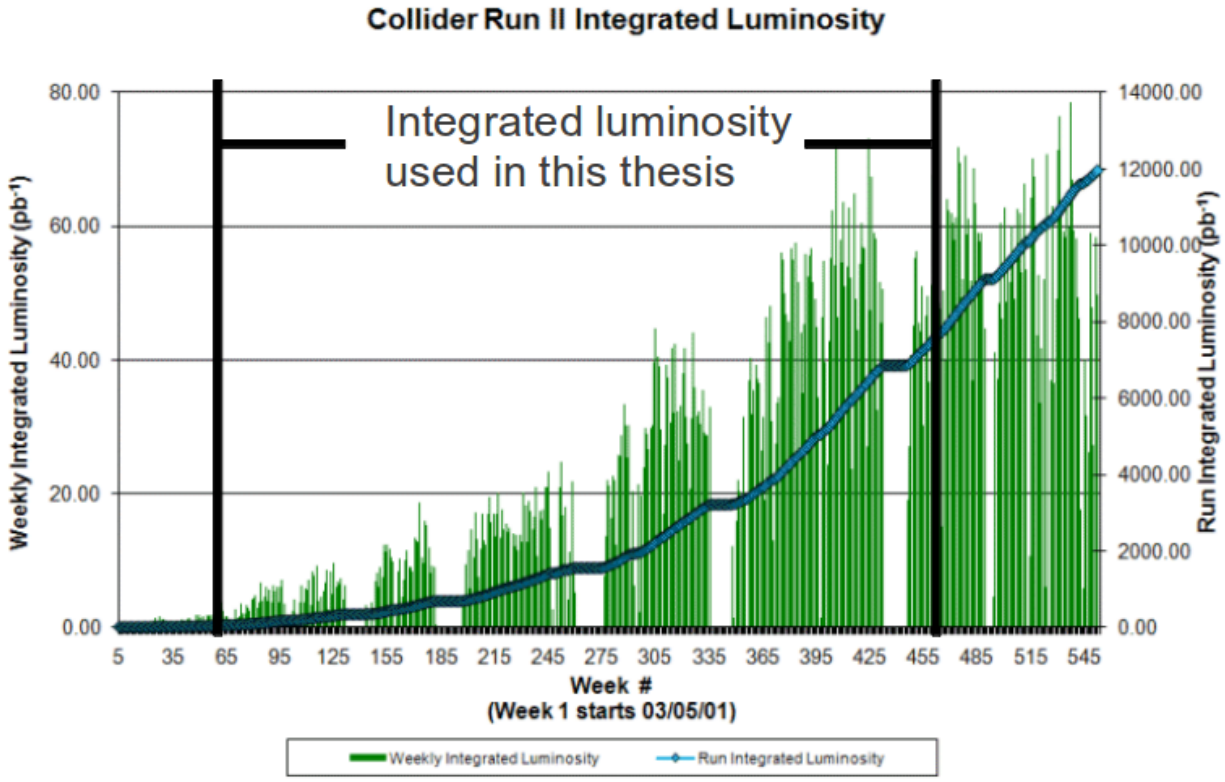

Figure 17: Integrated luminosity delivered by the Tevatron

3.2 THE CDF EXPERIMENT

The CDF II detector has taken data from June, 2001 until September, 2011 when the Tevatron shutdown. In this section, a brief overview of the detector will be given and a detailed description of the CDF II detector can be found in the detector technical design report [55].

3.2.1 Detector overview

The CDF II detector is a multipurpose detector designed for tracking of charged particles, energy measurement of electromagnetically and strongly interacting particles, and muon detection. Figure 18 shows the detector where the subsystems relevant to this thesis have been labeled, and will be discussed below. They include the tracking system and the muon system. The tracking system provides precise measurements of charged-particle trajectories near the $p\bar{p}$ interaction point. The muon system provides useful reconstruction information in the $J/\psi \to \mu^+ \mu^-$ decay chain in this analysis. Last, the trigger system, which is used to efficiently extract the most interesting physical events from the large number of events generated by the collider, is discussed. Other systems of the CDF detector that are not related to this thesis, such as the calorimetry system which measures the particle energy, are not discussed here.

In the CDF coordinate system, the positive z direction is defined as the proton direction, which runs clockwise in the Tevatron ring, with the origin at the interaction point. The positive x direction is the horizontal direction pointing away from the Tevatron ring. The positive y direction is the vertical direction pointing upwards as determined by the right-handed rule. Figure 19 shows the coordinate system with respect to the Tevatron ring.

The CDF II detector is azimuthally symmetric and a cylindrical coordinate system is used to describe the detector. In the transverse plane ($x - y$, or $r - \phi$ plane), r is defined as the the radius representing the distance to the interaction point, and ϕ is defined as the azimuthal angle counter-clockwise from the positive x direction. The polar angle θ is the

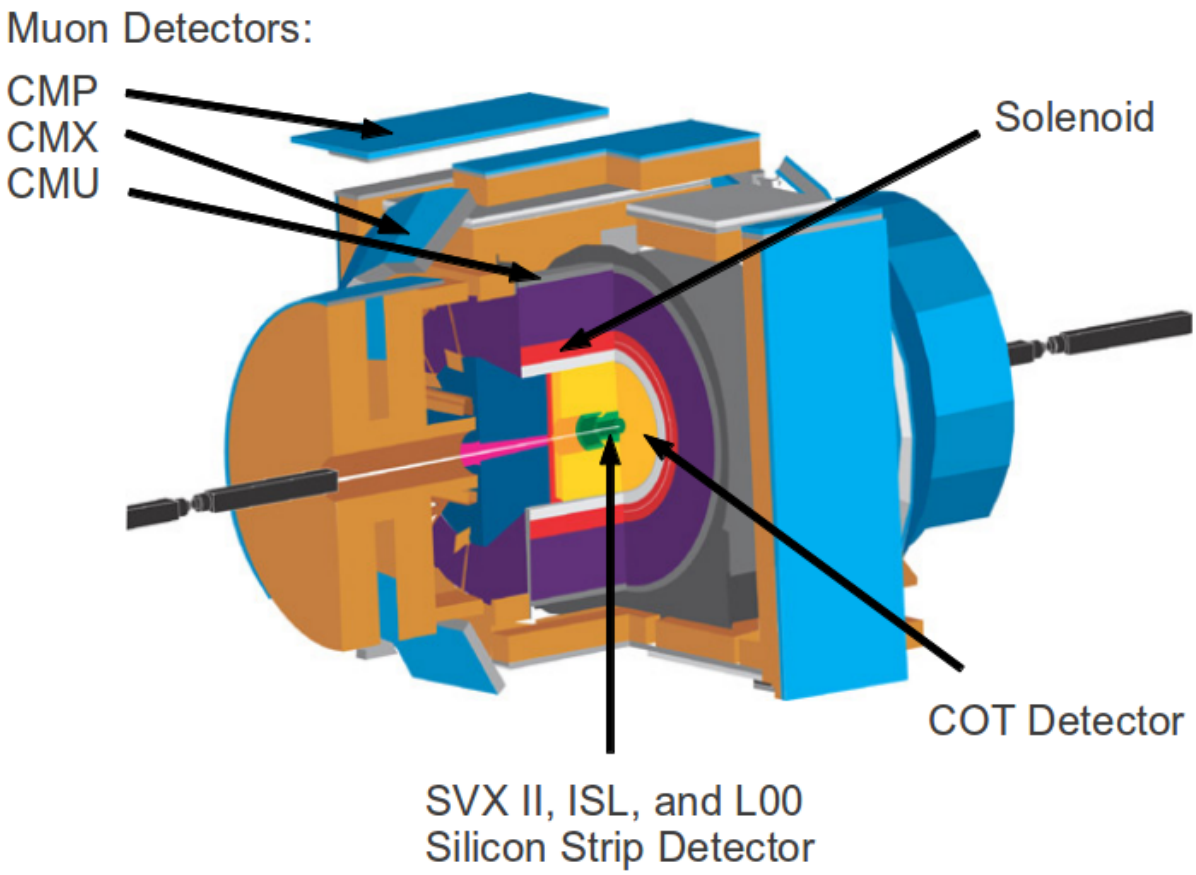

Figure 18: Detector view in 3D.

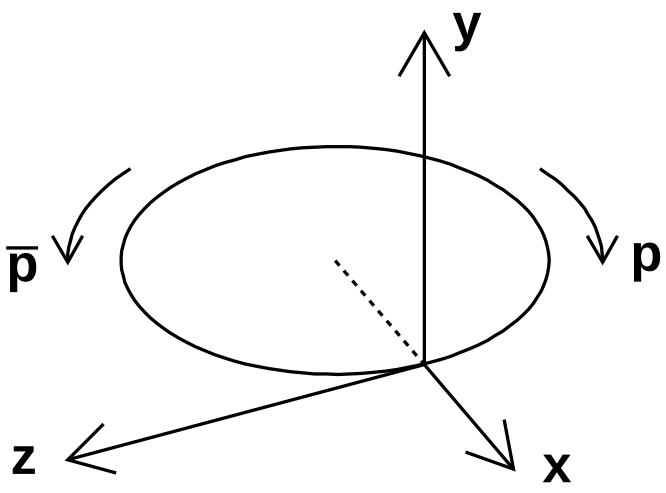

Figure 19: The coordinate system applied at CDF II Detector.

angle relative to the positive z direction. One useful kinematic quantity in collider physics is the rapidity, defined as

$$y = \frac{1}{2} \ln \left(\frac{E + p \cos\theta}{E - p \cos\theta} \right) \tag{3.2}$$

where E and p are the energy and momentum of the particle. This quantity has the virtue of invariance to a Lorentz boost along the z direction. In the relativistic limit where $E \sim p$, the rapidity can be approximated by the quantity called pseudorapidity η, defined as

$$\eta = \frac{1}{2} \ln \left(\frac{p + p \cos\theta}{p - p \cos\theta} \right) = - \ln \left(\tan \frac{\theta}{2} \right) \tag{3.3}$$

where $\theta = 0$ corresponds to the proton direction. Figure 20 shows the relationship between η and θ.

3.2.2 Tracking system

The tracking systems are immersed in a uniform 1.4 T solenoidal magnetic field coaxial with the beam line. They consist of silicon strip detectors [56] and a 96-layer drift chamber named the Center Outer Tracker (COT) [57], and are shown in Figure 21.

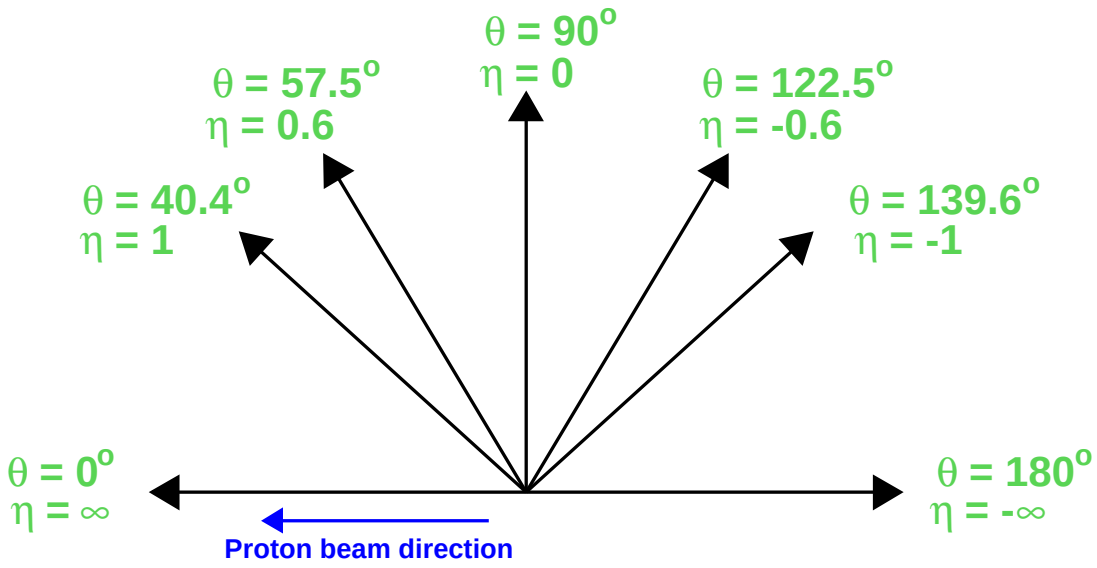

Figure 20: Illustration of the relationship between η and θ.

The tracking system provides three-dimensional charged-particle tracking with precise impact parameter measurement and excellent transverse momentum resolution, where the impact parameter, d, is defined as the distance of closest approach of a charged-particle trajectory to the beamline in the transverse plane. The typical resolution for the impact parameter provided from the tracking system is ~ 40 μm, which includes an approximate 30 μm contribution from the uncertainty of the primary interaction point. For the transverse momentum resolution, the COT detector alone can provide $\sigma(p_T)/p_T^2 \sim 0.0015$ $(\mathrm{GeV}/c)^{-1}$ for charged particles with $p_T > 250$ MeV/c. This resolution improves to 0.0007 $(\mathrm{GeV}/c)^{-1}$ when combined with the silicon detectors.

3.2.2.1 Silicon Detector The silicon detectors, the inner-most detectors of the CDF II detector, make precise measurements of charged-particle trajectories near the $p\bar{p}$ interaction point. This is essential to precisely measure the decay distance of short-lived particles such as the B_c^- meson. They consist of three silicon detector systems which cover different ranges of r, as shown in Figure 22. They are layer 00 (L00) located at $r \sim 1.35$ cm, the silicon

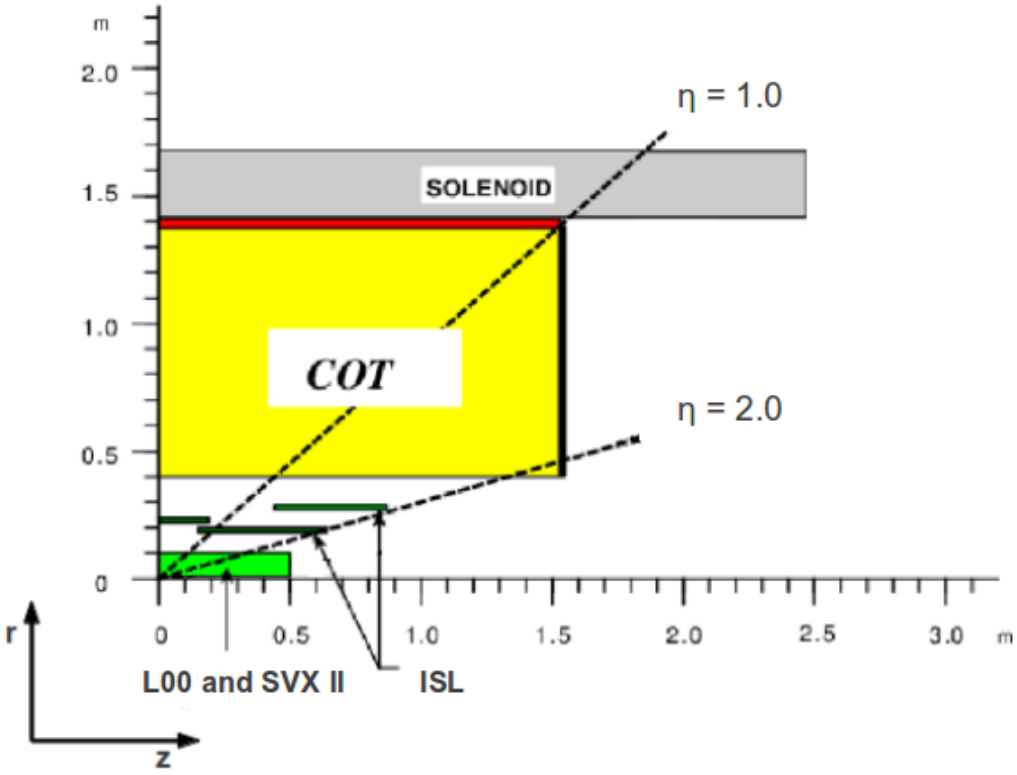

Figure 21: 1/4 section view of the tracking system in the $r - z$ plane.

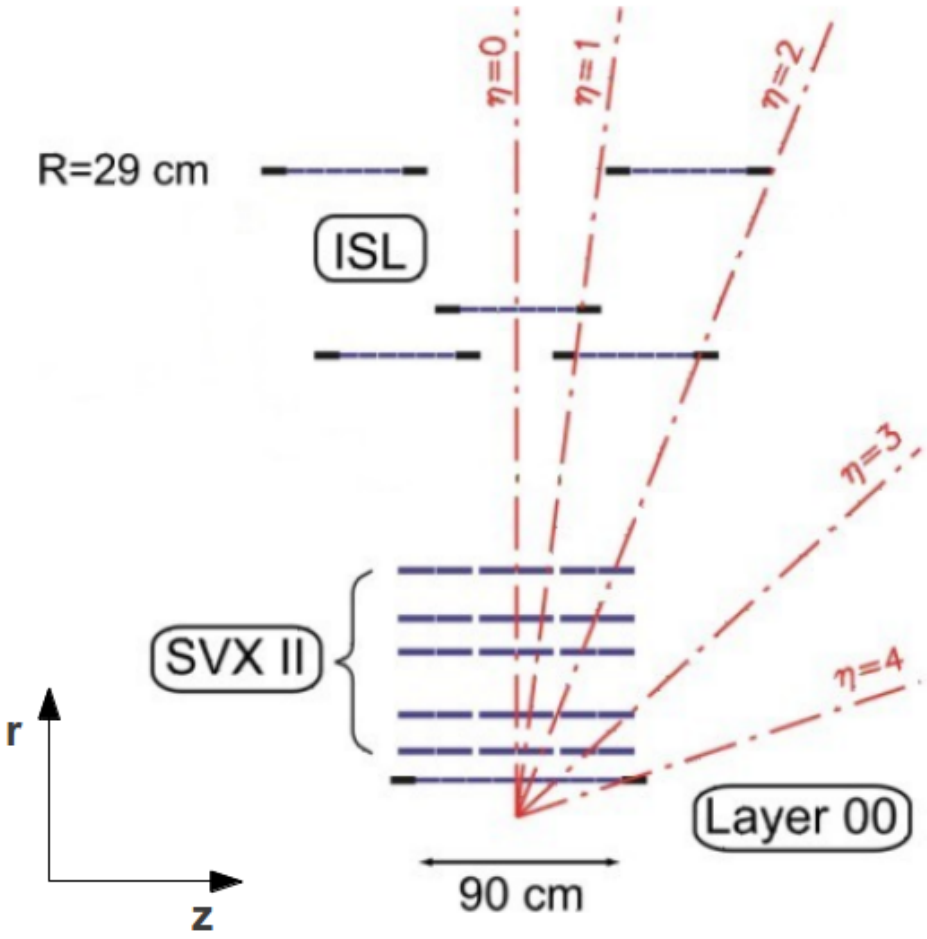

Figure 22: Arrangement of three silicon detectors in the $r - z$ plane.

vertex detector (SVX II) with five double-sided layers between $r \sim 2.5$ and ~ 10.6 cm, and the intermediate silicon layers(ISL) with three double-sided partial layers between $r \sim 20$ and ~ 29 cm. The silicon detectors all have high spatial resolution by high precision position measurement recorded by the silicon sensors. The sensors consist of a silicon wafer with p-n junction between the bulk and strips near the surface. These sensors are biased by high voltage that is used to increase the size of the depletion region of the p-n junction. When a charged-particle passes through a silicon sensor, it excites electron hole pairs that separate and move to the surfaces of the silicon strip sensor, where the charge is collected by a low noise charge sensitive amplifier. The amplified signal is then read out by electronics that include a storage pipeline and convert the analog signal to digital signal. The positions of the strips and the collected electrons are used to construct hits which provide a position measurement of the particle in the coordinate perpendicular to the orientation of the strip and in the plane of the detector.

Layer 00 (L00)

The L00 at $r \sim 1.35$ cm is a light-weight one layer single-sided silicon detector placed directly on the beam-pipe [58]. It consists of 12 AC-coupled silicon sensors which can be biased to high voltages to increase the depletion region. It recovers the degradation in impact parameter resolution for low-momentum tracks due to multiple scattering in the electronics and cooling system which are installed inside the tracking system. In addition, the L00, being made of radiation hard silicon, is used to extend the useful lifetime of the silicon vertex detector when the effects of radiation will degrade the performance of the inner-most layer of the silicon vertex detector. The L00 provides full azimuthal and $|z| < 47$ cm coverage. The strips are parallel to the beam direction and give the first position measurement in the $r - \phi$ plane. The sensors have strip pitch of 25 μm, and readout pitch of 50 μm achieved by reading out alternate strips.

Silicon Vertex Detector (SVX II)

The five layers of the SVX II detector are arranged in five coaxial cylindrical shells covering from r ~ 2.5 cm (Layer 0) to ~ 10.6 cm (Layer 4), and divided into three identical sections (barrels) along the beam line for a total z coverage of 90 cm. Each barrel is divided into 12 azimuthal wedges of 30° in the transverse plane as shown in Figure 23. The sensors

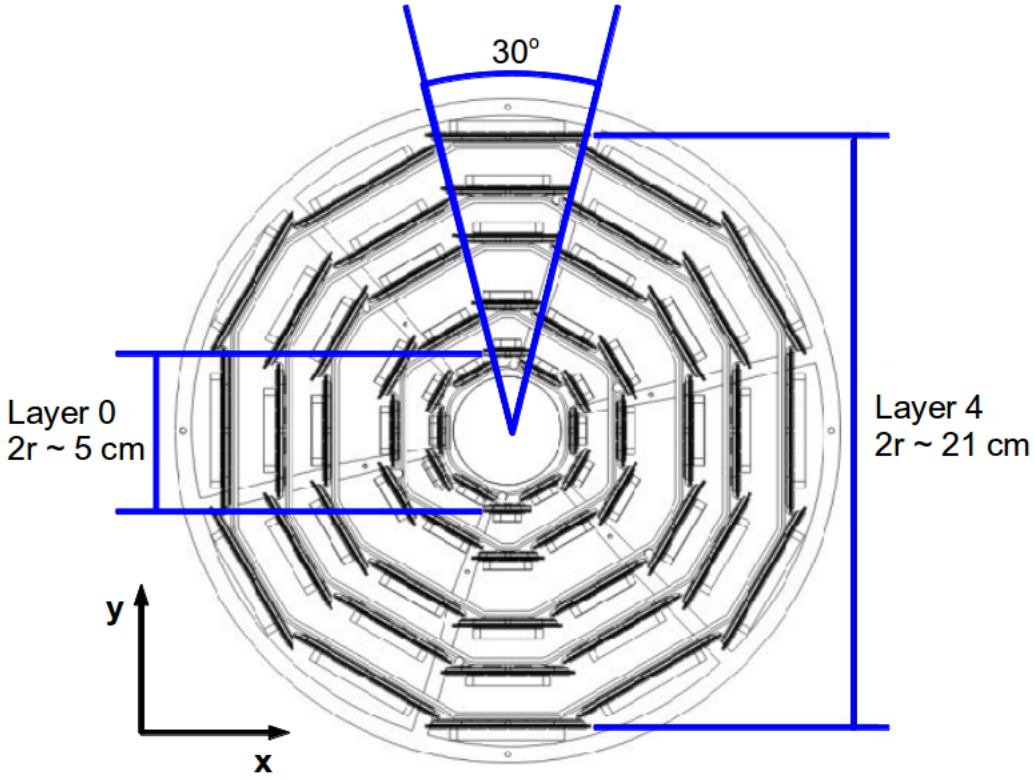

Figure 23: View of the five-layer SVX II detector in the transverse plane.

have strip pitches ranging from 60 μm to 140 μm depending on the radius. The double sided sensors have strips on both sides of the silicon to allow for two position measurement at each layer. All five layers have strips parallel to the beam direction on one side for ϕ measurement. Three layers have strips perpendicular to the beam direction on the other side measuring z position, while the remaining two layers have small angle stereo strips that are 1.2° relative to the ϕ strips. Hits in the small angle stereo sensors help remove the ambiguity involved in matching ϕ and z hits where there is more than one particle leaving hits in a given sensor.

Intermediate Silicon Layers (ISL)

The ISL is a double-sided silicon detector segmented into 12 wedges like SVX II. It has a single layer of silicon in the central regions at $r \sim 22$ cm with coverage $|\eta| < 1$, and two layers of silicon in the forward regions at $r \sim 20$ and ~ 29 cm with coverage $1 < |\eta| < 2$. The double-sided ISL has axial strips spaced by 55 μm on one side and small stereo strips spaced by 73 μm on the other. The stereo angle is 1.2°. The ISL serves as an extension of the SVX II to larger radius and its arrangement relative to the SVX II is shown in Figure 22.

3.2.2.2 Central Outer Tracker (COT) The 310 cm long COT detector is a cylindrical drift chamber filled with argon and ethane gas. It consists of potential wires, sense wires in 96 layers from $r = 40$ cm to $r = 137$ cm which are arranged into eight superlayers (SLs). High voltages are applied to the wires to create an electric field. As charged-particles travel through the COT detector, they leave a trail of ionization in the gas. The electric field then moves the electrons created from the ionization in one direction and collects them at the nearest sense wire. The collected electrons are then amplified and digitized by readout electronics before being sent to the data acquisition system.

1/6 section of the COT detector in the transverse plane is shown in Figure 24. Where the inner-most is SL 1 and the outter-most is SL 8, each SL contains 12 layers. Superlayers 1, 3, 5, 7 have their constituent sense wires oriented parallel to the beam direction for ϕ measurement, the other superlayers have their sense wires tilted 3° relative to the beam direction to give z measurement. In the COT detector the sense wires are less than 8 mm apart which gives a maximum drift time $\sim$ 100 ns, much shorter than the bunch spacing time of 396 ns, to provide enough time for processing data from the COT detector.

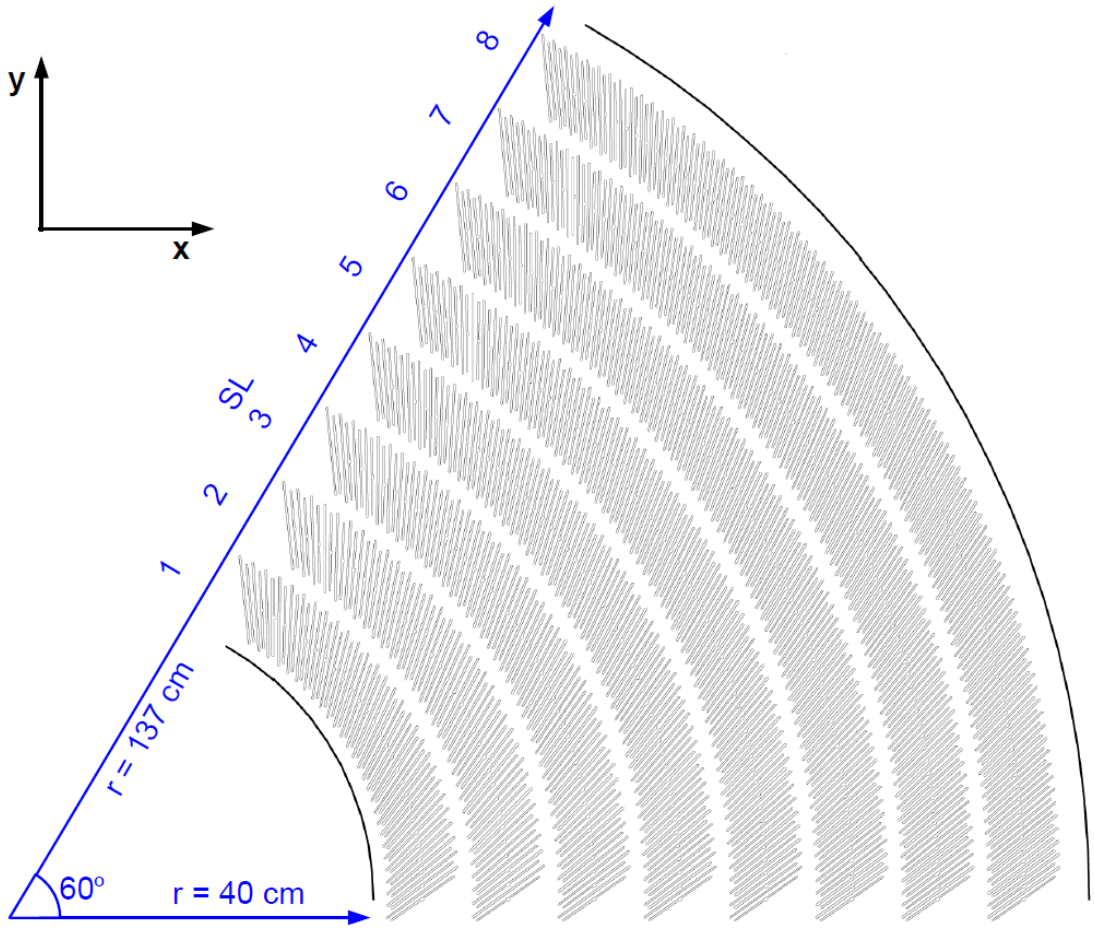

Figure 24: View of 1/6 section of COT detector in the transverse plane.

3.2.2.3 Solenoid The solenoid magnet surrounds both the COT and the silicon detector. The purpose of the solenoid is to bend the trajectory of charged particles in the tracking system. The solenoid has a radius of 1.5 m and is 4.8 m long along the z direction. The magnetic filed produced by the solenoid points to the negative z direction. The curvature of the trajectory of the charged-particles in the magnet field allows calculation of their momentum. The higher the curvature, the lower the momentum and vice versa. The solenoid is a superconducting magnet cooled by liquid helium. The helium lowers the temperature of the magnet to 4.7 K which reduces the resistance to zero, allowing the magnet to conduct high currents with minimal heating, and creating a powerful magnetic field of 1.4 T .

3.2.3 Muon system

Most muons survive to the region where they encounter the muon detector. The CDF muon system consists of four subsystems: central muon (CMU), central muon upgrade (CMP), central muon extension (CMX) and intermediate muon chamber (IMU). Figure 25 shows the pseudorapidity coverage region of these muon subsystems. Muon candidates identified as track segments in the muon system are called muon stubs. A muon stub is matched with a track measured by the tracking system to reduce background from the punch-through hadrons.

3.2.3.1 Central MUon system (CMU) The central muon detector is located outside the hadronic calorimeter at $r = 347$ cm and consists of a set of single wire drift cells covering $|\eta| < 0.6$. The CMU is segmented into 24 wedges of 12.6° in ϕ and 2.4° gaps between drift cell arrays, resulting in an overall ϕ coverage of 84%. Each wedge is further segmented into three modules each contains four layers of four drift cells. The drift cell arrays can thus make up to four position measurements in the $r - \phi$ plane that are used to form straight track segments with both position and slope. Muons with $p_T > 1.4$ GeV/c can reach the CMU.

3.2.3.2 Central Muon uPgrade (CMP) The central muon upgrade is a second set of muon drift chambers outside of the CMU with an additional 60 cm of steel to reduce punch-

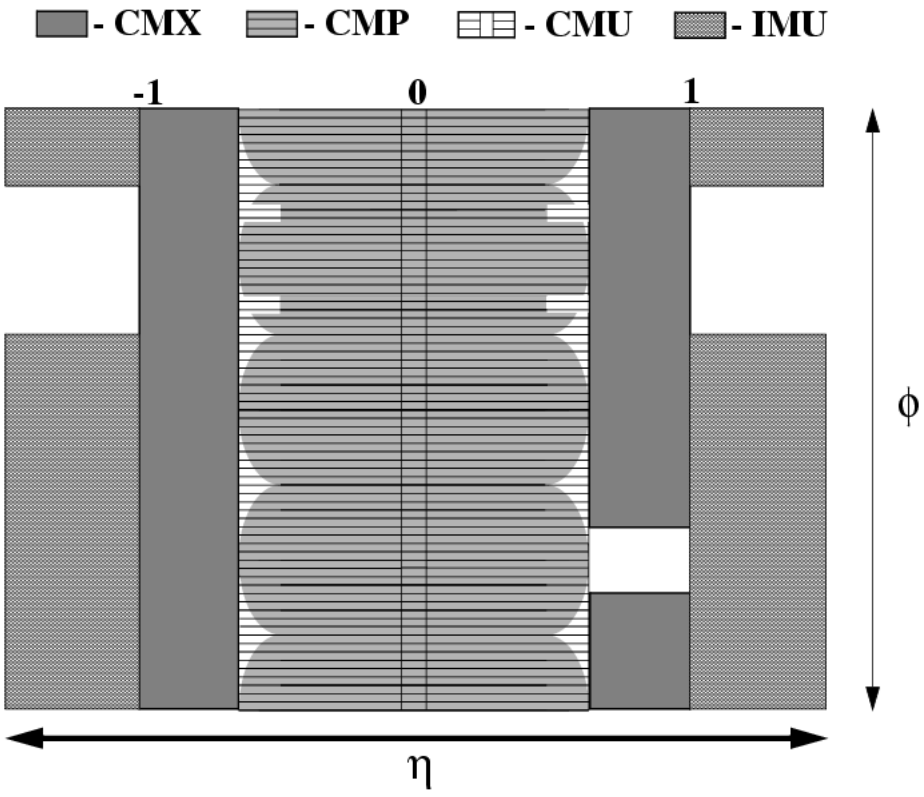

Figure 25: Pseudorapidity coverage of the muon detectors.

through hadrons. Thus, there are considerably fewer kaons and pions that penetrate to the CMP compared to the CMU. The CMP also covers the $|\eta| < 0.6$ region and the minimum p_T requirement for muons to reach CMP is 2.2 GeV/c. The CMP is arranged in a box that surrounds the CMU and serves as a confirmation of CMU muons for higher energy muons.

3.2.3.3 Central Muon eXtension (CMX) The central muon extension detector extends the CDF muon coverage to the kinematic region $0.6 < \eta < 1.0$. There are eight layers in CMX and a stereo angle to provides position measurement. There is no additional shielding added in front of the CMX because the long path through the calorimetry and the detector supports provide $6 \sim 10$ (depends on η) interaction lengths for hadron attenuation. Figure 26 shows the orientation and the position of the CMX in a side view of the CDF II detector.

3.2.3.4 Intermediate MUon system (IMU) The intermediate muon extends the coverage region to $1.0 < \eta < 1.5$. The IMU is not used in this analysis since no dimuon trigger, which will be discussed below, is available for this subsystem.

3.2.4 Trigger system

The Tevatron provides $p\bar{p}$ collisions at a rate of 2.7 MHz, while the typical CDF event size is $\sim$ 200 KB. This means the data produced per second would be $\sim$ 540 GB if all recorded. Since the CDF II detector can write only $\sim$ 20 MB/s to tape, it is necessary to reject 99.996% of the $p\bar{p}$ collision. In order to achieve the required reduction in rate and record the events relevant to the physics of interest, a three-level trigger system is used. Each level receives accepted events from the previous level, and uses more accurate detector information and time to process the data, and makes a decision to reject or accept the event. Figure 27 shows a schematic diagram of the CDF trigger system [55].

3.2.4.1 Level 1 (L1) trigger The L1 trigger is a dedicated hardware trigger that makes decision using information from the COT, calorimeter and muon system. It uses a track processor implemented in custom electronics (XFT) to reconstruct charged-particle trajectories.

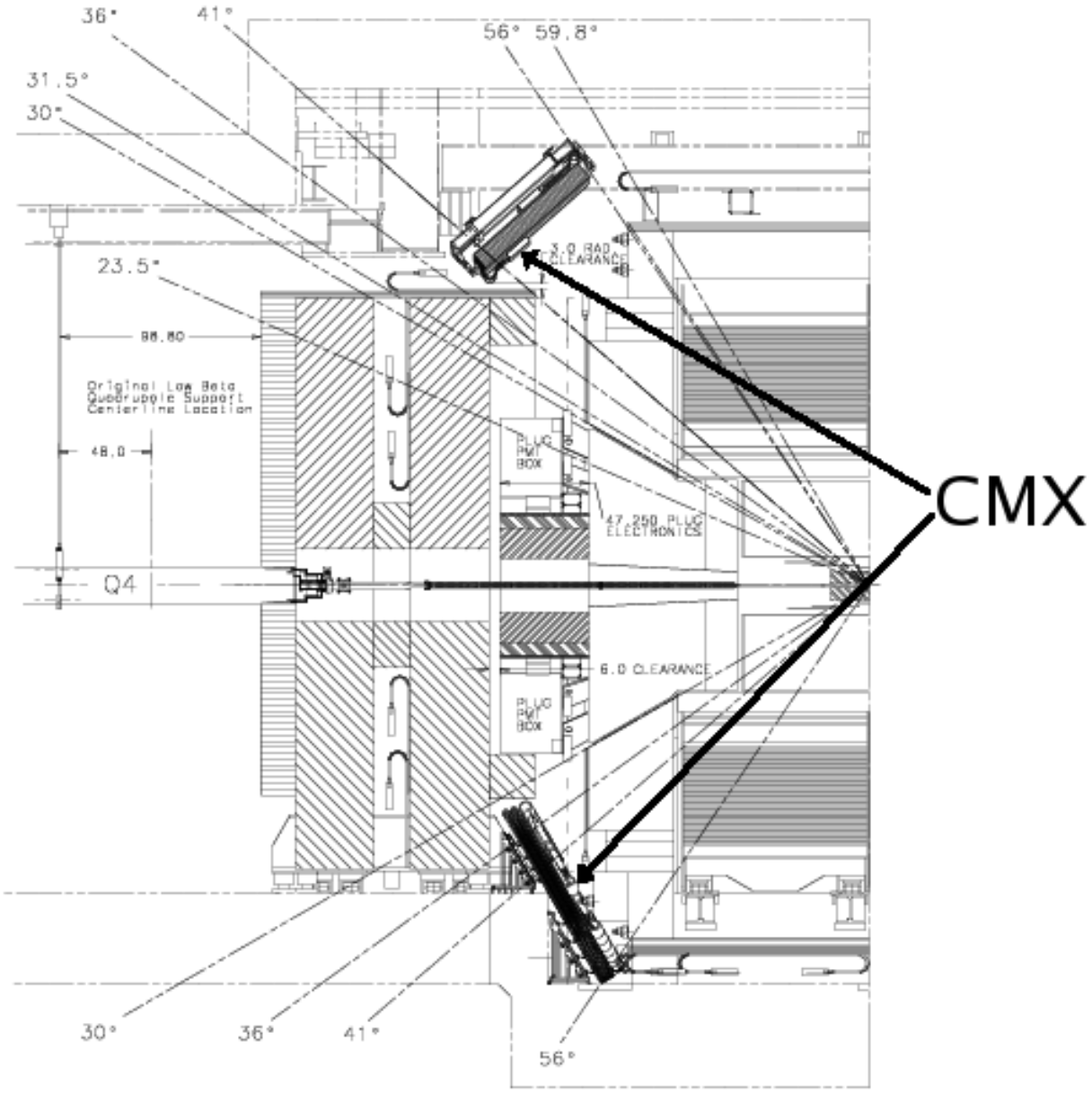

Figure 26: Side view of the CDF II detector showing the orientation and position of the CMX detector.

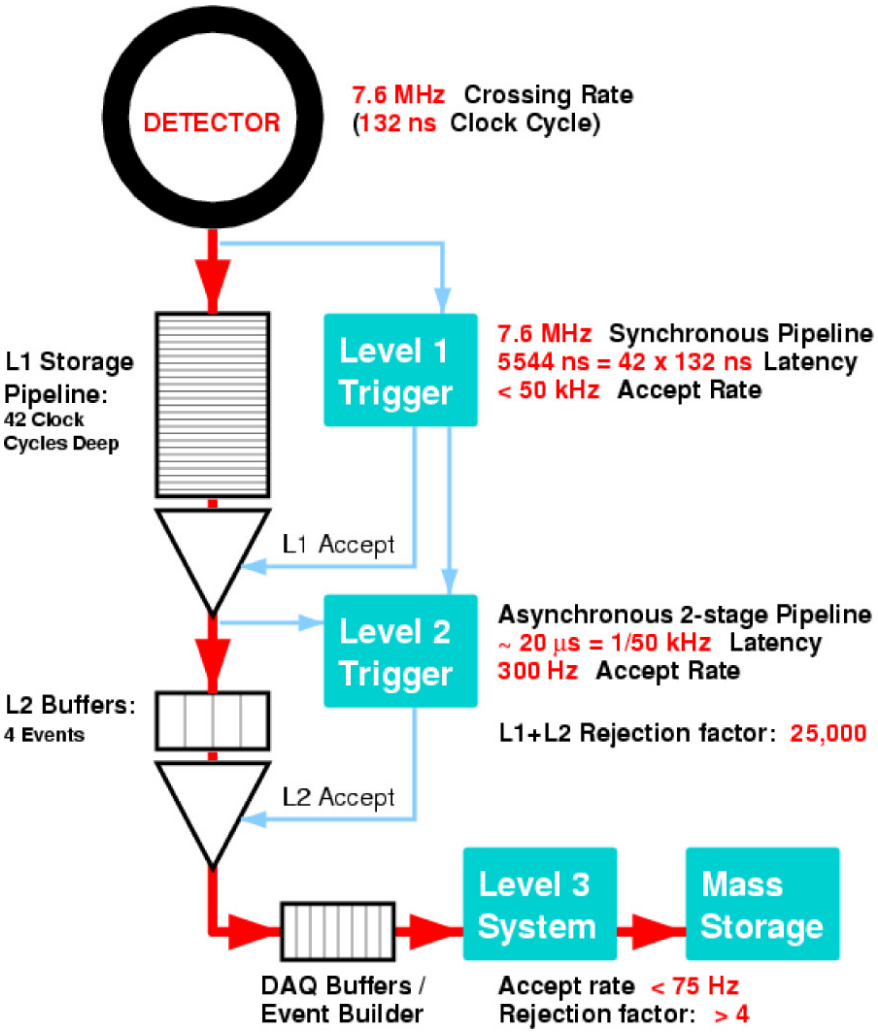

Figure 27: The CDF trigger system.

The L1 trigger is synchronized to the 132 ns clock cycle, and has a decision time ~ 5.5 μs, requiring a 42 buffer deep pipeline for the storage of events while decisions are made. The typical L1 accept rate is ~ 20 kHz while the maximum accept rate is ~ 50 kHz. For the analysis discussed in this thesis, events originate from one of two L1 dimuon triggers to select J/ψ candidates: two XFT tracks with $p_T > 1.5$ GeV/c are matched with the tracks in the CMU detector, or one XFT track with $p_T > 1.5$ GeV/c matched with CMU and another with $p_T > 2$ GeV/c matched with CMX.

3.2.4.2 Level 2 (L2) trigger The L2 trigger accepts input events from the L1 trigger and stores them into one of the four L2 buffers, which further reduces the accept rate to ~ 800 Hz. It uses a trigger processor named the silicon vertex trigger (SVT) to fully exploit the precise measurement of the silicon detectors. The SVT applies pattern recognition to SVX II silicon hits that are matched to XFT tracks and calculates impact parameters for the tracks with respect to the interaction point. This is very important to this analysis because the secondary vertex is normally several hundred microns away from the primary vertex, and L2 trigger can choose events with displaced vertices by requiring SVT tracks with non-zero impact parameters. The average decision time for L2 trigger is 20 μs.

3.2.4.3 Level 3 (L3) trigger After passing through the L2 trigger, events are sent to the L3 trigger where parallel processors are used for event reconstruction. The L3 trigger system runs on standard computer hardware and uses all available information to fully reconstruct the event. The output rate for L3 is ~ 100 Hz. In this analysis, the invariant dimuon mass is required to be between 2.7 and 3.5 GeV/c^2.

4.0 DATA SAMPLE AND MONTE CARLO SIMULATION

This chapter first describes the event reconstruction and selection used in this thesis to produce the data sample, from which the B_c^- meson lifetime is extracted. Then the MC simulation is discussed to study the effect of the selection requirements on the data sample.

4.1 EVENT RECONSTRUCTION

Both $J/\psi\ K^-$ and $J/\psi\ \pi^-$ combinations are reconstructed in this analysis. The relatively plentiful $B_u^- \to J/\psi\ K^-$ sample is used as a reference decay for $B_c^- \to J/\psi\ \pi^-$, the candidates used for the $B_c^- \to J/\psi\ \pi^-$ are obtained by assigning the π^- mass to the third track hadron instead of the K^- mass in the same sample used as $B_u^- \to J/\psi\ K^-$ candidates. In the following discussion B is used to represent either B_u^- or B_c^-, and h^- is used to represent either K^- or π^-.

4.1.1 Track quality requirements

To ensure the quality of the tracks, both the muon candidates tracks and the hadron candidates tracks are required to pass the following filters:

- Ten or more axial COT hits in at least two axial superlayers.
- Ten or more stereo COT hits in at least two stereo superlayers.
- Three or more axial silicon hits in at least three axial layers.
- $p_T > 1.5$ GeV/c for muon candidates.
- $p_T > 0.4$ GeV/c for h^- candidates.

4.1.2 J/ψ reconstruction

The dimuon trigger is used to select two oppositely charged muon candidates in two separate paths:

- CMUCMU1.5 Path: This path selects events with two oppositely charged $p_T > 1.5$ GeV/c XFT tracks that are matched to $p_T > 1.5$ GeV/c CMU stubs. The two muon candidates are required to have an invariant mass between 2.7 and 3.5 GeV/c^2.
- CMU1.5_CMX2 Path : This path requires one XFT track with $p_T > 1.5$ GeV/c that is matched to a $p_T >$ 1.5 GeV/c CMU stub and an oppositely charged XFT track with $p_T > 2.0$ GeV/c that is matched to a $p_T > 2.0$ GeV/c CMX stub. The two muon candidates are required to have an invariant mass between 2.7 and 3.5 GeV/c^2.

After the trigger, the muon pairs are then subject to a simultaneous mass and vertex constrained fit to select well-measured J/ψ candidates. The invariant mass of the dimuon is then required to be within 80 MeV/c^2 of the known J/ψ mass [21]. Figure 28 shows the invariant mass distribution of the dimuon that passes the mass and vertex fit, along with the fit result of a Gaussian signal distribution and a linear background distribution within 50 MeV/c^2 of the known J/ψ mass.

4.1.3 B meson reconstruction

The final reconstruction for the B meson involves the combination of the J/ψ candidates and the h^- candidates. The requirements imposed on the J/ψ h^- combination are as follows:

- Each J/ψ h^- combination has a loose invariant mass requirement imposed on it. For the B_u^- candidates, the invariant mass range is 5.1 to 5.5 GeV/c^2. For the B_c^- candidates, the invariant mass range is 6.0 to 6.6 GeV/c^2.
- The J/ψ h^- combination is then subject to a constrained fit of all three tracks which imposes the J/ψ mass constraint on the muon pair.

A minimum selection is made on kinematic quantities after the event reconstruction including $p_T(B) > 5$ GeV/c and $p_T(h^-) > 1.7$ GeV/c. All the events are then subject to the event selection requirements discussed below. Figure 29 and 30 show the reconstructed

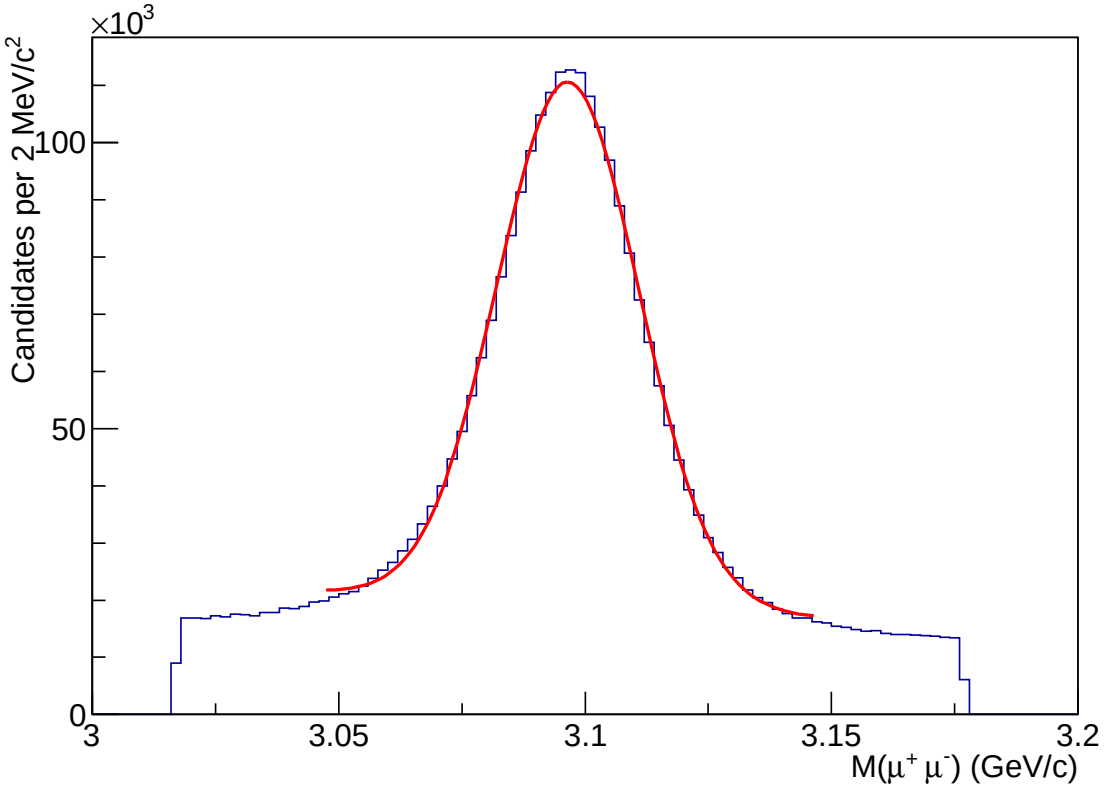

Figure 28: Invariant mass distribution of the dimuon that passes the simultaneous mass and vertex constrained fit. A fit is performed within 50 MeV/c^2 of the known J/ψ mass, where a Gaussian signal distribution and a linear background distribution are used in the fit.

invariant mass distributions of $J/\psi\ K^-$ and $J/\psi\ \pi^-$ after the reconstruction process. The hatched areas in Figure 29 are the sideband regions that are used to compare the distribution of the selection variables between signal events and background events. A clear excess for $J/\psi\ K^-$ invariant mass distribution can be found in Figure 29 even before any further event selections, while the $J/\psi\ \pi^-$ invariant mass distribution looks like nothing but pure background events. Thus, a set of selection criteria is needed to effectively reject background events in order to observe the signal events from the $B_c^- \to J/\psi\ \pi^-$ decay.

4.2 EVENT SELECTION

After event reconstruction, the data samples are then subject to a set of selection criteria to effectively reject background events while keeping the signal events. This set of selection criteria is expected to enhance a small, short-lived, and soft signal compared to a large backgrounds. The selection variables used in this analysis are listed below and their definitions are given as well.

- $p_T(h^-)$: The transverse momentum of the hadron track candidate. The hadron could be a K^- or a π^- in this analysis.
- $p_T(B)$: The transverse momentum of the B meson candidate. The B meson could be a B_u^- or a B_c^- meson depending on the assumption of h^- which is combined with the J/ψ meson.
- $P(\chi^2)$: The probability of the chi-square returned from the vertex and mass constraint fit of the $J/\psi\ h^-$ combination.
- $|d(B)|/\sigma_{d(B)}$: The impact parameter of the B meson candidate with respect to the primary vertex in units of its uncertainty.
- β_T: The pointing angle between $\vec{L}_T$ and $\vec{p}_T(B)$.
- I_B: The isolation of the B meson candidate, which is defined as $I_B \equiv p(B)/(p(B) + |\sum_i \vec{p}_i|)$, where $\sum_i \vec{p}_i$ is the sum of momenta over all other tracks not used in the $J/\psi\ h^-$ combination within $\sqrt{(\Delta\eta)^2 + (\Delta\phi)^2} < 0.7$, $\Delta\eta$ and $\Delta\phi$ are the relative pseudorapidity and azimuthal angle of tracks with respect to $\vec{p}(B)$.

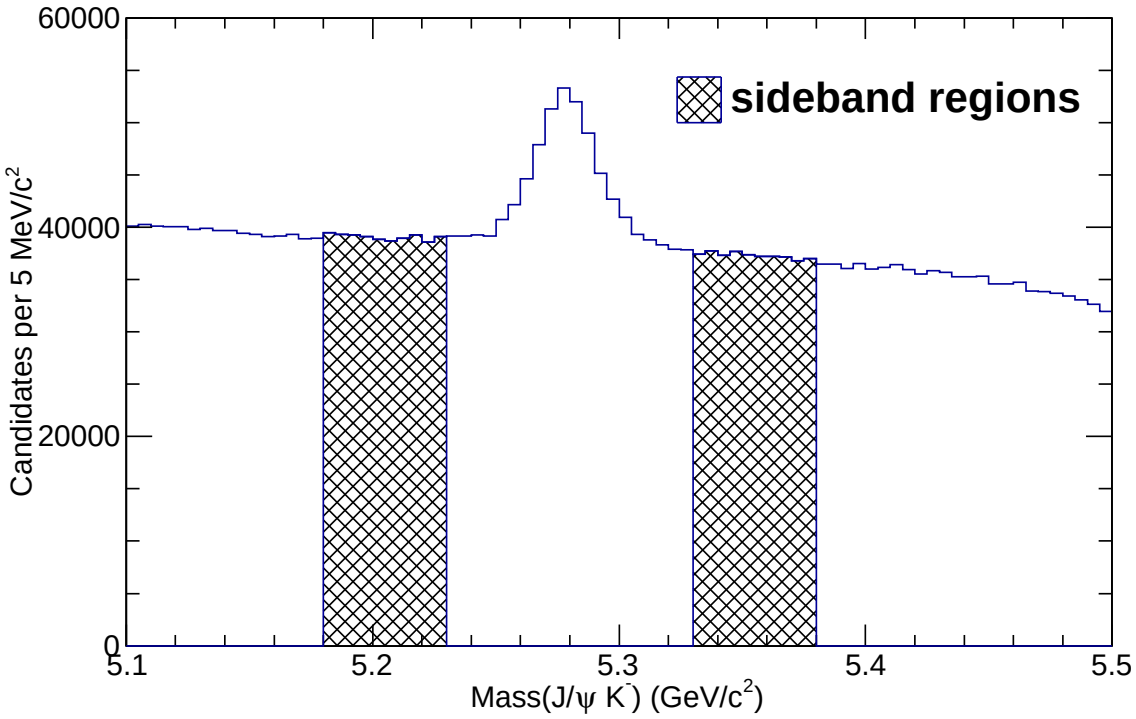

Figure 29: Reconstructed mass distribution for $B_u^- \to J/\psi\ K^-$.

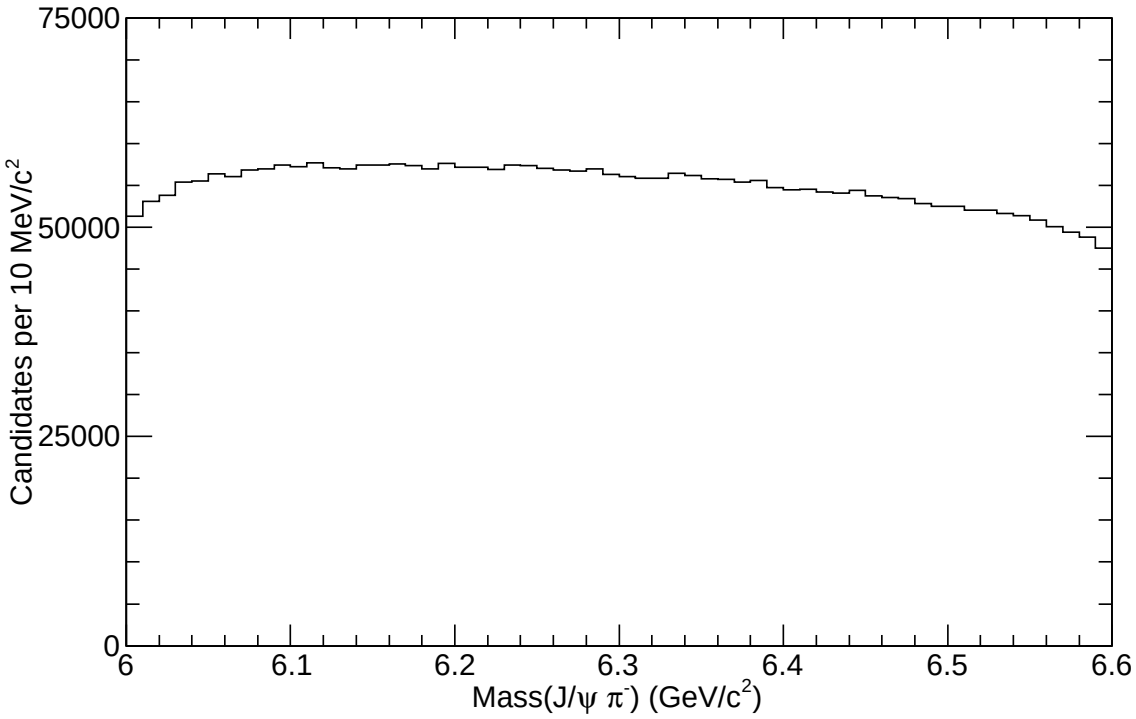

Figure 30: Reconstructed mass distribution for $B_c^- \to J/\psi\ \pi^-$.

- $\sigma_m(B)$: The uncertainty of the B meson candidate mass.
- $\sigma_{ct}(B)$: The uncertainty of the B meson candidate proper decay length.
- $ct(B)$: The proper decay length of the B meson candidate.

Since the $B_u^- \to J/\psi\ K^-$ and the $B_c^- \to J/\psi\ \pi^-$ decays are common in having a set of three tracks, two of which are muon tracks and the third being the hadron track, and these three tracks form a secondary vertex that is displaced from the primary vertex, The relatively plentiful $B_u^- \to J/\psi\ K^-$ decay is used to demonstrate that these selection variables could be used to discriminate the signal events from the background events. Figure 31 shows the comparison of the distributions of these selection variables between the background and signal events for $B_u^- \to J/\psi\ K^-$ decay, where the background distributions are obtained from the hatched areas in Figure 29, which include a lower sideband (from 5.18 to 5.23 GeV/c^2) and an upper sideband (5.33 to 5.38 GeV/c^2), and the signal distributions are obtained by subtracting the normalized distribution of the sideband regions from the signal region (from 5.23 to 5.33 GeV/c^2), which lies between the sideband regions. The area of the background distributions shown in Figure 31 have been normalized to the area of the signal distribution. Since the lifetime of B_u^- meson is 492 μm [21] which is much larger than the predicted B_c^- meson lifetime, similar distributions for events with $80 < ct < 300$ μm of $B_u^- \to J/\psi\ K^-$ decay are shown in Figure 32 to evaluate the impact of selections on the short-lived B_u^- sample. It can be seen from both Figure 31 and 32 that the $|d(B)|/\sigma_{d(B)}$ variable is more powerful to discriminate the background from the signal for small ct candidates, while the $\sigma_m(B)$ is almost identical for the background and signal. The $P(\chi^2)$ distribution is peaked at zero and decreases very fast for both signal and background. All other selections variables provide a powerful discrimination between the background and signal, even for short-lived B_u^- candidates.

These selection variables are then used to optimize the selections by maximize the quantity $S^2/(S+B)$ of $B_c^- \to J/\psi\ \pi^-$ decay, where S is the signal and B is the background under the $B_c^- \to J/\psi\ \pi^-$ signal. The signal is estimated by calculating the area under a Gaussian distribution, which is used to fit the signal of the $J/\psi\ \pi^-$ mass distribution. The Gaussian distribution has a fixed width of σ_m =20 MeV/c^2 which is roughly the typical mass resolution. The background shape in the fit is assumed to be linear and the background under the

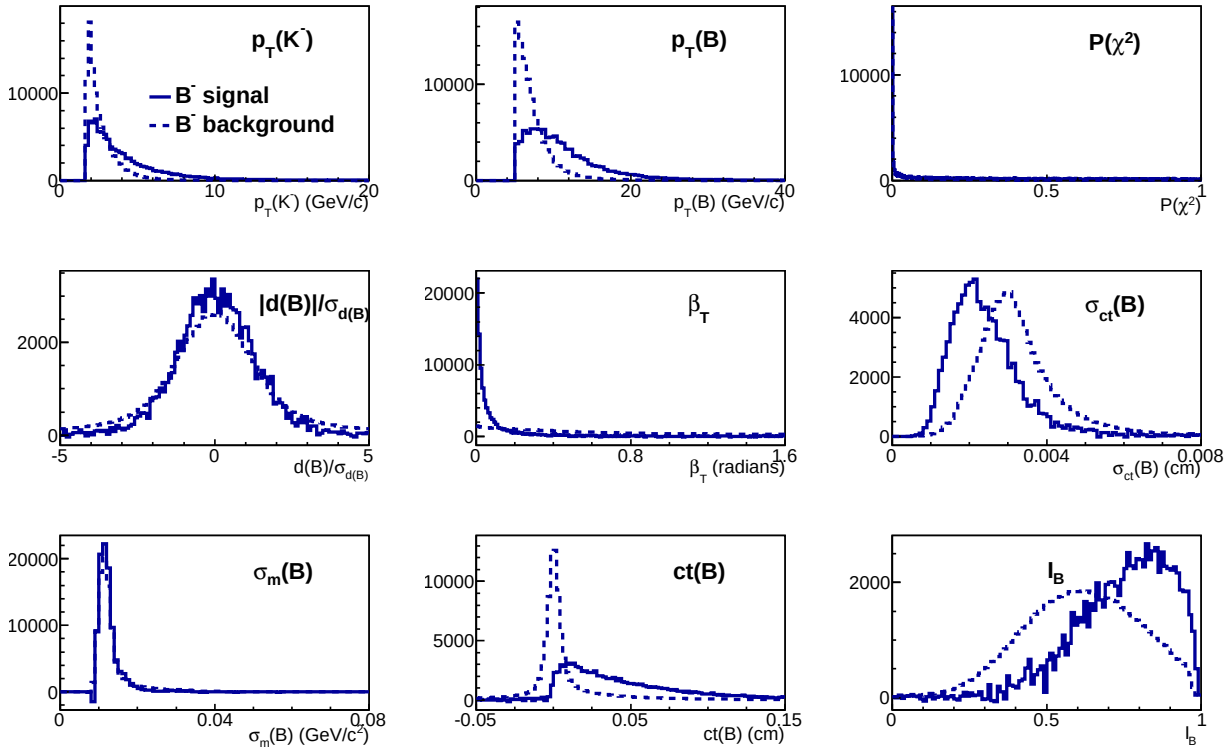

Figure 31: Comparison of the distributions of the selection variables between background events and signal events for $B_u^- \to J/\psi\ K^-$ decay. The background distributions are obtained from events in the hatched areas shown in Figure 29. The signal distributions are obtained by subtracting the normalized background distribution from the signal region events, which lies between the hatched areas in Figure 29. The area of the background distributions have been normalized to the area of the signal distribution.

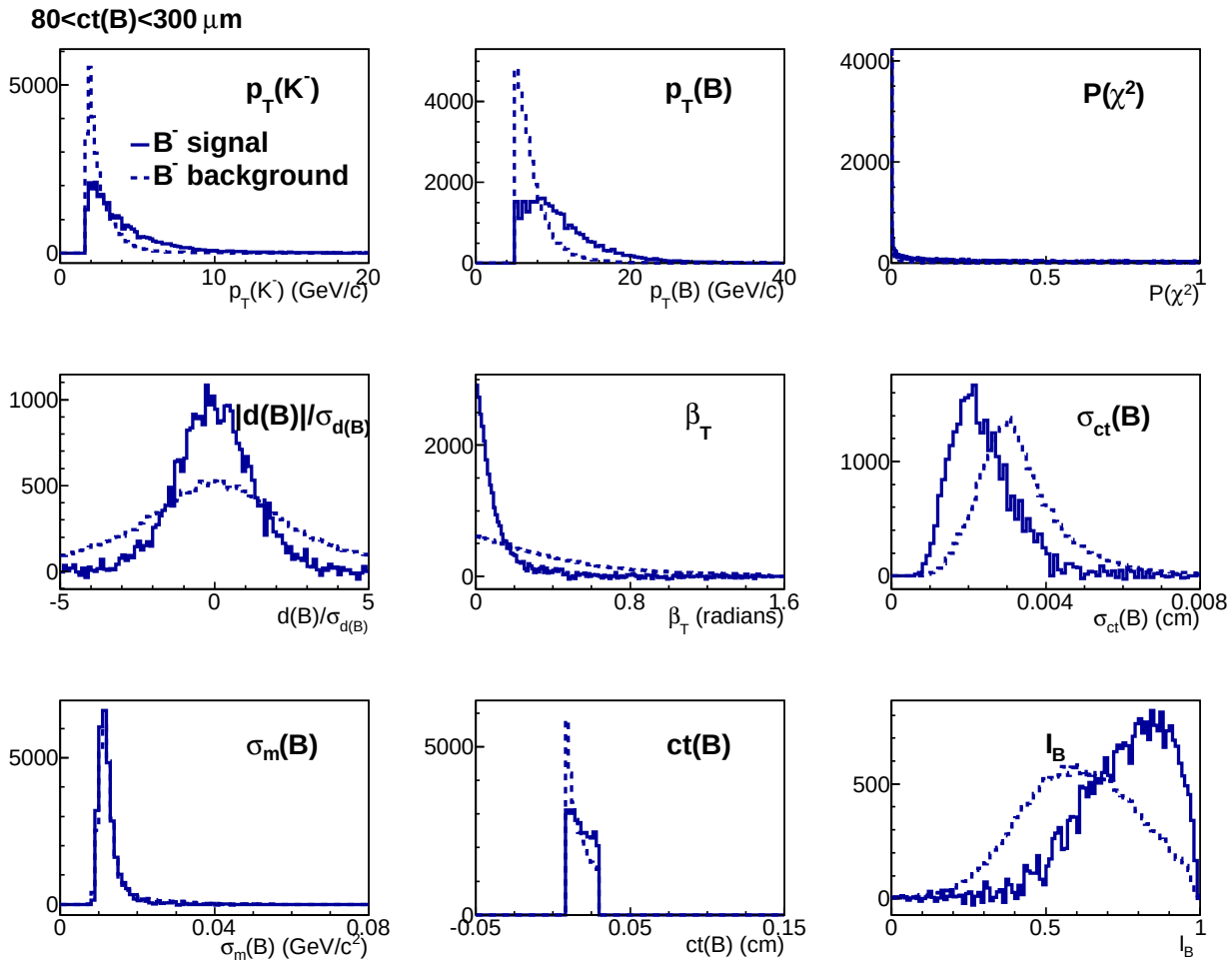

Figure 32: Comparison of the distributions of the selection variables between background events and signal events with $80 < ct < 300$ μm for $B_u^- \to J/\psi\ K^-$ decay. The background distributions are obtained from events with $80 < ct < 300$ μm in the hatched areas shown in Figure 29. The signal distributions are obtained by subtracting the normalized background distribution from the signal region events with $80 < ct < 300$ μm, which lies between the hatched areas in Figure 29. The area of the background distributions have been normalized to the area of the signal distribution.

signal is found by calculating the area of the background under a $\pm 2\sigma_m$ range around the mean of the Gaussian signal. Due to the large background of $B_c^- \to J/\psi\ \pi^-$ decay shown in Figure 30, some initial selections have to be made before any evidence of $B_c^- \to J/\psi\ \pi^-$ decay can be seen. These selection include $ct(B) > 80\ \mu$m, $P(\chi^2) > 0.001$, and $p_T(B) > 6.5$ GeV/c. The $J/\psi\ \pi^-$ mass distribution after these initial selections is shown in Figure 33.

4.2.1 $ct(B)$ requirement

The default minimum proper decay length requirement is chosen to be 80 μm, which is the same as in the earlier mass measurement of the B_c^- meson [5]. This requirement can be changed in the lifetime calculation later, if desired.

4.2.2 $p_T(B)$ requirement

The minimum p_T requirement of the B_c^- candidate is 6.5 GeV/c, this requirement will be varied between 5.0 to 7.5 GeV/c to study the effect on the remaining selection requirements.

4.2.3 β_T requirement

As shown in Figure 31 and 32, a small pointing angle β_T is very powerful in discriminating the signal and background for the $B_u^- \to J/\psi\ K^-$ decay. Figure 34 shows the $J/\psi\ \pi^-$ mass distribution for several values of maximum β_T requirement, along with all initial selection requirements. Figure 35 shows the quantity $S^2/(S+B)$ as a function of maximum β_T, for several requirements on $p_T(B)$. It can be seen that a requirement of maximum β_T between 0.1 and 0.2, depending on $p_T(B)$, maximizes the quantity $S^2/(S+B)$. To keep the default requirement of $p_T(B) > 6.5$ GeV/c, a requirement of $\beta_T\ < 0.2$ is chosen as the requirement on pointing angle.

4.2.4 I_B requirement

With the initial selection requirements, the isolation requirement is varied from 0.5 to 0.85 to test the quantity $S^2/(S+B)$. Figure 36 shows the $J/\psi\ \pi^-$ mass distribution for these

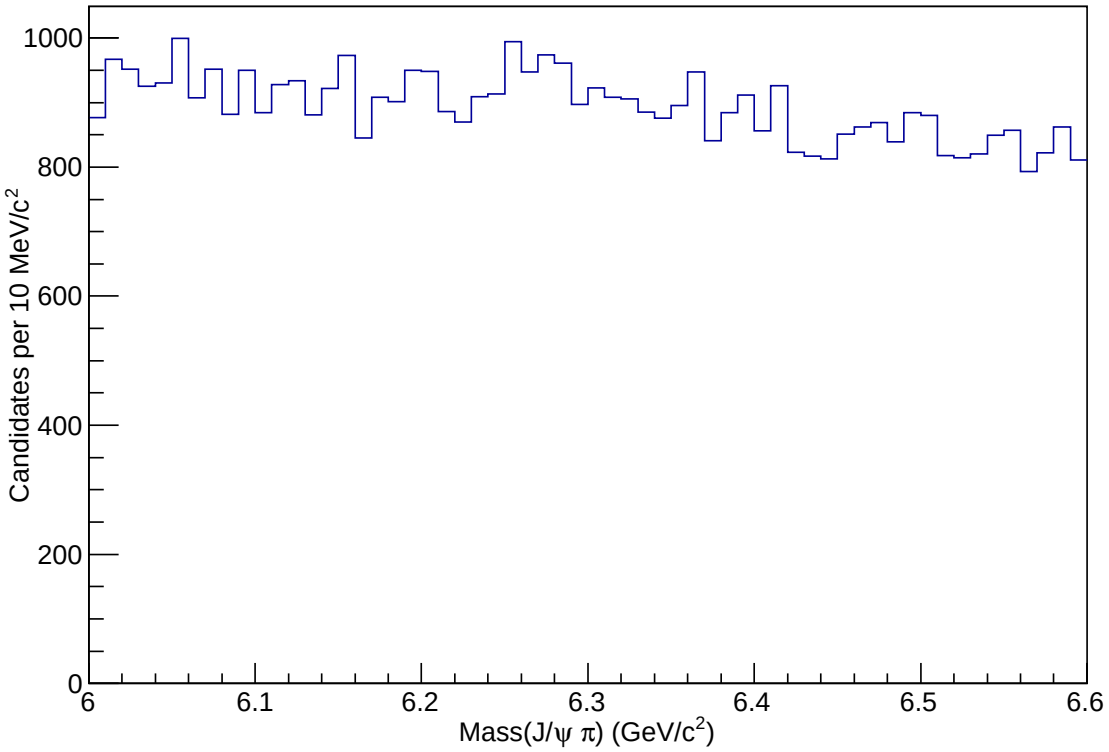

Figure 33: $J/\psi\ \pi^-$ mass distribution after the initial selections including $ct(B) > 80\ \mu$m, $P(\chi^2) > 0.001$, and $p_T(B) > 6.5$ GeV/c.

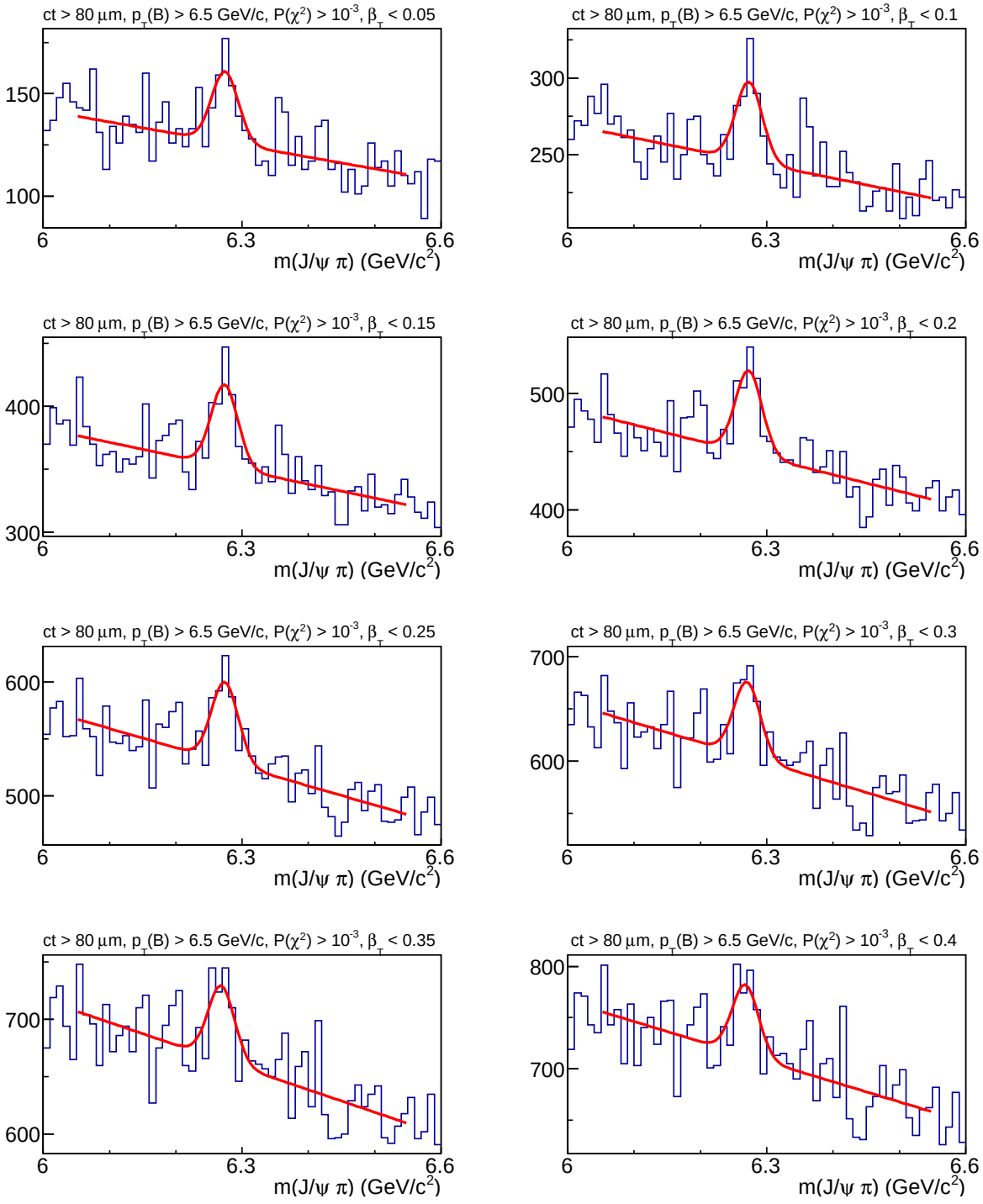

Figure 34: $J/\psi\ \pi^-$ mass distributions for several requirements on maximum β_T, along with the initial selection requirements.

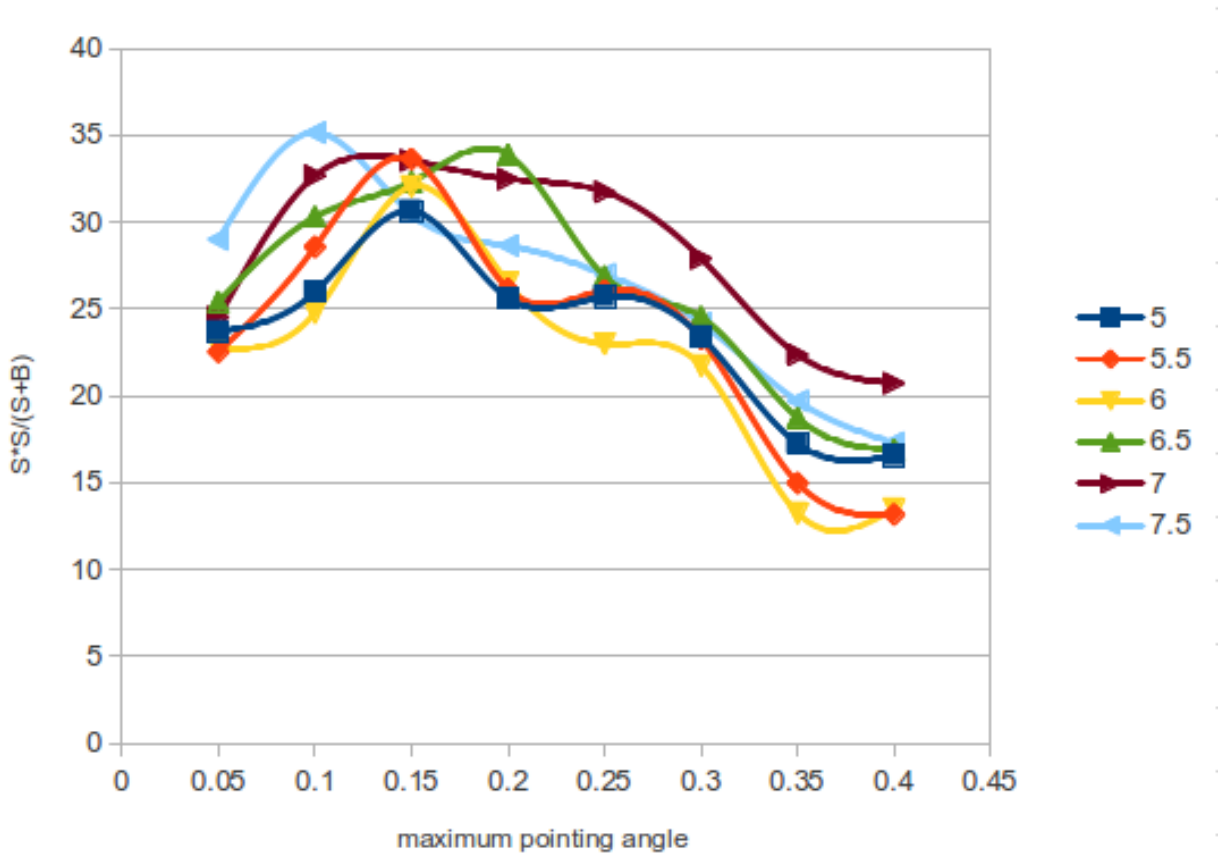

Figure 35: $S^2/(S+B)$ as a function of β_T, for several different requirements on $p_T(B)$.

different requirements on isolation. Figure 37 shows the quantity $S^2/(S+B)$ as a function of minimum I_B, for several requirements on $p_T(B)$. It can be seen that a requirement of minimum I_B between 0.6 and 0.7 maximizes the quantity $S^2/(S+B)$, and a requirement of 0.6 on I_B is chosen to allow more signal events.

4.2.5 $\sigma_{ct(B)}$ requirement

It can be seen from Figure 31 and 32 that the proper decay length uncertainty could be very useful to reject background events. It is also noted that $\sigma_{ct(B)}$ varies inversely with $p_T(B)$. Thus, the requirement on $\sigma_{ct(B)}$ for low p_T events ($p_T < 10$ GeV/c) varies as a linear function of p_T, i.e. $\sigma_{ct(B)} < C + S\ (10 - p_T(B))$ μm, where C and S are two parameters determined by the optimization of $S^2/(S+B)$. For high p_T events ($p_T \geq 10$ GeV/c), the requirement is fixed at $\sigma_{ct(B)} < C$ μm.

When studying the $\sigma_{ct(B)}$ requirement, the p_T requirement is fixed at $p_T > 5$ GeV/c rather than varying between 5.0 to 7.5 GeV/c. The $p_T = 5$ GeV/c is the minimum value allowed after the reconstruction. Figure 38 and 39 show the $J/\psi\ \pi^-$ mass distributions for different C and S parameters. Figure 40 shows the quantity $S^2/(S+B)$ as a function of different C values, for several values of S. It can be seen from Figure 40 that $C = 25$ μm and $S = 1$ (GeV/c)$^{-1}$ μm give the maximum $S^2/(S+B)$, but the number of B_c^- candidates after this selection is only $\sim$ 7000, which means the efficiency is too low even for signal events. The requirement is then set as $C = 35$ μm and $S = 3$ (GeV/c)$^{-1}$ μm which preserve $\sim$ 74000 B_c^- candidates.

4.2.6 $d(B)/\sigma_{d(B)}$ requirement

By comparing Figure 31 and 32, one can find that the distribution of impact parameter significance, $d(B)/\sigma_d(B)$, is quite useful to distinguish background from signal for events with smaller ct. Thus, the impact of this parameter for the B_c^- candidates is also evaluated.

Figure 41 shows the $J/\psi\ \pi^-$ mass distributions for different $d(B)/\sigma_{d(B)}$ requirements, along with the initial selection requirements. Figure 42 shows the quantity $S^2/(S+B)$ as a function of $d(B)/\sigma_{d(B)}$, for different requirements on $p_T(B)$. It can be seen from Figure 42

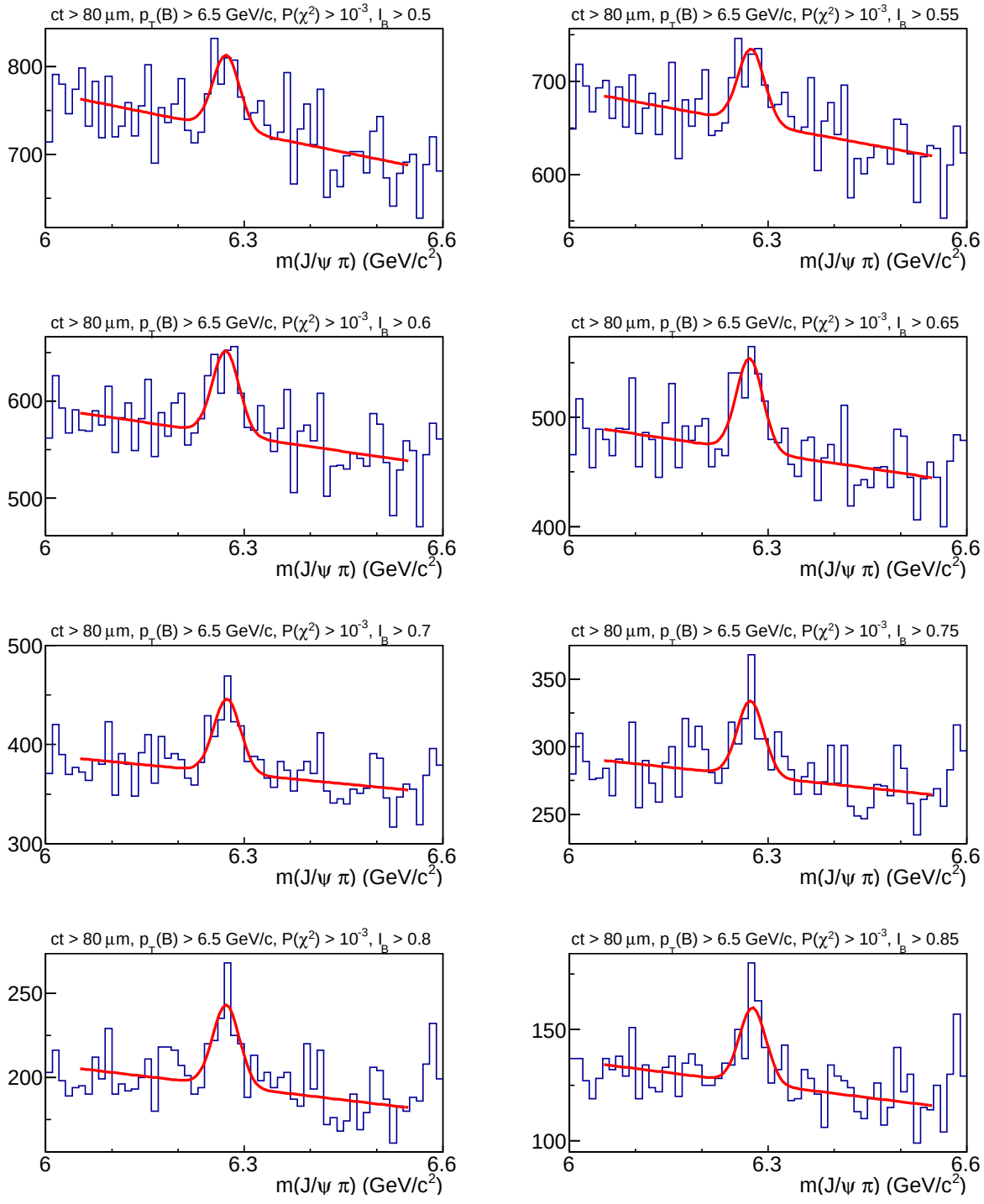

Figure 36: $J/\psi\ \pi^-$ mass distributions for several requirements on I_B, along with the initial selection requirements.

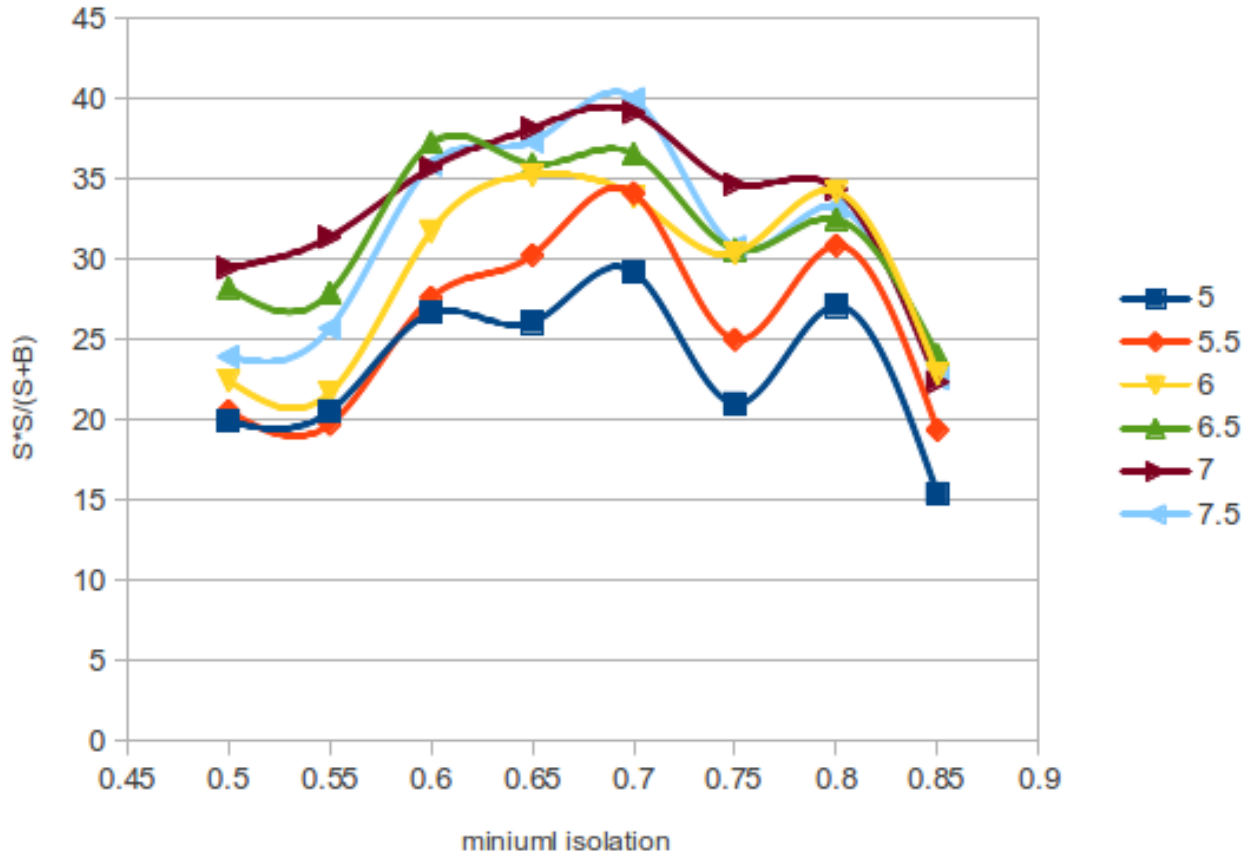

Figure 37: $S^2/(S+B)$ as a function of I_B, for several different requirements on $p_T(B)$.

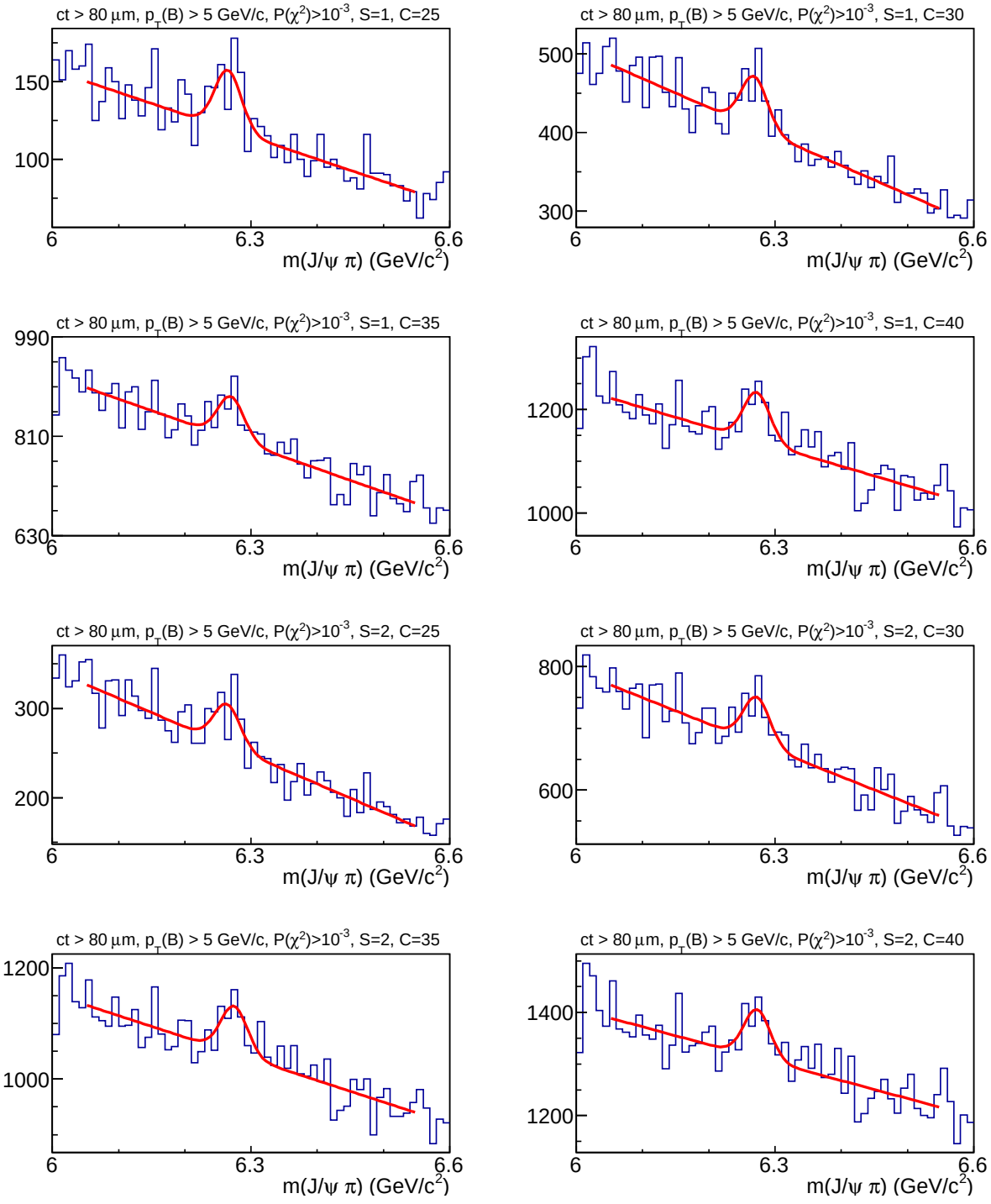

Figure 38: $J/\psi\ \pi^-$ mass distributions for different C parameters, for $S = 1$ and 2 $(\mathrm{GeV}/c)^{-1}\mu m$, along with the same requirement on $ct(B) > 80\ \mu\mathrm{m}$, $p_T(B) > 6.5\ \mathrm{GeV}/c$, and $P(\chi^2) > 0.001$. The parameter C is the $\sigma_{ct(B)}$ requirement for events with $p_T(B) \geq 10\ \mathrm{GeV}/c$. The parameter S is the slope that relaxes the $\sigma_{ct(B)}$ requirement for events with $p_T(B) < 10\ \mathrm{GeV}/c$.

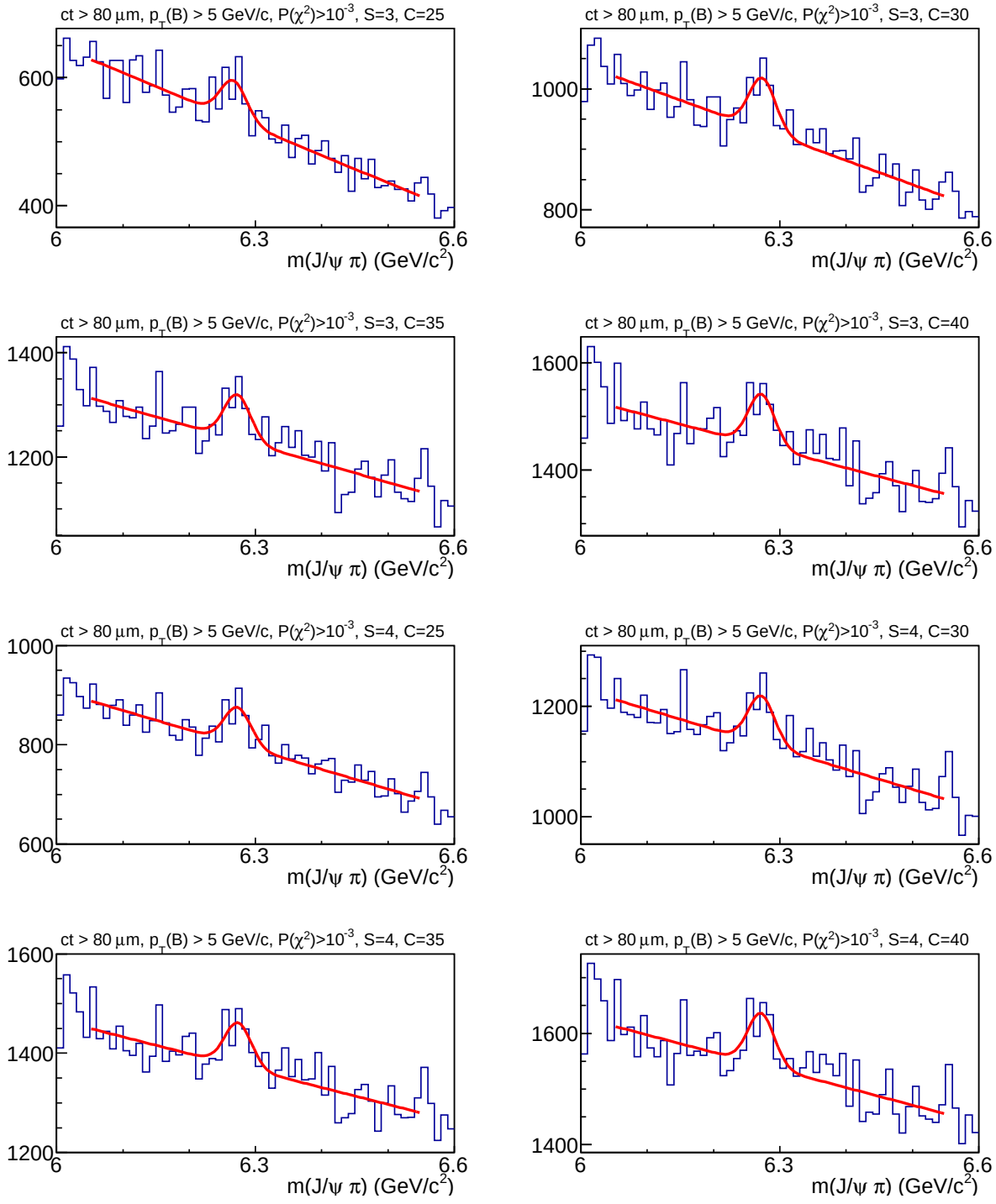

Figure 39: $J/\psi\,\pi^-$ mass distributions for different C parameters, for $S = 3$ and 4 $(\mathrm{GeV}/c)^{-1}\mu m$, along with the same requirement on $ct(B) > 80$ μm, $p_T(B) > 6.5$ GeV/c, and $P(\chi^2) > 0.001$. The parameter C is the $\sigma_{ct(B)}$ requirement for events with $p_T(B) \geq 10$ GeV/c. The parameter S is the slope that relaxes the $\sigma_{ct(B)}$ requirement for events with $p_T(B) < 10$ GeV/c.

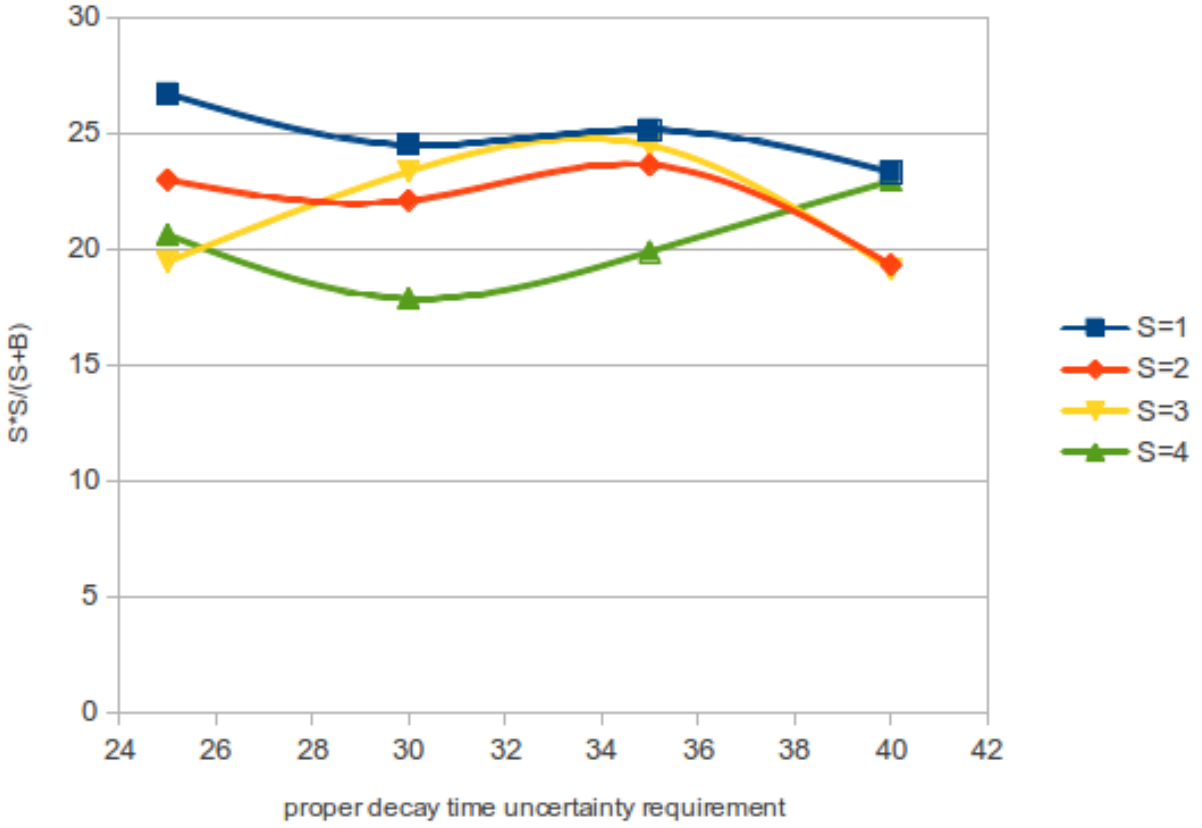

Figure 40: $S^2/(S+B)$ as a function of C, for several different values of S. The parameter C is the $\sigma_{ct(B)}$ requirement for events with $p_T(B) \geq$ 10 GeV/c. The parameter S is the slope that relaxes the $\sigma_{ct(B)}$ requirement for events with $p_T(B) <$ 10 GeV/c.

that a requirement of maximum $d(B)/\sigma_{d(B)}$ between 2.0 and 3.0 with $p_T(B) = 6.5$ GeV/c gives the maximum $S^2/(S+B)$. The $d(B)/\sigma_{d(B)} < 2.0$ is chosen as the final requirement to get more signal events.

4.2.7 $P(\chi^2)$ requirement

The default minimum $P(\chi^2)$ requirement is chosen to be 0.001. Figure 43, 44 and 45 show the $J/\psi\ \pi^-$ mass distributions for several different choices of $P(\chi^2)$ between 0.0001 and 0.1, and with different p_T requirements. Figure 46 shows the quantity $S^2/(S+B)$ as a function of minimum requirement of $P(\chi^2)$, for several values of minimum requirement of $p_T(B)$. It can be seen that the quantity $S^2/(S+B)$ does not change too much between 0.0001 and 0.01 for a given requirement of $p_T(B)$, but decreases for the choice of 0.1. The requirement is set as 0.001, which lies between 0.0001 and 0.1.

4.2.8 $p_T(\pi)$ requirement

The impact of $p_T(\pi)$ requirement on the $J/\psi\ \pi^-$ mass distribution are shown in Figure 47, 48, and 49. Figure 50 shows the quantity $S^2/(S+B)$ as a function of $p_T(\pi)$, for several requirements of $p_T(B)$. It can be seen in Figure 50 that the maximum $S^2/(S+B)$ occurs for samples with a minimum $p_T(B)$ requirement between 6.5 and 7.0 GeV/c. The minimum $p_T(\pi)$ requirement between 1.8 and 2.4 GeV/c does not change the quantity $S^2/(S+B)$ too much for these two $p_T(B)$ values. The requirement is set as $p_T(\pi) > 2.0$ GeV/c for this variable.

4.2.9 $\sigma_M(B)$ requirement

It can be seen from Figure 31 and 32 that the $\sigma_M(B)$ distributions are very similar between signal and background for $B_u^- \to J/\psi\ K^-$ decay. Thus, no further study is performed with this selection variable to maximize $S^2/(S+B)$. A loose requirement of $\sigma_M(B) < 40$ MeV/c^2 is set to reject the B_c^- candidates with poorly measured mass.

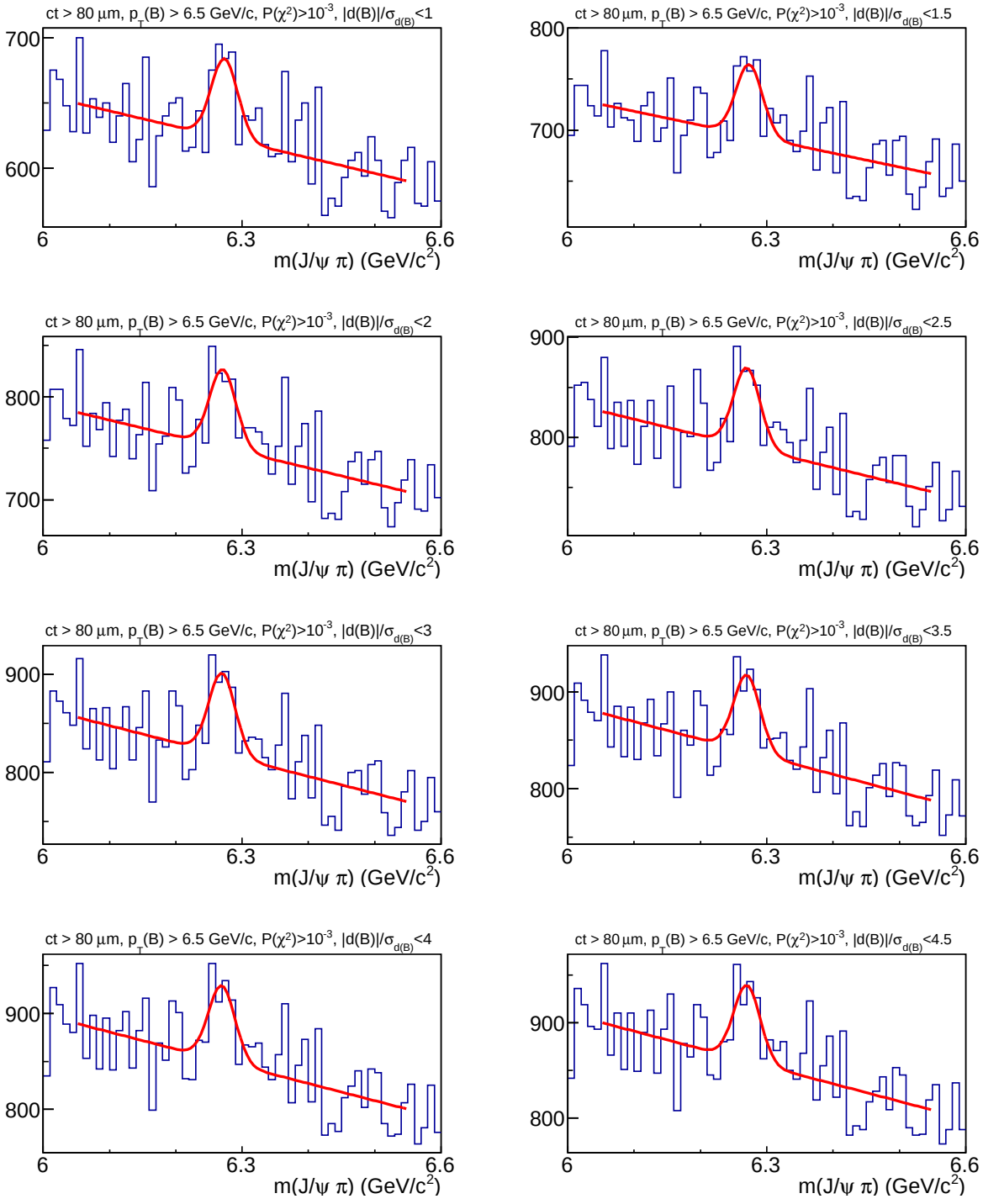

Figure 41: $J/\psi\ \pi^-$ mass distributions for several requirements on $d(B)/\sigma_{d(B)}$, along with the same requirement on $ct(B) > 80\ \mu$m, $p_T(B) > 6.5$ GeV/c, and $P(\chi^2) > 0.001$.

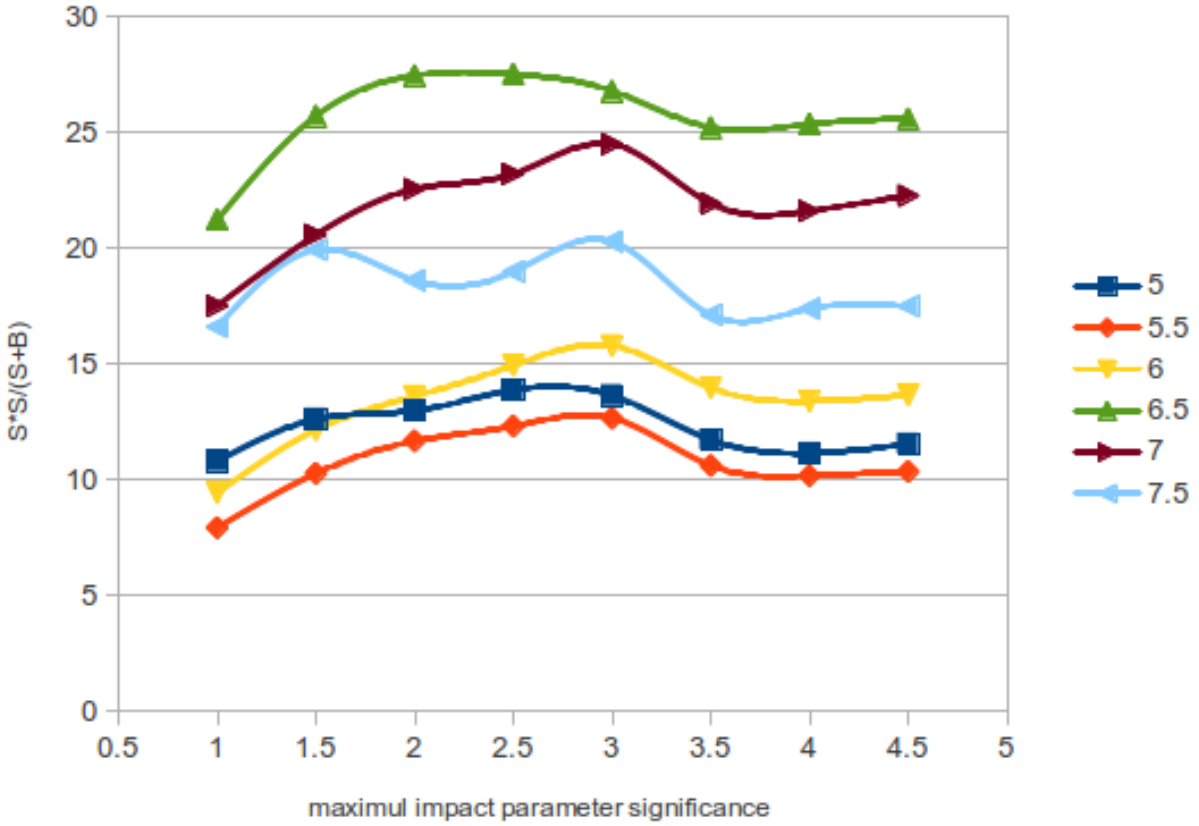

Figure 42: $S^2/(S+B)$ as a function of $d(B)/\sigma_{d(B)}$, for several different requirement on $p_T(B)$.

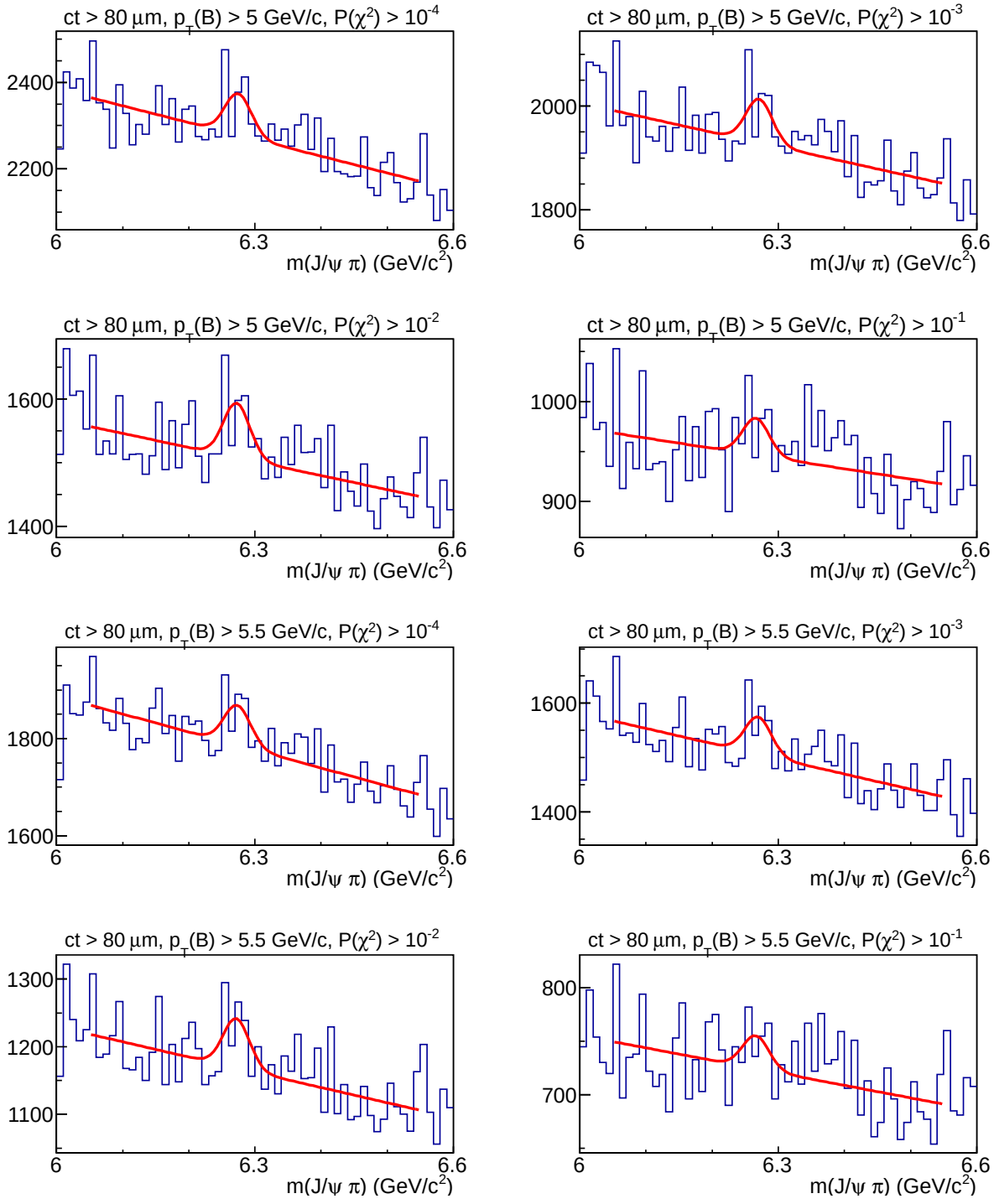

Figure 43: $J/\psi\ \pi^-$ mass distributions for several requirements on minimum $P(\chi^2)$, for $p_T\ >$ 5 and 5.5 GeV/c.

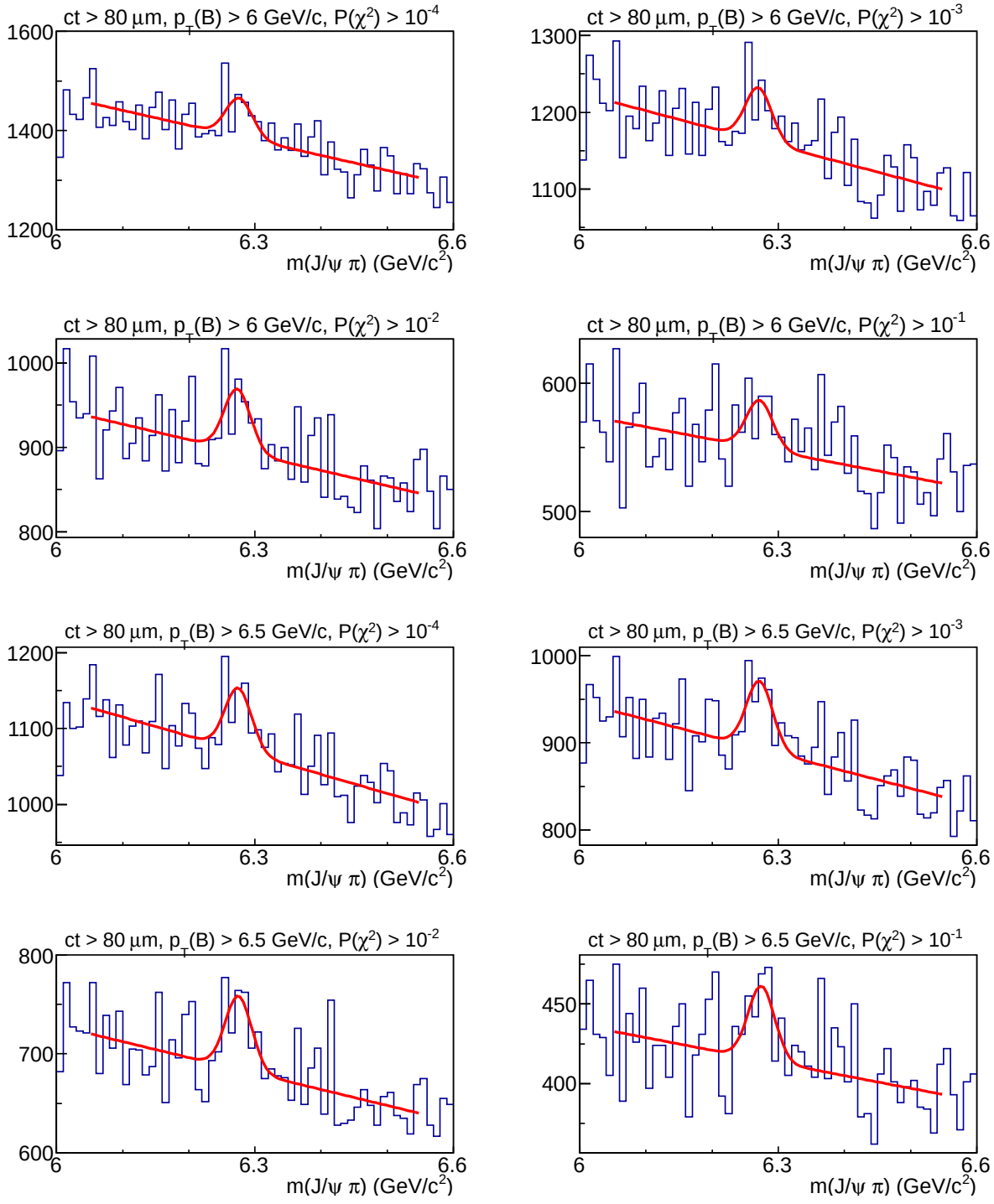

Figure 44: $J/\psi\ \pi^-$ mass distributions for several requirements on minimum $P(\chi^2)$, for $p_T\ >$ 6 and 6.5 GeV/c.

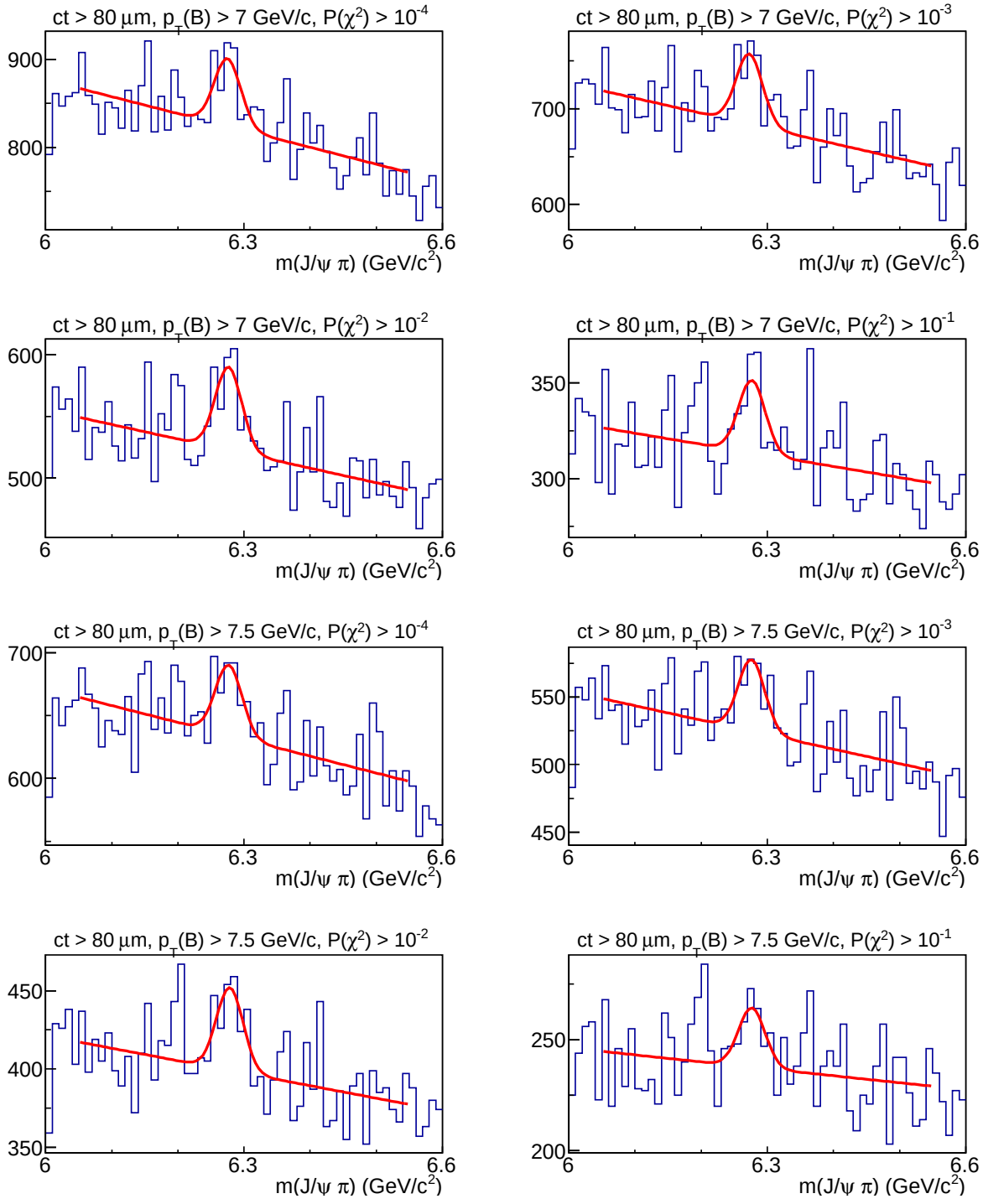

Figure 45: $J/\psi\ \pi^-$ mass distributions for several requirements on minimum $P(\chi^2)$, for $p_T\ >$ 7 and 7.5 GeV/c.

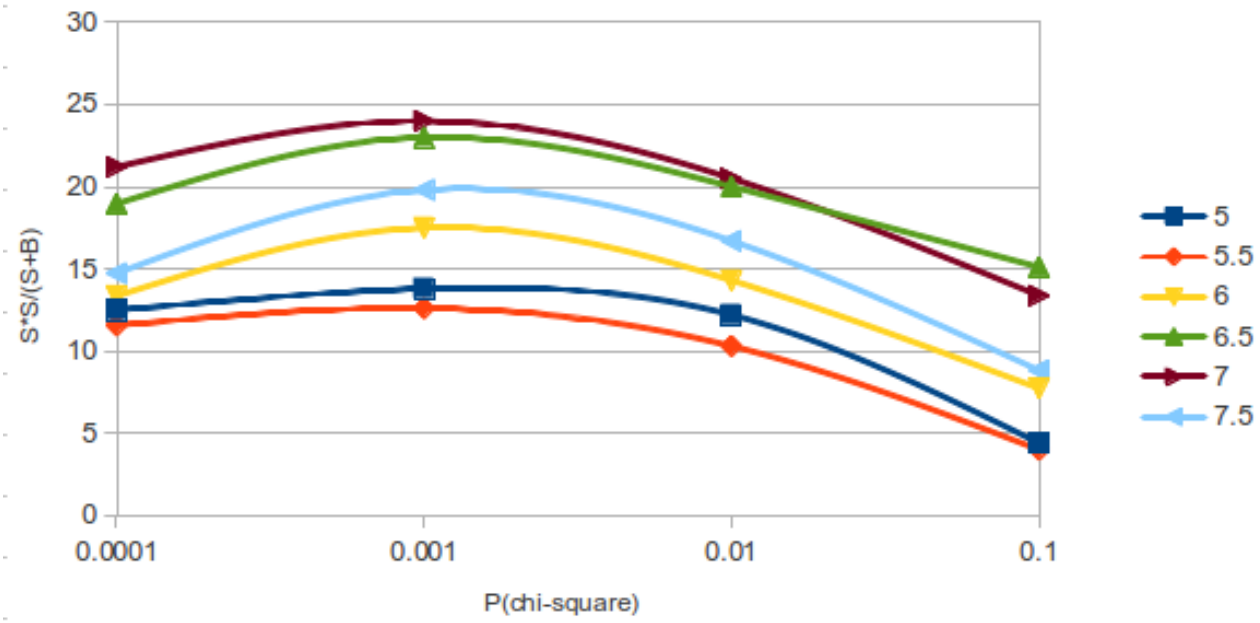

Figure 46: $S^2/(S+B)$ as a function of minimum requirement of $P(\chi^2)$, for several values of minimum requirement of $p_T(B)$.

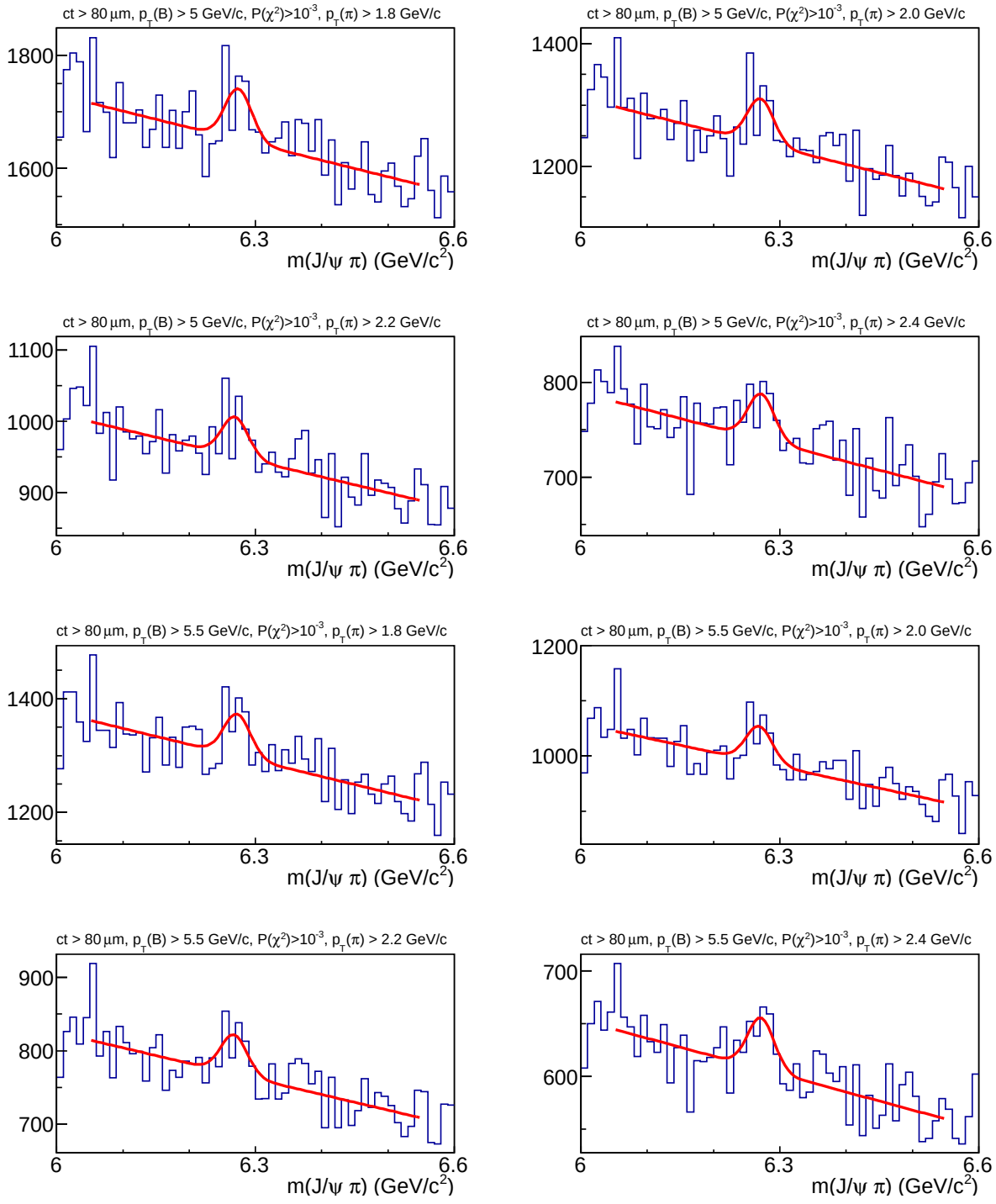

Figure 47: $J/\psi\ \pi^-$ mass distributions for several requirements on $p_T(\pi)$, while the minimum $p_T(B)$ requirements are 5.0 and 5.5 GeV/c, respectively.

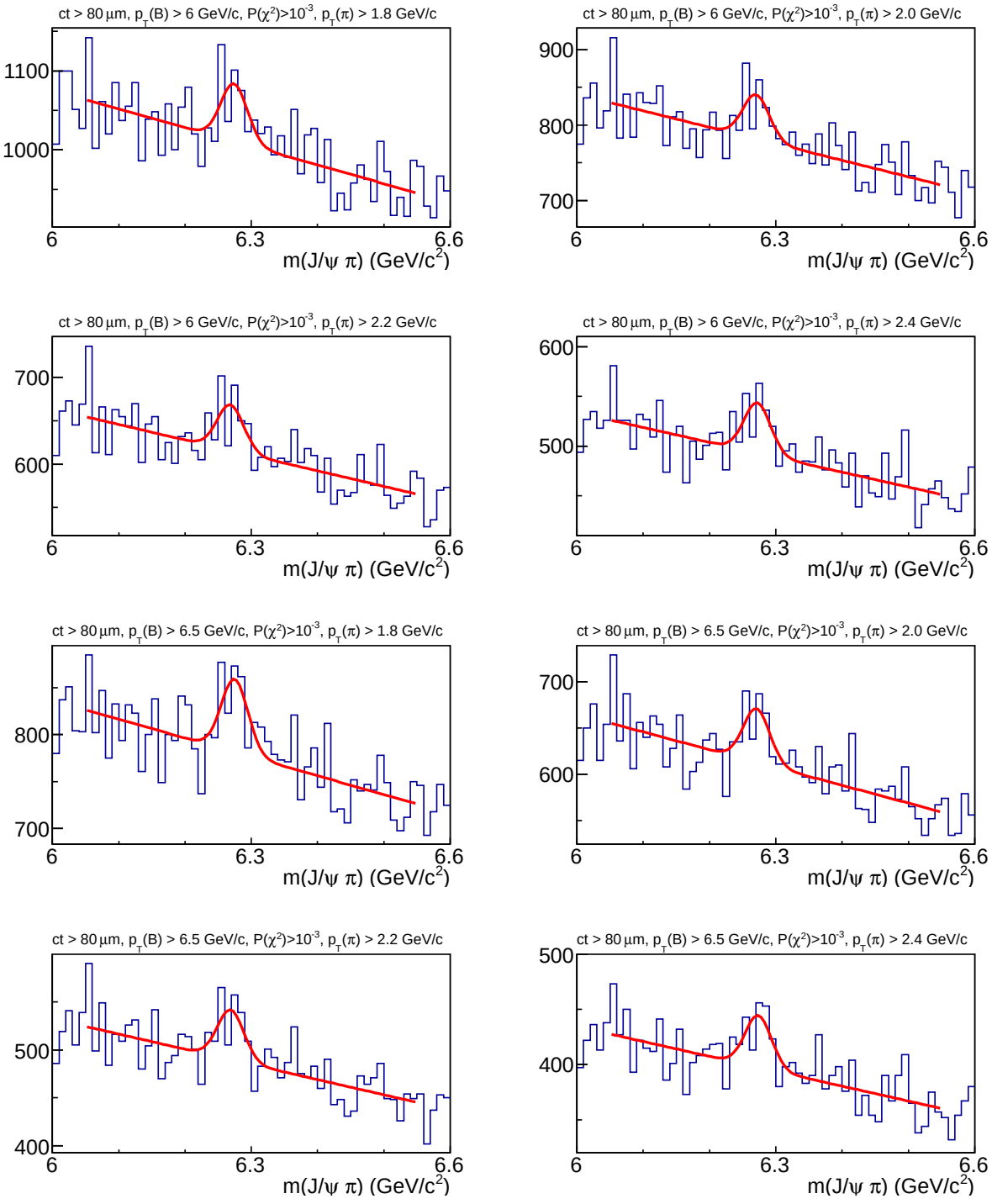

Figure 48: $J/\psi\ \pi^-$ mass distributions for several requirements on $p_T(\pi)$, while the minimum $p_T(B)$ requirements are 6.0 and 6.5 GeV/c, respectively.

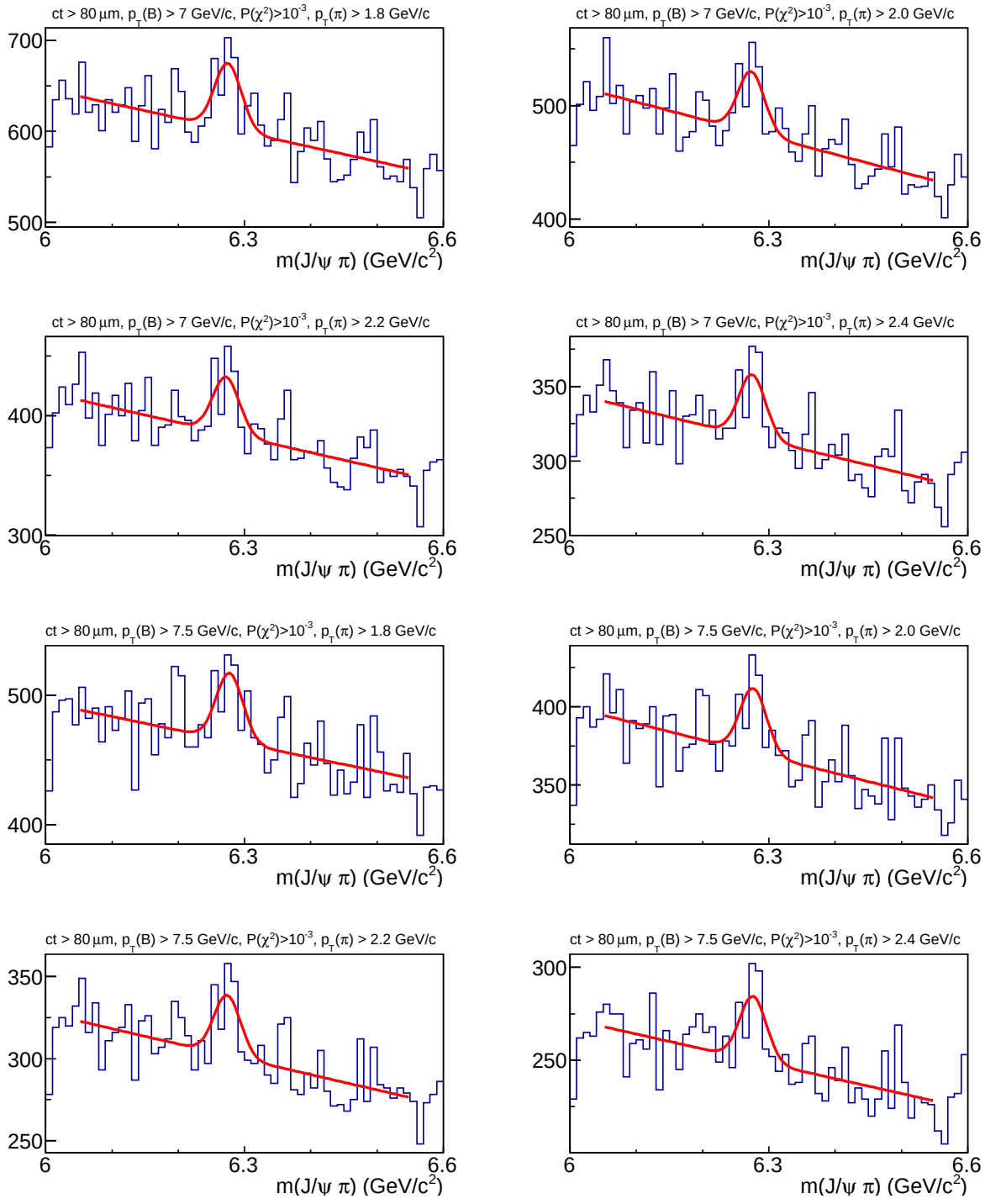

Figure 49: $J/\psi\ \pi^-$ mass distributions for several requirements on $p_T(\pi)$, while the minimum $p_T(B)$ requirements are 7.0 and 7.5 GeV/c, respectively.

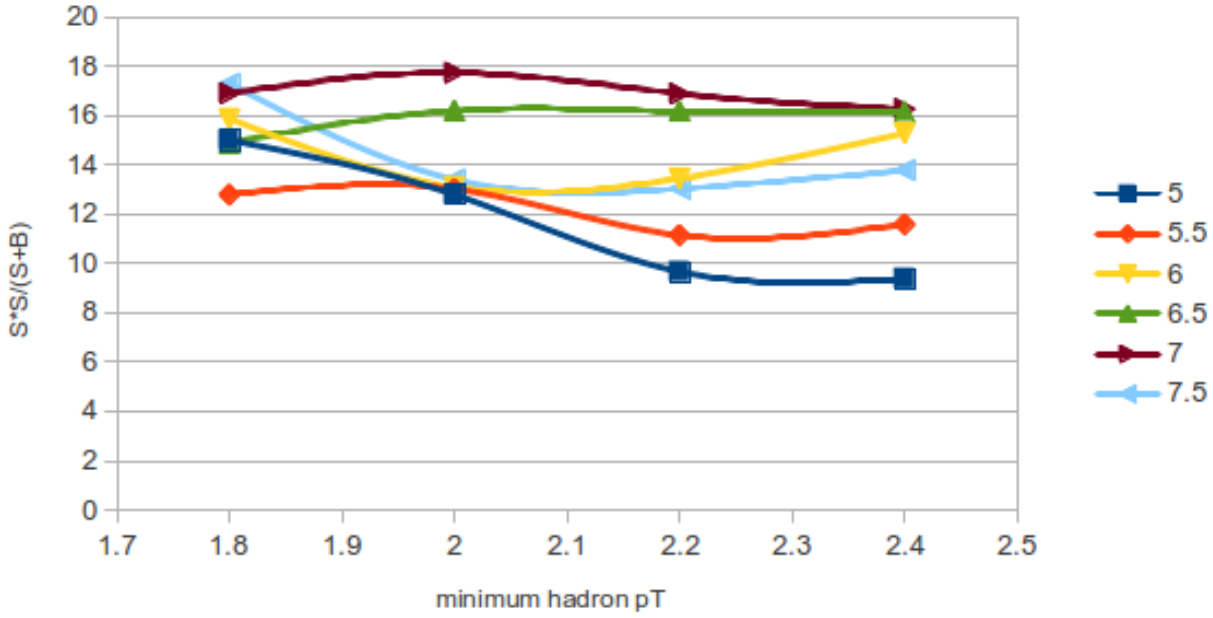

Figure 50: $S^2/(S+B)$ as a function of $p_T(\pi)$, for several different requirements on $p_T(B)$.

4.2.10 Summary of selections

The selection requirements used in this analysis are summaries in Table 6. Note that the

Table 6: Selection variables and requirements as described in the text. Here "h^-" refers to the third track combined with the J/ψ and may be a K^- or π^- candidate, "B" refers to the combination of J/ψ h^- and may be a B_u^- or B_c^- candidate depending on h^-.

Selection variable	Requirement
$p_T(h^-)$	> 2.0 GeV/c
$p_T(B)$	> 6.5 GeV/c
$P(\chi^2)$	$> 0.1\%$
$\lvert d(B)\rvert/\sigma_{d(B)}$	< 2.0
β_T	< 0.2 radians
I_B	> 0.6
$\sigma_m(B)$	< 40 MeV/c^2
$ct(B)$	> 80 μm
$\sigma_{ct}(B)$	$< max[35, 35 + 3 \times (10 - p_T(B))(\text{GeV}/c)]$ μm

same selection requirements are applied to both the B_u^- and the B_c^- candidates while the only difference between the two samples is the mass assignment of the hadron track h^-.

Applying the selection criteria, the reconstructed mass distribution for the B_u^- candidates is shown in Figure 51. Two background sideband regions of the B_u^- candidates are the same as defined in Figure 29: a lower sideband from 5.18 to 5.23 GeV/c^2 and an upper sideband from 5.33 to 5.38 GeV/c^2, as shown in the hatched areas. The total number of events in the sideband regions is 4003. The signal region lies between the lower and upper sidebands, and has 46268 B_u^- candidates.

The reconstructed mass distribution for the B_c^- candidates is shown in Figure 52. The sideband regions of B_c^- candidates consist of a lower sideband from 6.16 to 6.21 GeV/c^2 and an upper sideband from 6.33 to 6.60 GeV/c^2 as shown in the hatched areas. The lower sideband is narrow to avoid background events from semileptonic B_c^- decays where the lepton

is misidentified as a pion and causes the reconstructed mass to fall into the otherwise wider lower sideband. The total number of events in the sideband regions is 3031. The signal region lies between the lower and upper sidebands, and has 1496 B_c^- candidates.

4.3 MONTE CARLO SIMULATION

One may wonder whether the selection criteria will distort the exponential distribution of the proper decay time and to what extent. This is an essential issue in the construction of the likelihood fitter because the signal proper decay time model must include this effect accordingly in order to yield a reasonable result. In order to study the efficiency of the selection criteria, Monte Carlo (MC) simulations are used in this analysis by generating particles produced in the $p\bar{p}$ collision and simulating the decays and interactions of the particles in the CDF II detector.

Both $B_u^- \to J/\psi\ K^-$ and $B_c^- \to J/\psi\ \pi^-$ MC simulations are generated to study the selection efficiency. The BGENERATOR program [59, 60], which takes a p_T and η spectrum as its input for the generated B meson, is used for the simulation. The decays of the particles such as the B meson or J/ψ are simulated by the EVTGEN program [61] which has a decay table to specify the branching fractions for a given decay channel as well as the physics model to use in the decay. For particles that live long enough to pass through the CDF II detector such as muons, the CDFSIM [62] program is used to simulate their interaction with the detector. The performance of the simulation is tested by comparing the detector response in the simulation to that in the experimental data, and it is found to be in good agreement [63]. In addition, the TRIGSIM [64] program is also used to simulate the trigger performance of the detector.

The Fixed-Order plus Next-to-Leading Logarithms (FONLL) p_T spectrum [65], which shows good agreement with the $B_u^- \to J/\psi\ K^-$ data, is used for the B_u^- production spectrum. For the B_c^- spectrum, the theoretical prediction on the B_c^- production [1] is used. It has the following advantages: it includes both the ground state and the excited state production; it includes the dominant contribution from the interaction of gluons and heavy sea quarks as

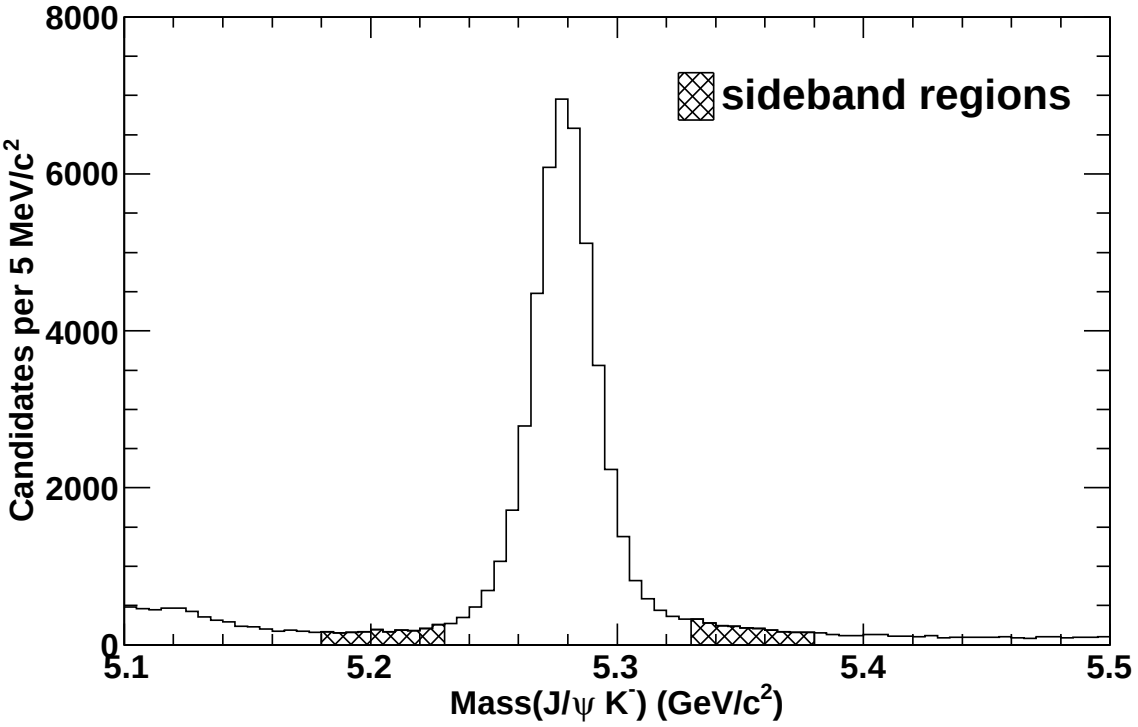

Figure 51: The invariant-mass distribution of $J/\psi\ K^-$ combinations. The hatched areas are the sideband regions and the signal region lies between them.

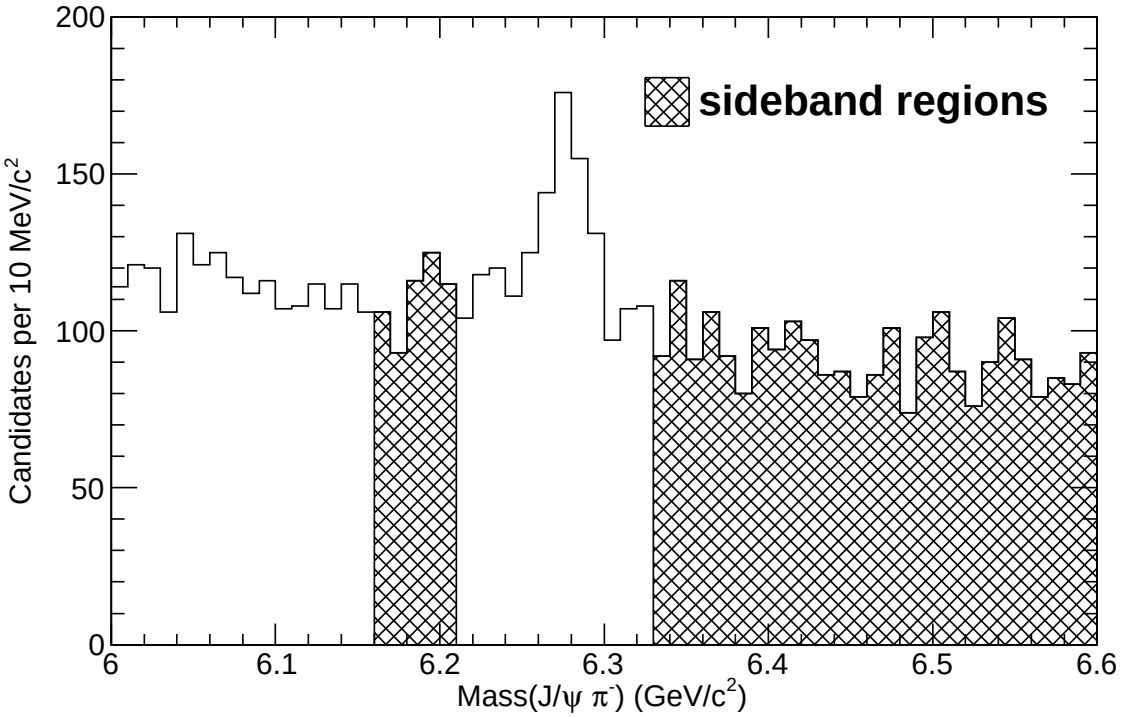

Figure 52: The invariant-mass distribution of $J/\psi\ \pi^-$ combinations. The hatched areas are the sideband regions and the signal region lies between them.

well as pure gluon fusion; and it includes a small contribution from $q\bar{q}$ production. Table 7 shows the fractions of different contributions to the B_c^- MC spectrum used in this analysis. Figure 53 shows the contribution to the final B_c^- spectrum from these different production processes for B_c^- and B_c^{*-}.

Table 7: The B_c^- and B_c^{*-} production fractions based on Ref. [1], where gb+gc+gg represents the combined contributions from the interactions between gluons and heavy sea quarks, and pure gluon fusion, $q\bar{q}$ represents the contribution from quark-antiquark production mechanism.

Production fractions	$gg + gb + g\bar{c}$	$q\bar{q}$	Fraction of total σ
B_c^-	0.994	0.006	$\frac{\sigma(B_c^-)}{\sigma(B_c^- + B_c^{*-})}$ =0.237
B_c^{*-}	0.991	0.009	$\frac{\sigma(B_c^{*-})}{\sigma(B_c^- + B_c^{*-})}$ =0.763

The p_T spectrum of the B_u^- production is shown for both experimental data and MC simulation in Fig. 54, where the experimental data distribution is found by subtracting the p_T distribution of the sideband region from that of the signal region.

The area of the simulated p_T distribution is normalized to the area of the experimental data distribution. Reasonable consistency between experimental data and MC simulation is observed above 6 GeV/c. Also shown in Figure 54 is the MC simulation of the B_c^- production. To further validate the $B_u^- \to J/\psi\ K^-$ MC simulation, The distributions of the selection variables listed in Table 6 are compared for experimental data and MC simulation which are shown in Figure 55.

Generally, good agreement between experimental data and MC simulation is observed for all selection variables except for I_B and $\sigma_{ct}(B)$. The disagreement of the distribution for the I_B variable is due to the fact that MC simulation generates signal events that are free of background contamination. As a result, the isolation obtained from the MC simulation is peaked at 1. As for the disagreement in the $\sigma_{ct}(B)$ distribution, the selection requirement on σ_{ct} shown in Table 6 is tuned for MC simulation by looking for an equivalent set of σ_{ct} selection values that produce the same effect in the MC simulation as the values given in Table reftab:sel produce in the experimental data. These σ_{ct} selection values for MC

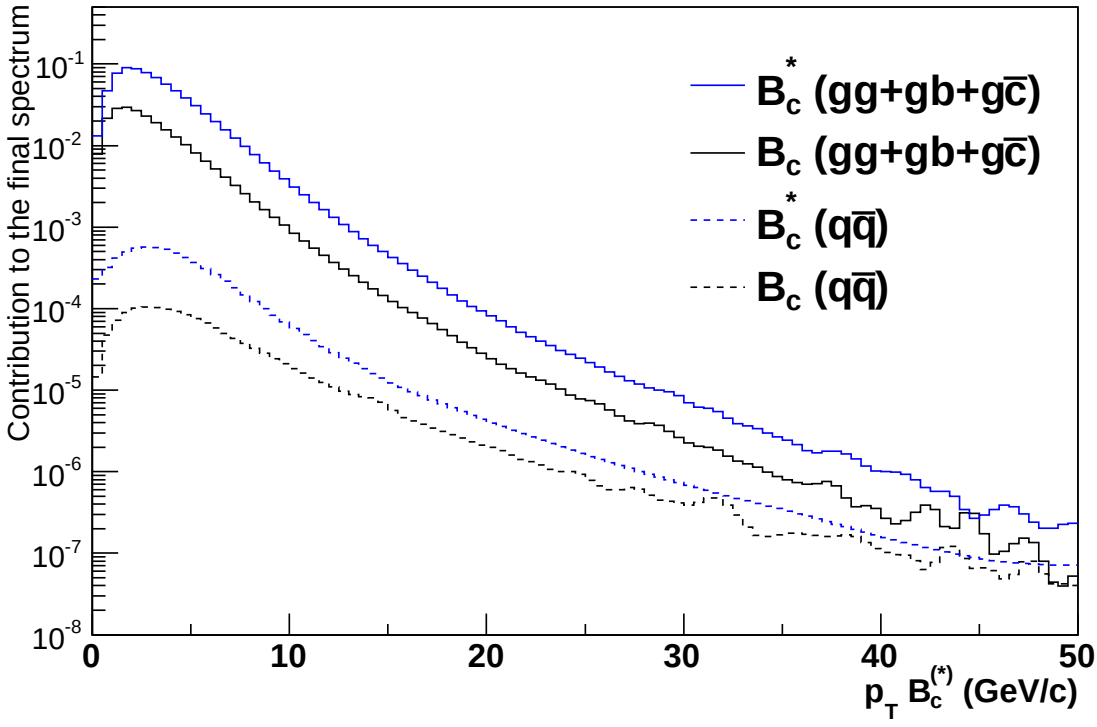

Figure 53: B_c^- and B_c^{*-} spectra due to different production processes are shown. The processes are scaled to reflect the weight used in composing the final spectrum.

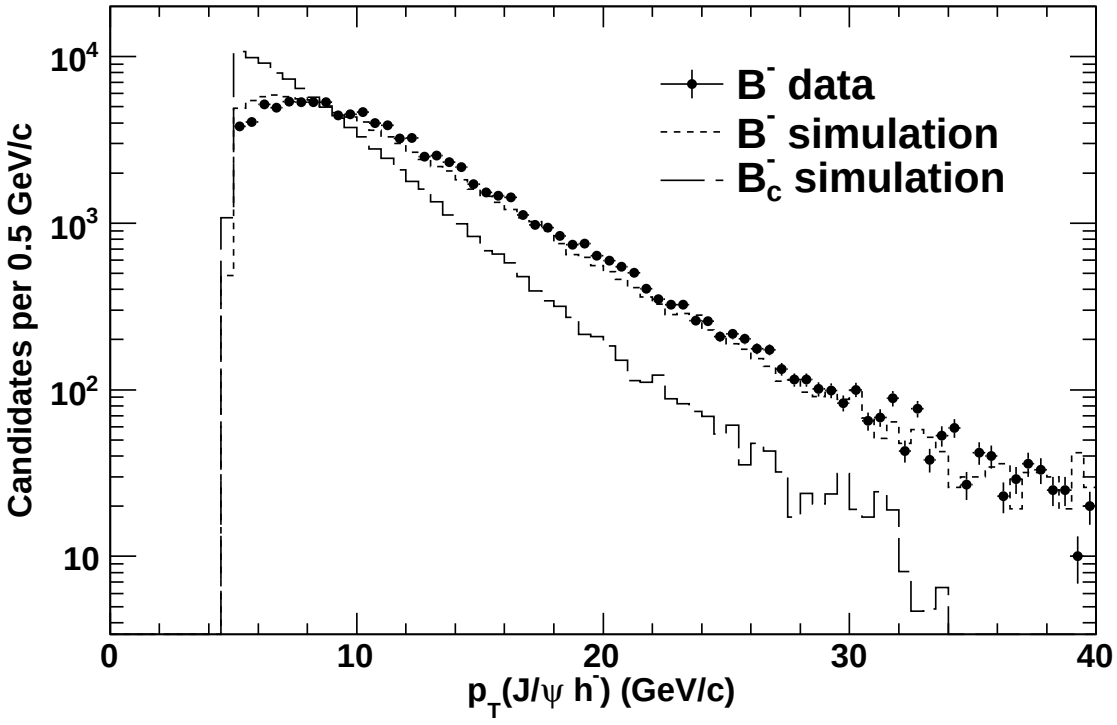

Figure 54: The p_T spectrum for $B_u^- \to J/\psi\ K^-$ used in the simulation is compared with the p_T distribution observed in data. The data distribution is found by subtracting the distribution of the sideband region from that of the signal region. Also shown is the B_c^- spectrum used in the simulation. The "h^-" refers to either a K^- or a π^- for B_u^- or B_c^- respectively.

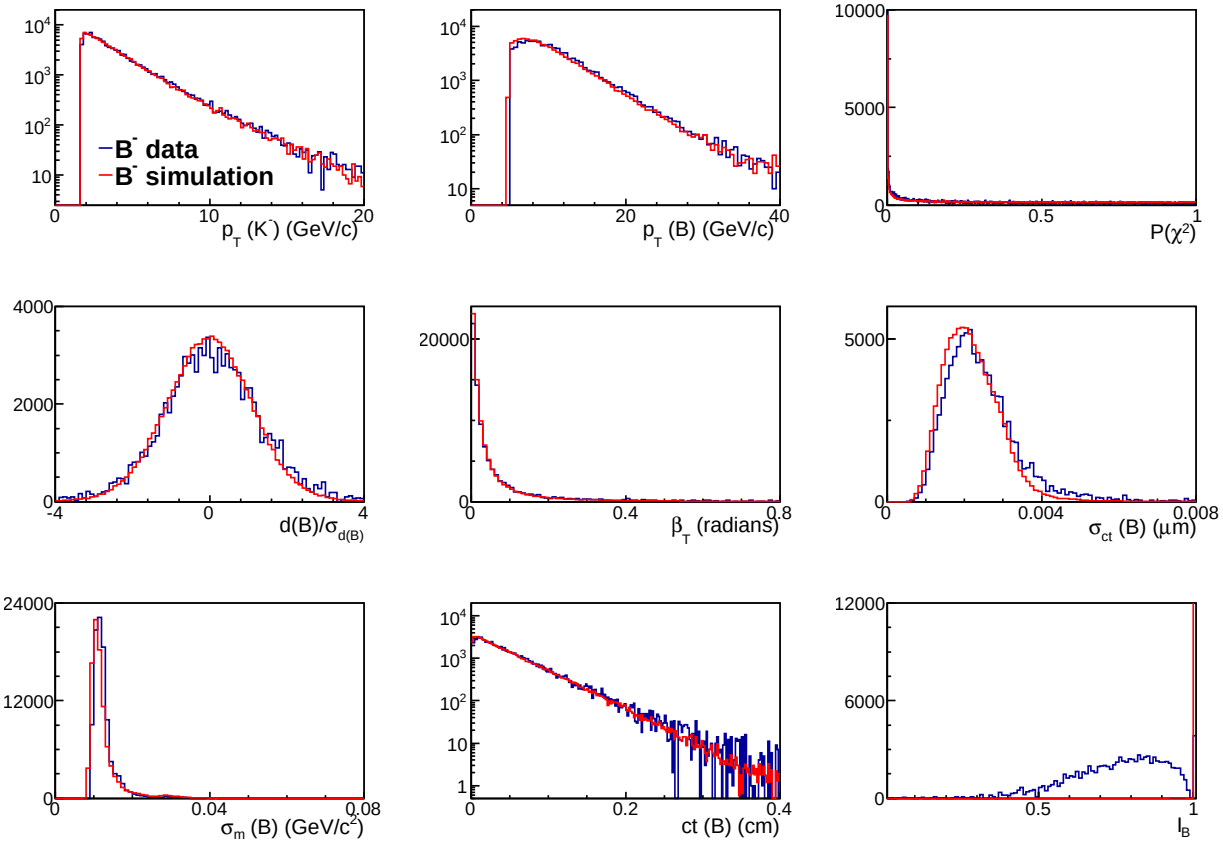

Figure 55: The distribution of the selection variables for $B_u^- \to J/\psi\ K^-$ obtained from the simulation is compared with data. The data distribution is found by subtracting the distribution of the sideband region from that of the signal region.

simulation are also p_T dependent and the p_T threshold remains the same, the only change is to require $\sigma_{ct}(B)$ to be less than 35 μm instead of 50 μm for $p_T(B) \geq 10$ GeV/c and $\sigma_{ct}(B)$ to be less than 25 μm instead of 35 μm for $p_T(B) = 5$ GeV/c. This systematic tuning between MC simulation and experimental data for σ_{ct} has an associated systematic uncertainty which will be discussed in Chapter 6. Figure 56 shows the distributions of the selection variables obtained from the $B_c^- \to J/\psi\ \pi^-$ MC simulation.

4.3.1 Selection efficiency

First,the selection efficiency of each selection requirement as a function of proper decay length is shown. The efficiency of the selection criteria is found by dividing the proper decay length distribution after applying the selection variable of interest by the distribution obtained from the minimum selection and correctly propagating the uncertainties. Figure 57 shows the efficiency comparison between MC simulation and experimental data for $B_u^- \to J/\psi\ K^-$ decay. Note that the efficiency of selection variable $ct(B)$ is not shown since its efficiency as a function of $ct(B)$ is trivial, i.e., the efficiency is 0% for events with $ct(B) < 80$ μm, and 100% for events with $ct(B) \geq 80$ μm. Also, the efficiency for $ct(B) < 80$ μm is not shown since these events will eventually be rejected. The discrepancy of the efficiencies for the isolation variable is not surprising since the MC generates pure signal events, and the isolation variable distribution is quite different from that of the experimental data as shown in Figure 55. The important point of the efficiency is that an overall scale constant in the efficiency curve does not change the exponential distribution of the signal proper decay time. Thus, this discrepancy is not a problem. Figure 58 shows similar efficiency for $B_c^- \to J/\psi\ \pi^-$ simulations. It can be seen that the efficiencies for most of the selection variables are flat as a function of proper decay length, and in general the simulation agrees with the experimental data. The β_T is an exception in the sense that the efficiency is distorted for events with small ct. Figure 59 shows the efficiency comparison between MC simulation and experimental data for $B_u^- \to J/\psi\ K^-$ decay, when the selection variable of interest is the last one applied. Figure 60 shows similar efficiency for $B_c^- \to J/\psi\ \pi^-$ simulations. These figures suggest that the efficiencies of all selection variables except β_T are uniform over the

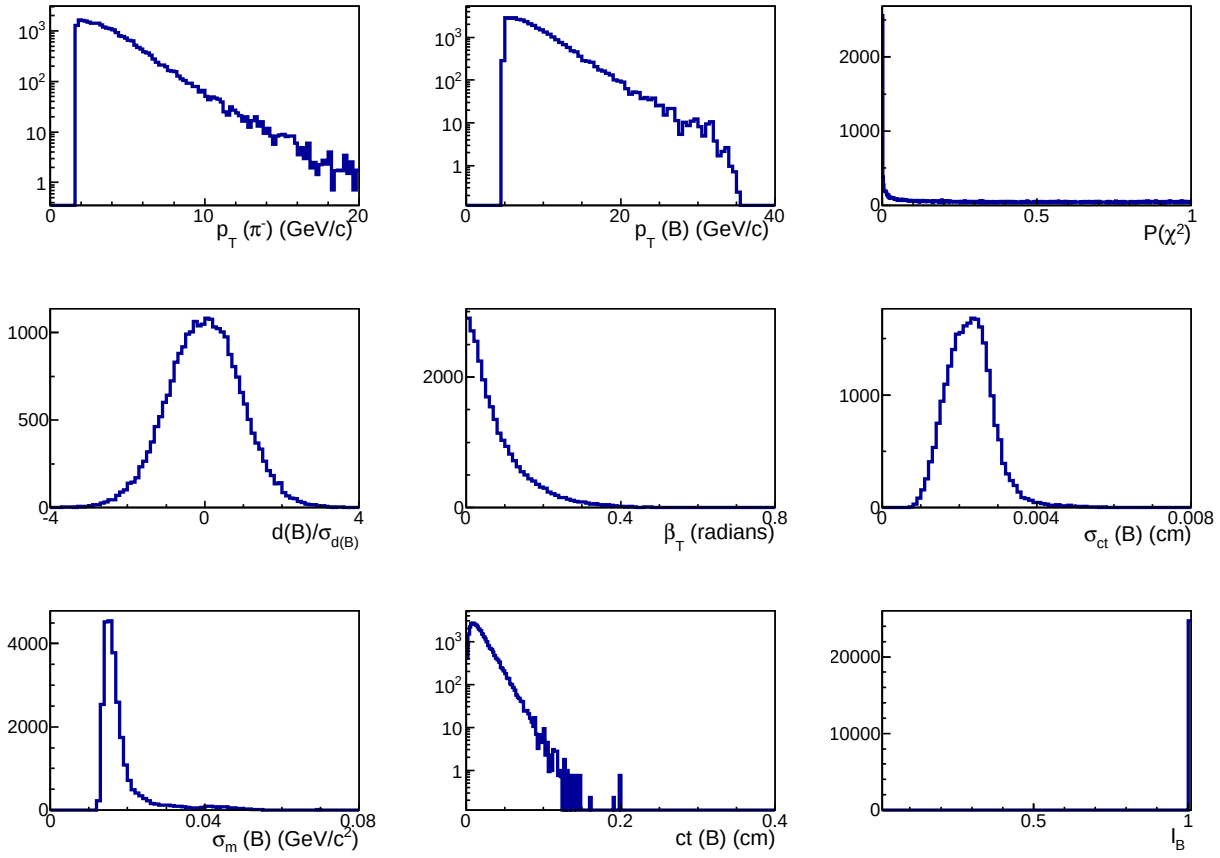

Figure 56: The distributions of the selection variables for $B_c^- \to J/\psi\, \pi^-$ decay obtained from the simulation.

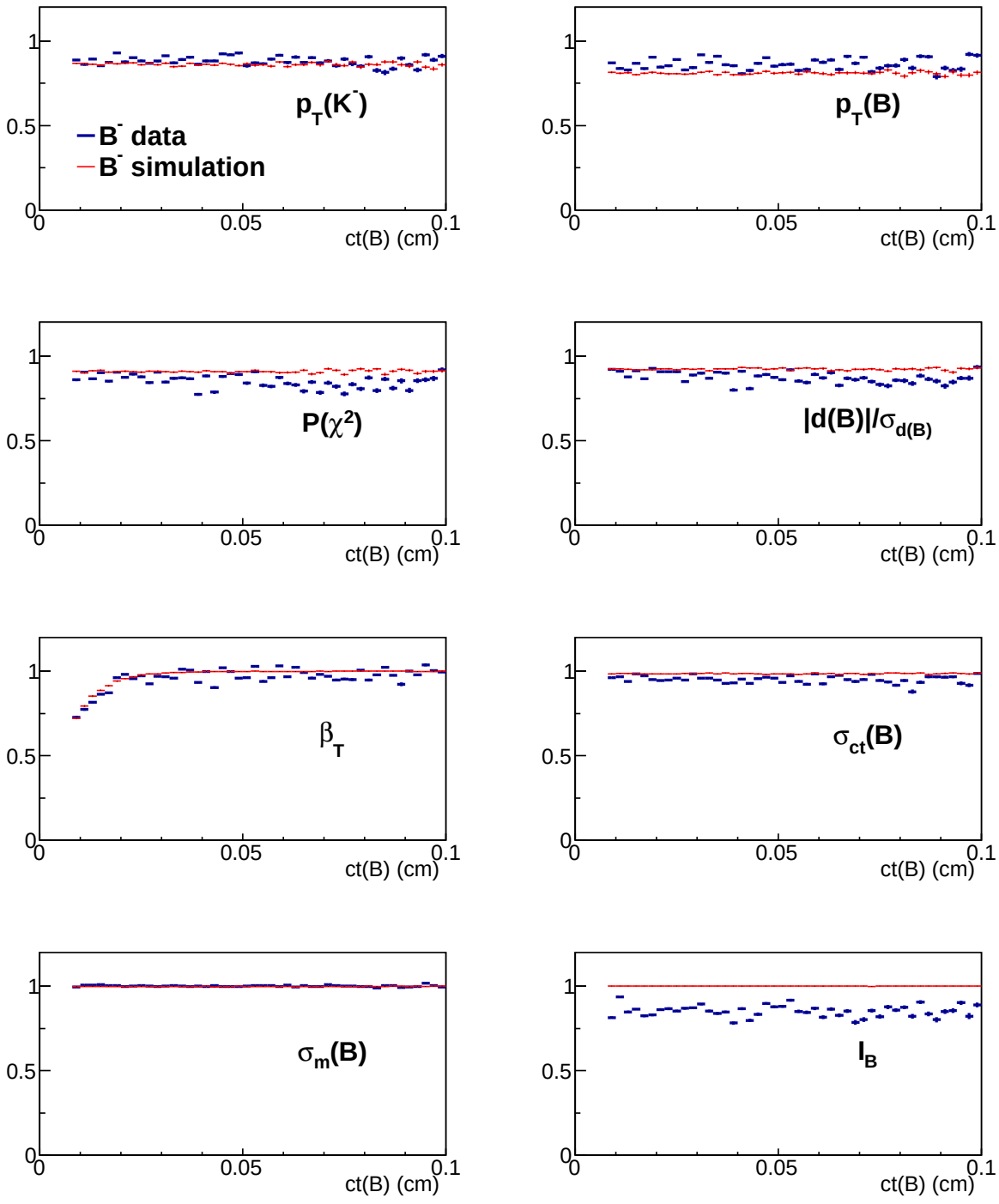

Figure 57: The comparison of efficiencies between MC simulation and experimental data for $B_u^- \to J/\psi\ K^-$ decay for each selection variables, if it is the first one applied.

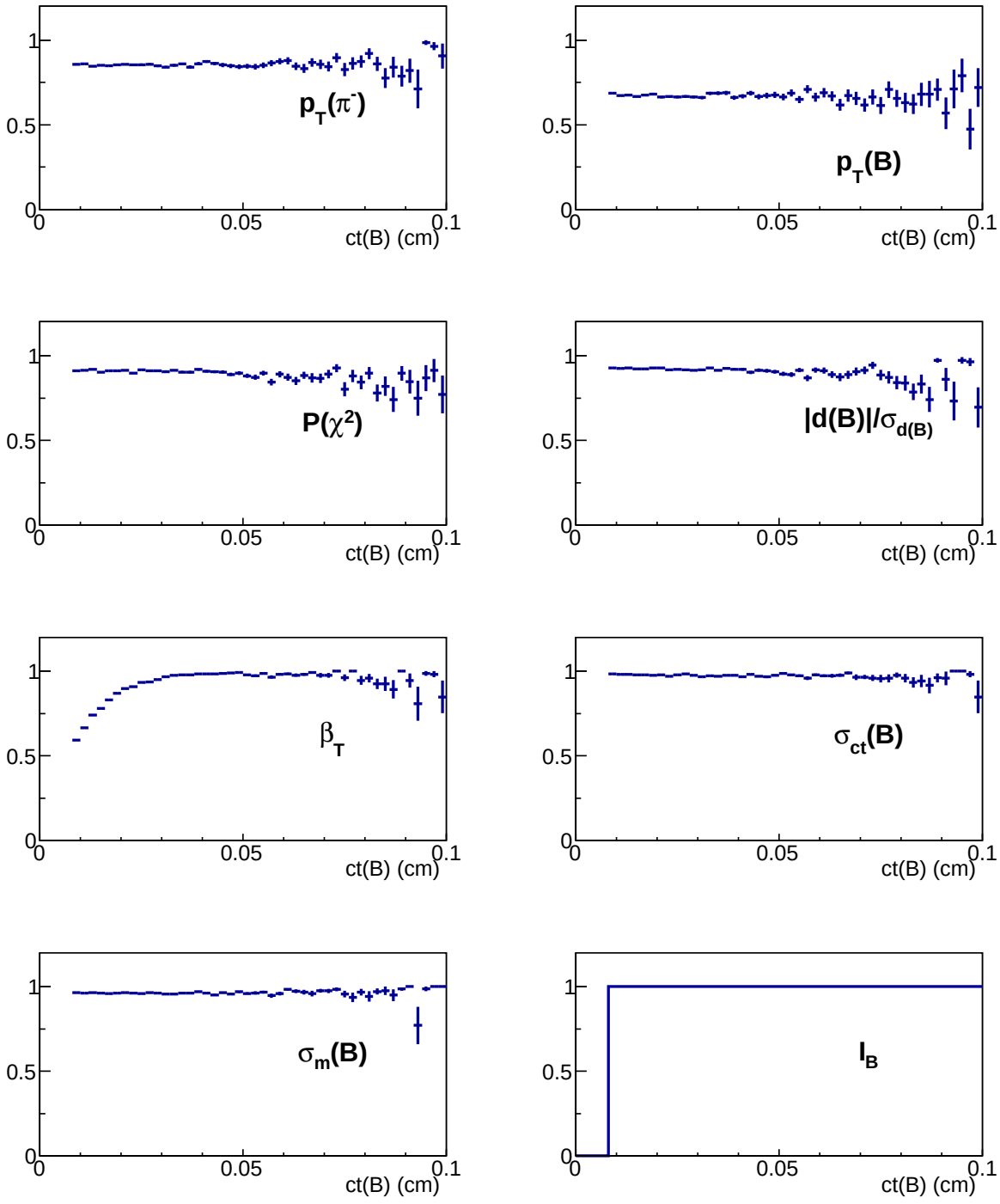

Figure 58: The efficiencies obtained from the MC simulation for $B_c^- \to J/\psi\, \pi^-$ decay for each selection variables, if it is the first one applied.

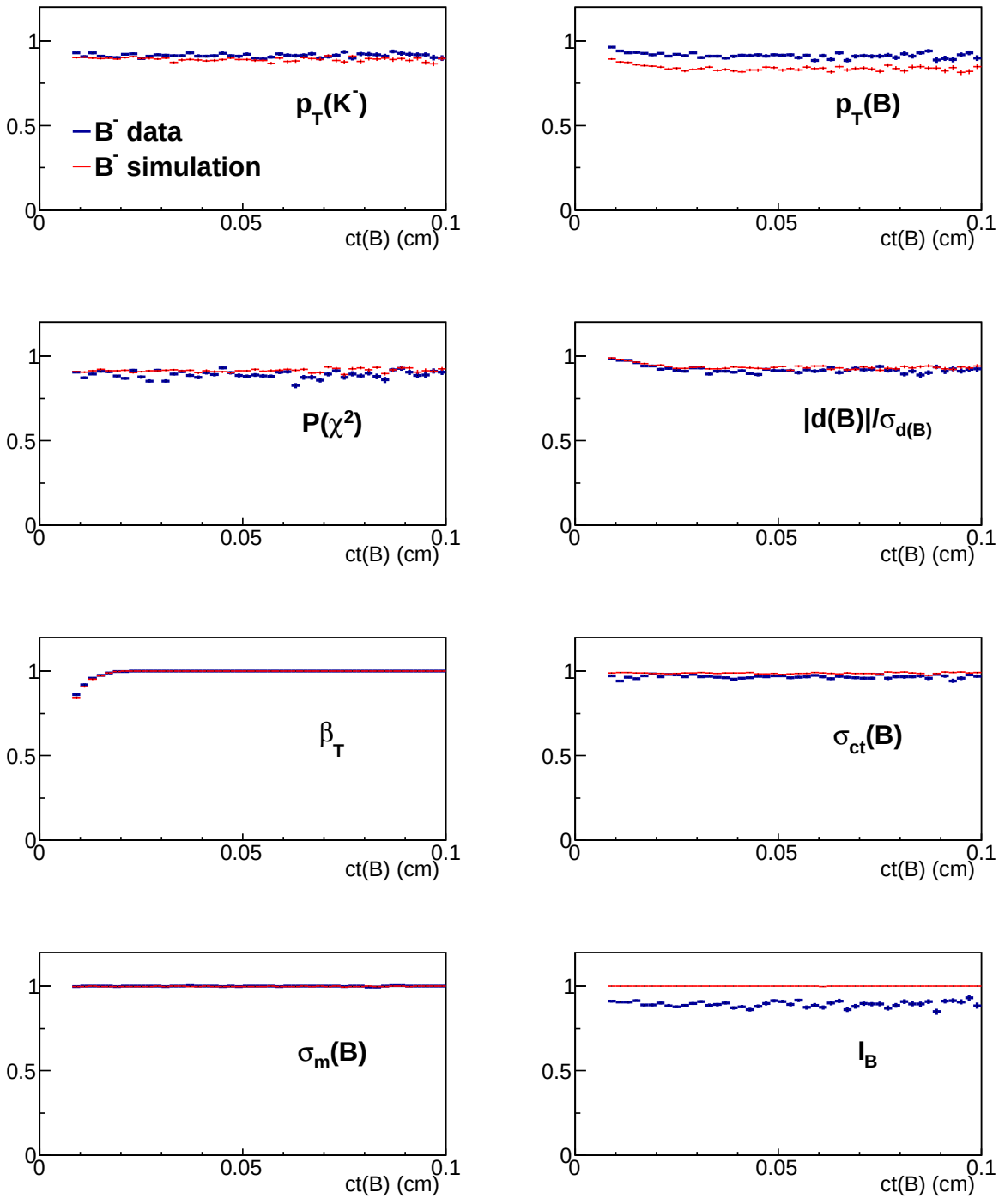

Figure 59: The comparison of efficiencies between MC simulation and experimental data for $B_u^- \to J/\psi\ K^-$ decay for each selection variables, if it is the last one applied.

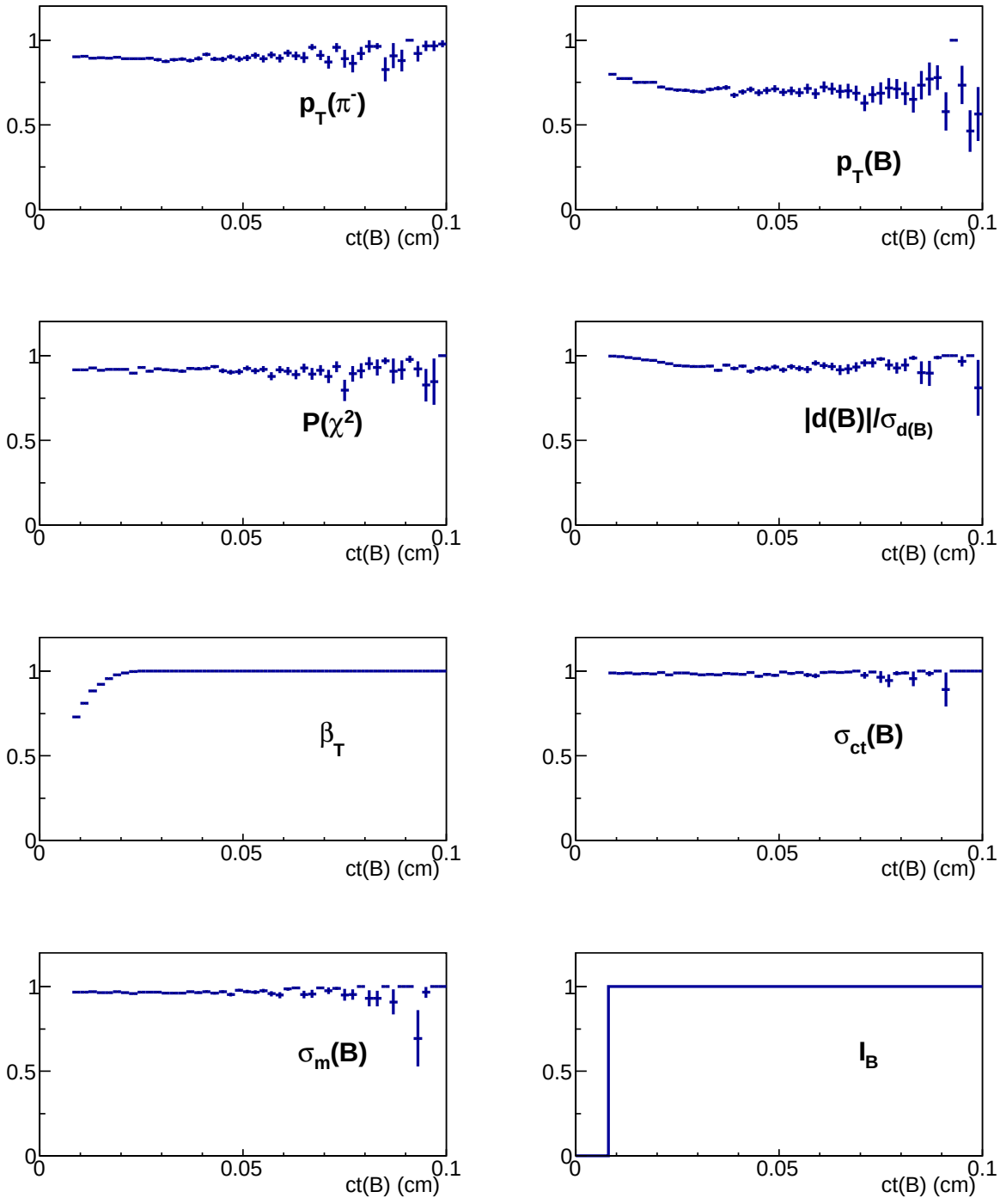

Figure 60: The efficiencies obtained from the MC simulation for $B_c^- \to J/\psi\, \pi^-$ decay for each selection variables, if it is the last one applied.

proper decay length, and the efficiency of β_T tends to be less for events with small proper decay length, and gradually increases to stable at large proper decay length.

Figure 61 shows the overall efficiency obtained from selections in Table 6 for experimental data of $B_u^- \to J/\psi\ K^-$ decay, as well as the fit result of the efficiency determined from the MC simulation. The efficiency obtained from the MC simulation is subject to a chi-square fit to a function of the form:

$$\epsilon(ct) = C \times \left[1 - \exp\left(\frac{a - ct}{b}\right)\right] \tag{4.1}$$

where C, a, b are parameters to be fit. It is noted that the parameter C in Eq. (4.1) is not necessary in the lifetime fit because only the relative shape of the efficiency function matters. The good agreement between the simulated efficiency and the data-determined efficiency indicates that this approach can be used to determine the efficiency in $B_c^- \to J/\psi\ \pi^-$ as well. The efficiency for $B_c^- \to J/\psi\ \pi^-$ determined from MC simulation is also obtained by chi-square fit and also shown in Figure 61. Table 8 shows the fit result of the efficiency function for both $B_u^- \to J/\psi\ K^-$ and $B_c^- \to J/\psi\ \pi^-$ MC simulations.

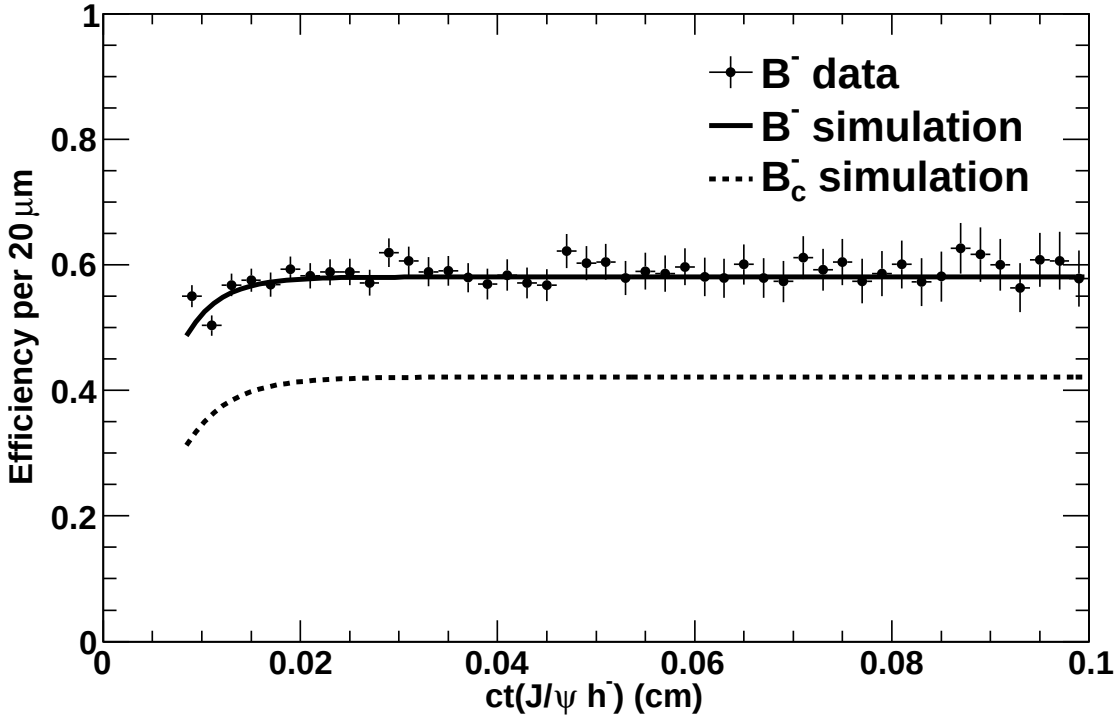

Figure 61: The comparison of efficiency for $B_u^- \to J/\psi\ K^-$ obtained from data and the fit result from simulation. Also shown is the fit result for $B_c^- \to J/\psi\ \pi^-$ simulation. The "h^-" refers to either a K^- or a π^- for B_u^- or B_c^- respectively.

Table 8: The fit result of the efficiency function for both $B_u^- \to J/\psi\ K^-$ and $B_c^- \to J/\psi\ \pi^-$ MC simulations.

Decay	C	a (μm)	b (μm)
$B_u^- \to J/\psi\ K^-$	0.5806 ± 0.0018	21.74 ± 12.37	34.49 ± 5.67
$B_c^- \to J/\psi\ \pi^-$	0.4213 ± 0.0028	26.76 ± 7.45	42.72 ± 4.75

5.0 LIFETIME FITTER AND RESULTS

This chapter first describes the likelihood function used in this thesis, then the lifetime result using the maximum log-likelihood method is presented.

5.1 LIKELIHOOD FUNCTION

An unbinned maximum log-likelihood fit is used in this analysis which simultaneously fits the mass and proper decay length of the B meson candidates. The likelihood function consists of signal and background parts, and each part has a mass term and a proper decay length term. For a data set consisting of N events, the likelihood $\mathcal{L}_i$ for event i is given by

$$\mathcal{L}_i = f_s \; P_s(m_i) \; T_s(ct_i) + (1 - f_s) \; P_b(m_i) \; T_b(ct_i) \tag{5.1}$$

where f_s is the signal fraction, m_i and ct_i are the reconstructed mass and proper decay length of the B meson candidates for event i. $P_s(m)$ and $T_s(ct)$ are the normalized probability density functions for mass and proper decay length of the signal model, $P_b(m)$ and $T_b(ct)$ are the corresponding functions of the background model. The total likelihood of the data set is the product of the likelihood of these N events:

$$\begin{aligned} \mathcal{L} &= \prod_{i=1}^{N} \mathcal{L}_i \\ &= \prod_{i=1}^{N} \left(f_s \; P_s(m_i) \; T_s(ct_i) + (1 - f_s) \; P_b(m_i) \; T_b(ct_i) \right) \end{aligned} \tag{5.2}$$

Normally, one does not maximize the quantity given in Eq. 5.2 directly. It is usually more convenient to maximize its logarithm. Since the logarithm is a monotonically increasing

function, the parameter values which maximize $\mathcal{L}$ will also maximize $\log \mathcal{L}$. The logarithm of the likelihood function Eq. 5.2 can be written as

$$\begin{aligned} \log \mathcal{L} &= \log \left(\prod_{i=1}^{N} \mathcal{L}_i \right) \\ &= \sum_{i=1}^{N} \log \mathcal{L}_i \\ &= \sum_{i=1}^{N} \log \left[f_s \; P_s(m_i) \; T_s(ct_i) + (1 - f_s) \; P_b(m_i) \; T_b(ct_i) \right] \end{aligned} \tag{5.3}$$

This quantity is then maximized by varying the parameters in the function. The maximization is carried out with the MIGRAD algorithm from the MINUIT fitting software [66]. In order to obtain the error matrix that describes the uncertainty for the parameter values as well as their correlations, the HESSE or MINOS algorithm from the MINUIT package is used after the MIGRAD step. The HESSE algorithm returns symmetric uncertainties for all parameters by assuming the log-likelihood function is parabolic around the maximum value. The MINOS algorithm, on the other hand, provides a full scan of $\log \mathcal{L}$ for varying values of the parameters, returning asymmetric uncertainties if the log-likelihood function is not parabolic. Thus, the MINOS algorithm takes more time in determining the asymmetric uncertainties. If the log-likelihood is approximately parabolic in shape around the maximum value, both algorithms will return a similar uncertainty. If the uncertainties returned from HESSE and MINOS are substantially different, this implies the log-likelihood shape is not parabolic at the maximum. The quoted (statistical) uncertainty corresponds to a 0.5 decrease in $\log \mathcal{L}$ since this would represent a one standard derivation of the log-likelihood if it were parabolic. Each component of the likelihood function is discussed in more detail in the following subsections.

5.1.1 Signal mass model

The signal mass model $P_s(m)$ is described by two Gaussian distributions with the same mean m_0 and different widths σ_{m1} and σ_{m2}. It can be written as:

$$P_s(m) \equiv P_s(m; f_m, m_0, \sigma_{m1}, \sigma_{m2}) = f_m \; \frac{1}{\sqrt{2\pi}\sigma_{m1}} \; e^{-\frac{(m-m_0)^2}{2\sigma_{m1}^2}} + (1 - f_m) \; \frac{1}{\sqrt{2\pi}\sigma_{m2}} \; e^{-\frac{(m-m_0)^2}{2\sigma_{m2}^2}} \tag{5.4}$$

where f_m is the fraction of the first Gaussian. All these four parameters, f_m, m_0, σ_{m1} and σ_{m2}, are floating parameters to be determined by the likelihood fit. The lower and upper limits for the mass window used in the likelihood fit are $m_{min} = 5.18$ and $m_{max} = 5.38$ GeV/c^2 for the B_u^- candidates, which is about ± 100 MeV/c^2 from its world average mass of 5.279 GeV/c^2 [21]. For the B_c^- candidates, $m_{min} = 6.16$ and $m_{max} = 6.60$ GeV/c^2 are used. The upper limit for the B_c^- candidates is the same value as used in the reconstruction process, which is about 330 MeV/c^2 higher than its world average mass of 6.277 GeV/c^2 [21]. The lower limit is chosen to be higher than the lower limit used in the reconstruction process, in order to avoid background events from semileptonic decays $B_c^- \to J/\psi\ \ell^-\ X$, where the lepton ℓ^- is misidentified as a pion. Because the neutrino's energy is not taken into account for these semileptonic decays, the reconstructed B_c^- mass is thus less than the true B_c^- meson mass and falls into the otherwise wider mass window. The typical mass resolution is less than 30 MeV/c^2, and the mass windows for B_u^- and B_c^- candidates are 200 and 440 MeV/c^2 wide. Thus, it is reasonable to assume the integral of the signal mass model given in Eq. 5.4 is 1, and does not need further normalization.

5.1.2 Signal decay time model

The signal proper decay length model, $T_s(ct)$, is an exponential distribution with characteristic lifetime $c\tau$ first smeared by the detector resolution, then multiplied by the efficiency function given in Eq. 4.1. The detector resolution, which is modeled as a Gaussian distribution centered at zero with a width of $\sigma_{ct} = 20$ μm, is chosen to be consistent with calibration using promptly decaying background events [67]. The σ_{ct} parameter is fixed in the likelihood fit, and will be varied for possible systematic effect in the next chapter. The expression of $T_s(ct)$ is given by

$$\begin{aligned} T_s(ct) &\equiv T_s(ct; c\tau, a, b, \sigma_{ct}) \\ &= N_1'\ E(ct; a, b) \int \frac{1}{c\tau} e^{-ct'/c\tau}\ \frac{1}{\sqrt{2\pi}\sigma_{ct}} e^{-\frac{(ct-ct')^2}{2\sigma_{ct}^2}}\ d(ct') \\ &= N_1\ (1 - e^{(a-ct)/b}) \int \frac{1}{c\tau} e^{-ct'/c\tau}\ \frac{1}{\sqrt{2\pi}\sigma_{ct}} e^{-\frac{(ct-ct')^2}{2\sigma_{ct}^2}}\ d(ct') \end{aligned}$$

(5.5)

where N_1 is the normalization parameter determined by

$$\int_{ct_{min}}^{ct_{max}} T_s(ct; c\tau, a, b)\ d(ct) = 1 \tag{5.6}$$

ct_{min} and ct_{max} are the lower and upper limit of the proper decay length used in the likelihood fit. $ct_{min} = 80$ μm is chosen for both B_u^- and B_c^- candidates to reject promptly produced background. $ct_{max} = 4000$ (2000) μm is chosen for B_u^- (B_c^-) candidates to account for their different lifetime. The parameter a and b are used to describe the selection efficiency, as discussed in Eq. 4.1. Note that the parameter C in Eq. 4.1 is not necessary in Eq. 5.5 as it is absorbed into the parameter N_1.

5.1.3 Background mass model

The background mass model, $P_b(m)$, is described by a normalized first-order polynomial:

$$P_b(m) \equiv P_b(m; \lambda) = N_2(1 + \lambda\ m) \tag{5.7}$$

where λ is a floating parameter of the likelihood fit, and N_2 is the normalization parameter determined by the requirement

$$\int_{m_{min}}^{m_{max}} P_b(m; \lambda)\ dm = 1 \tag{5.8}$$

5.1.4 Background decay time model

The background decay time model, $T_b(ct)$, is described by a linear combination of three exponential distributions which can be written as

$$\begin{aligned} T_b(ct) &\equiv T_b(ct; c\tau_1, c\tau_2, c\tau_3, f_1, f_2) \\ &= f_1 \frac{e^{-ct/c\tau_1}}{c\tau_1 \left(e^{-ct_{min}/c\tau_1} - e^{-ct_{max}/c\tau_1}\right)} \\ &\quad +(1-f_1)\ f_2 \frac{e^{-ct/c\tau_2}}{c\tau_2 \left(e^{-ct_{min}/c\tau_2} - e^{-ct_{max}/c\tau_2}\right)} \\ &\quad +(1-f_1)\ (1-f_2) \frac{e^{-ct/c\tau_3}}{c\tau_3 \left(e^{-ct_{min}/c\tau_3} - e^{-ct_{max}/c\tau_3}\right)} \end{aligned} \tag{5.9}$$

The three $c\tau_i$ $(i = 1, 2, 3)$ are the characterized lifetimes of the background events, and the two f_i $(i = 1, 2)$ are the fraction parameters. All these five parameters are floating parameters determined by the likelihood fit. It can be shown that Eq. 5.9 is properly normalized to 1 between ct_{min} and ct_{max} since

$$\begin{aligned} \int_{ct_{min}}^{ct_{max}} T_b(ct; c\tau_1, c\tau_2, c\tau_3, f_1, f_2)\ d(ct) &= f_1 \int_{ct_{min}}^{ct_{max}} \frac{e^{-ct/c\tau_1}\ d(ct/c\tau_1)}{e^{-ct_{min}/c\tau_1} - e^{-ct_{max}/c\tau_1}} \\ &\quad +(1-f_1)\ f_2 \int_{ct_{min}}^{ct_{max}} \frac{e^{-ct/c\tau_2}\ d(ct/c\tau_2)}{e^{-ct_{min}/c\tau_2} - e^{-ct_{max}/c\tau_1}} \\ &\quad +(1-f_1)\ (1-f_2) \int_{ct_{min}}^{ct_{max}} \frac{e^{-ct/c\tau_2}\ d(ct/c\tau_2)}{e^{-ct_{min}/c\tau_2} - e^{-ct_{max}/c\tau_1}} \\ &= f_1 + (1-f_1)\ f_2 + (1-f_1)\ (1-f_2) \\ &= 1 \end{aligned} \tag{5.10}$$

5.1.5 Summary of the likelihood function

The floating parameters used in the likelihood function are summarized in Table 9. The two parameters for the selection efficiency, a and b, are allowed to float with a Gaussian constraint determined by the efficiency fit on the simulated events. All other parameters are allowed to float freely in the fitting in order to maximize the likelihood value.

Table 10 shows the fixed parameters used in the likelihood fit, these parameters are not allowed to float in the fit, but can be varied to study possible systematic effects.

5.2 THE LIFETIME FIT

Using the likelihood function discussed above, the unbinned maximum log-likelihood fit is carried out first to the B_u^- candidates with MIGRAD and HESSE algorithms. The B_u^- candidates used in the fit are shown in Figure 51 in both the signal region and the sideband regions, with a total of 50271 events. The projections of the likelihood function on proper decay length and mass are shown in Figure 62 and 63, where the experimental data distributions are shown as well.

The residual and the residual significance (pull) for the proper decay length and mass distribution are shown in Figure 64 and 65. The residual is defined as (Data-Fit) for each bin, and its significance is the residual divided by the uncertainty (error) on data for that bin. The error, for a bin with N events, is $\sqrt{N}$ since the number of events follows a Poisson distribution. The fit lifetime of the B_u^- meson is $c\tau = 489.3 \pm 2.5$ μm which agrees with the known value f 492.0 ± 2.4 μm [21]. The fit mass of the B_u^- meson is 5278.8 ± 0.07 MeV/c^2, which also agrees with the world average value of 5279.25 ± 0.17 MeV/c^2. The fit results for all the parameters are shown in Table 11. For each fit projection, the χ^2/ndf quantity is calculated to test the goodness-of-fit. The χ^2 is obtained by summing the squares of the residual significance over the bins, and the ndf is the Number of Degree of Freedom in the fit which is the number of bins less the number of floating parameters. The fit result is thus considered reasonable if the quantity χ^2/ndf is less than or around one, and not reasonable if it is much larger than one. For the B_u^- fit, the goodness-of-fit is presented in Figure 64 and 65, where both quantities are around one, indicating the fit result is reasonable.

The likelihood function is then applied to the B_c^- candidates, which include the events from both the signal region and the sideband regions shown in Figure 52. The total number of the B_c^- candidates used in the likelihood fit is 4527. It is noted that the σ_{m2} parameter, which represents the second Gaussian distribution in the signal mass model, favors an unreasonably large value. The possible reason is that, due to the low statistic and the low signal yield in the B_c^- candidates sample, the second Gaussian distribution in the signal mass model is redundant. Thus, the σ_{m2} parameter and the f_m parameter are not used in the B_c^- candidates fit. The signal mass model is then a single Gaussian with mean m_0 and width σ_m.

The maximum log-likelihood fit from the MIGRAD and HESSE algorithms finds the B_c^- meson lifetime to be $c\tau = 134.8 \pm 14.8$ μm ($\tau = 0.449 \pm 0.049$ ps), with the B_c^- signal yield of 272 ± 42 candidates. The B_c^- meson mass of 6274.7 ± 2.6 MeV/c^2 returned from the fit is in good agreement with previous CDF result of $6275.6 \pm 2.9 \pm 2.5$MeV/c^2 [5]. The MINOS algorithm is then applied to obtain asymmetric uncertainty for the $c\tau$ parameter. The result of the $c\tau$ parameter is $c\tau = 134.8^{+16.2}_{-14.4}$ μm ($\tau = 0.449^{+0.054}_{-0.048}$ ps), which is consistent with the HESSE algorithm. This asymmetric uncertainty is used as the statistical uncertainty since it is obtained by a full scan of the log-likelihood function. Figure 66 and Figure 67 show the proper decay length and mass distribution of the B_c^- candidates for experimental data as well as the fit result. The residual and the residual significance for the proper decay length and mass distribution are shown in Figure 68 and 69. The fit results for all the parameters are shown in Table 12. The χ^2/ndf quantities for the projections on proper decay length and mass are also shown in Figure 68 and 69, and they both indicate the fit result is reasonable.

Table 9: Summary of floating parameters used in the likelihood function. The two parameters for the selection efficiency, a and b, are allowed to float with a Gaussian constraint determined by the efficiency fit. All other parameters are allowed to float freely in the fitting in order to maximize the likelihood value.

Name	Description	Comment
f_s	Signal fraction	Signal, background
m_0	B meson mass	Signal, mass
f_m	Fraction of signal with mass resolution 1	Signal, mass
σ_{m1}	B meson mass resolution 1	Signal, mass
σ_{m2}	B meson mass resolution 2	Signal, mass
$c\tau$	B meson lifetime	Signal, proper decay length
a	Selection efficiency offset of B meson lifetime	Signal, proper decay length
b	Selection efficiency slope of B meson lifetime	Signal, proper decay length
λ	Background mass intercept	Background, mass
$c\tau_1$	Background lifetime 1	Background, proper decay length
$c\tau_2$	Background lifetime 2	Background, proper decay length
$c\tau_3$	Background lifetime 3	Background, proper decay length
f_1	Fraction of background which is lifetime 1	Background, proper decay length
f_2	Fraction of remainder which is lifetime 2	Background, proper decay length

Table 10: Summary of fixed parameters used in the likelihood function. These parameters are not allowed to float in the fit, but can be varied to study possible systematic effects.

Name	Description	Value
σ_{ct}	B meson decay length resolution	20 μm
ct_{min}	Minimum ct used in the fit	80 μm
ct_{max} (B_u^-)	Maximum ct used in the B_u^- fit	4000 μm
m_{min} (B_u^-)	Minimum mass used in the B_u^- fit	5.18 GeV/c^2
m_{max} (B_u^-)	Maximum mass used in the B_u^- fit	5.38 GeV/c^2
ct_{max} (B_c^-)	Maximum ct used in the B_c^- fit	2000 μm
m_{min} (B_c^-)	Minimum mass used in the B_c^- fit	6.16 GeV/c^2
m_{max} (B_c^-)	Maximum mass used in the B_c^- fit	6.60 GeV/c^2

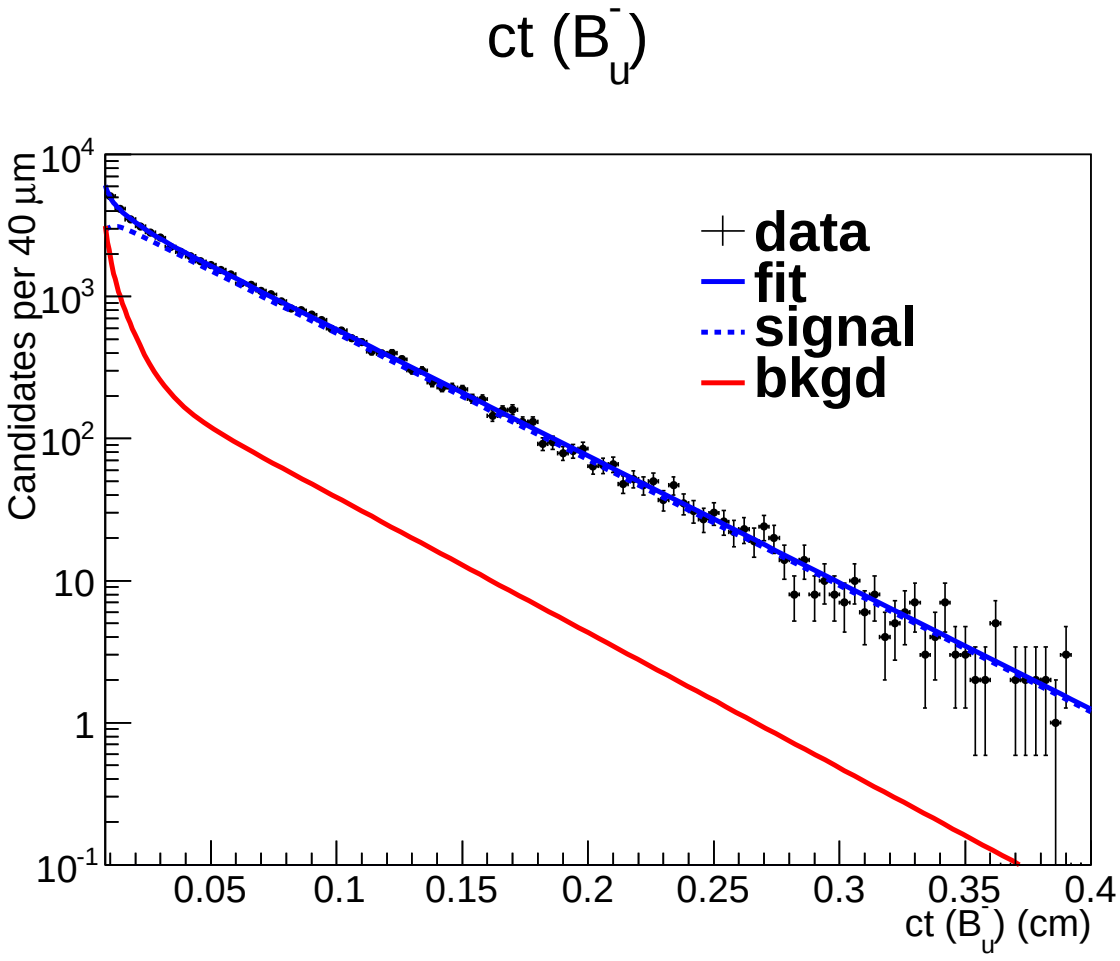

Figure 62: Proper decay length distribution of the B_u^- candidates overlaid with the fit results.

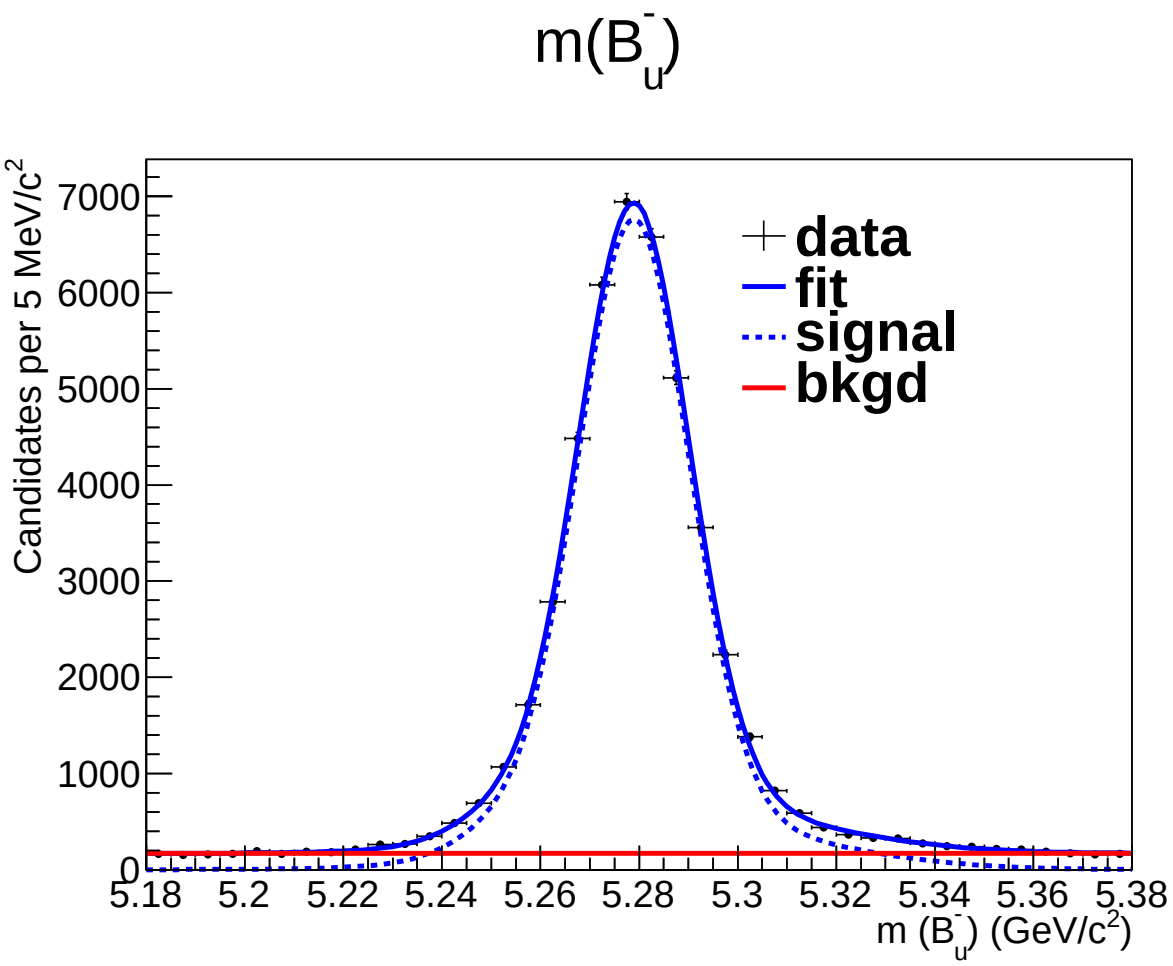

Figure 63: Invariant mass distribution of the B_u^- candidates overlaid with the fit results.

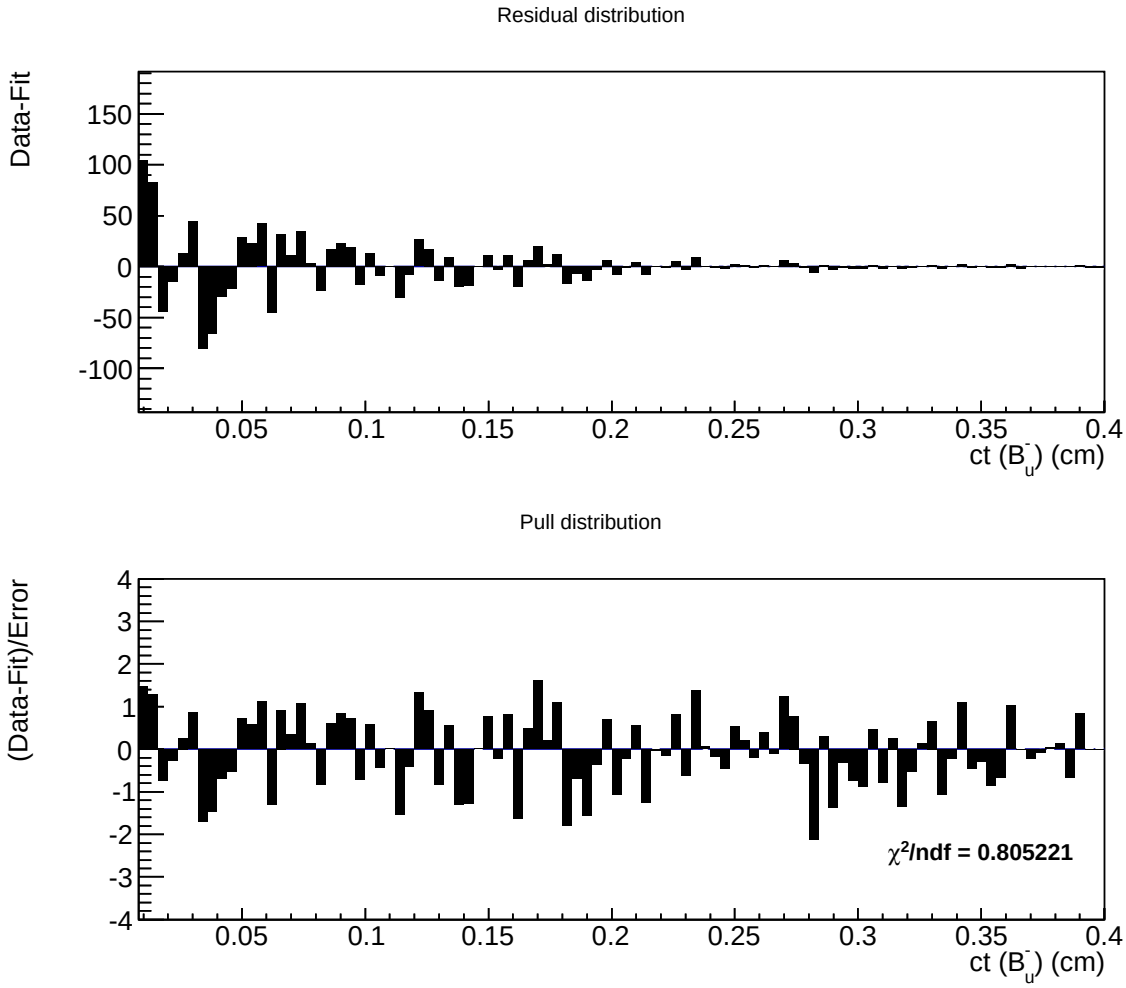

Figure 64: Residual of the proper decay length distribution of the B_u^- candidates.

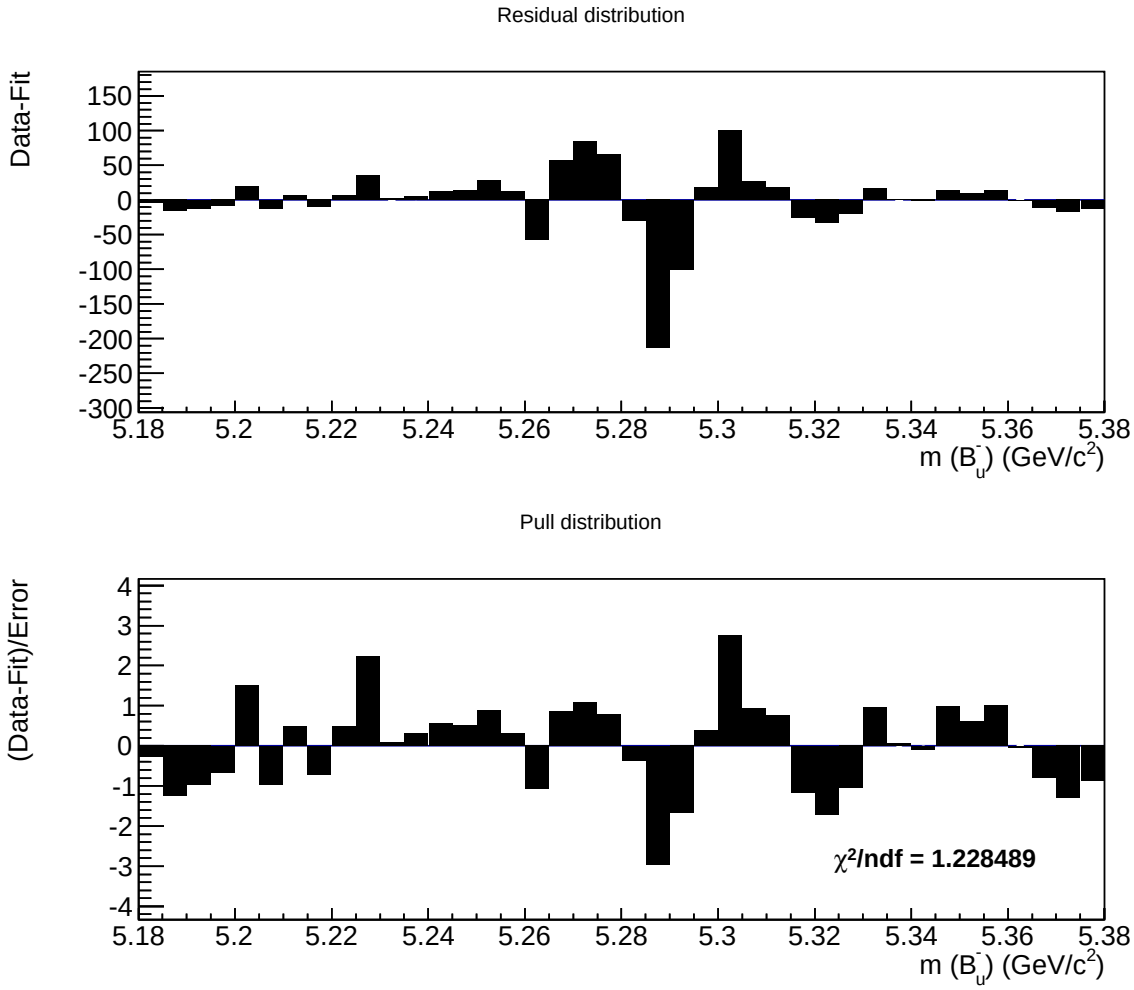

Figure 65: Residual of the invariant mass distribution of the B_u^- candidates.

Table 11: Fit result returned from the likelihood function for the B_u^- candidates.

Name	Result	Uncertainty	Unit
f_s	0.8615	0.0034	-
m_0	5278.8	0.07	MeV/c^2
f_m	0.7662	0.0165	-
σ_{m1}	11.1	0.1	MeV/c^2
σ_{m2}	25.5	1.1	MeV/c^2
$c\tau$	489.3	2.5	μm
a	21.29	10.1	μm
b	34.67	4.69	μm
λ	0.0045	0.0097	(GeV/c^2)$^{-1}$
$c\tau_1$	18.32	5.46	μm
$c\tau_2$	73.37	8.59	μm
$c\tau_3$	456.6	18.28	μm
f_1	0.0861	0.0389	-
f_2	0.4703	0.0269	-

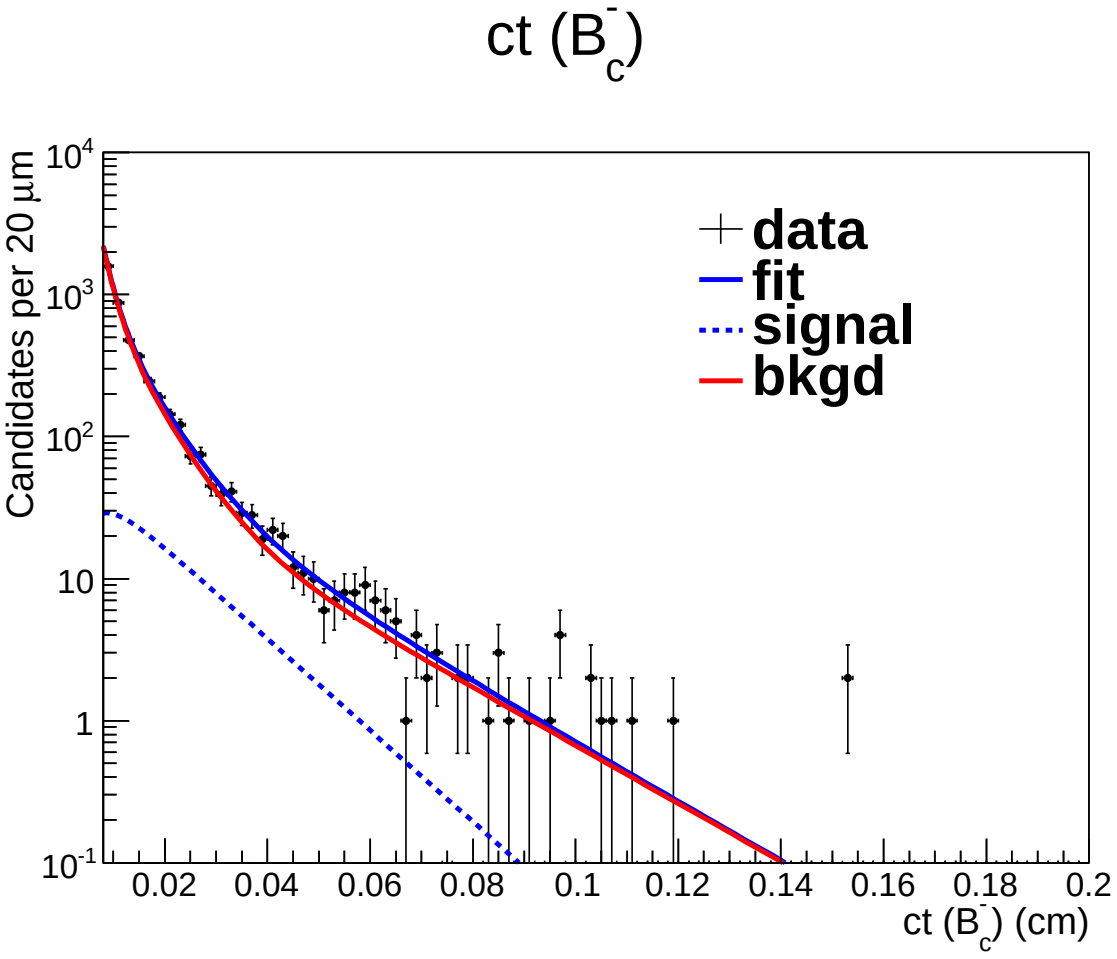

Figure 66: Proper decay length distribution of the B_c^- candidates overlaid with the fit results.

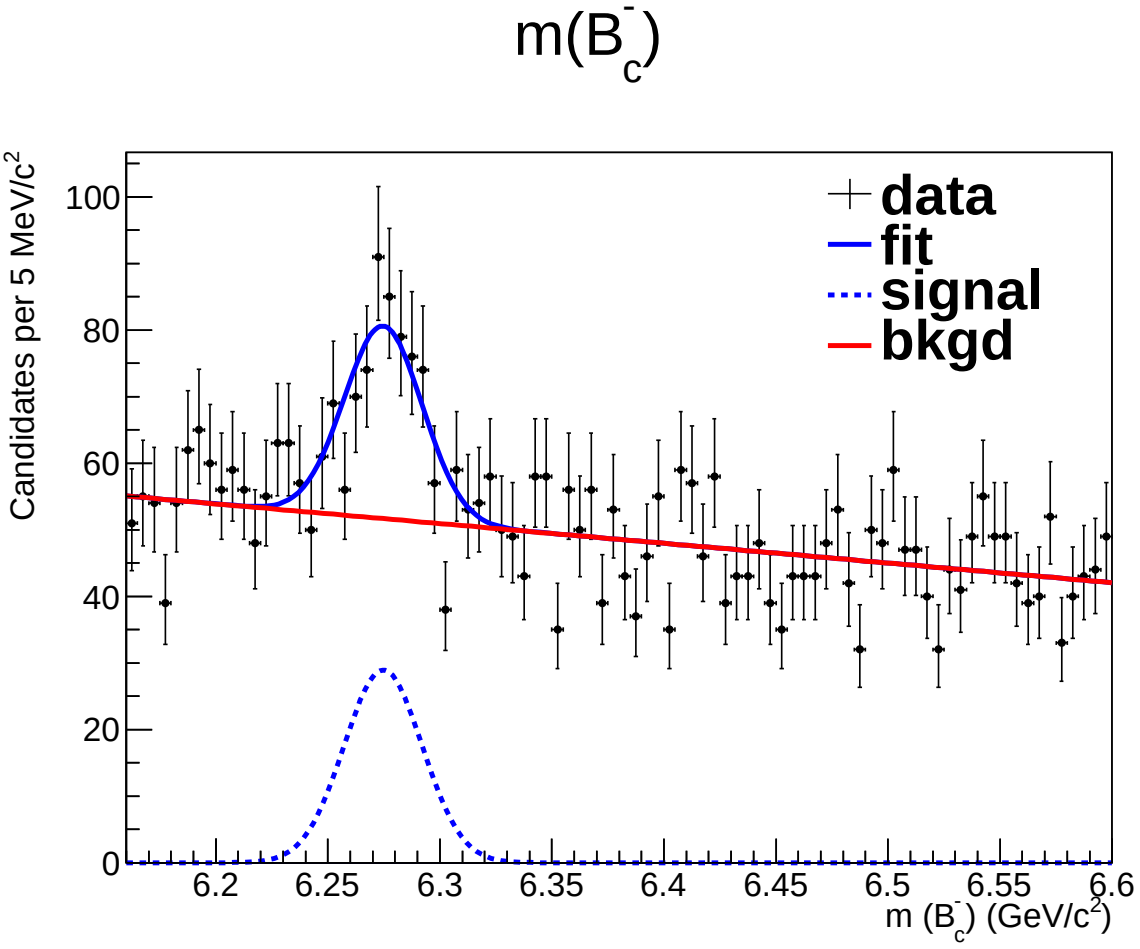

Figure 67: Invariant mass distribution of the B_c^- candidates overlaid with the fit result.

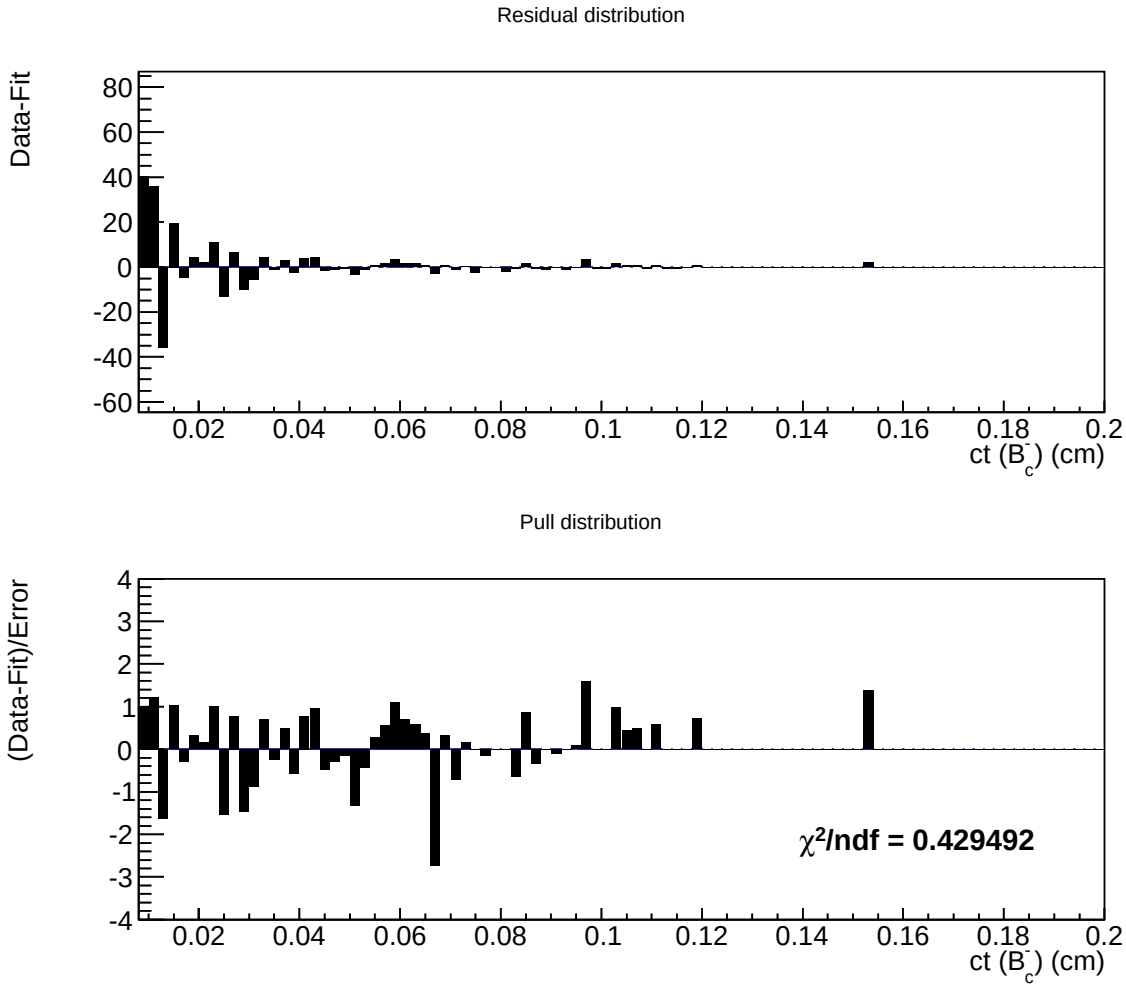

Figure 68: Residual of the proper decay length distribution of the B_c^- candidates.

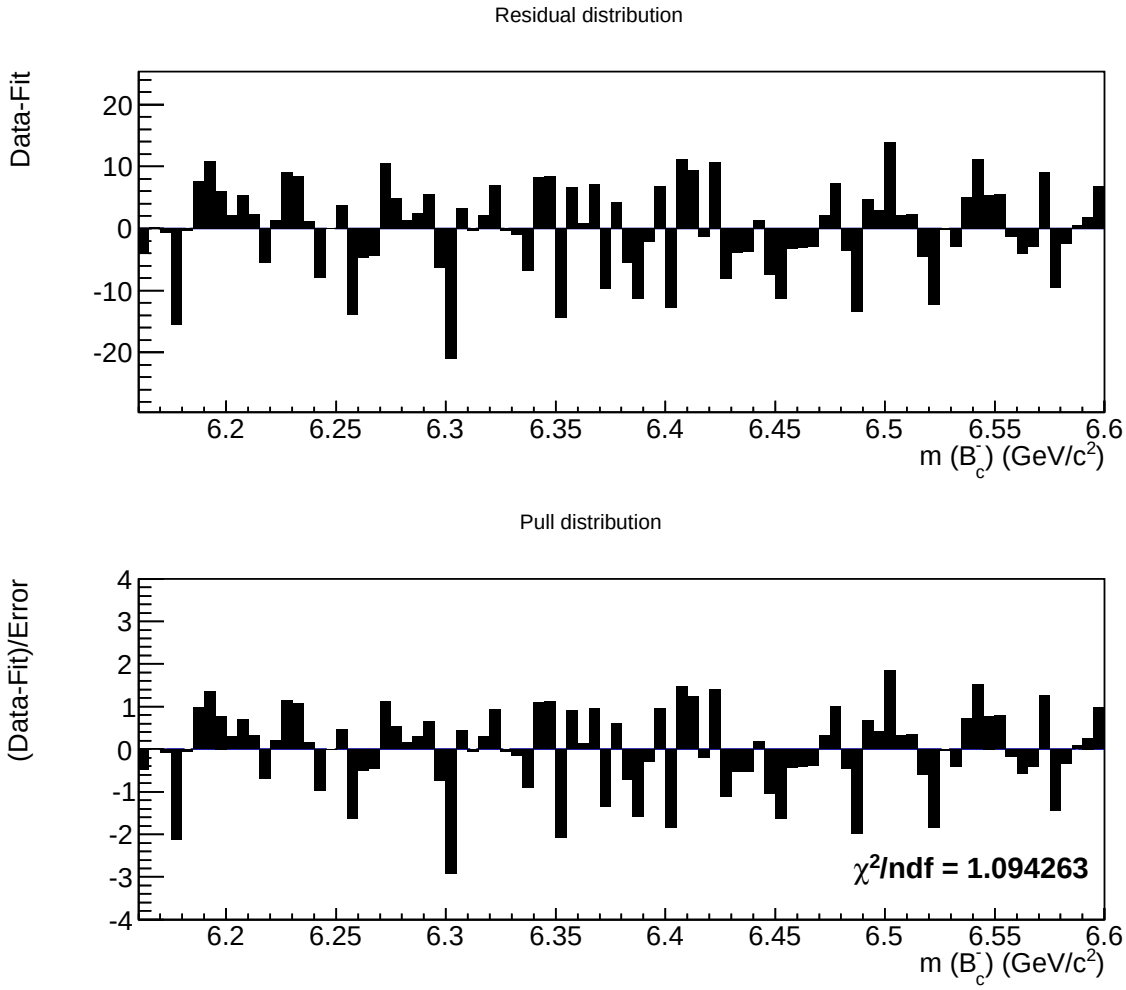

Figure 69: Residual of the invariant mass distribution of the B_c^- candidates.

Table 12: Fit result returned from the likelihood function for the B_c^- candidates. All uncertainties are from the HESSE algorithm, except for the cτ uncertainty which is calculated with the MINOS algorithm.

Name	Result	Uncertainty	Unit
f_s	0.0560	0.0093	-
m_0	6274.7	2.6	MeV/c^2
σ_m	17.5	3.9	MeV/c^2
$c\tau$	134.8	$^{+16.2}_{-14.4}$	μm
a	26.80	5.27	μm
b	42.70	3.37	μm
λ	-0.1247	0.0055	(GeV/c^2)$^{-1}$
$c\tau_1$	63.53	7.94	μm
$c\tau_2$	19.70	2.85	μm
$c\tau_3$	212.86	25.96	μm
f_1	0.5559	0.0608	-
f_2	0.7183	0.0919	-

6.0 SYSTEMATIC UNCERTAINTY

This chapter describes the systematic uncertainty study in the analysis. For each source of possible systematic uncertainty, the alternate model is used to fit the B_c^- candidates, and the difference in the fitted lifetime is recorded. Statistical trials based on the best fit of the data using alternate models are then generated, the default fitter is used to extract the lifetimes from these trials. The residual of each trial is defined as $c\tau_i$ - $c\tau$, where $c\tau_i$ is the fitted lifetime of trial i and $c\tau$ is the input (true) lifetime of the trial. The mean residual of the trials gives the systematic uncertainty of choosing one particular model instead of another. The pull is define as $(c\tau_i - c\tau)/\sigma_{c\tau_i}$, where $\sigma_{c\tau_i}$ is the statistical uncertainty on the fitted lifetime for trial i. The pull distribution of the trials is expected to be a normal distribution if the fitting technique is unbiased and the statistical error returned from the fit is reliable. The reliability of the statistical error is tested by the width of the pull distribution. The statistical error should be corrected by multiplying the width of the pull distribution if it is not consistent with 1. More detail of the pull distribution can be found at Ref. [68].

6.1 SIGNAL MASS MODEL

A Cabibbo-suppressed decay mode $B_c^- \to J/\psi\ K^-$ is included in the signal mass model. The total contribution of this decay mode to the signal yield is fixed at 5% as determined from the Cabibbo angle and comparable to the Cabibbo-suppressed $B^- \to J/\psi\ \pi^-$ decay. Based on previous study of this Cabibbo-suppressed decay [69], it is modeled as a Gaussian distribution which is centered at 60 MeV/c^2 below the B_c^- mass with a width of 30 MeV/c^2.

The lifetime of the B_c^- meson obtained from this alternate signal mass model changes by

–1.0 μm compared with the default model. Figure 70 and 71 show the proper decay length and the mass distribution with the fit result overlaid. Since the total signal yield is small, the Cabibbo-suppressed contribution, which is only 5% of the total signal yiled, can hardly be seen from Figure 71. Figure 72 shows the fit projection in more detail, where a small Gaussian distribution representing the Cabibbo-suppressed decay is under the total signal shape.

Statistical trials are generated, based on parameters that obtained from this alternate models. These statistical trials are then fitted by the likelihood function using the default model. Figure 73 shows the residual and the pull distributions of the fit result. It can be seen that the difference of the fitted lifetime between these two models, on average, changed by 0.7 μm, which is consistent with the difference observed in the experimental data. Thus, the systematic uncertainty due to the signal mass model is set to be 1.0 μm.

6.2 BACKGROUND MASS MODEL

The default background mass model is a linear distribution. An alternate option for this model is to use a bilinear distribution where the background mass distribution could have two different slopes below and above the B_c^- mass. This is motivated by the fact that contaminations from the B_c^- semileptonic decays, though mainly removed by the use of a narrow lower sideband, could still show up below the B_c^- mass. Using this bilinear mass model, the fitted lifetime changed by –1.3 μm relative to the default result. Figure 74 and 75 show the proper decay length and the mass distribution with the fit result overlaid.

Using the parameters obtained from this bilinear model, statistical trials are generated and fitted. The residual and the pull distributions of the fitted lifetime are shown in Figure 76. The difference in the fitted lifetime, on average, is 3.0 μm. Thus, the systematic uncertainty due to the background mass model is set to be 3.0 μm.

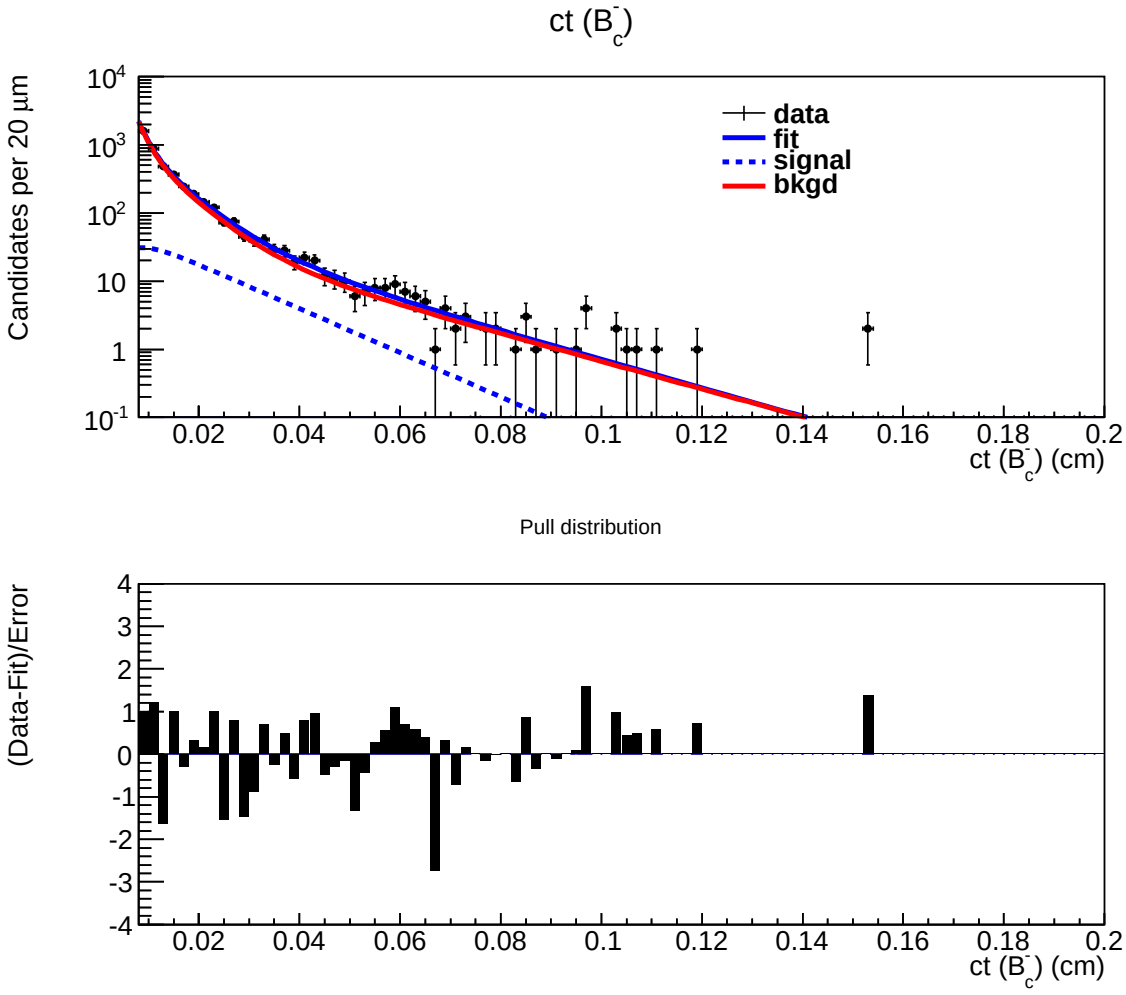

Figure 70: Proper decay length projection of the B_c^- candidates overlaid with the fit. A 5% Cabibbo-suppressed contribution is assumed in the signal mass shape.

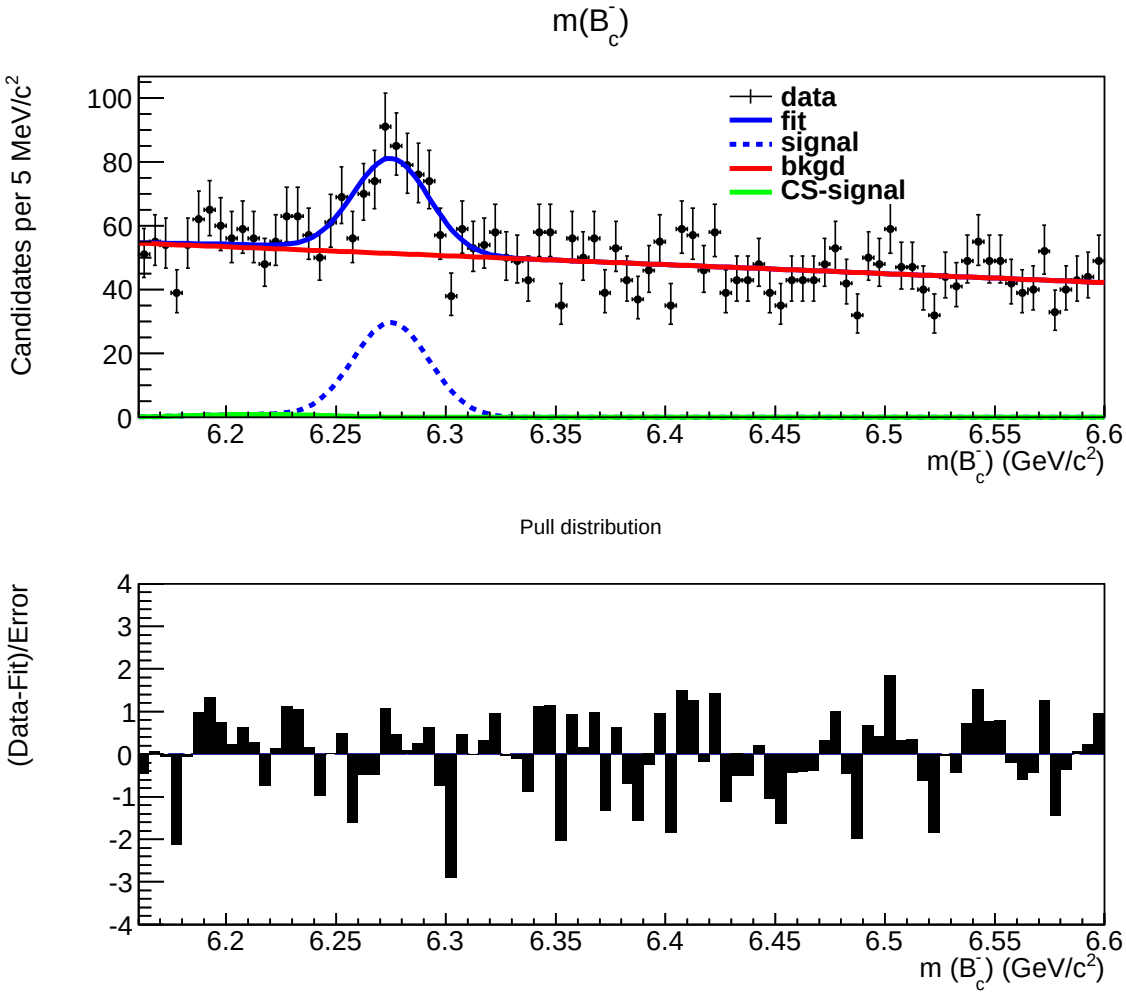

Figure 71: Invariant mass projection of the B_c^- candidates overlaid with the fit. A 5% Cabibbo-suppressed contribution is assumed in the signal mass shape.

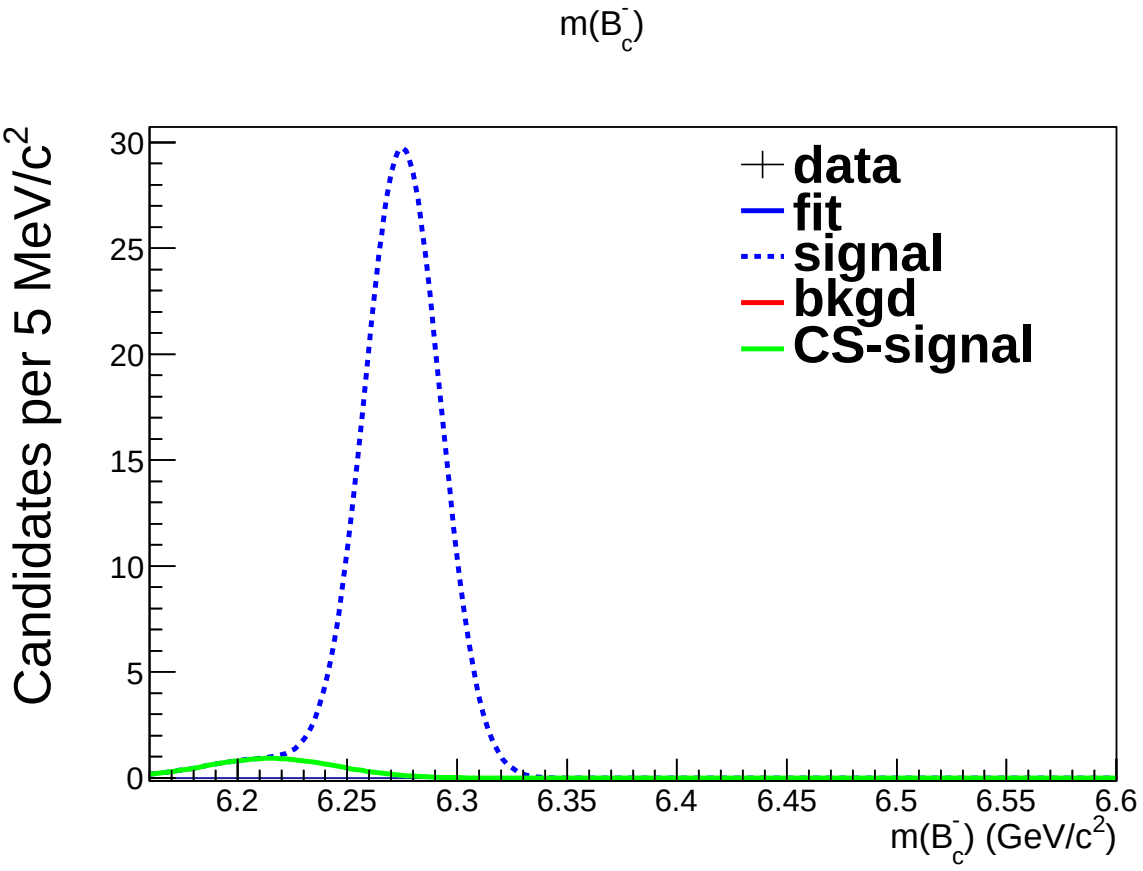

Figure 72: Zoom in of the Invariant mass projection of the B_c^- candidates overlaid with the fit. A 5% Cabibbo-suppressed contribution is assumed in the signal mass shape.

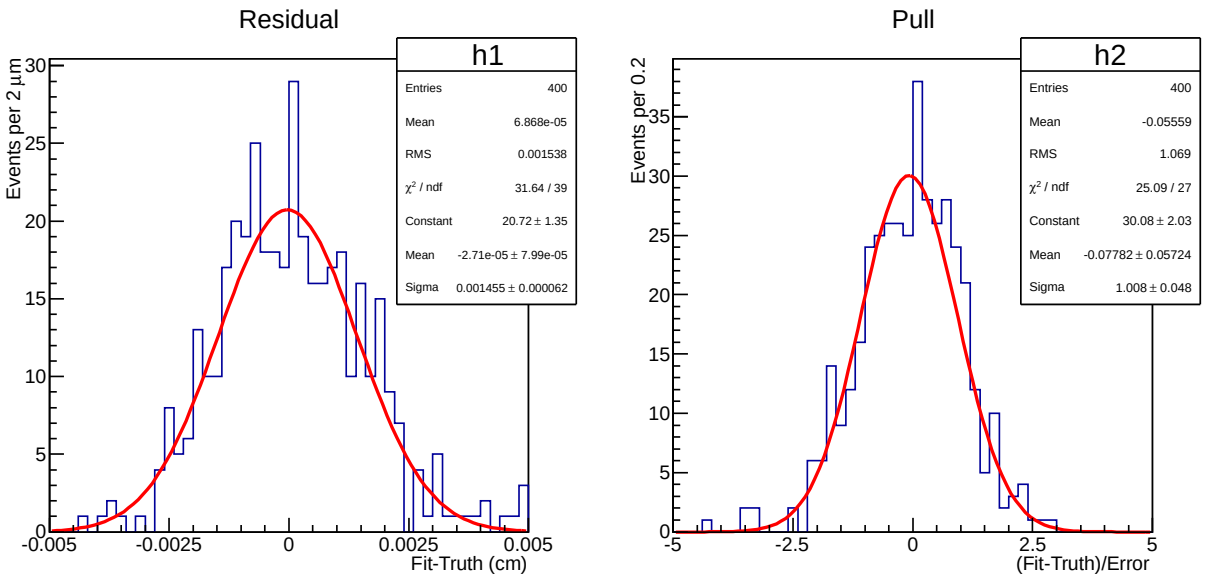

Figure 73: Residual and pull distributions of the fitted B_c^- lifetime when a Cabibbo-suppressed $B_c^- \to J/\psi\ K^-$ decay is included in the signal mass model.

6.3 SIGNAL DECAY-TIME MODEL

The signal decay-time model mainly involves the efficiency determined from the MC simulation. Its systematic uncertainty has been studied in several sources and is described below.

6.3.1 Tunning on the σ_{ct} requirement

The effect of the tunning on the σ_{ct} requirement has been studied by using the same numerical value as the σ_{ct} requirement on MC simulation as on experimental data. Table 13 shows the efficiency parameters obtained with or without the tunning. Figure 79 shows the efficiency function as a function of proper decay length, with or without the tunning. Using the efficiency parameters without the tunning, the fitted B_c^- lifetime changed by –0.7 μm relative to the default method. Figure 77 and 78 show the proper decay length and the mass

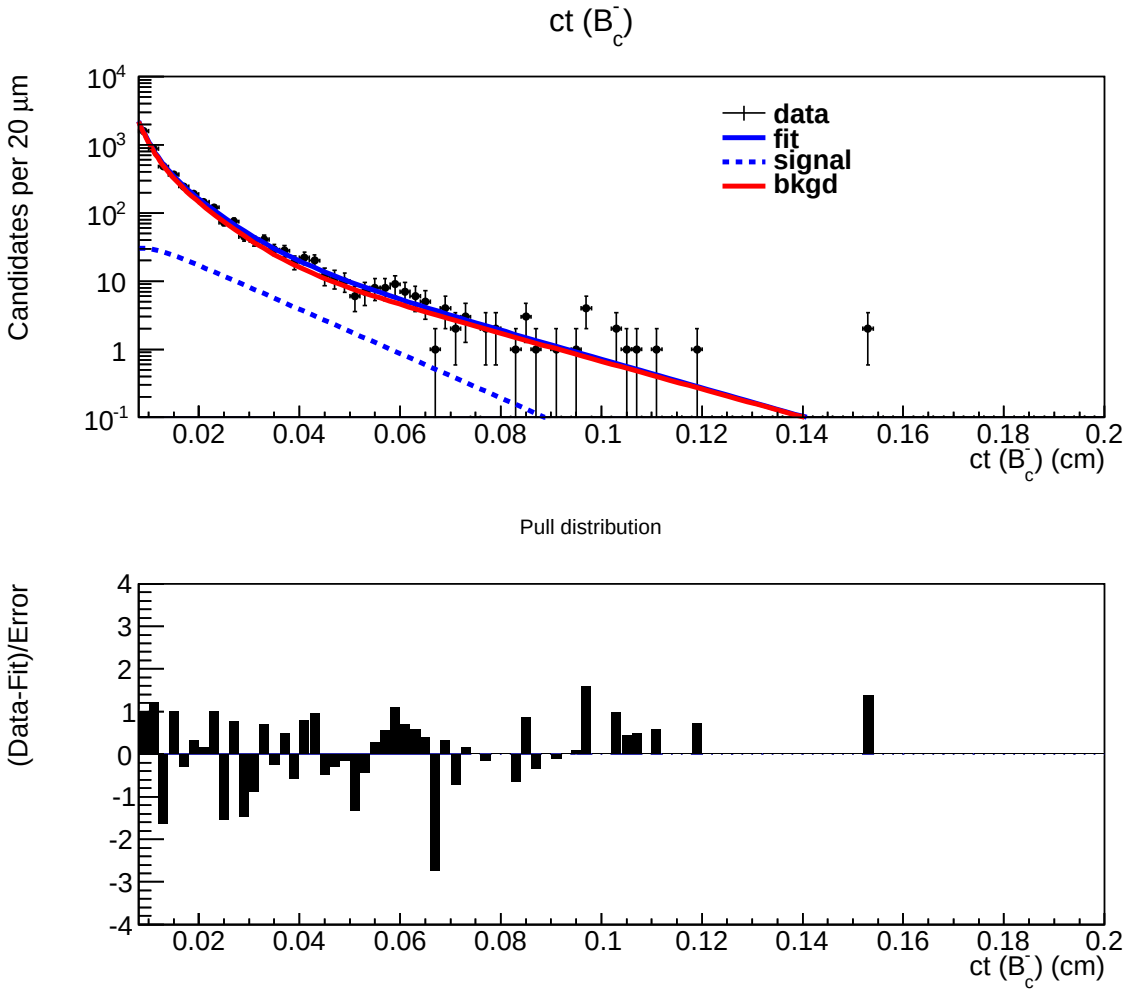

Figure 74: Proper decay length projection of the B_c^- candidates overlaid with the fit. A bilinear function is assumed in the background mass shape.

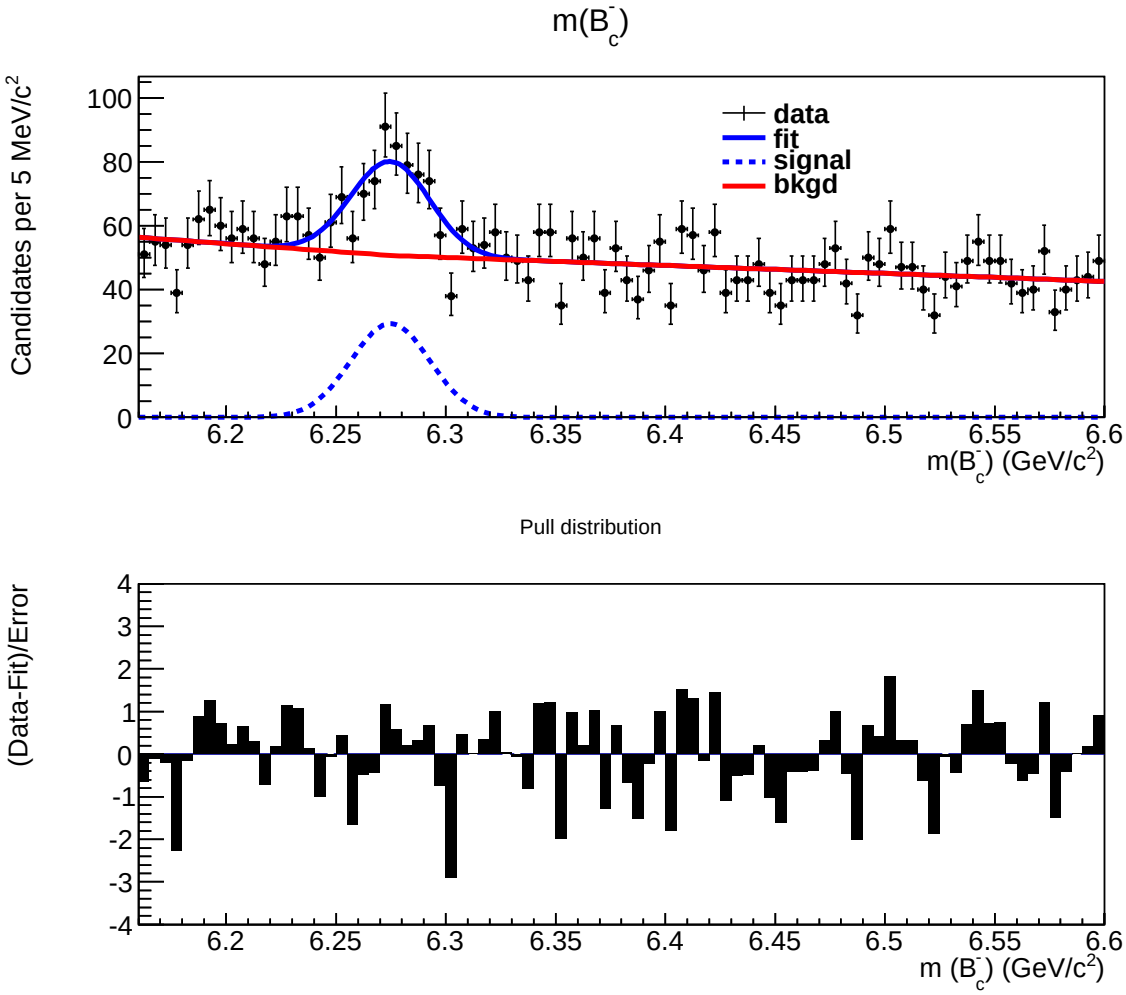

Figure 75: Invariant mass projection of the B_c^- candidates overlaid with the fit. A bilinear function is assumed in the background mass shape.

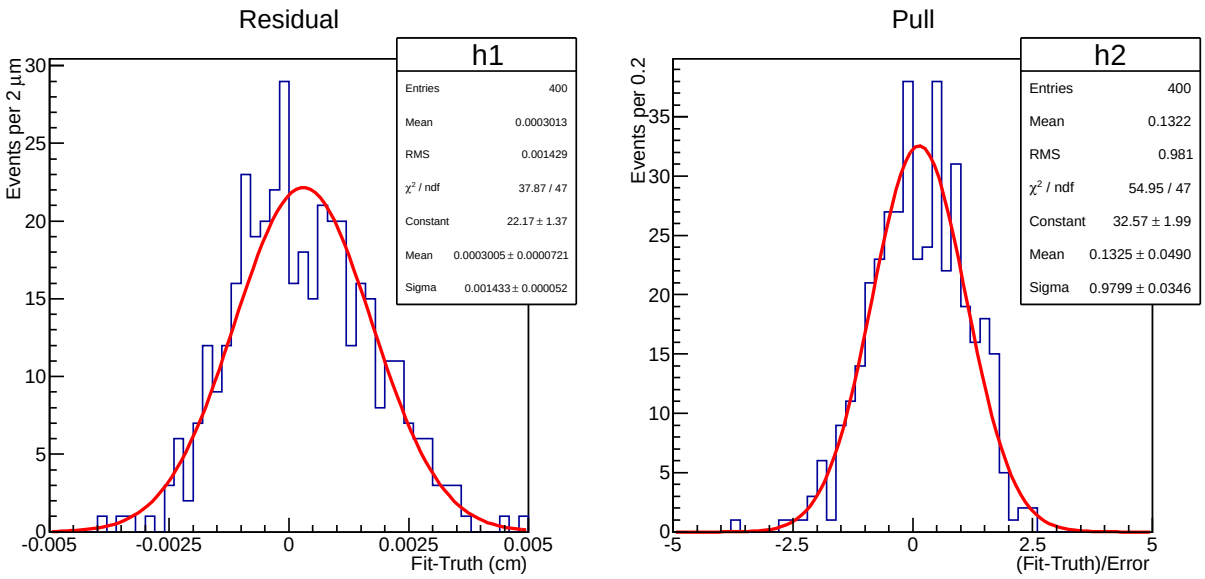

Figure 76: Residual and pull distributions of the fitted B_c^- lifetime when a bilinear distribution is used in the background mass model.

distribution with the fit result overlaid.

Statistical trials are generated based on the untuned efficiency parameters, and then fitted using the tuned parameters. The residual and the pull distributions of the fitted lifetime are shown in Figure 80. The difference in the fitted lifetime, on average, is –0.4 μm, which is consistent with the difference observed in the data.

6.3.2 Variation of the tuned efficiency parameters

To account for possible uncertainty in determining the efficiency parameters, the efficiency function is shifted towards lower and higher proper decay length by 20 μm. This 20 μm shift is approximately three standard deviations of the parameter a in the efficiency function shown in Table 13. This variation gives a difference of +2.0 (-3.0) μm for shifts to the lower (higher) side. Statistical trials are generated using the shifted efficiency parameters. The default fitting model is used to extract the lifetime in these statistical trials. Figure 81

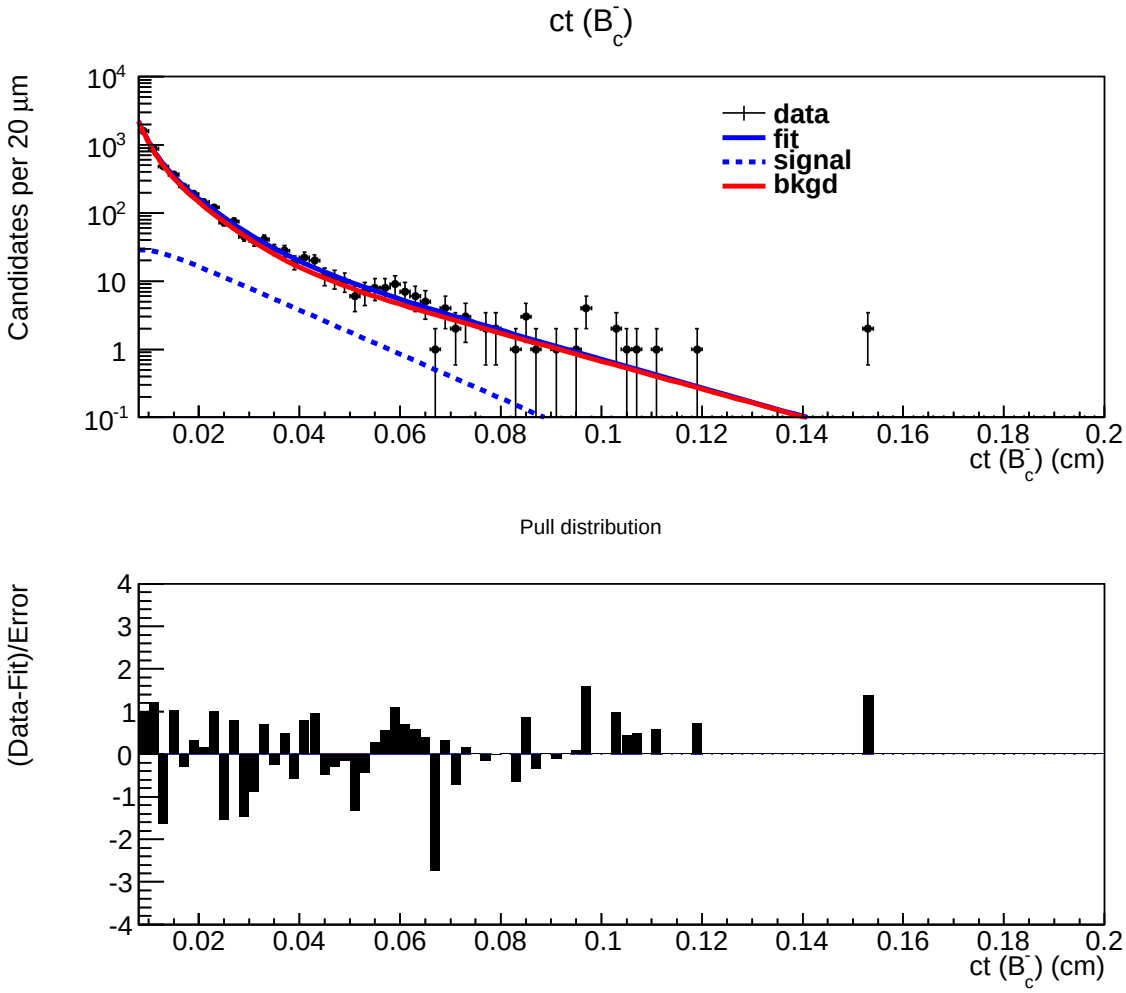

Figure 77: Proper decay length projection of the B_c^- candidates overlaid with the fit. The tunning on the σ_{ct} requirement is not used to obtained the efficiency parameters.

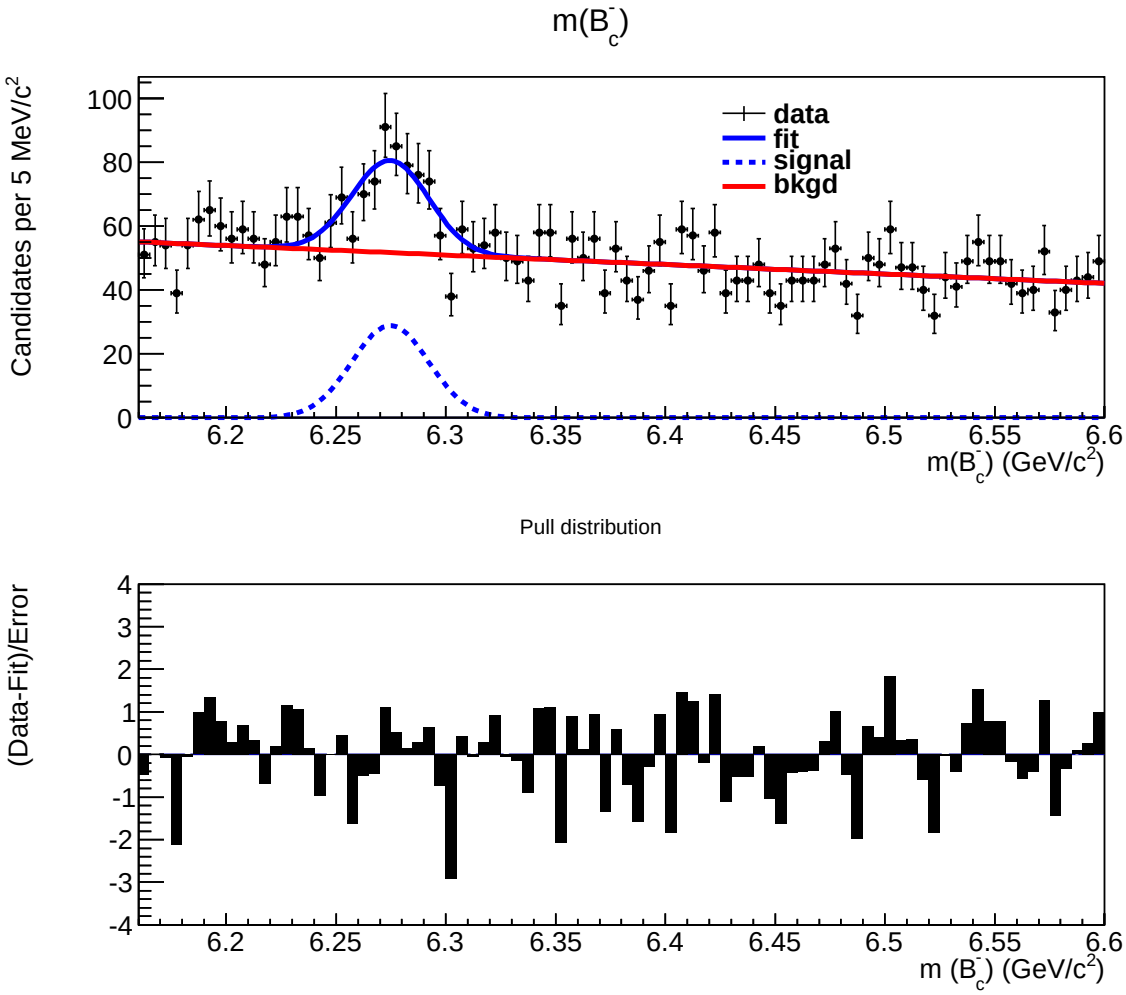

Figure 78: Invariant mass projection of the B_c^- candidates overlaid with the fit. The tunning on the σ_{ct} requirement is not used to obtained the efficiency parameters.

Table 13: The fit results for the efficiency parameters in $B_c^- \to J/\psi\ \pi^-$ simulation with or without the tunning.

	C	a (μm)	b (μm)
Untune	0.4704 ± 0.0029	24.11 ± 6.62	46.74 ± 4.40
Tune	0.4213 ± 0.0028	26.76 ± 7.45	42.72 ± 4.75

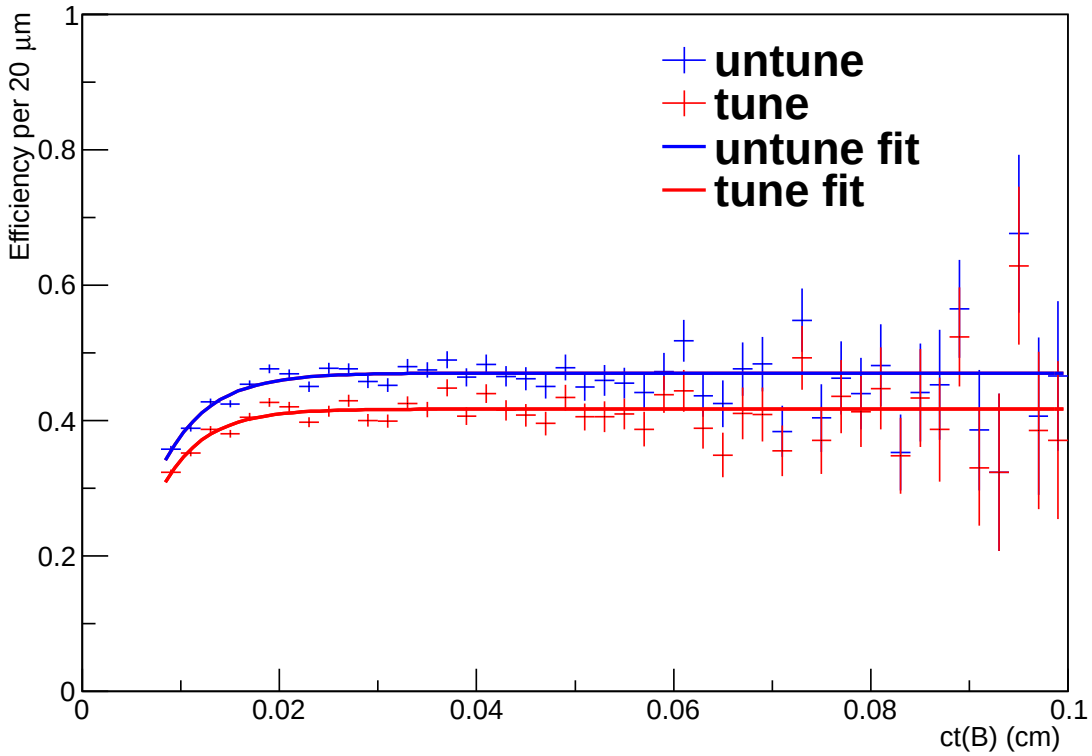

Figure 79: The efficiency functions with or without the tunning made on σ_{ct} variable, along with their fit results.

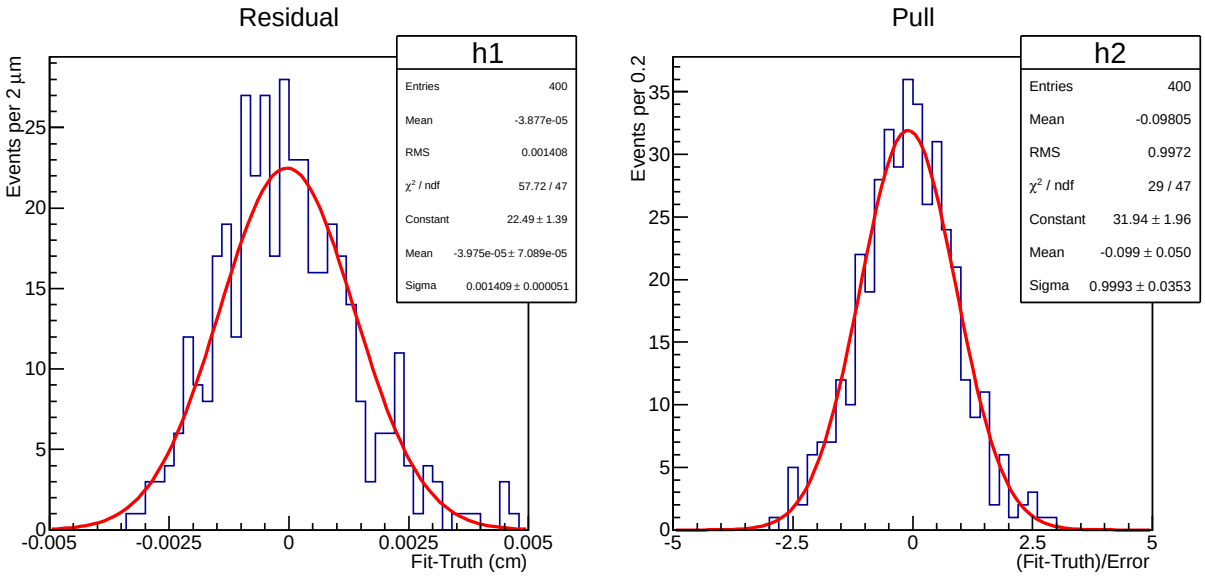

Figure 80: Residual and pull distributions of the fitted B_c^- lifetime when the tunning made on the σ_{ct} variable is not used in the simulation.

and 82 show the residual and pull distribution of the fitted lifetime when the trials are generated according to the efficiency parameters shifted towards lower and higher ct. The mean differences in the fitted lifetime with this variation are –0.5 and +3.1 μm for shifting towards lower and higher ct, respectively.

6.3.3 Variation of B_c^- production spectrum

Since the production spectrum of B_c^- meson consists of four difference mechanisms, which include both the ground state and excited state production, each of which includes the interactions between gluons, gluons and quarks or heavy sea quarks. Their corresponding contributions to the total B_c^- production have been varied in a reasonable way, and the resulting efficiency parameters are listed in Table 14. The default spectrum is a mixture of the four contributions as shown in Table 7. The Fixed-Flavor-Number (FFN) spectrum [1] is a slightly different prediction of the B_c^- production compared to the GM-VFN spectrum.

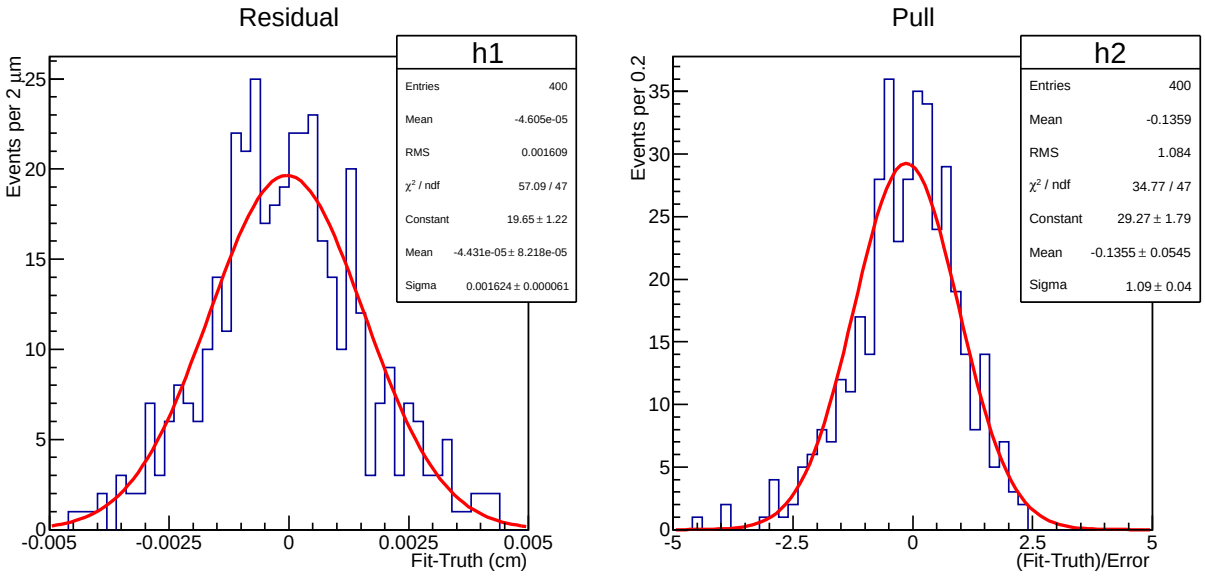

Figure 81: Residual and pull distributions of the fitted B_c^- lifetime when the efficiency function is shifted towards lower ct value.

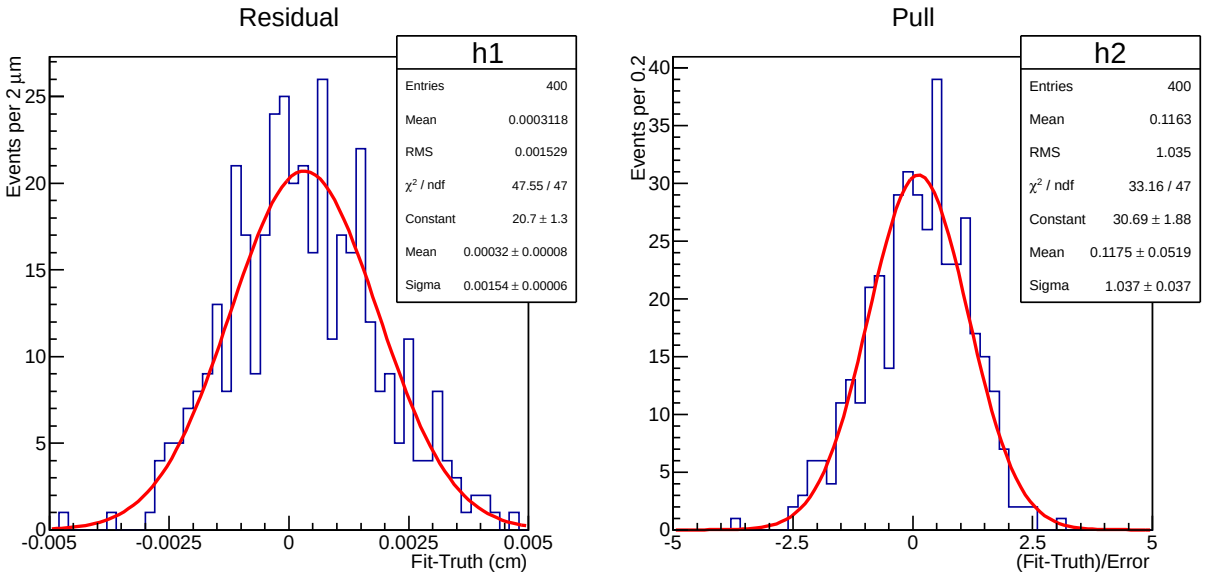

Figure 82: Residual and pull distributions of the fitted B_c^- lifetime when the efficiency function is shifted towards higher ct value.

The double $q\bar{q}$ contribution is a variation that doubles the small contribution from the heavy sea quark interaction compared to the default contribution. The ground state B_c^- production variation includes only the ground state B_c^- production rather than the combined B_c^- and B_c^{*-} production. The maximum difference of the fitted lifetime observed from these variations is –1.6 μm, as can be expected from the fact that these efficiency parameters do not change substantially compared to the default values.

Table 14: The fit results of the efficiency parameters for different variations of the B_c^- production spectrum.

B_c^- spectrum	C	a (μm)	b (μm)
Default	0.4213 ± 0.0028	26.76 ± 7.45	42.72 ± 4.75
FFN spectrum	0.4513 ± 0.0026	25.70 ± 5.26	49.46 ± 3.76
Double $q\bar{q}$ contribution	0.4329 ± 0.0029	21.99 ± 7.35	48.47 ± 4.94
Ground state B_c^- only	0.4406 ± 0.0035	34.46 ± 6.58	43.56 ± 4.76

6.3.4 Summary

The systematic uncertainty in the signal decay time model involves the determination of the efficiency parameters. The systematic uncertainty has been studied in three different sources, where the largest difference observed is 3.0 μm. This is consistent with the results from the statistical trials, which gives a mean residual of 3.1 μm. Thus, the total systematic uncertainty due to the signal decay time is taken as 3.1 μm.

6.4 BACKGROUND DECAY TIME MODEL

One concern in the decay time distribution is the modeling of the long tails. Instead of using the combination of three exponential distributions for the background decay time model, an alternate model which consists of two exponential and one linear distributions is used to test

possible systematics in this model. At large decay length, the contribution from the linear background function dominates the total background, and slightly changes the background decay time shape. The fitted B_c^- lifetime changed by –0.6 μm compared with the default result. Figure 83 and 84 show the proper decay length and the mass distribution with the fit result overlaid.

Statistical trials are generated using parameters from this alternate model, the residual and pull distributions of the trials are shown in Figure 85. The average difference between the fitted lifetime using the default model and the true value is 1.3 μm. Thus, a systematic uncertainty of 1.3 μm is assigned for the background decay time model.

6.5 FITTING TECHNIQUE

To study possible systematic uncertainty in the fitting technique, one is interested in whether there is a bias between the input lifetime and the fitted lifetime returned from the fitting function. To answer this question, statistical trials are generated assuming B_c^- lifetime values of 120, 135 and 150 μm, corresponding to the fitted result and $\pm 1\sigma$ of statistical uncertainty. These statistical trials are then used to fit the B_c^- lifetime, and compare with the input B_c^- lifetime. Figure 86, 87 and 88 show the residual and pull distribution of the fitted B_c^- lifetime for input lifetime value of 120, 135 and 150 μm, respectively. It can be seen that the fitted lifetime, on average, changed by no more than 2.0 μm compared with the input value.

To understand whether the fitting function works well for different background contaminations, other trials are also generated by varying the signal fraction from 4.6% to 6.6%, corresponding to the fitted signal fraction $\pm 1\sigma$ of statistical uncertainty. The input lifetime used in these trials is 135 μm. Figure 89 and 90 show the residual and pull distribution of the fitted B_c^- lifetime for input signal fraction value of 4.6% and 6.6%, respectively. The fitted lifetime, on average, changed by less than 1 μm compared with the input value. Thus, the conclusion is that the fitting technique gives a reasonable result for various signal fractions and lifetime values, a systematic uncertainty of 2 μm is assigned to the fitting technique for the bias observed in the trials.

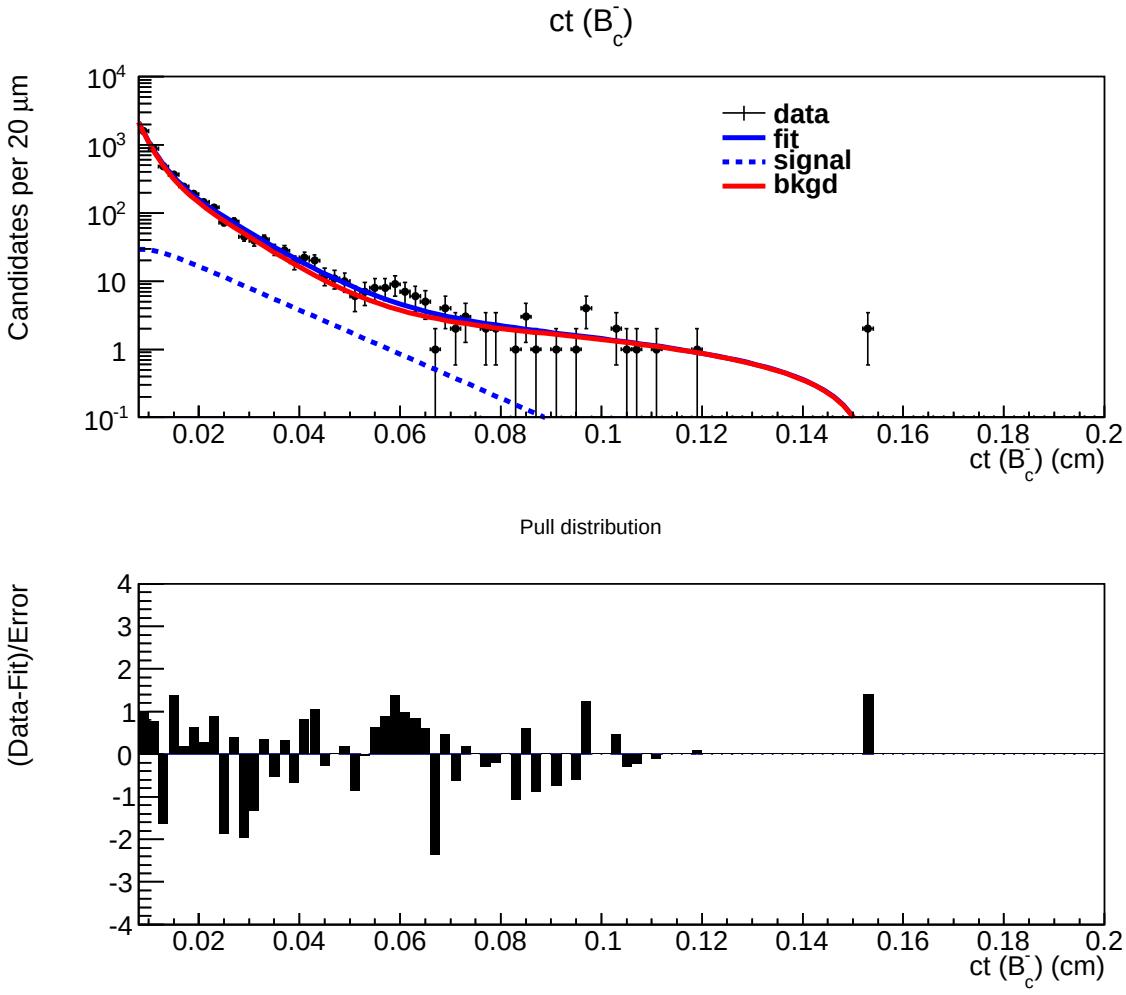

Figure 83: Proper decay length projection of the B_c^- candidates overlaid with the fit. A linear distribution is assumed in the background decay time shape.

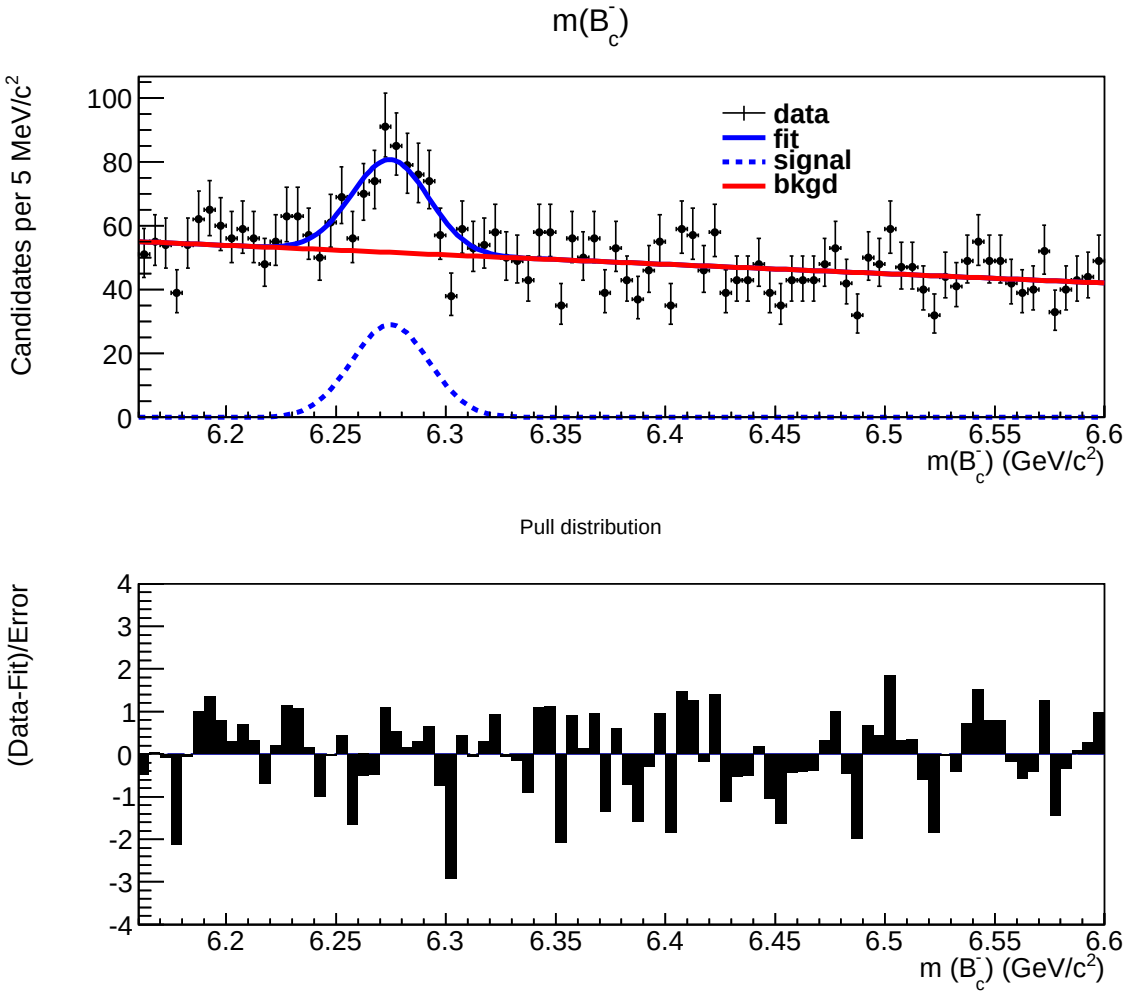

Figure 84: Invariant mass projection of the B_c^- candidates overlaid with the fit. A linear distribution is assumed in the background decay time shape.

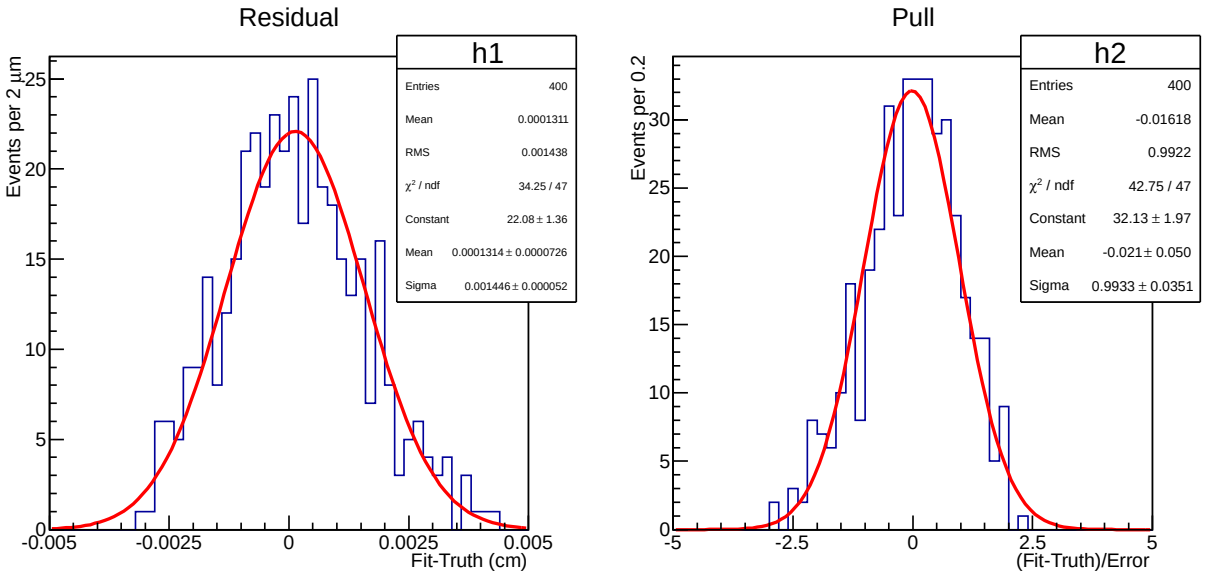

Figure 85: Residual and pull distributions of the fitted B_c^- lifetime when a linear function is included in the background decay time model.

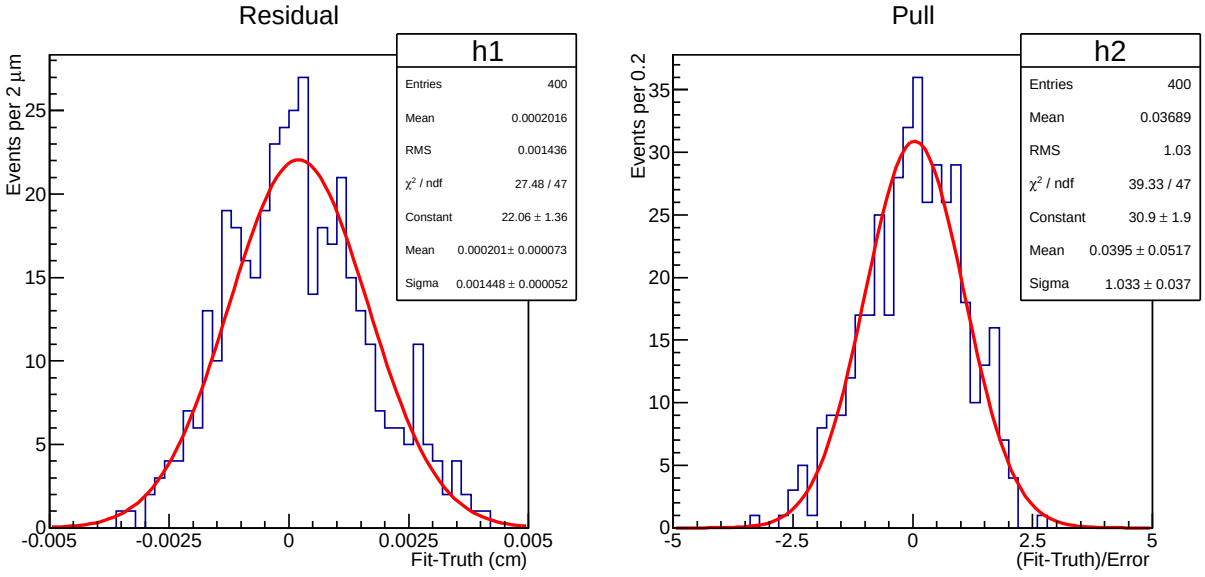

Figure 86: Residual and pull distribution of the fitted B_c^- lifetime for input lifetime value of 120 μm.

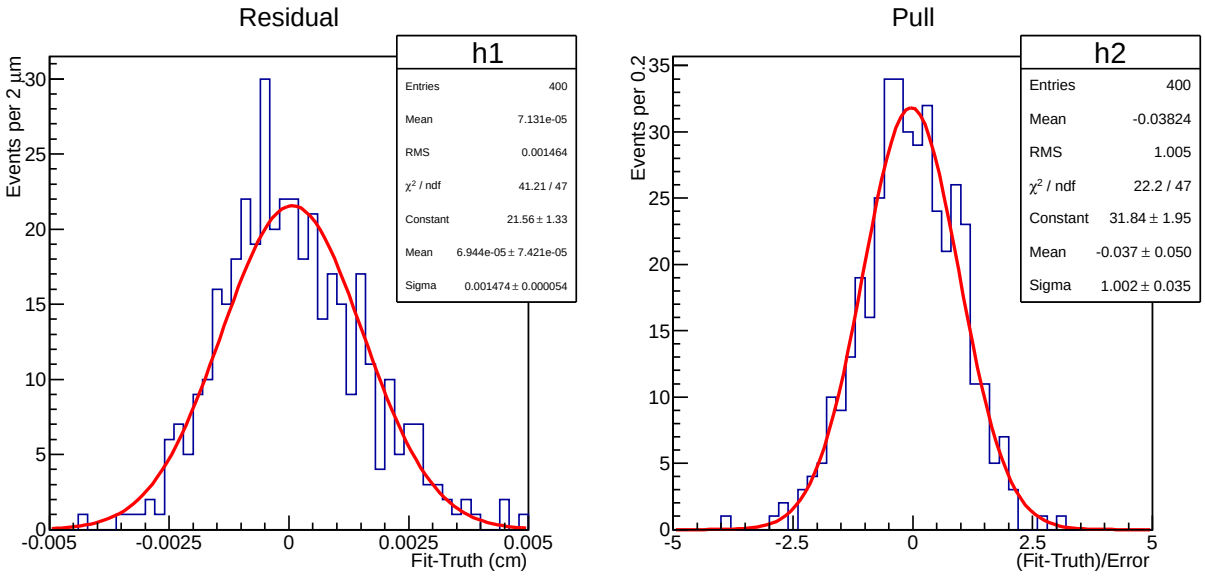

Figure 87: Residual and pull distribution of the fitted B_c^- lifetime for input lifetime value of 135 μm.

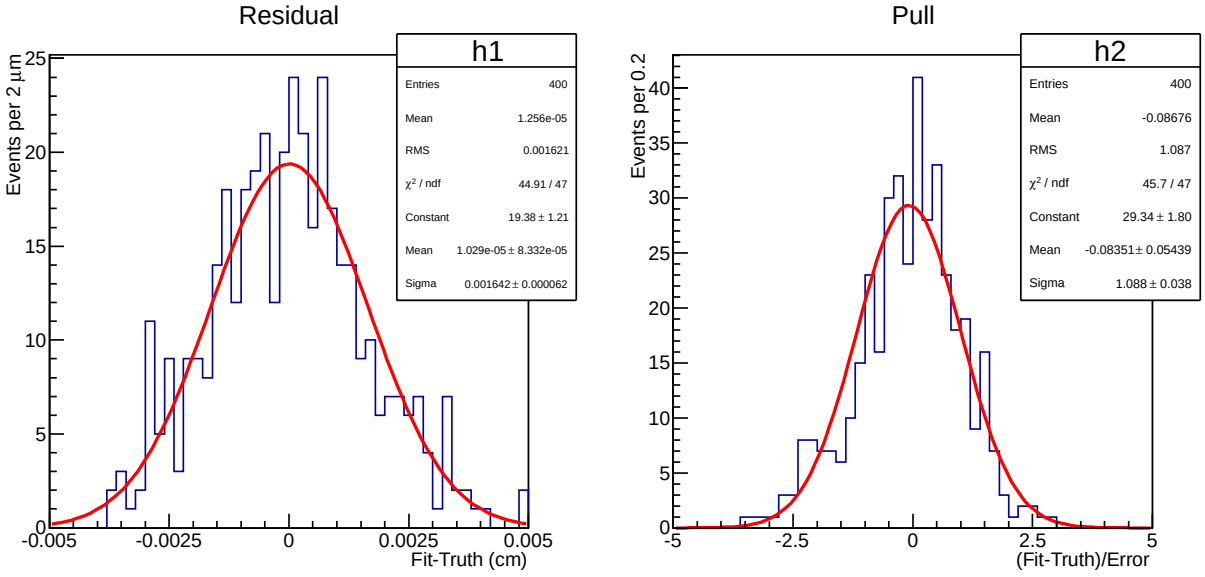

Figure 88: Residual and pull distribution of the fitted B_c^- lifetime for input lifetime value of 150 μm.

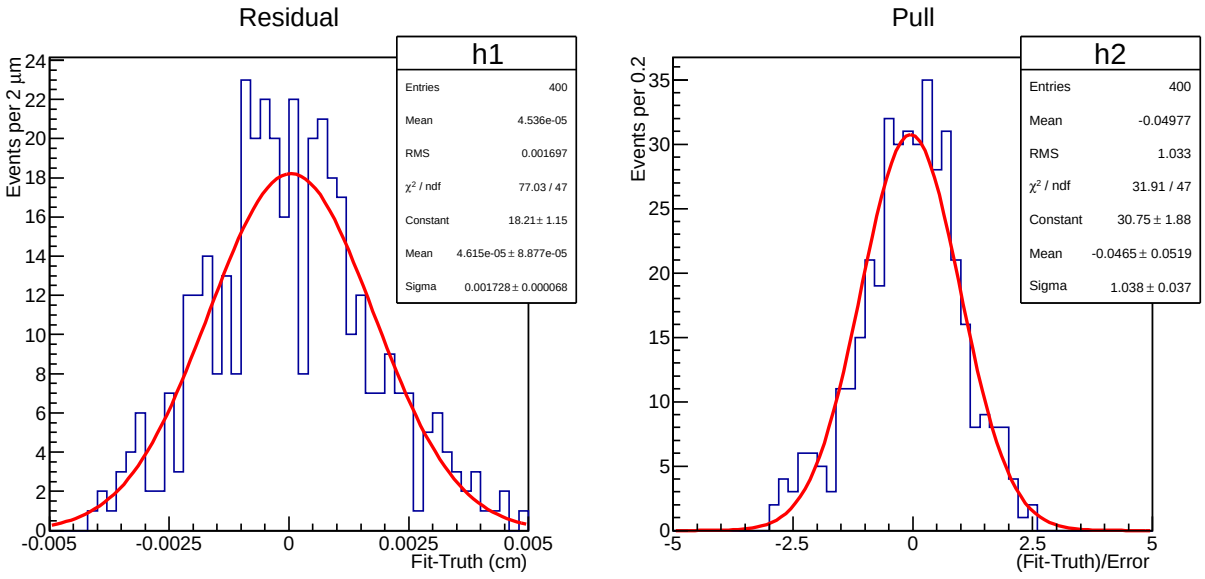

Figure 89: Residual and pull distribution of the fitted B_c^- lifetime for input signal fraction value of 4.6%.

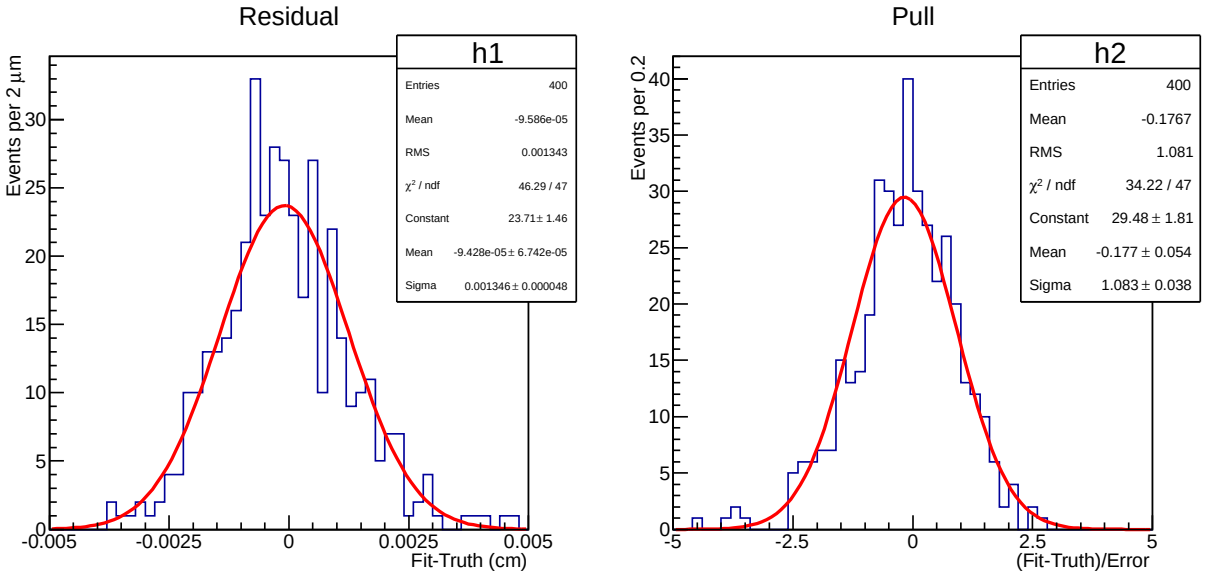

Figure 90: Residual and pull distribution of the fitted B_c^- lifetime for input signal fraction value of 6.6%.

6.6 DETECTOR ALIGNMENT

A systematic uncertainty is applied to account for the misalignment of the silicon detectors. This uncertainty is related to the exact position of the sensors in the silicon detectors. The type of displacement that mostly affects the lifetime result is a radial dilation or contraction of the detectors, such as the bowing of the ladder in the silicon detectors. When two ends of a ladder are pinned to the detector frame, the ladder in most cases bends outward so that two central wafers are at a radius larger than its nominal value. The CDF collaborators have evaluated the effect of this uncertainty by generating simulated samples with radial displacement of individual sensors as well as translation and rotation of the silicon detector relative to the COT [70]. An uncertainty of 2.0 μm is assigned due to the detector misalignment.

6.7 CORRELATION

To study correlation between lifetime result and the fixed parameters used in the fits, variations are made on those quantities which could affect the B_c^- lifetime. They include the choice of the mass region used in the fit, the choice of the proper decay time region used in the region, and the detector resolution function.

6.7.1 Choice of the mass window

The mass window used in the fit is 6.16 $< m(B_c^-) <$ 6.60 GeV/c^2, this range includes a wide upper sideband and a narrow lower sideband. To study possible correlation between the lifetime and the mass window, two variations on the ranges are made. The first one uses only the upper sideband, the mass range for the first variation is 6.21 $< m(B_c^-) <$ 6.60 GeV/c^2, where the lower edge is about three standard derivations below the B_c^- mass. The fitted results of the mass and ct projection are shown in Figure 91 and 92. The fitted lifetime changed by –2.0 μm compared to the default result. The second variation uses a narrower upper sideband as well as the narrow lower sideband, the mass range is 6.16 $< m(B_c^-) <$ 6.50

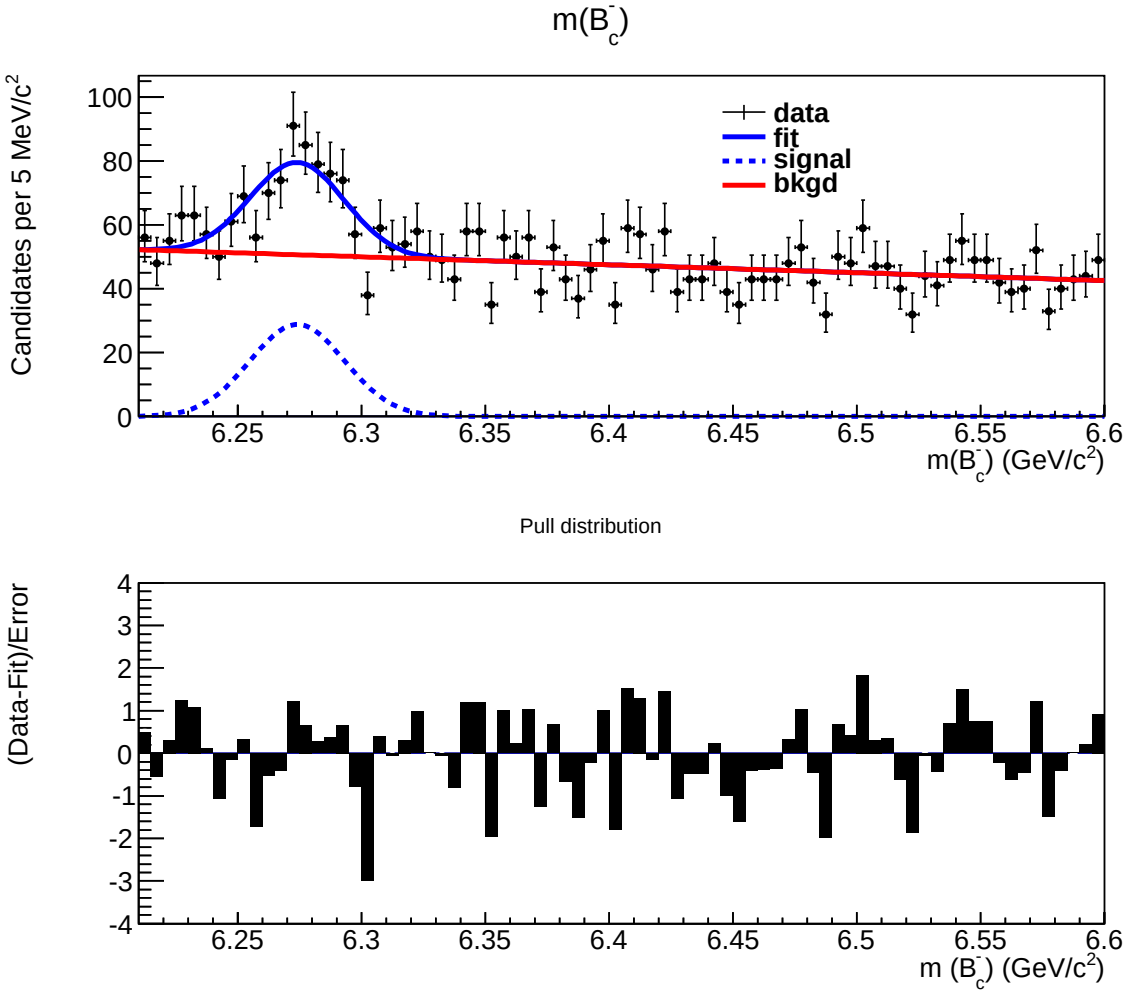

Figure 91: Invariant mass projection of the fit result when the mass range is from 6.21 to 6.60 GeV/c^2.

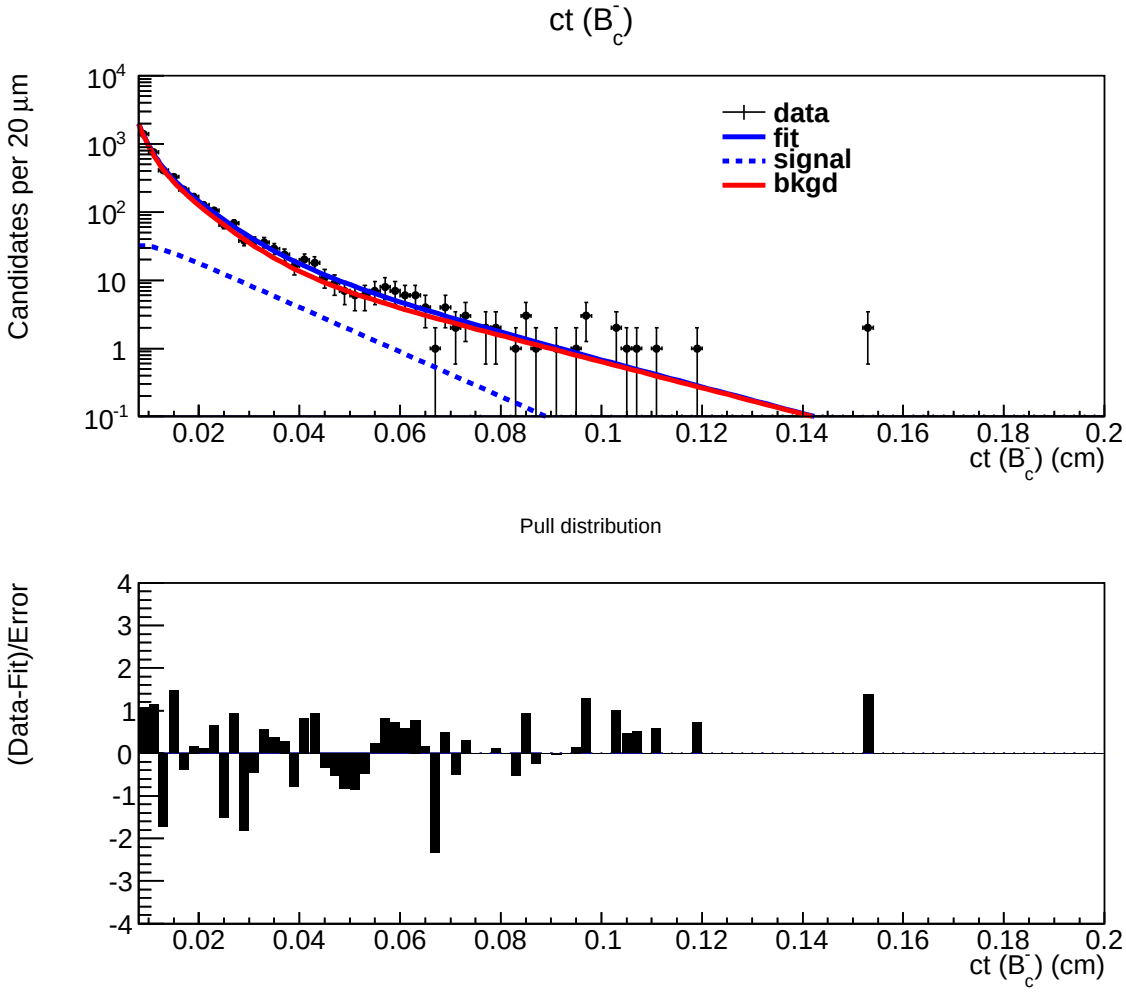

Figure 92: Proper decay length projection of the fit result when the mass range is from 6.21 to 6.60 GeV/c^2.

GeV/c^2, where the upper sideband is about half of the full upper sideband. The fitted results of the ct and mass projection are shown in Figure 93 and 94. The fitted lifetime changed by –1.6 μm compared to the default result. Thus, the systematic uncertainty introduced by the choice of the mass window is set to be 2.0 μm.

6.7.2 Choice of the ct range

The choice of the ct range is also varied to study possible systematic uncertainty. The first variation is to change the upper ct limit, which is set as 2000 μm in the default model. This number is changed to 1000 μm and the lifetime obtained from this variation changed by –1.0 μm compared to the default result. The fitted results of the ct and mass projection are shown in Figure 95 and 96.

The second variation is to change the lower ct limit from 80 μm to 100 μm. The lifetime result from this variation changed by +0.4 μm compared to the default result. The fitted results of the ct and mass projection are shown in Figure 97 and 98. Thus, the systematic uncertainty introduced by the choice of the ct range is set to be 1.0 μm.

6.7.3 Variation of the resolution model

The detector resolution is modeled as a Gaussian distribution centered at zero with a width of 20 μm, and it is necessary to study possible systematic uncertainty due to this model. Since the default width of 20 μm is taken from calibration in the detector using promptly decaying background events [67], it is reasonable to assume that the actual width will not be too far away from this value. Thus, the width is changed to 25 and 30 μm to evaluate the systematic uncertainty.

First, Figure 99 shows, for different width used in the Gaussian resolution, how the detector resolution changes the proper decay length distribution for $0 < ct < 500$ μm, assuming $c\tau = 140$ μm. All the distributions have been normalized to one. In the ideal situation where the resolution is a delta function, the proper decay length is exponentially distributed. With a typical detector resolution with width between 20 and 30 μm, the proper decay length distribution is distorted mostly at lower value, and the distortion becomes

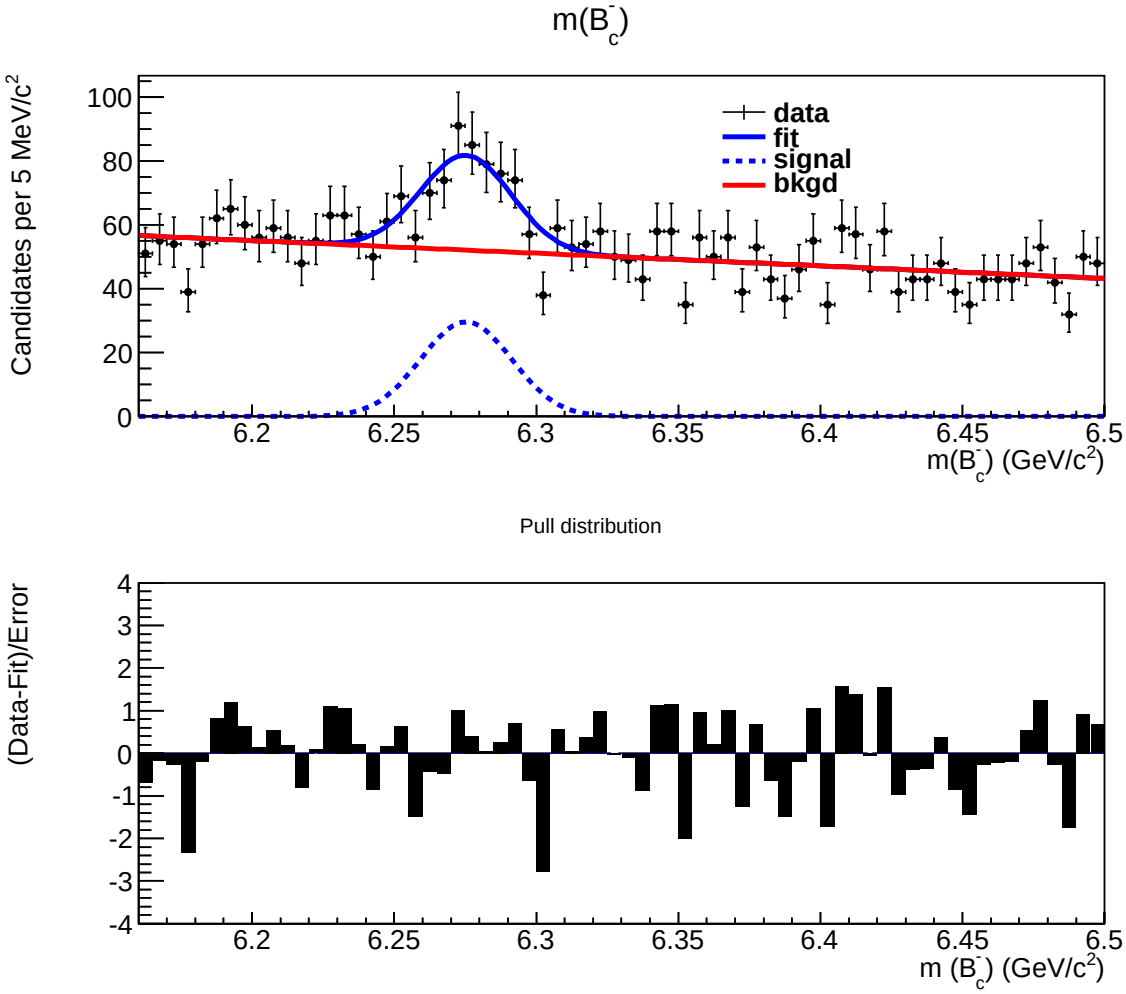

Figure 93: Invariant mass projection of the fit result when the mass range is from 6.16 to 6.50 GeV/c^2.

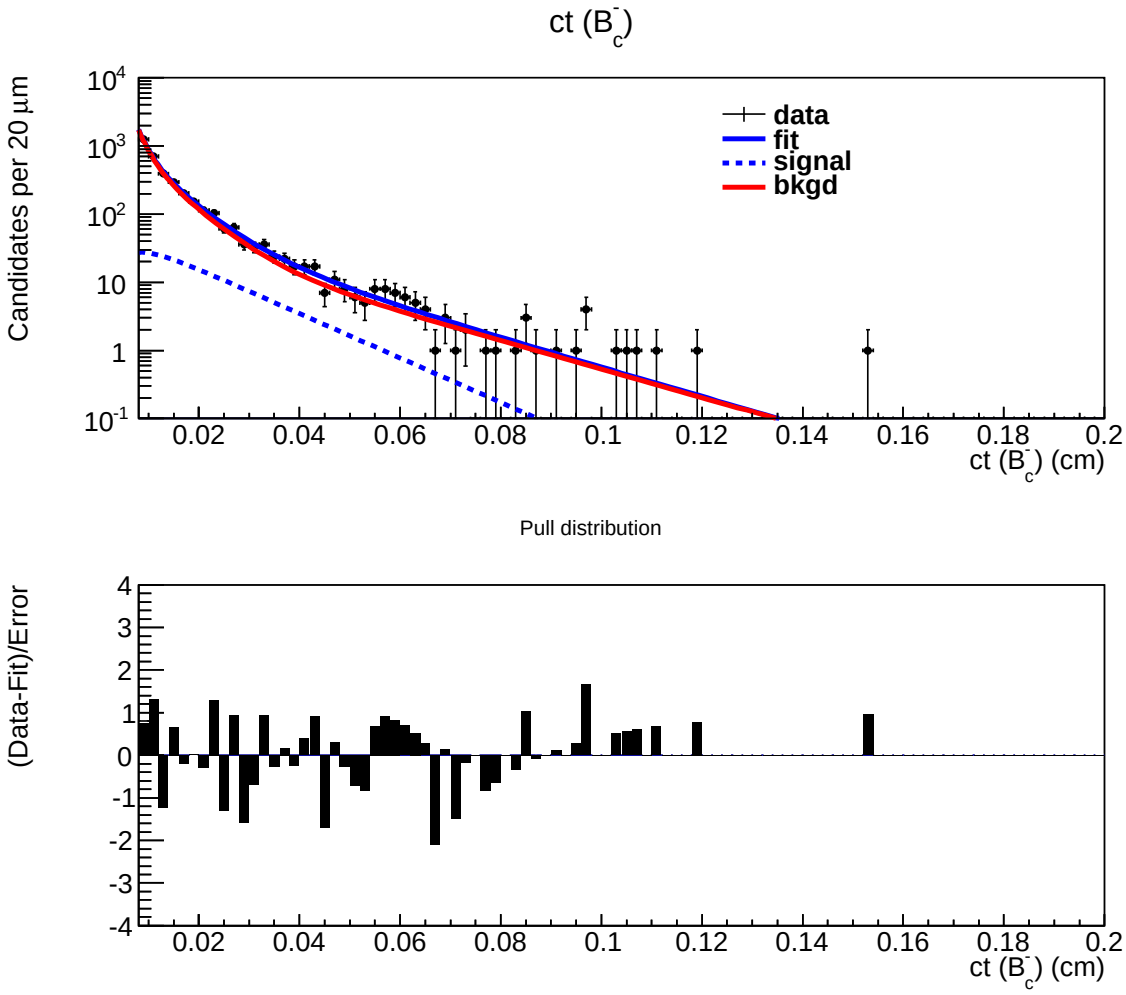

Figure 94: Proper decay length projection of the fit result when the mass range is from 6.16 to 6.50 GeV/c^2.

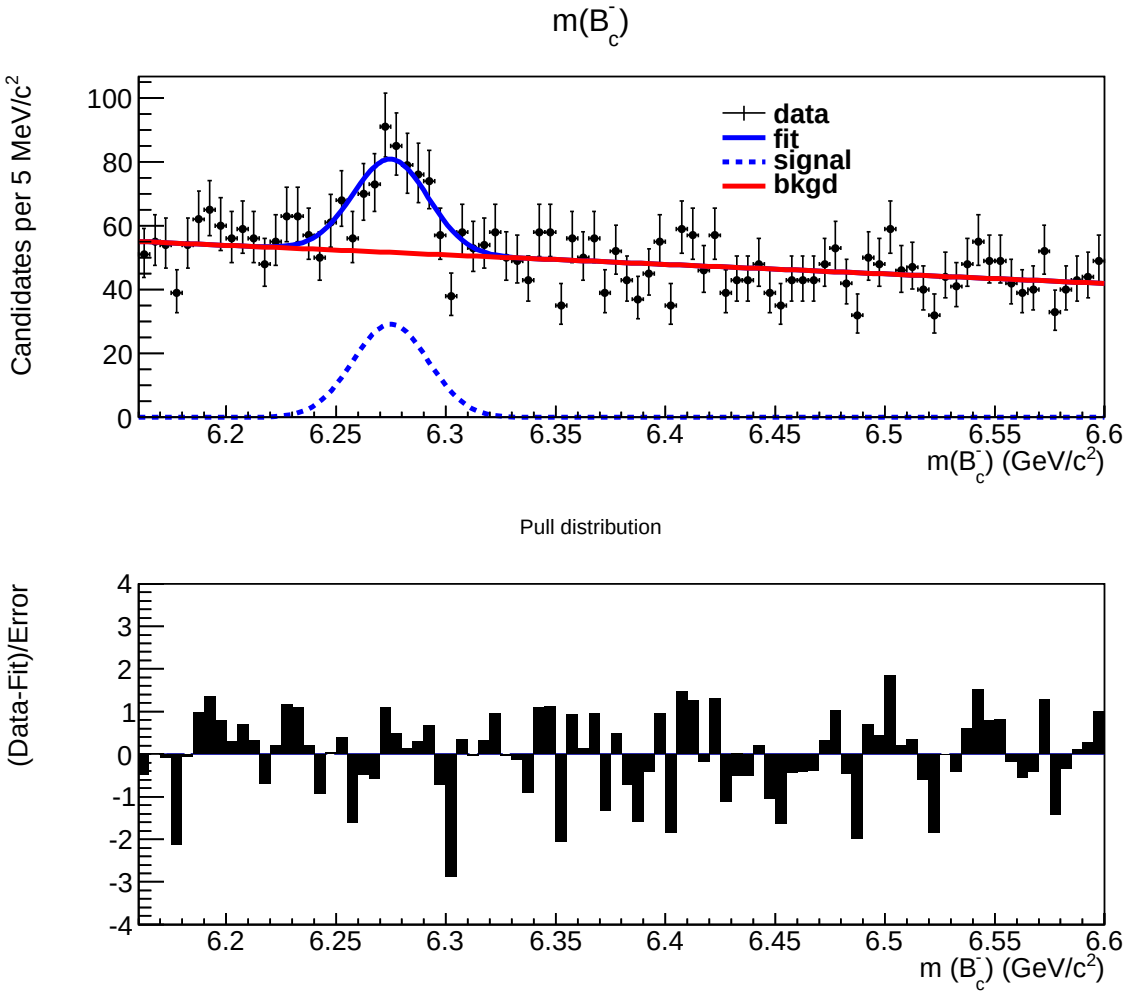

Figure 95: Invariant mass projection of the fit result when the proper decay length range is from 80 to 1000 μm.

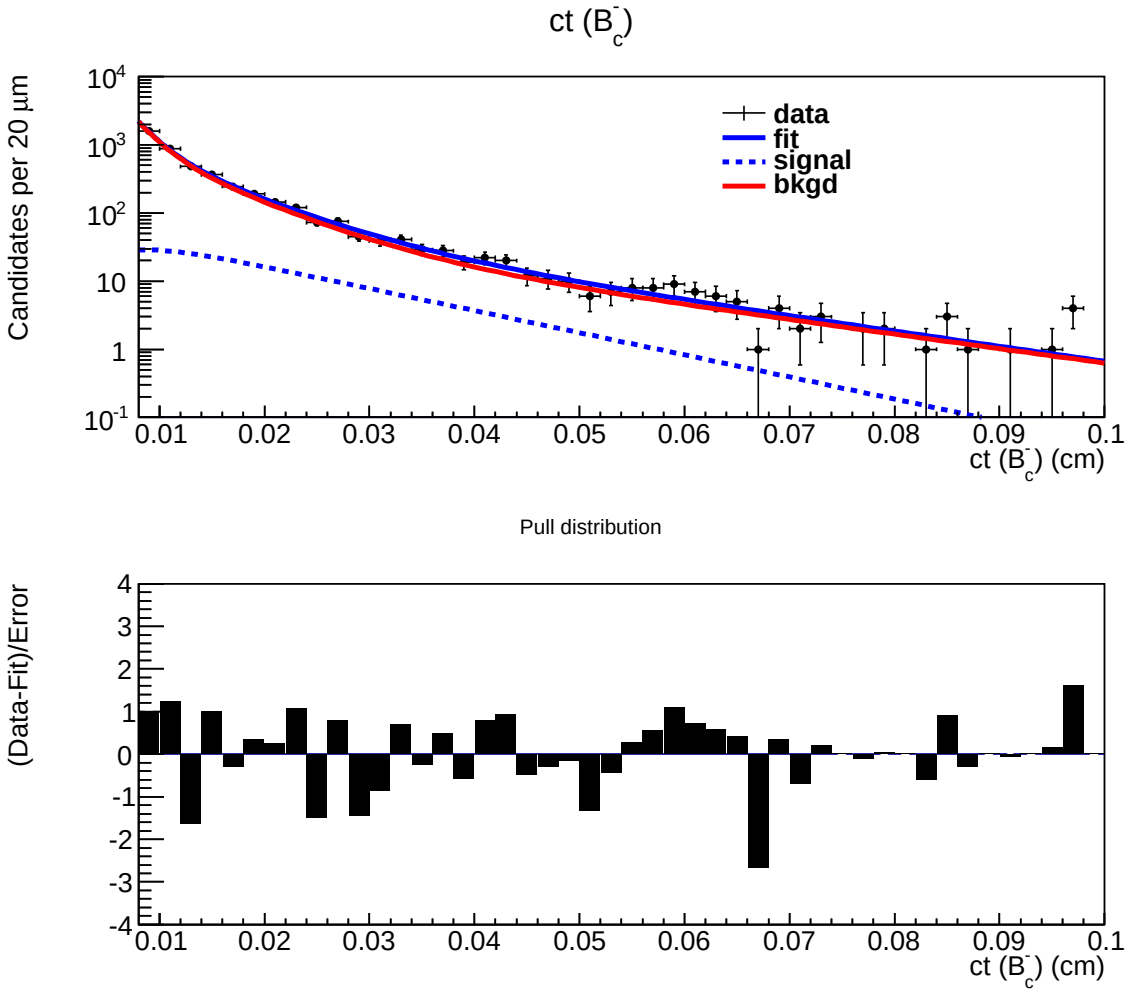

Figure 96: Proper decay length projection of the fit result when the proper decay length range is from 80 to 1000 μm.

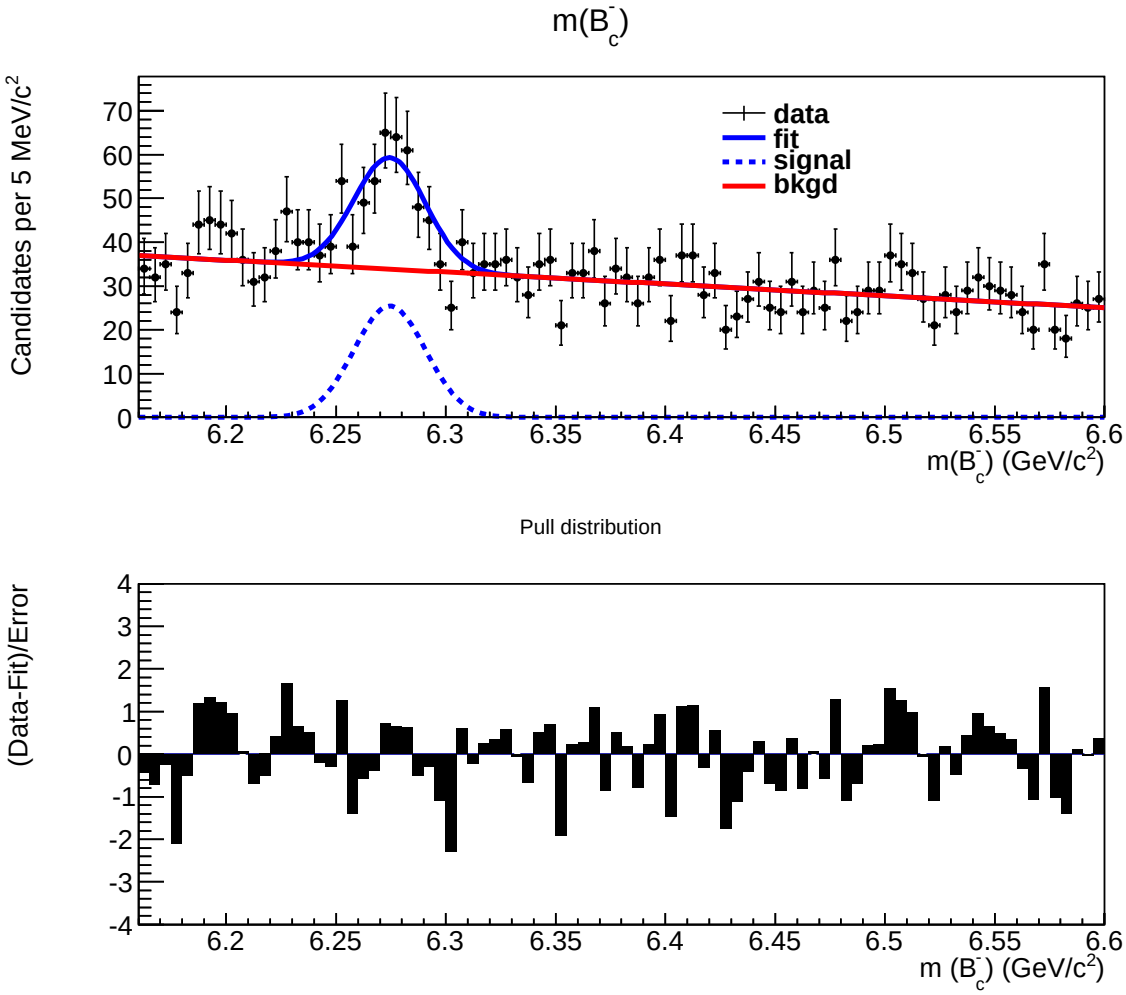

Figure 97: Invariant mass projection of the fit result when the proper decay length range is from 100 to 2000 μm.

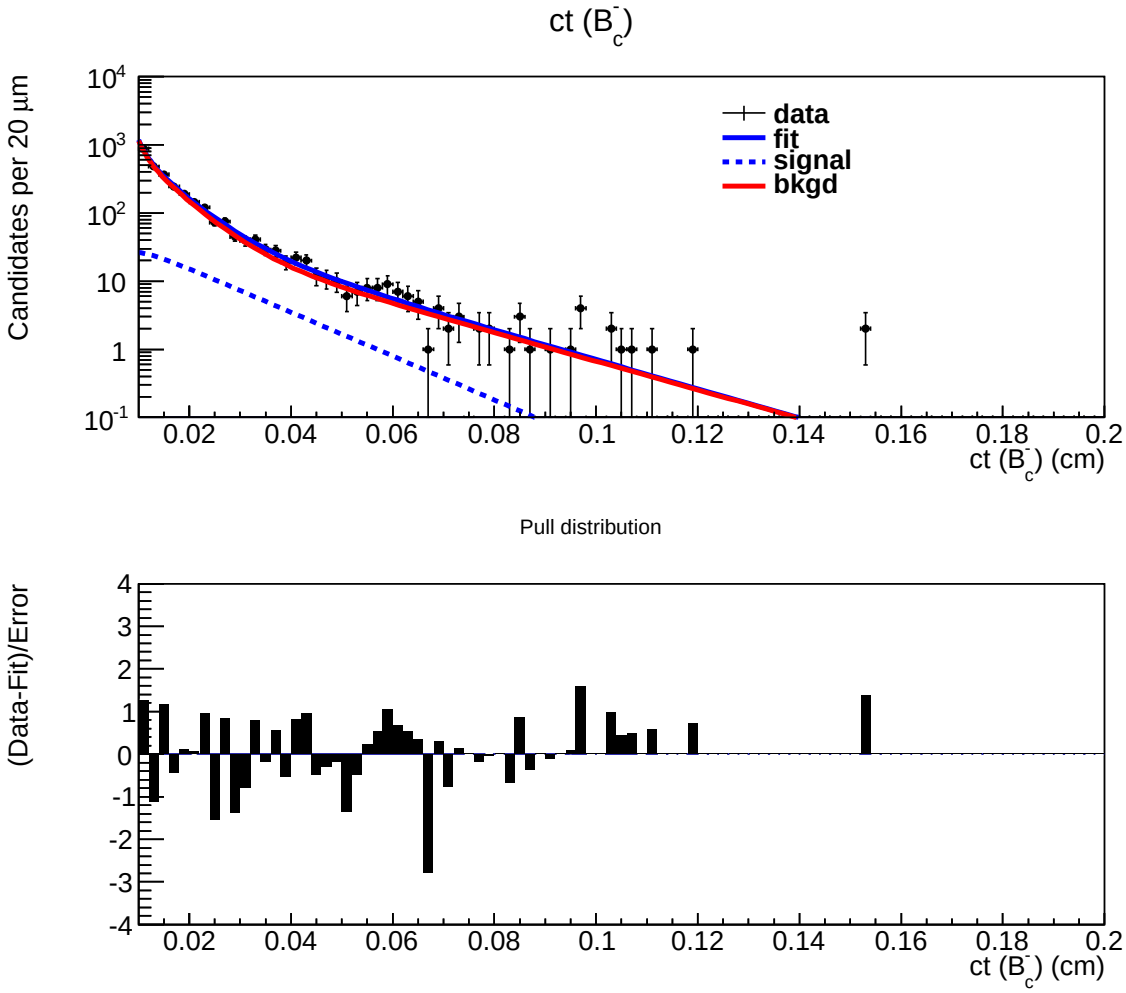

Figure 98: Proper decay length projection of the fit result when the proper decay length range is from 100 to 2000 μm.

smaller for higher ct. Since a minimum ct requirement of 80 μm is made in this analysis, the probability density function used in the likelihood fit is normalized from 80 μm. It is then interesting to see how much effect the resolution has for $ct > 80$ μm. Figure 100 shows the proper decay length distribution for $80 < ct < 500$ μm with ideal situation and resolution with width of 30 μm. The distributions are normalized to one for $80 < ct < 500$ μm. It can be seen that, even for the resolution with width of 30 μm, the effect of the resolution on the proper decay length distribution is small when a minimum proper decay length is required.

Based on the comparison of the proper decay length distribution shown in Figure 100, one would expect the Gaussian resolution would have very small effect on the lifetime result. In fact, changing the default Gaussian resolution width of 20 μm to 30 μm, the obtained lifetime result changed by only 0.1 μm compared to the default lifetime result. Assuming a delta function for the resolution model, the fitted lifetime is essentially the same as the result obtained using a Gaussian model with a width of 20 μm. Thus, the systematic uncertainty due to the resolution model is negligible, and set to be zero.

6.7.4 Summary

The total systematic uncertainty due to the correlation between the lifetime and the fixed parameters are obtained by adding the uncertainty from each source in quadrature, and a systematic uncertainty of 2.2 μm is assigned.

6.8 TOTAL SYSTEMATICS

Table 15 summaries the systematic uncertainties from each source, in the order of their magnitudes. The total systematic uncertainty is determined by adding each uncertainty in quadrature, and a result of 5.8 μm is obtained.

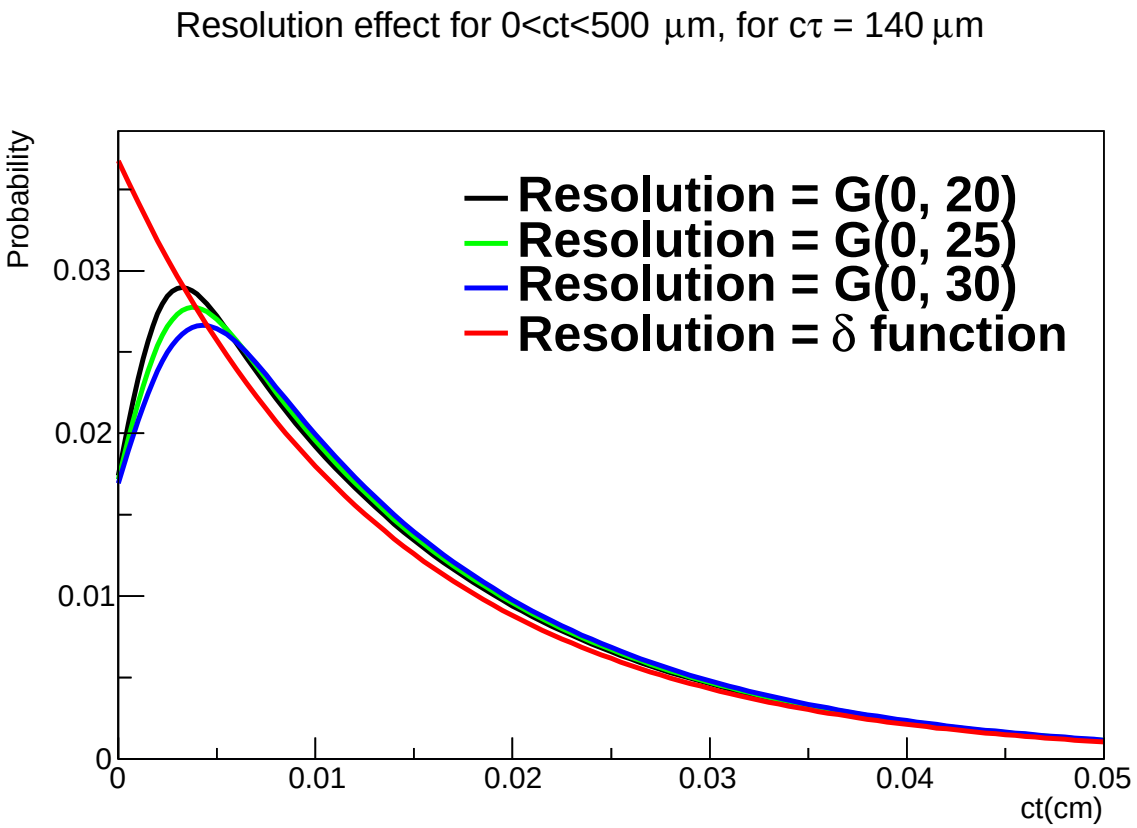

Figure 99: Proper decay length distribution for a lifetime of 140 μm, with or without the detector resolution. The distributions are normalized between 0 and 500 μm.

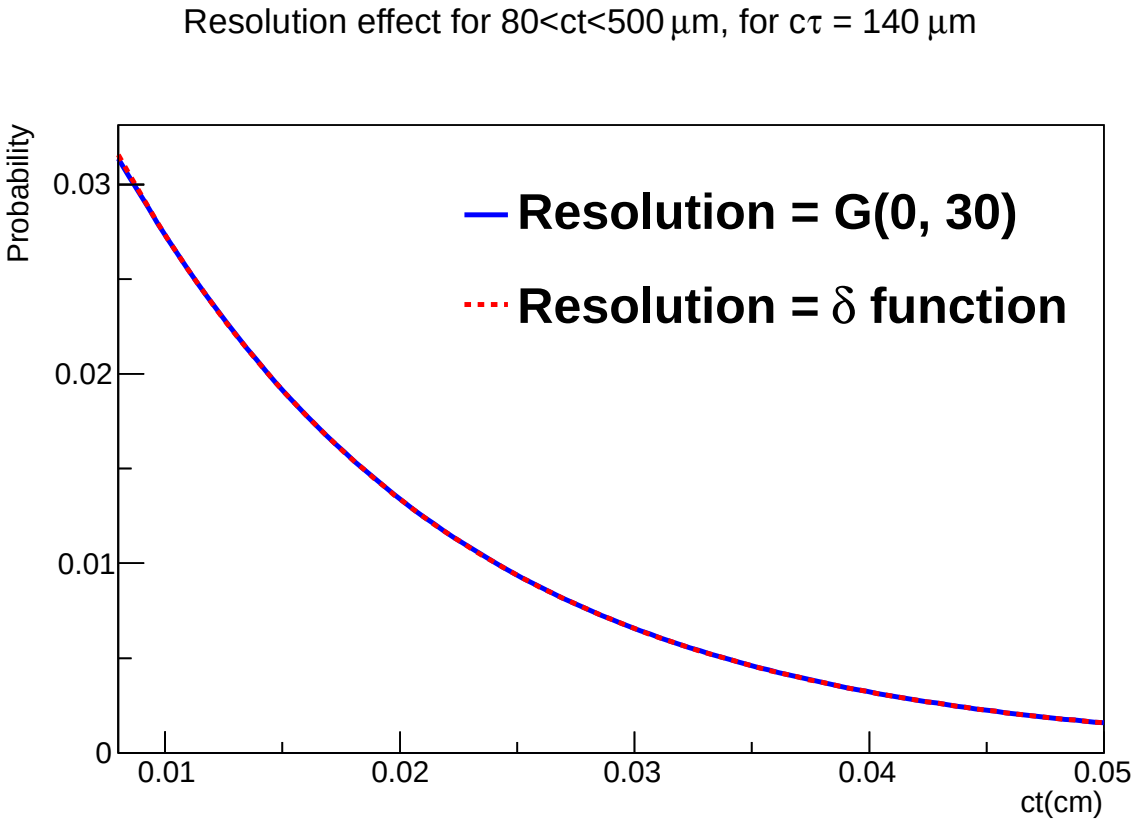

Figure 100: Proper decay length distribution for a lifetime of 140 μm, with or without the detector resolution. The distributions are normalized between 80 and 500 μm.

Table 15: Summary of systematic uncertainty.

Source	Uncertainty (μm)
Signal decay time model	3.1
Background mass model	3.0
Correlation	2.2
Fitting technique	2.0
Detector alignment	2.0
Background decay time model	1.3
Signal mass model	1.0
Total	5.8

7.0 CONCLUSION

7.1 COMPARISON TO RESULTS IN SEMILEPTONIC CHANNEL

This thesis has presented a measurement of the B_c^- lifetime.

$$c\tau = 134.8\ ^{+16.2}_{-14.4}(stat.)\ \pm 5.8(syst.)\ \mu m$$

$$\tau = 0.449\ ^{+0.054}_{-0.048}(stat.)\ \pm 0.019(syst.)\ \text{ps}$$

Previous measurements of the B_c^- lifetime have been carried out by CDF and D0. All these previous measurements are made in the semileptonic decay modes, either in the specific electron or muon channel or in the combined channels. The result of these measurements along with the one from this thesis are listed in Table 16. The measurement presented in

Table 16: Summary of the B_c^- lifetime measurements result.

Experiment	Luminosity	Decay mode	Measured B_c^- meson lifetime τ
CDF Run I	110 pb^{-1}	$B_c^- \to J/\psi\ \ell^-\ X$	$0.46\ ^{+0.18}_{-0.16}(stat.) \pm 0.03(syst.)$ ps [3, 4]
CDF Run II	360 pb^{-1}	$B_c^- \to J/\psi\ e^-\ X$	$0.463\ ^{+0.073}_{-0.065}(stat.) \pm 0.036(syst.)$ ps [9]
D0 Run II	1.4 fb^{-1}	$B_c^- \to J/\psi\ \mu^-\ X$	$0.448\ ^{+0.038}_{-0.036}(stat.) \pm 0.032(syst.)$ ps [10]
CDF Run II	1.0 fb^{-1}	$B_c^- \to J/\psi\ \ell^-\ X$	$0.475\ ^{+0.053}_{-0.049}(stat.) \pm 0.018(syst.)$ ps [11]
CDF Run II	6.7 fb^{-1}	$B_c^- \to J/\psi\ \pi^-$	$0.449\ ^{+0.054}_{-0.048}(stat.) \pm 0.019(syst.)$ ps

this thesis in consistent with the previously measured values of the B_c^- lifetime. Combining statistical and systematical uncertainties, the measurement presented in this thesis provides a precision similar to that of the D0 Run II and the most recent CDF Run II results. Even

though the integrated luminosity in this thesis is several time larger than the D0 and most recent CDF II measurements, the branching ratio of the $B_c^- \to J/\psi\ \pi^-$ decay is only about 10% of the semileptonic decays, this is why the precision does not get better in this thesis.

The combined result of the B_c^- lifetime from each measurement can provide the most precise experimental value which can be compared with the theoretical predictions. To combine previous experimental results, the value obtained from Ref [9] is not used since that data set is already included in Ref [11]. All other measurements are independent and should be combined according to their corresponding uncertainty. The total uncertainty of each measurement is obtained by taken the square root of the sum over the square of the statistical and systematic uncertainties. Since the statistical uncertainty is asymmetric in each measurement, the total uncertainty is asymmetric as well. The usual approach that weights each measurement by the reciprocal of its variance no longer works. The procedure to combine results with asymmetric uncertainty outlined in Ref [71] is used, and a result of $\tau = 0.457\ ^{+0.030}_{-0.029}$ ps is obtained. Figure 101 shows a comparison of the results from the CDF Run I&II and the D0 Run II measurements, as well as the combined result.

7.2 COMPARISON TO THEORETICAL PREDICTIONS

Given the combined result of the B_c^- meson lifetime being $\tau = 0.457^{+0.030}_{-0.029}$ ps, the theoretical prediction on the same quantity can be compared to test the precision of different theoretical approaches. As shown in Table 5, these predictions using various approaches give different results: $\tau = 0.4$ ps when estimating the B_c^- lifetime from B, D mesons [39], $\tau = 0.4 - 0.7$ ps using operator product expansion [6] and $\tau = 0.48 \pm 0.05$ ps using sum rules [7]. The first approach gives a result that is about two standard derivation below the combined result, indicating that the naive estimation from the B and D meson decay widths does not give a precise prediction, but the result is roughly reasonable. The operator product expansion approach, as pointed out in Chapter 2, has its largest uncertainty from the mass of the c quark. For c quark masses of 1.4, 1.5, and 1.6 GeV/c^2, the method gives a result for the B_c^- lifetime of 0.7, 0.52, and 0.4 ps, respectively. The combined result suggests that the c

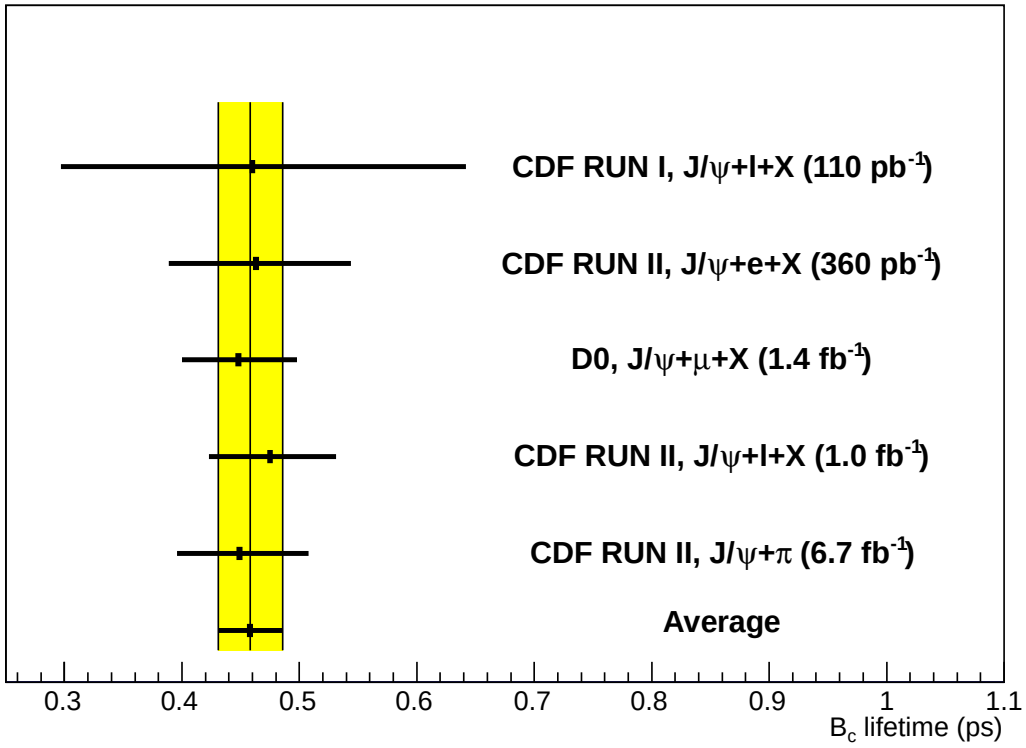

Figure 101: Comparison of the B_c^- meson lifetime for the CDF Run I, D0 Run II, and CDF Run II experiments. The average is taken assuming no correlations between uncertainties.

quark mass is near the higher end of the range. The prediction of the B_c^- meson lifetime using QCD sum rules is a good match with the combined experimental result since the predicted value is within one standard derivation of the combined experimental result, and the combined experimental result is also within one standard derivation of the prediction. Since the uncertainty in the QCD sum rules is about twice the uncertainty in the combined experimental result, a more precise prediction in the theory is now needed.

7.3 CONCLUSION

The first measurement of the B_c^- meson lifetime in an exclusive hadronic channel has been presented in this thesis. The measured value of

$$\tau = 0.449\ ^{+0.054}_{-0.048}(stat.)\ \pm 0.019(syst.)\ \text{ps}$$

is in good agreement with previous semileptonic measurements. The combined results of all measurements give an experimental value with precision of 0.030 ps. With this level of precision, the experimental value provides a strong check on the various theoretical predictions.

BIBLIOGRAPHY

[1] C.-H. Chang, C.-F. Qiao, J.-X. Wang, and X.-G. Wu, Phys. Rev. D **72**, 114009 (2005).

[2] A particular charge state implies the conjugate unless explicitly stated.

[3] CDF Collaboration, F. Abe *et al*, Phys. Rev. D **58**, 112004 (1998).

[4] CDF Collaboration, F. Abe *et al*, Phys. Rev. Lett. **81**, 2432 (1998).

[5] CDF Collaboration, T. Aaltonen *et al.*, Phys. Rev. Lett. **100**, 182002 (2008).

[6] M. Beneke and G. Buchalla, Phys. Rev. D **53**, 4991 (1996).

[7] V. Kiselev, A. Kovalsky, and A. Likhoded, Nucl. Phys. B **585**, 353 (2000).

[8] C.-H. Chang, S.-L. Chen, T.-F. Feng, and X.-Q. Li, Phys. Rev. D **64**, 014003 (2001).

[9] CDF Collaboration, A. Abulencia *et al.*, Phys. Rev. Lett. **97**, 012002 (2006).

[10] D0 Collaboration, V. M. Abazov *et al.*, Phys. Rev. Lett. **102**, 092001 (2009).

[11] CDF Collaboration, A. Abulencia *et al.*, CDF Public Note 9294 (2008).

[12] S. L. and Glashow, Nucl. Phys. **22**, 579 (1961).

[13] A. Salam and J. Ward, Phys. Lett. **13**, 168 (1964).

[14] S. Weinberg, Phys. Rev. Lett. **19**, 1264 (1967).

[15] P. W. Higgs, Phys. Rev. Lett. **13**, 508 (1964).

[16] F. Hasert *et al.*, Phys. Lett. B **46**, 138 (1973).

[17] G. Arnison *et al.*, Phys. Lett. B **126**, 398 (1983).

[18] CDF Collaboration and D0 Collaboration, T. Aaltonen *et al.*, Phys. Rev. Lett. **109**, 071804 (2012).

[19] G. Aad *et al.*, Phys. Lett. B **716**, 1 (2012).

[20] S. Chatrchyan *et al.*, Phys. Lett. B **716**, 30 (2012).

[21] Particle Data Group, K. Nakamura *et al.*, J. Phys. G **37**, 075021 (2010).

[22] M. Gell-Mann, Phys. Lett. **8**, 214 (1964).

[23] O. W. Greenberg, Phys. Rev. Lett. **13**, 598 (1964).

[24] D. J. Gross and F. Wilczek, Phys. Rev. Lett. **30**, 1343 (1973).

[25] H. D. Politzer, Phys. Rev. Lett. **30**, 1346 (1973).

[26] S. Bethke, The Eur. Phys. J. C **64**, 689 (2009).

[27] D. J. Gross and F. Wilczek, Phys. Rev. D **8**, 3633 (1973).

[28] M. Kobayashi and T. Maskawa, Prog. Theor. Phys. **49**, 652 (1973).

[29] N. Cabibbo, Phys. Rev. Lett. **10**, 531 (1963).

[30] B. Andersson, G. Gustafson, G. Ingelman, and T. Sjstrand, Phys. Rep. **97**, 31 (1983).

[31] C.-H. Chang, C.-F. Qiao, J.-X. Wang, and X.-G. Wu, Phys. Rev. D **71**, 074012 (2005).

[32] F. I. Olness, R. J. Scalise, and W.-K. Tung, Phys. Rev. D **59**, 014506 (1998).

[33] W. Beenakker, H. Kuijf, W. L. van Neerven, and J. Smith, Phys. Rev. D **40**, 54 (1989).

[34] E. J. Eichten and C. Quigg, Phys. Rev. D **49**, 5845 (1994).

[35] Y.-Q. Chen and Y.-P. Kuang, Phys. Rev. D **46**, 1165 (1992).

[36] CDF Collaboration, A. Abulencia *et al.*, Phys. Rev. D **75**, 012010 (2007).

[37] V. V. Kiselev, arXiv High Energy Physics - Phenomenology e-prints (2003), arXiv:hep-ph/0308214.

[38] M. Lusignoli and M. Masetti, Z. Phys. C **51**, 549 (1991).

[39] C.-H. Chang and Y.-Q. Chen, Phys. Rev. D **49**, 3399 (1994).

[40] K. G. Wilson, Phys. Rev. **179**, 1499 (1969).

[41] M. Shifman, A. Vainshtein, and V. Zakharov, Nucl. Phys. B **147**, 385 (1979).

[42] M. J. Dugan and B. Grinstein, Phys. Lett. B **255**, 583 (1991).

[43] M. A. Shifman, Nucl. Phys. B **388**, 346 (1992).

[44] L. Reinders, H. Rubinstein, and S. Yazaki, Phys. Rep. **127**, 1 (1985).

[45] A. V. Radyushkin, arXiv High Energy Physics - Phenomenology e-prints (2001), arXiv:hep-ph/0101227.

[46] A. Khodjamirian, QCD Sum Rules - a Working Tool for Hadronic Physics, in *Continuous Advances in QCD 2002*, pp. 58–79, 2002, arXiv:hep-ph/0209166.

[47] L. Reinders, H. Rubinstein, and S. Yazaki, Phys. Lett. B **97**, 257 (1980).

[48] G. Källén, Helv. Phys. Acta **25**, 417 (1952).

[49] H. Lehmann, Nuovo Cimento **11**, 342 (1954).

[50] B. Ioffe, Nucl. Phys. B **188**, 317 (1981).

[51] E. Borel, Ann. Sci. École. Norm. Sup. **16**, 9 (1899).

[52] G. Buchalla, A. J. Buras, and M. E. Lautenbacher, Rev. Mod. Phys. **68**, 1125 (1996).

[53] V. Kiselev, A. Likhoded, and A. Onishchenko, Nucl. Phys. B **569**, 473 (2000).

[54] S. S. Gershtein *et al.*, arXiv High Energy Physics - Phenomenology e-prints (1998), arXiv:hep-ph/9803433.

[55] CDF Collaboration, FERMILAB-PUB-96/390-E (1996).

[56] A. Sill *et al.*, Nucl. Instrum. Methods, A **447**, 1 (2000).

[57] T. Affolder *et al.*, Nucl. Instrum. Methods, A **526**, 249 (2004).

[58] C. S. Hill, Nucl. Instrum. Methods, A **511**, 118 (2003).

[59] P. Nason, S. Dawson, and R. Ellis, Nucl. Phys. B **303**, 607 (1988).

[60] P. Nason, S. Dawson, and R. Ellis, Nucl. Phys. B **327**, 49 (1989).

[61] D. J. Lange, Nucl. Instrum. Methods, A **462**, 152 (2001).

[62] J. Freeman, FERMILAB-Conf-87/230 (1987).

[63] E. Gerchtein and M. Paulini, arXiv Physics e-prints (2003), arXiv:physics/0306031.

[64] S. Rolli, J. D. Lewis, H. Ray, J. Nachtman, and M. Worcester, Hardware Trigger Simulation at CDF, in *Proceeding of International Conference on Computing in High Energy and Nuclear Physics*, 2000.

[65] M. Cacciari, S. Frixione, M. L. Mangano, P. Nason, and G. Ridolfi, J. High Energy Phys. **07**, 033 (2004).

[66] F. James and M. Roos, Comput. Phys. Commun. **10**, 343 (1975).

[67] CDF Collaboration, T. Aaltonen *et al.*, Phys. Rev. Lett. **100**, 161802 (2008).

[68] L. Demortier and L. Lyons, CDF Public Note 5776 (2002).

[69] P. T. Lukens and W. Wester, (Private Communication).

[70] CDF Collaboration, T. Aaltonen *et al.*, Phys. Rev. Lett. **106**, 121804 (2011).

[71] R. Barlow, arXiv Physics e-prints (2004), arXiv:physics/0406120.